Search for anisotropies in the arrival directions of charged cosmic rays with AMS-02

Zur Erlangung des akademischen Grades eines

DOKTORS DER NATURWISSENSCHAFTEN

an der Fakultät für Physik des
Karlsruher Institut für Technologie (KIT)

angenommene

DISSERTATION

von

Dipl.-Phys. Stefan Zeißler
aus Darmstadt

Tag der mündlichen Prüfung: 2. Februar 2018

Referent: Prof. Dr. Wim de Boer
              Institut für Experimentelle Teilchenphysik

Korreferent: Prof. Dr. Ulrich Husemann
              Institut für Experimentelle Teilchenphysik

I declare that I have developed and written the enclosed thesis completely by myself, and have not used sources or means without declaration in the text.

Karlsruhe, January 17th, 2018

. . . .
(Stefan Zeißler)

Contents

Introduction

The story of astroparticle physics started about 100 years ago when Viktor Hess discovered an ionizing radiation of extraterrestrial origin in a series of balloon flights in 1912. His discovery of what was later called cosmic radiation (CR) was awarded with the Nobel prize in 1936 and led towards the founding of the new field applying methods of particle physics to the field of astrophysics and cosmology. The particle nature of cosmic rays was settled by Bothe and Kolhörster in 1929 shortly after its discovery.

Later on, the observation of a latitudinal variation in the cosmic rays intensity proved that the particles are deflected by the Earth's magnetic field and consequently are charged and, as a follow-up, a longitudinal variation known as "East-West-Effect", proving that the charge is mostly positive. The measurement of the East-West-Effect was the first observation of an anisotropy, a directional dependence in the cosmic rays flux with high impact on the understanding of the phenomenon.

Even though without its origin revealed, a series of discoveries was made studying cosmic radiation as a source of particles, such as the first detection of antimatter in the form of the positron, as predicted in theories of Paul Dirac, by Carl Anderson in 1932 (Nobel prize 1936). Other examples are the discovery of the muon in 1937, which extended the particle zoo with one more leptonic family, and the pion as first proof of the strong interaction in 1947.

In today's picture, cosmic rays consist of mainly protons, heavier nuclei, electrons, positrons, gamma rays, and neutrinos. Their origin still is an item of constant debate, pinned down to an unknown high energetic extragalactic contribution and a galactic component at lower energies, believed to originate from shell *supernova remnants* (SNR).

With the development of particle accelerators in the 1950s, cosmic rays lost some of their impact, when particle interactions could be studied in a controlled environment independent from nature. From these experiments, a *standard model of particle physics* (SM) was established with tremendous success in explaining most observations and predicting unknown phenomena. At the same time, the understanding of the universe has been pushed forward by continuous observations finding its peak in the discovery of the *Cosmic Microwave Background* (CMB) by Penzias and Wilson in 1965 (Nobel prize 1978) as it has been predicted by the big bang theory. The confirmation of this nowadays widely accepted model, in which the universe has been created in an infinitely small point expanding ever since, showed the deep understanding of the universe but also revealed observations which are in contradiction to particle physics knowledge. To provide a complete picture both, the observation of the huge universe as well as the studies of the tiniest particles, have to complement one another.

A major point in which the SM struggles is to provide a mechanism in which the observed matter-antimatter asymmetry is explained. In SM scenarios matter and antimat-

ter are produced in the same quantities while the observable universe demands a matter dominated production. Another burning question addresses a mismatch between mass needed in a stable universe and the mass that can be observed. First hints of this later called *Dark Matter* (DM) were seen in the rotation of galaxy clusters by Fritz Zwicky in 1933 and the confirmation in the smaller pendant of galactic rotation curves by Vera Rubin since the 1960s.

An estimate of the contributing mass of DM to the universe, which amounts to 83% of the total mass, is gathered from the analysis of small-scale anisotropies in the CMB. In most models that try to explain the nature of the Dark Matter a novel particle, so far not discovered or closely restricted by measurements, is assumed. If the hypothetical Dark Matter particle is a thermal relic from the early Universe, created by energetic collisions of standard model particles, it must annihilate into standard model particles today wherever the Dark Matter density is high enough. Such annihilations yield pairs of protons and antiprotons, electrons and positron, as well as photons and neutrinos as their stable annihilation products - the same particles that constitute cosmic rays. The discovery potential puts cosmic rays as a mediator between particle physics and cosmology back in focus.

With the installation of the Alpha Magnetic Spectrometer (AMS-02) aboard the International Space Station (ISS) in May 2011, a new era in the research of charged galactic cosmic rays started. By measuring charged cosmic rays outside of any disturbing atmospheric influences with a precision never seen before, the model predictions for cosmic rays propagation are challenged. Structures in the flux of positrons [1–4], protons [5], and helium [6] can currently not be explained by consistent propagation scenarios. A straightforward solution to this problem is to assume non-standard sources of cosmic rays within the local environment or to introduce modifications to the local diffusion. Most of such scenarios come with a directional variation of the cosmic rays arrival direction, referred to as anisotropy.

It is to note that magnetic fields in the *Interstellar Medium* (ISM) deflect charged particles and thereby cover up all information about the origin. Moreover, the flux is made highly isotropic, and structures in the spectra are washed out. To interpret the measured data, the journey of a CR particle from its source to the detector, referred to as propagation, has to be modeled using only information accessible from Earth. The measurement of an anisotropy in the fluxes might point to non-standard local sources which are needed for the interpretation of all measurements in charged cosmic rays. Such a signal would be expected in particular at high energies where statistics is low, which makes the measurement a challenging task.

To measure a variation in the particles flux the hypothesis of isotropy first needs to be constructed and compared to the measured data. Since no detector is perfectly isotropic, scans the sky isotropically, and every detector is subject to time- and direction dependent operational instabilities, an image of an isotropic sky measured with the detector in the respective data taking period needs to be created. Any significant deviations from this picture may then be detected as anisotropy. The hypothesis of isotropy can be created in multiple ways and is called *reference map*.

Attempts in finding directional dependent signals in charged cosmic rays have been published by many experiments proposing several analysis methods with different constructions of reference maps, most of which cannot be applied to AMS-02 for its small

field of view and the rough orbit conditions. Often a measurement is done by normalizing particle counts to a reference particle of another species which is assumed to be isotropic on a high level. However, this approach is limited in significance and results are not straightforward to use in interpretation as numbers are only given *relative* to the reference particle, which can introduce a bias. Moreover, this approach is not available for all particle species measured by AMS-02. A map of the *absolute* distribution of particles incoming direction that can be applied to all particle species is desired to study the incoming directions in multiple coordinate systems to enhance signals of different origin and thereby identify its source.

In the framework of this thesis, a novel method to construct a map of the isotropic sky, as it would be seen by the detector, based on fundamental detector characteristics such as the livetime and acceptance was developed and applied to AMS data. This method, for the first time, allows to construct reliable limits on the absolute anisotropy in the arrival directions of cosmic rays. Limits on the absolute dipole anisotropy of positrons, electrons and protons are reported using data taken with AMS-02 in the period from May 2011 to May 2016. In total, 69,394 positron and 913,421 electron events were selected in an energy range from 16 GeV to 350 GeV, and 51 million proton events were selected in a rigidity range from 18 GV to 1800 GV.

Chapter 1 gives an overview of the physics of charged cosmic rays, their origin, and propagation. Even though cosmic rays arrive at Earth in a high level of isotropy, scenarios will be introduced which are capable of introducing an anisotropy of some level and what can be learned from making such an observation. Also, an overview of currently available results in search of anisotropies in the cosmic rays arrival direction by other experiments will be given. In Chapter 2, the AMS-02 detector is presented. A detailed understanding of the detector capabilities, its functionality, and its operation is crucial to understand effects that propagate to data maps and therefore directly to the analysis of directional information. The tools which were used or developed for the analysis presented in Chapter 4 are introduced in the previous Chapter 3. Finally, in Chapter 5 the obtained results will be discussed and put in context to other experiments and expectations from the theory presented earlier. The work will be concluded in Chapter 6.

1. Propagation and sources of cosmic rays

The observation of cosmic radiation started in 1912 with its discovery by Viktor Hess who monitored the rate with which electroscopes discharged with the altitude above sea level in a series of balloon flights. The loss of charges in an electroscope is caused by ionization from a background radiation assumed to be of geological origin at that time. Viktor Hess proved that the rate of ionization increases with altitude which contradicts this assumption and suggested a source outside of the Earth's atmosphere. Measurements during nights and solar eclipse disfavored a solar origin of the background radiation, later established as cosmic rays (CRs).

Since then CRs have been continuously under study and provided fundamental knowledge about the universe and our galaxy. Their origin, however, is still not fully understood even though progress was made in answering this question involving a large number of experiments all over the world and even in outer space.

1.1. Origin and propagation of charged cosmic rays

Cosmic rays have been introduced as ionizing radiation of interstellar origin. They spread over a huge energy range over many orders of magnitude from keV up to EeV. Figure 1.1 shows the spectrum of the flux of CRs over this range in energy. The flux quantifies the number of particles with energy E, measured in GeV, that are expected to cross a virtual area of 1 m^2 in one second per opening angle in steradian (sr). Because of the huge energy range, the flux is measured by a variety of experiments dedicated to a fraction of this energy range. The spectrum decreases rapidly, such that huge detection areas are needed to collect a reasonable amount of high energetic CRs. For example, only one particle with kinetic energy greater than 10 PeV is expected to cross an area of 1 m^2 per year. The flux is well described by a power law of $\Phi(E) \propto E^{-\gamma}$ and γ ranging between 2.7 and 3.0. A break in the all-particle spectrum shows up at 10^{15} eV, called the *knee*, as in combination with a hardening at higher energies, called the *ankle*, the spectrum follows a shape similar to a human leg. In general, all these features are only visible if the shapes are magnified with weighting the flux by some power of the energy. The knee is followed by a second, weaker, one at 10^{18} eV.
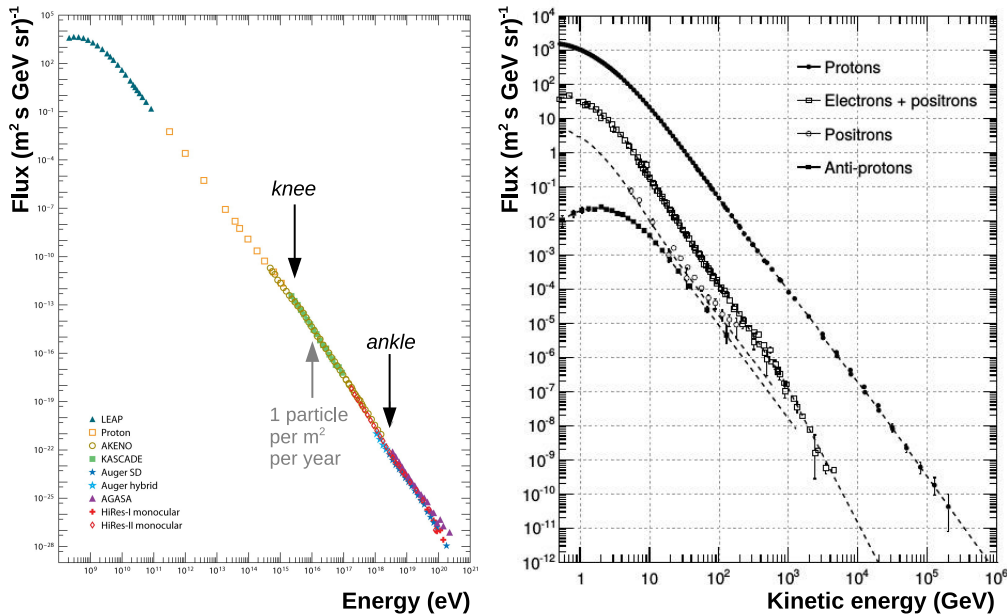
Figure 1.1.: **Left:** Spectrum of the flux of CRs over a wide range with energy [7]. Two spectral features, the *knee* and *ankle* are marked. **Right:** Spectra of the singly-charged components of cosmic radiation as function of kinetic energy up to the *knee*, measured by different experiments before AMS-02. For each species, the dashed line represents a weighted average of recent measurements [8].

In general, CRs consist of a variety of charged particles including electrons, positrons, protons, and heavier nuclei and an uncharged component of gamma rays and neutrinos which, even though of great importance for astroparticle physics, will not be discussed in the frame of this Thesis. On the right-hand side of Figure 1.1, the CR spectrum is shown separately for different particles of unit charge up to an energy of PeV. Towards higher energies, the identification of a particle is harder to achieve, as it will be discussed later in this section, and composition measurements are stated. The CR flux is largely dominated by protons, which make up about 90% of the charged component.

Because of the charge, CR particles scatter at magnetic turbulences in interstellar magnetic fields and lose all information about their origin on the way to Earth. They also interact with interstellar material. Any information on the source and the propagation has to be modeled using statistical methods, which makes the particles local spectra and chemical composition a valuable information desired to be known with high precision. Features in the spectrum are directly connected to the underlying physical process. In fact, the *knee* and the *ankle* carry the most fundamental information about the origin of CRs, as they are interpreted to form a transition of particles with a galactic origin, towards an extragalactic source starting to contribute significantly. AMS-02 has been designed for the measurement of charged cosmic particles with energies up to TeV, and therefore galactic origin.

An indication of where Galactic CRs are produced can be obtained from measurements like the one presented in Figure 1.2. In there, the composition of Galactic CRs is compared to their abundance in the solar system, which is of a similar level for most elements. Differences in lithium, beryllium, and boron, and in the sub-iron region (Z=22 to Z=25) bear information on the propagation process; they are produced in interactions of heavier nuclei with the interstellar medium (ISM), so-called secondary production. The
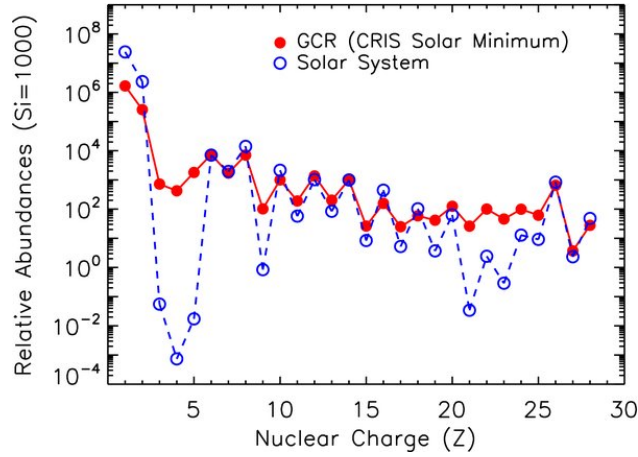
Figure 1.2.: Comparison of the relative composition of galactic cosmic rays during solar minimum, as measured by the CRIS experiment at energies below GeV/nucleon, to the solar system chemical abundance [9]. The data are normalized to Si=1000. The similar composition suggests that both quantities are of the same environmental origin. Differences observed for lithium, beryllium, and boron, and in the sub-iron region (Z=22 to Z=25) are explained by secondary production of these elements in interactions of the abundant proton and helium nuclei with the ISM.

similarities for most of the species imply that galactic CRs originate in an environment similar to the solar system.

While the sun itself can only be a local source of low-energetic electrons and protons, it is commonly believed that Galactic CRs are formed mainly in shell supernova remnants (SNR). A supernova marks the end of the fusion activity of a massive star with 1.4 solar masses or more. At this point, where the fusion pressure cannot counteract the stars gravitational force anymore, the star collapses and is wiped out in an explosion where an enormous amount of matter is ejected into space. In this state, the temperature is high enough to enable the synthesis of higher charge nuclei up to iron, which explains the observed CR composition discussed before. The ejected matter forms a front of charged particles and strong magnetic fields. Assuming a supernova explosion in the galaxy once every 50 years with an energy budget of 10^{51} erg, a power of about 5×10^{41} erg/s is emitted into the galactic space. To explain the measured cosmic rays power of 3×10^{40} erg/s, 1% to 10% of the supernova's energy has to be converted into CRs acceleration, which is in good agreement with current supernova models. In fact, supernovae have been found to be a source of cosmic rays in X-ray observations of high energy electrons' synchrotron radiation, bremsstrahlung, and inverse-Compton radiation, as well as neutral pion decay produced in inelastic collisions between energetic ions and thermal gas. However, supernovae cannot explain all cosmic rays observations and cannot be used to constrain cosmic rays acceleration models in detail, yet [10].

In a first approach to create an acceleration mechanism of CRs, based on the observed power-law behavior of the spectra, Enrico Fermi suggested a statistical acceleration process from elastic collisions of charged particles with moving magnetic clouds [11]. Magnetic clouds are not capable of accelerating charged particles from their enclosed magnetic fields, as they are not capable of performing work. An exchange of energy that can be negative or positive results from collisions with the moving objects. Fermi noticed that the net energy gain in such a diffusive process is positive. However, because of the isotropic distribution of the cloud velocities $\vec{u}$, the mean energy gain in such a process
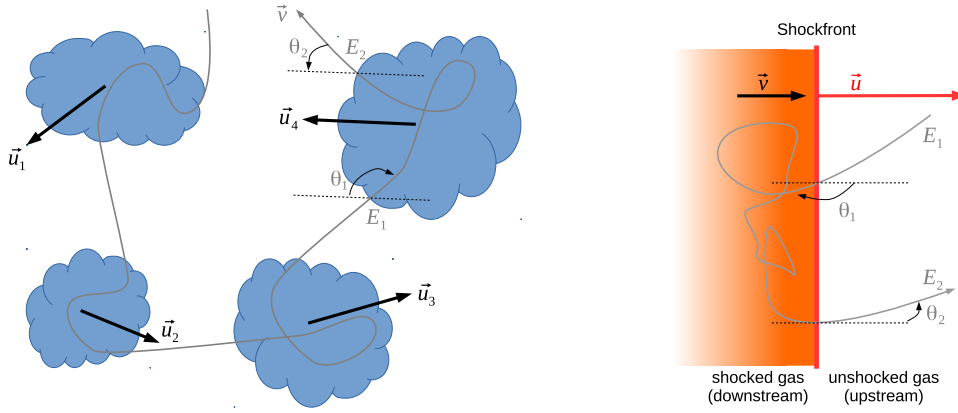
Figure 1.3.: Fermi Acceleration of first and second order. **Left:** Stochastic acceleration from in-
elastic scattering on moving magnetized could, or *second-order* Fermi acceleration.
Right: Diffusive shock acceleration, or *first-order* Fermi acceleration. A gain in effi-
ciency is achieved by the directed shock front acceleration, rather than the diffusive
process. Diffusive shock acceleration is believed to be the dominant injection process.
Stochastic acceleration causes re-acceleration in the propagation of CRs.

is only of second order $(\frac{u}{v})^2$, where v is the velocity of the relativistic charged parti-
cles. Therefore, the mechanism is inefficient, and acceleration rates are low. The basic
principle of this so-called *second-order* Fermi acceleration, is sketched on the left side of
Figure 1.3. It has been realized that the same principle can be adapted to the so-called
diffusive shock acceleration (DSA) [12], or *first order* Fermi acceleration (even though
not invented by Fermi himself).

In a shock wave, a reference frame exists in which charged particles scatter off magnetic
fields similar to inelastic collisions at the shock front and gain energy linear in the speed
of the shock wave $(\frac{u}{v})$. With every crossing of the shock front, the particle gains energy
with a constant factor $\rho = \frac{\Delta E}{E}$. After n interactions of this kind, a particle of initial
energy E_0 has accumulated an energy of $E_n = E_0(1 + \rho)^n$. With every interaction the
particle has a probability $p_{esc} = \frac{\Delta N}{N}$ of leaving the acceleration process, resulting in a
number of particles that still take part after n interactions of $N_n = N_0(1 - p_{esc})^n$. From
here, the number of particles after n interactions can be calculated to $N_n = N_0 \left(\frac{E_n}{E_0}\right)^p$
with $p = \frac{ln(1-p_{esc})}{ln(1+\rho)}$. Integrated over the energy the spectral shape is calculated to be of a
power law shape

$$\frac{dN}{dE} \propto \left(\frac{E}{E_0}\right)^{-\gamma} \quad . \tag{1.1}$$

With input from models $\gamma = (p + 1)$ ranges from 2.1 to 2.4, which is softer than the ob-
served γ ranging between 2.7 and 3.0. The softer spectrum is explained by energy losses
and escape from the galaxy, which is more likely for higher energies, during propaga-
tion. In a consistent picture, CR particles are injected into the propagation process by
efficient acceleration in a shock front and are re-accelerated in magnetic clouds on large
timescales.

A measure of the timescales CRs spend in the diffusion process can be gathered from
non-stable isotopes, so-called *cosmic clocks*. A widely used isotope is beryllium-10 with
a half-life of 1.39×10^6 years, beryllium-9 is stable. The observable is the ^{10}Be/^{9}Be-ratio,
which decreases during propagation due to the decay of ^{10}Be. As discussed from Figure
1.2, beryllium is produced in secondary interactions of mainly protons with the ISM.
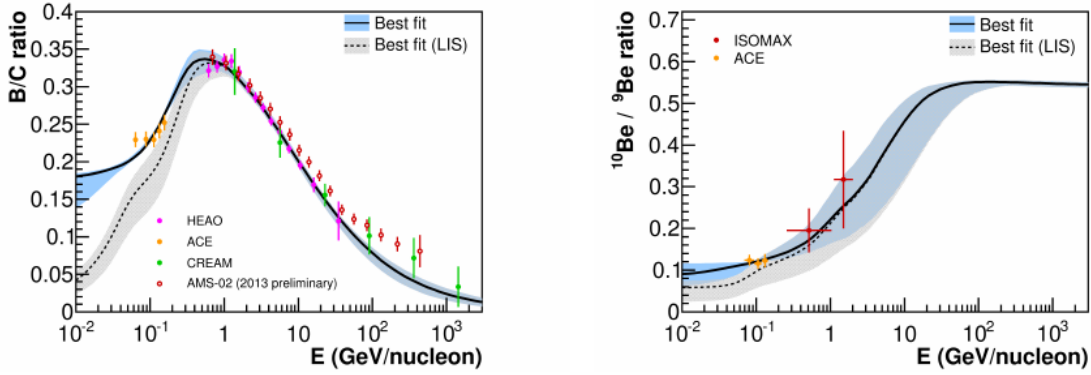
Figure 1.4.: Observables that are used to constrain basic parameters in the propagation process with a prediction from propagation models [13]. **Left:** A collection of measurements of the B/C ratio. From the ratio of secondary to primary particles the interaction rate of CRs with the ISM can be derived. **Right:** A collection of measurements of the ^{10}Be/^{9}Be ratio. From the ratio of unstable to stable isotopes, the confinement time of CRs in the galaxy is derived. The blue band denotes a set of models that describe the data at position of the Earth taking solar modulation into account. The grey band represents the same models in the local interstellar medium (LIS), outside of the Heliosphere.

From fixed-target experiments, the production ratio of ^{10}Be/^{9}Be can be measured and used as ratio at injection time. The production ratio is compared to the measurement of the same quantity at the Earth after the propagation. With the known half-life time of Beryllium-10, the age of CRs can be restricted to $\tau_{esc} \approx 10^7$ years.

A similar approximation can be made for the matter density of the ISM, that CRs traverse, from the ratio of secondary over primary CRs. A typical example would be the B/C ratio, where carbon is produced in the Supernova and injected in propagation. Boron is produced by fragmenting carbon with the ISM C+ISM→B+p+X. From the fraction of boron, produced in interactions, in the flux of primary carbon the interaction rate can be evaluated. Data of the ^{10}Be/^{9}Be and B/C ratio with a model fit are shown in Figure 1.4. The combination leads to the conclusion that CRs are part of the propagation process for a long time, but spend most of the diffusion time in the Galactic Halo of low density.

During propagation, CRs experience energy losses depending on their interaction cross-sections. Nuclei suffer mostly ionization and Coulomb scattering in the ISM. Lightweight electrons are subject to significant energy losses due to synchrotron radiation, inverse Compton scattering, and emission of bremsstrahlung. Figure 1.5 gives an estimate of the energy loss times with energy, dependent on the CR particle. While protons and heavier nuclei have loss times larger than their escape time τ_{esc}, the propagation process for electrons and positrons is limited by the efficient loss of energy in the galactic magnetic field.

1.1.1. Isotropy of CRs and challenges for transport models

Due to the long propagation time in the galactic magnetic fields, CRs lose all directional information about their source and get isotropized to a high degree. An angular anisotropy is expected from the galactic center, where the source density is high, such that the effective diffusion direction is away from the center. Only nuclei could be sensitive to
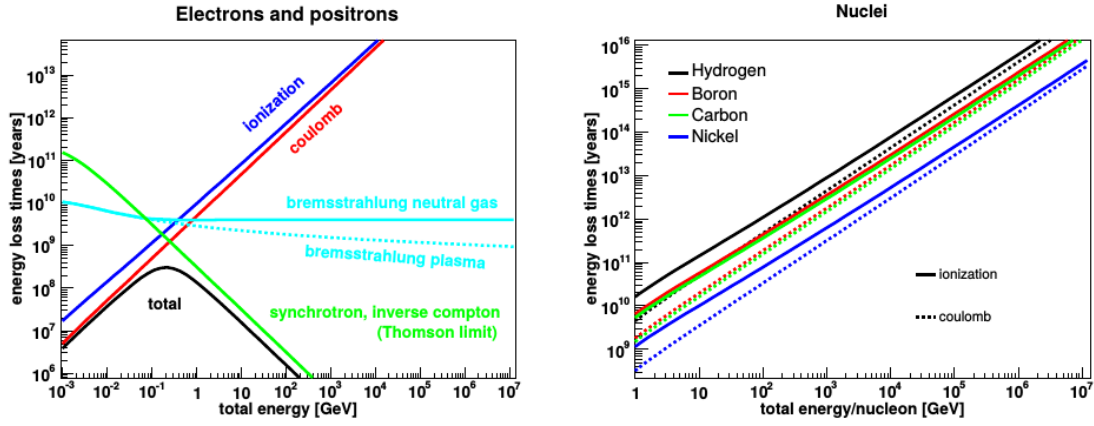
Figure 1.5.: Estimate of the time in which CRs lose their kinetic energy [14]. A smaller time means a more efficient energy loss. **Left:** Energy loss for electrons and positrons. Towards higher energies, synchrotron radiation and inverse Compton scattering efficiently limit the energy loss time, and therefore the distance of propagation for electrons and positrons. For the calculation, the energy density of photons and the magnetic field have been assumed to be identical (Thomson limit) at 1 eV/cm^3. **Right:** Energy loss time for nuclei. Here ionization and Coulomb losses are dominant which allows for an increased propagation distance, compared to electrons. An average gas density of n_{ISM}=0.01/cm^3 is assumed.

such an angular dependence, for their long propagation time. As the particles get more resistant to deflections from magnetic fields towards higher energies and, at the same time, energy losses become less efficient, the sensitivity to such an anisotropy rises with increasing energy. For leptons, the propagation length is limited by the efficient energy losses, as described. Only in the presence of a local source, an angular anisotropy would be expected.

Recent measurements by AMS-02 challenge our understanding of CR transport. Figure 1.6 shows the fraction of positrons in the flux of electrons and positrons, the so-called *positron fraction* [1, 2]. In the standard paradigm of CR transport, positrons are believed
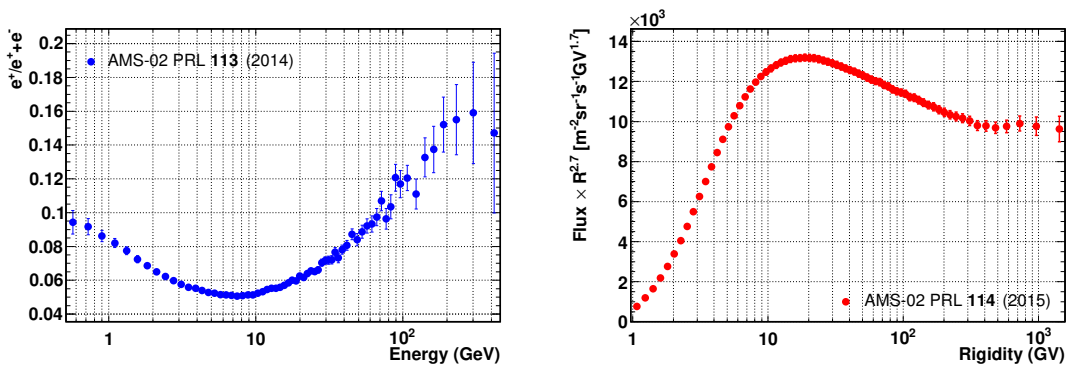
Figure 1.6.: AMS-02 Measurements of the positron fraction **(left)** [2] and the proton flux **(right)** [5]. Both measurements show features, which were not expected by the standard paradigm of CR propagation. Both the features might be connected to additional exotic sources.
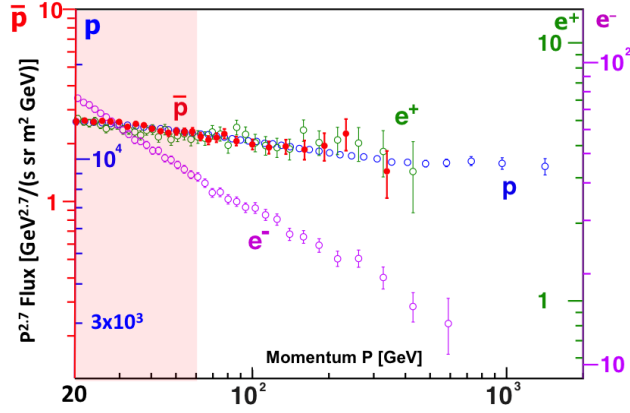
Figure 1.7.: AMS-02 particle flux measurements of protons [5], anti protons [15], electrons, and positrons [3] at momentum larger than 20 GeV. The fluxes are plotted with individual y-axis, scaled in such a way that the fluxes are overlayed, and the spectral shape can be compared.

to be produced purely as secondaries from the interaction of protons with the ISM

$$p + X_{ISM} \rightarrow X^* + e^+ \quad .$$
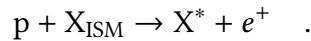
At the place of interaction the positron flux, therefore, follows the flux of protons, which is assumed to be the same as measured at the Earth's position, convoluted with the energy dependence of the production cross-section, which is weak. The different energy losses during propagation cause a migration of the positron flux with energy which has to be modeled. Electrons, on the other hand, are mainly produced as primary CRs and directly injected in the propagation process. In this standard paradigm, a positron fraction decreasing exponentially with energy is expected. The measurement reveals a significant rise at energies above 10 GeV, which can be explained by an additional population of positrons. This observation cannot be explained in the standard picture and suggests a non-standard source of positrons. As already argued, the efficient energy loss in positrons and electrons demands a sufficiently local production of the exotic positron population. In the following sections sources in discussion will be introduced, but first, the picture of CR propagation painted by AMS-02 needs to be completed.

The right-hand side of Figure 1.6 shows the measurement of the proton flux up to a rigidity of 1.8 TV [5]. The rigidity R is a measure commonly used in astroparticle physics and describes the bending of a trajectory in a magnetic field which is proportional to the particle's momentum divided by the absolute charge. The flux is multiplied by $R^{2.7}$ to emphasize a hardening in the flux at rigidities larger than 300 GV. The deviation from the expected power law behavior needs to be connected to a change in the propagation mode, or an additional source of protons. Such a source would be, from current knowledge, completely independent from the positrons. In the helium flux a hardening, similar to the one in the proton flux, is observed [6].

Figure 1.7 shows the flux of primary protons and electrons together with secondary antiprotons and positrons with momentum larger than 20 GeV. The y-scale is set individually for every particle such that the fluxes are overlayed, and the spectral shape can be compared. It is remarkable that the flux of antiprotons and positrons precisely follows the spectral shape of the protons. The electron flux is more steep, which can be understood from the faster energy losses of electrons compared to protons, if both are

produced in the same source. The same would be assumed for the positrons, which is not confirmed by the measurement. Positrons are produced locally in the interaction of primary protons in the ISM and then propagated to detection at the position of the Earth. During propagation, the positrons suffer more energy losses than antiprotons, which are a pure secondary as well, and the spectrum is expected to become steeper. A possible explanation for the same spectral index of positrons and antiprotons could be a local production of positrons, which corresponds to a short propagation time with no significant energy loss. However, the ratio of unstable isotopes limits the propagation time, as discussed. A detailed discussion on limits of local production can be found in [16].

In conclusion, AMS-02 observations challenge the standard paradigm of CR propagation in the galaxy without suggesting a consistent alternative. Promising explanations for the excess in the positron fraction in form of Dark Matter annihilation [17–31], astrophysical sources [32–42], or exotic secondary production [43–48] are widely discussed in the literature. If the additional positron population or the hardening in the flux of protons is produced by an astrophysical source, an anisotropy in the particles arrival direction is expected. In the case of DM annihilation, such an anisotropy in the produced standard model particles would not be expected. Between the different hypothesis, the measurement of the anisotropy is a powerful discriminating variable.

1.2. Exotic sources of CRs

Various hypotheses on the source of exotic positrons are discussed in the literature, two of which are commonly favored: pulsars, and Dark Matter annihilation. The two represent two different types of sources which are point-sources, in the case of pulsars, and diffusive distributed sources, in the case of Dark Matter. The point-source type would inject particles at one or more specific positions, and therefore, delivers the particles dominantly from this direction in the sky which could be observed as an anisotropy. A diffusive distributed source would inject particles isotropically and consequently without anisotropy. If an anisotropy is found or excluded up to a high degree, one or the other source type can be excluded.

1.2.1. Pulsars

Pulsars are fast-spinning neutron stars with a strong magnetic field. Neutron stars form as a leftover from a massive star's collapse at the end of its fusion process. The high gravitational pressure pushes electrons into the atomic core, where they interact into neutrons via $p + e^- \rightarrow n + \nu_e$. Neutron stars are of a high density of the order of the atomic nucleus, with a size of a few 10 km in radius. Due to the conservation of angular momentum during the collapse, the star rotates fast with a period of seconds, reaching relativistic velocities at the surface. At this point, the neutron star becomes a pulsar. The magnetic field axis is tilted with respect to the rotation axis, such that radio signals, emitted in a light cone at the magnetic poles, are observed as pulses similar to a lighthouse. The first pulsar (PSR1919+21[1]) was discovered in 1967 in a series of regular radio pulses with a period of 1.33 s.

---

[1]The measured radio pulses that lead to the discovery of PSR1919+21 are used in the artwork for the cover of the post-punk band Joy Division's first album *Unknown Pleasures*, and became an iconic icon in the Indy-rock scene.
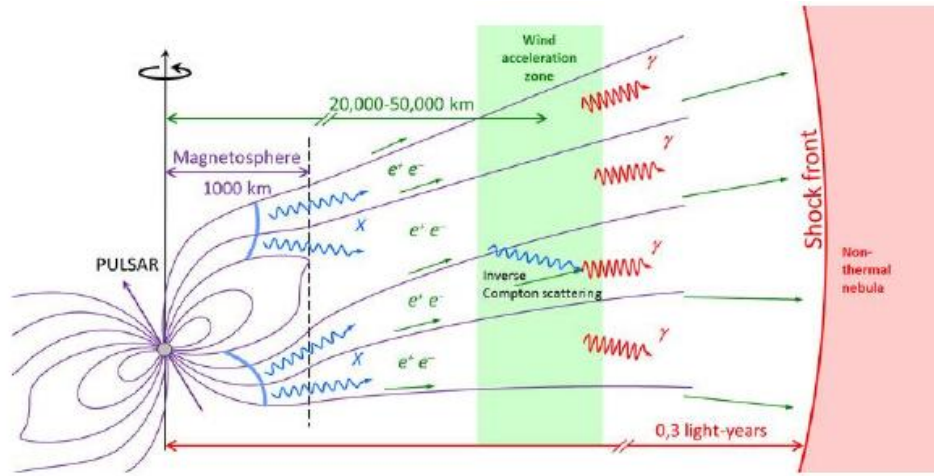
Figure 1.8.: Schematic view of a pulsar [49]. Charges on the surface create the pulsar's magnetosphere with high magnetic field strengths. Particles are removed from the pulsar's surface by the strong magnetic field and flow into the magnetosphere following the magnetic field lines. Towards the poles, magnetic field lines cannot flow back, without violating the speed of light limitation, and particles can escape into the interstellar space.

On the surface, where the gravitational pressure is smaller, heavier nuclei, mainly iron, with residual electrons are still present. The fast rotation of charges creates the pulsar's magnetosphere with high magnetic field strengths. The high magnetic fields pull out surface electrons, which flow into the magnetosphere as electric current, following the magnetic field lines. The surface electrons emit highly energetic synchrotron radiation from the curved trajectory in the pulsar's magnetosphere from which secondary electron/positron pairs are produced. In an electromagnetic cascade thousands of electron/positron pairs are produced from a single surface electron.

The pulsar's magnetosphere reaches an expansion at which magnetic field lines cannot flow back to the pulsar's surface without violating the speed of light limitation. The field lines are *open* towards the magnetic poles. In this so-called *light cylinder*, particles can escape the environment and can be accelerated in the interstellar space. Figure 1.8 shows the pulsars magnetosphere environment the creation process of the electron/positron pairs in a schematic view.

The injection of electron/positron pairs into the CRs propagation process is widely accepted in the literature to explain the features in the positron spectra. Positrons created in a nearby pulsar could provide an explanation for the rise in the positron fraction. The production in the interstellar neighborhood, of distances smaller than the positrons energy loss range, would induce an anisotropy in the angular arrival direction of positrons, which might be detected by experiments. The hypothesis is explored in propagation models, e.g. in [50], with focus on an induced anisotropy as discriminating variable.

1.2.2. Dark Matter searches in galactic cosmic rays

The observation of a massive invisible component in the mass distribution of galaxy clusters, first measured in 1933, is one of the most striking aspects of astroparticle physics and cosmology, in the recent years. The existence of *Dark Matter* (DM) has been established in a variety of independent observations on various scales. Still models, DM
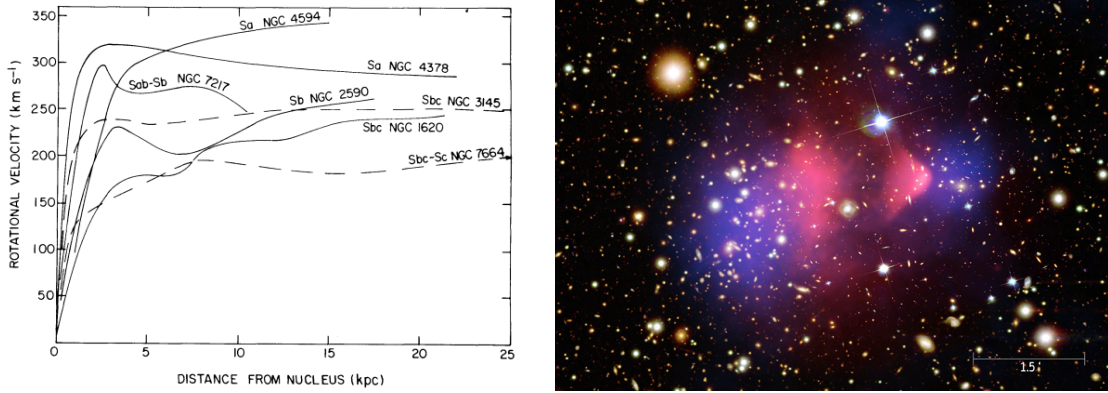
Figure 1.9.: Observations that are explained by the presence of Dark Matter. **Left:** Rotational curve of seven spiral galaxies, measured through their redshift. A roughly constant orbit velocity is measured with the distance to the galactic center, which is in contradiction to the expectation from the visible mass distribution in the disk [52]. **Right:** Overlay image of the Bullet Cluster composed of a picture in the visible spectrum by the Hubble space telescope, gas distribution in pink from x-ray observations by the Chandra telescope, and the mass distribution from gravitational lensing in blue [53].

interacts with standard particles with couplings typical for weak interaction, and matter and antimatter could be produced in pairs. It is considered as an exotic source of CRs.

1.2.2.1. Evidence for Dark Matter

First observations linked to DM were made by the observation of the mean velocity of the galaxies in the Coma Galaxy Cluster, measured via the individual galaxies redshift [51]. With classical mechanics calculations, it was concluded that the cluster of more than 1000 galaxies cannot be bound together from the gravitational pull of the visible matter alone. An additional invisible form of matter, by a factor of 400 more massive, was assumed to exist within the cluster, therefore the term *Dark Matter*.

The same effect was observed in the rotation curves of spiral galaxies starting in the 1960s. It was measured that the orbit velocity of stars stays more or less constant with their distance to the galactic center. From the visible matter in a galactic disc alone, a decrease in orbit velocity would be expected following Kepler's law. The centrifugal force would slingshot the matter out of the gravitationally bound system. The left-hand side in Figure 1.9 shows the measured rotational curve of seven spiral galaxies. All show the described behavior which is consistent with a uniform, roughly spherical, mass distribution surrounding the galactic disk, the so-called *Halo*.

In more recent measurements, more observations could be made that confirmed the presence of DM as a significant contribution to the universe's matter budget. With the method of gravitational lensing, mass distributions can be determined, even if they do not interact electromagnetically. In general relativity, a mass can bend the path of light. The effect is observed if a large mass accumulates between an observer and a distant light source. One of the most convincing observations interpreted by the existence of DM, using the technique of gravitational lensing, has been made with the discovery of the *Bullet Cluster*. It consists of two independent galaxy clusters colliding. Because of interactions between atomic matter, the two clusters merged, which can be seen visibly and is confirmed by x-ray observations. The two massive components, determined by
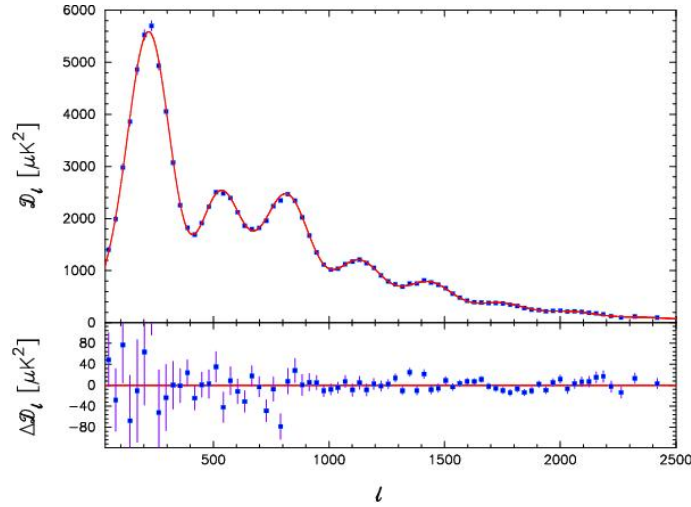
Figure 1.10.: Planck CMB power spectrum compared with a ΛCDM model with the residuals below [61]. The power spectrum shows irregularities at different angular scales which are connected to the evolution, and the matter and energy content of the universe.

gravitational lensing, passed without visible disturbance. An overlay image in the different observation channels of the Bullet Cluster is shown on the right-hand side of Figure 1.9.

The Bullet Cluster reveals an important property of the Dark Matter: It is barely interacting with atomic matter or itself. As no particle matching these requirements is known in physics, an exotic new form of matter is widely assumed to constitute DM.

On a side note, since the discovery of neutrino oscillation during the last years, it is commonly established that neutrinos carry mass [54, 55]. Even though the mass of the different neutrino generations has not been measured yet, upper limits on the mass are in the order of eV, which is too small for neutrinos to be bound gravitationally [56]. Nevertheless, neutrinos do contribute to the DM budget as so-called *Hot* Dark Matter, the highly relativistic fraction of the overall Dark Matter budget. In recent years, theories of *Warm* Dark Matter (WDM) got more attention. Candidates are exotic particles like sterile neutrinos or axions [57–60].

A class of CDM candidates is exotic Weakly Interacting Massive Particles (WIMPs). Cosmological models from the observation of the Cosmic Microwave Background (CMB) are consistent with a dominating *Cold* Dark Matter (CDM) component, and therefore massive particles. Observations of the angular distribution of the CMB are evidence for a cosmological model with CDM and an accelerated expansion of the universe, born in a Big Bang. The CMB is a (thermal) relict of the early universe, in which a plasma of charged particles was in thermal equilibrium under the exchange of photons, and cooled down by expansion. At a critical temperature, the particles bound and formed neutral hydrogen atoms. The universe suddenly got transparent for residual photons which form a snapshot of the freeze out, about 380,000 years after the Big Bang. In the first order, the CMB is an isotropic blackbody spectrum with temperature T_{CMB}=2.726 K. On a 10^{-5} level irregularities on different angular scales can be observed. Figure 1.10 shows the CMB power spectrum, measured by the Planck satellite with a fit of a ΛCDM model, where Λ is the cosmological constant, associated with Dark Energy. The model fits the data extremely well.
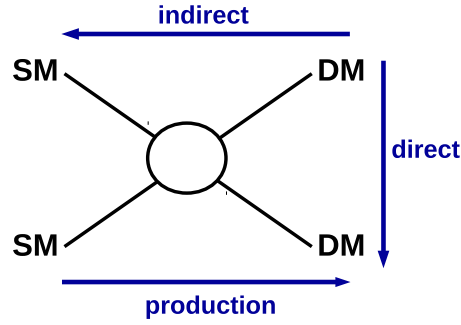
Figure 1.11.: Dark Matter to Standard Model Matter interaction graph to show the three search categories for WIMP DM. Depending on the time axis, interaction can be interpreted as a scattering process (direct search), a production process (collider production), or a decay process (indirect search).

1.2.2.2. Searches for Dark Matter

In the Standard Model of particle physics (SM) no WIMP candidate is provided. A promising candidate is contained in supersymmetric extensions to the SM. Supersymmetry provides a group of models in which each fermion is associated with a bosonic partner with same quantum numbers but the so-called R-parity $R = (-1)^{3(B-L)+2s}$, with the baryon number B, the lepton number L, and the spin s. SM particles have R=+1 assigned, supersymmetric particles R=-1. Interactions need to preserve R-parity, such that supersymmetric particles can only be produced in pairs, and decays can only produce other supersymmetric particles. In this way, the lightest supersymmetric particle is stable and is a suitable WIMP candidate. In standard supersymmetric models, the lightest supersymmetric particles is denoted as neutralino χ. If the symmetry were exact, supersymmetric partners would share the mass with their SM counterpart. An exact symmetry is disproven by experiments, such that Supersymmetry needs to be broken.

Most experiments searching for DM are focusing on the search of a WIMP, which is motivated by a consistent theoretical framework. The experiments can be divided into three categories: Direct detection, indirect detection, and production experiments. For all of the types, a variety of detectors can be named. Figure 1.11 gives an idea on how WIMP searches are conducted. Depending on the time axis, the WIMP to SM interaction can be interpreted as a scattering process, a production process, or a decay process.

Direct detection experiments are searching for an inelastic scattering process of DM particles with a target material. As the interaction cross-section of WIMPs with SM particles is tiny, the expected scattering rate in the detector is marginal, as well as the transferred energy. The measuring of a single scattering signal is challenging and requires extremely sensitive detectors in a background-free environment. To reduce background, the experiments are operated deep underground, shielded from cosmic particles. Also, the target material needs to be of high mass to improve the interaction probability. Promising target materials are pure Germanium crystals, used in EDELWEISS experiment in Modane Underground Laboratory in France [62] and the Cryogenic Dark Matter Search (CDMS) experiment in Stanford [63], or liquid xenon, used in Xenon experiment located at the Gran Sasso Underground Laboratory [64] and the Large Underground Xenon experiment (LUX) at the Sanford Underground Laboratory [65]. In the target detectors, an ionization signal, a heat disposal as phonon, or light emission can be measured in a unique signal depending on the detector construction and scattered particle.
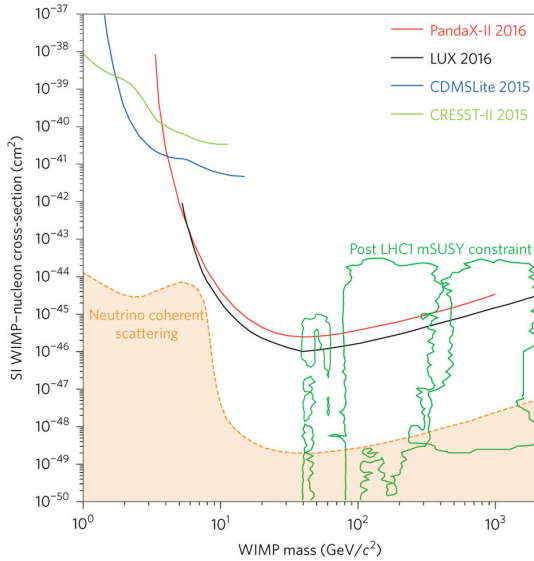
Figure 1.12: Upper limits on the spin-independent WIMP-nucleon scattering cross-section set by leading experiments, as of beginning of 2017 [66]. With additional data, the upper limits were further improved by [67] and [68], recently.

In this way, direct detection experiments are mostly model independent and have good discovery potential. So far vast areas in the scattering cross-section of WIMPS with SM particles have been excluded as a function of the WIMP mass, as shown in Figure 1.12.

A central role in the search for DM, is the production and analysis of beyond standard model (BSM) particles in collider experiments, like the CMS [69] and ATLAS [70] detectors at the Large Hadron Collider (LHC) at CERN in Geneva. The systematic study of particles in a clean laboratory environment is the only possibility to retrieve the full particle information. At the LHC, the largest accelerator built, proton pairs are brought to interaction by collisions with a center-of-mass energy up to 14 TeV. In such collisions, all sorts of particles can be produced. On the downside, the interpretation of collider data is usually model dependent. A WIMP-pair, produced in the proton-proton collision via $p + p \rightarrow \chi + \chi$ (or Figure 1.11 read from left to right), will not be visible in the detector, as they do not carry a charge, and do not interact with the detector material. The event signature of a DM pair production would be a missing part in the total momentum budget in the plane transverse to the collision, determined from momentum conservation. Sets of final states of a decay chain with traces predicted by theoretical frameworks are investigated. To reduce the model dependence, an Effective Field Theory (EFT) approach is used in which DM and SM particles interact through a four-point effective (contact) interaction. Interactions are mediated by a heavy particle on which the interaction characteristics are mapped. Observables can simply be transferred to the DM particle properties. The EFT approach is an attractive tool to encapsulate the relevant degrees of freedom and phenomenology for WIMP interactions without the need for the full theoretical framework [71, 72].

The third approach in the search for DM is the indirect search in CRs. In some sense it is the reverse concept of the production channel: Products of WIMP-WIMP annihilation into SM particles are searched for over the dominating background of conventionally produced CRs.

Possible annihilation products are γ-rays, neutrinos, and light charged CR particles like electrons, protons, and their antiparticle, in particular. Each channel comes with different features related to the production or propagation mechanism and the specific background. Annihilation occurs with a probability proportional to the DM density squared,

and thus regions of high DM density are monitored with priority by γ and neutrino observatories.

The most studied channel in indirect DM searches is in γ-rays, which are produced at high rates and can be detected with high efficiency. They are without charge and therefore carry the directional information from the source. The measured flux of γ-rays is integrated over the line of sight, and multiple sources overlap in energy and position. The spectral shape has to be correlated with the observation area in the analysis to disentangle individual components. Telescopes contributing to indirect DM searches in the γ-channel is the High Energy Stereoscopic System (H.E.S.S.) [73], a ground-based telescope that measures leptonic air-showers from their emitted Cherenkov radiation, and the Fermi Large Area Telescope (Fermi-LAT) [74], a space-borne observatory. In fact, the observation of an overabundance of a few GeV γ-rays towards the central galactic region with Fermi-LAT has been interpreted to be caused by DM annihilation [75–77]. The excess can serve as an example for the difficulties in indirect DM searches. The galactic center is a location of high activity, and a number of processes produce γ-rays, not all of which are well understood. The excess above the large background might also be explained by new astrophysical sources that contribute, such as molecular clouds [78] or millisecond pulsars citemspulsars.

The remarks made for γ-rays also apply to the neutrino channel. The detection efficiencies are extremely low due to the small interaction cross-section of neutrinos with detector material. The channel is just at the beginning of being practicable, but neutrino astronomy is a growing field. In the ideal case, information of the neutrino channel and γ-rays are combined in a multi-messenger approach. The largest observatory of neutrino astronomy today is the IceCube observatory at the South-Pole [79].

Different from the γ-ray and neutrino channel, charged cosmic rays lose directional information on their origin during propagation in the intergalactic magnetic fields such that DM annihilation cannot be studied explicitly in the Galactic Halo. A variety of annihilation products, originating in the local surrounding, are investigated. The analysis of the spectral energy in the annihilation channel is the only possibility to study DM annihilation products. The spectral shape is modulated in the particle's propagation, which is model dependent and washes out the DM spatial and spectral signatures: Additional annihilation signals need broad interpretation. Charged cosmic rays come in a variety of different particles in different quantities, as discussed in Section 1.1. Different messengers have different sensitivity to additional sources, depending on their abundance. Positrons and antiprotons are the most relevant for the DM search. As they are mostly secondaries, the abundance of conventionally produced CRs is low, such that particles produced in exotic sources are easier to identify.

In fact, an anomalous abundance of positrons has been found in CRs, first measured by PAMELA [80], and later confirmed and measured with higher precision by AMS-02 [1, 2]. Both experiments measured the fraction of positrons in the leptonic component of CRs. From CR propagation an exponential decrease with energy would be expected. AMS-02 also observed that the rise in the fraction is due to additional positrons, and not due to a loss of electrons [3]. The additional positron population cannot be explained by standard CR processes and requires an additional source which could be Dark Matter annihilation. Figure 1.13 shows the positron fraction as measured by AMS-02 with a leptophilic DM annihilation model fitted. The model does not to fit the data, but the DM hypothesis is still not ruled out because it allows for many degrees of freedom. The same
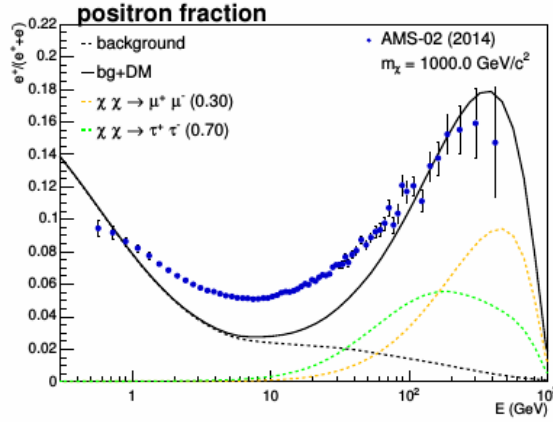
Figure 1.13.: AMS-02 positron fraction fitted with a leptophilic DM annihilation model. An abrupt drop of the positron fraction is predicted [13].

is true for pulsars which can fit the positron fraction depending on how many pulsars are included.

From the efficient energy loss processes in the propagation of high energetic positrons, exotic positrons have to be produced in the nearby environment. For DM annihilation scenarios no arrival direction of additional positrons is expected to be preferred. For astrophysical scenarios, like electron/positron pairs produced in pulsars, the point source injection would induce an anisotropy in the arrival direction that might survive the propagation process. A detection of an anisotropy in the angular distribution of positrons would instantly rule out DM scenarios. Typical predictions on the anisotropy of positrons, taking known pulsars into account, are of the order 10^{-2} [42] to 10^{-4} [81] above 100 GeV.

An important part in the search for anisotropies is the local environment which can introduce or diminish a signal, depending on the model assumption. Recent investigations on the anisotropy in positrons given by pulsars, taking the local environment into account, state a variation of an expected anisotropy by the local environment in the range of 0.6% to 325% above 16 GeV [50]. An anisotropy from proton propagation is predicted and found to be boosted up to 344%, or weakened to 0.3% at rigidities above 80 GV [50].

1.3. The local environment

Additional astrophysical sources should be considered from the recent AMS-02 measurements, as mentioned earlier. To be visible and not washed out, these sources should be present in the local environment. Figure 1.14 shows a map of the local Solar neighborhood. Numerous astrophysical objects are identified, some of which might be considered as an astrophysical source. It should be noted that even if the map gives the impression that the local environment is well known, many potential sources are still hidden. This is true especially for pulsars which are only detectable if the emitted radio pulses at the poles point towards Earth.

The yellow HI regions mark areas of higher ISM density, compared to the blue regions. The Sun is located in the center of the plot, inside a blue circular area surrounded by a yellow wall. This structure is called the *local bubble*. Inside of the yellow HI regions, the
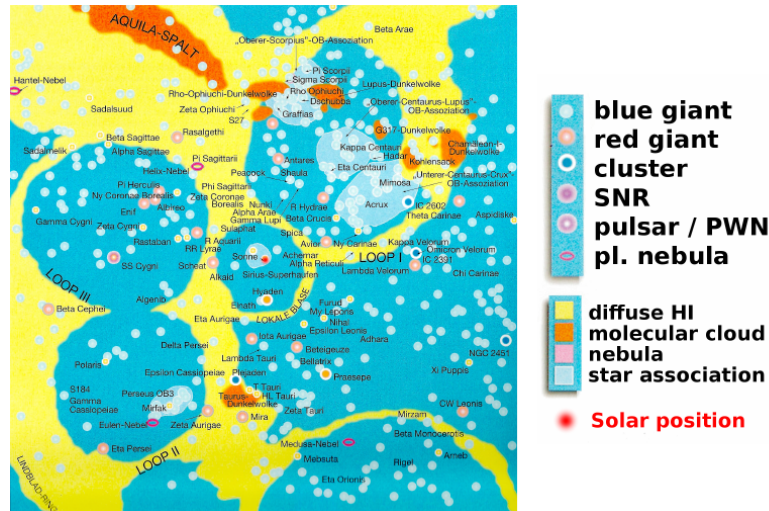
Figure 1.14.: Map of the solar neighborhood [82]. The map has a width of about 480×480 pc^2. Parsec is the common unit to measure astronomical distances and corresponds to $648000/\pi$ astronomical units (which is the average distance from Sun to Earth). The Sun is nearly central the picture located inside the local bubble. Numerous astrophysical objects are identified in the local environment. The map was created using combined measurements of dust extinction, radio emission of the 21cm line, and distance estimates from stars in star birth regions.

diffusion coefficient is modulated, which affects the propagation. In molecular clouds, secondary production might be enhanced, such that secondary particles originating from the clouds could be measured. Contributing point sources could be pulsars and the SNRs, as assumed in standard re-acceleration scenarios. The effect of the variations in the ISM density, in the yellow regions, on the flux of CRs is, so far, not well understood.

1.3.1. The Heliosphere

The sun constantly emits a flow of low energetic charged particles, consisting mainly of protons, called the solar wind. A thin current sheet is formed in the dipolar solar magnetic field, with opposite hemispherical polarities on either side of the solar magnetic equator. The charged particles confine the magnetic fields from the Sun's surface and carry them into space, following the magnetic field lines. The resulting, so-called interplanetary magnetic field is of a roughly radial structure. Towards large distances, the magnetic field is twisted by the Sun's rotation into a spiral structure, called the Parker spiral.

The Sun itself is not a quiet star but is subject to constant turbulent variations in the magnetic field, called solar activity. The main fraction of the solar activity can be linked to sunspots, regions of reduced surface temperature caused by concentrations of the magnetic field flux. On average, sunspot appearance varies periodically on an 11 years cycle and so does the solar activity. This also affects the space weather conditions at Earth's, leading to a deformation of the Geomagnetic field.

The constant particle flow away from the sun pushes incoming low energetic CR particles away. This happens up to the so-called termination shock, where the outflow of the solar particles cannot overcome the counter-pressure from the incoming CRs anymore. The solar wind is affecting low energetic CRs which get deflected or decelerated. The
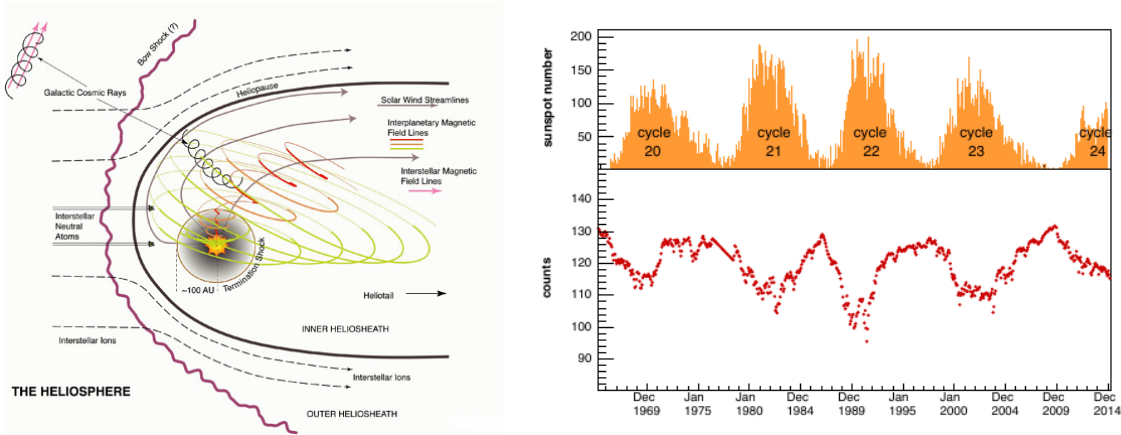
Figure 1.15.: The influence of the Sun on CRs. **Left:** Schematic of the Heliosphere [83]. **Right:** Sunspot number with time since 1965 correlated to neutron monitor counts [84]. Neutron monitor counts are a measure of the intensity of CRs measured at the Earth's ground level. A periodic variation of 11 years can be identified, the solar cycle.

local low energetic flux is reduced. This so-called solar modulation influences CRs up to energies of a few tens of GeV and is modeled by the Force Field Approximation, in which the flux in the local interstellar medium (LIS), outside of the Heliosphere, (Φ_{LIS}) is modulated by the solar wind to be

$$\Phi_{Mod} = \frac{E^2 - m^2}{(E + Ze\phi)^2 - m^2} \Phi_{LIS}(E + ZE\phi) \tag{1.2}$$

for particles with charge Ze and mass m at the energy E. ϕ denotes the effective solar modulation potential which describes the typical energy losses of CR particles in the Heliosphere. Typical values range from hundreds of MeV to GeV, depending on the solar activity. A higher solar activity leads to a lower particle flux. The interplanetary magnetic field can also introduce a charge sign dependence in the curvature and drift of charged CRs. Such effects have to be taken into account when comparing low energetic matter and antimatter fluxes in the Heliosphere.

Figure 1.15 shows the Sun's activity since 1965 starting from solar cycle 20. AMS-02 will provide a continuous measurement of the CR flux over a complete solar cycle (24), which helps to understand local CR propagation in the Heliosphere. In the context of anisotropies, the Heliosphere has been studied intensively in order to investigate variations in the angular distribution of particles measured by ground-based telescopes [85–87]. Effects were studied at the 1 TeV energy with large impact on the redistribution of incoming CRs. Such analyses are strongly model dependent without prediction capabilities. A measurement of the angular distribution of CRs with different charges and masses by AMS-02 can give valuable insights in the understanding of the propagation of charged CRs in the Heliosphere.

1.3.2. The Earth's magnetic field

The Earth is shielded by a magnetic field that prevents low energetic charged particles from reaching the atmosphere. What has been a valuable protection for life on Earth[2],

---

[2] Abundant low energetic cosmic rays would strip away the upper atmosphere and destroy the protecting ozone layer.
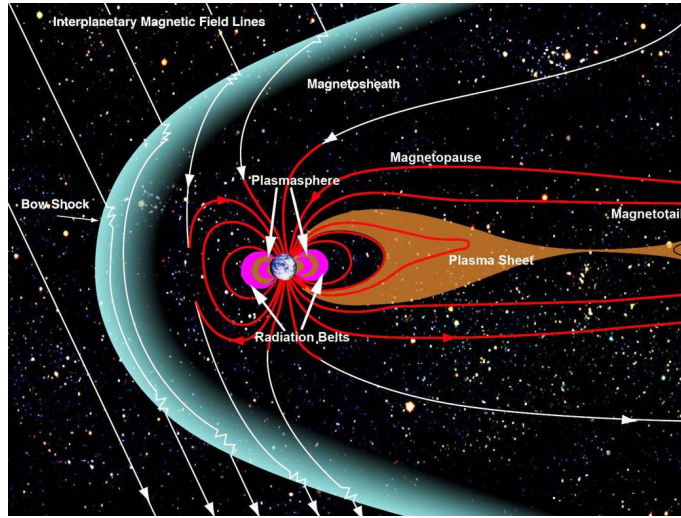
Figure 1.16.: Schematic drawing of the Earth magnetic field [89]. In first order approximation, the Magnetosphere is a dipole field. The solar wind and the interstellar magnetic field deform the outer field. In the Van-Alleen radiation belts, low energetic particles get trapped and reach the Earth atmosphere only at the polar regions.

hinders CR particle detection towards low energies. The Geomagnetic field is, in first approximation, a magnetic dipole with its axis shifted by about 400 km and tilted by 11° compared to the Earth's rotation axis. What exactly causes the magnetic field is still unknown, but it is believed that currents in the conductive material of Earth core create a dynamo effect [88].

Particles can get trapped in the Geomagnetic field in the so-called Van Allen belts. Due to distortions from the solar wind, the trapped particles get pushed towards lower altitudes. A permanent relict of this effect is the South Atlantic Anomaly (SAA). In this region, the CR flux is overlayed by trapped particles. The varying solar activity notably introduces field deformations changing in time. In a CR study, the geomagnetic field needs to be modeled to reject trapped particles. A minimum rigidity can be introduced, below which CR particles are deflected and cannot reach a detector at a certain altitude and position. The minimum rigidity is called Geomagnetic rigidity cutoff R_C and can be evaluated analytically in a simple dipole model known as the Stoermer approximation [90]

$$R_C = \frac{M \cos^4 \lambda}{r^2 (1 \pm \sqrt{1 - \sin \epsilon \sin \xi \cos^3 \lambda})^2} \tag{1.3}$$

with the geomagnetic field dipole moment $M \approx 8 \cdot 10^{17}$ Tm^2, the geomagnetic latitude λ, the zenith angle ϵ, the azimuthal angle of the north magnetic pole χ, and the distance from the dipole axis r. The ±-sign describes the charge dependence. In more advanced models the magnetic dipole field is modeled more accurately by a spherical harmonics expansion up to higher orders $l > 1$. These are the International Geomagnetic Reference Field (IGRF) models and are produced for certain time periods[3]. The Earth's magnetic field is under pressure of the solar wind, which deforms the dipole field as shown in Figure 1.16. The solar activity, and therefore the shape of the Magnetosphere, is constantly varying with time. To account for the time-dependent deformation, an external field model is applied on top of the internal IGRF field, called Tsyganenko model [91].

---

[3]For example, IGRF-11 describes the geomagnetic field updated in 2011

The model provides a semi-empirical representation of the Earth's magnetic field, based on satellite observations. The complex fields cannot provide the rigidity cutoff from an analytical expression but have to be determined numerically.

The Geomagnetic field introduces a charge-dependent angular anisotropy in the dipole plane, called East-West effect. The East-West effect is removed in the data analysis by backtracing particles in the Geomagnetic field, as it will be discussed in Section 3.3.4.1 and actively cutting away regions in which the East-West effect introduces signals.

1.3.3. Compton-Getting effect

A rather indirect effect in the measurement of the angular arrival direction in CRs arises from the relative motion of an observer to the resting cosmic ray plasma. For example, the movement of the Earth around the Sun with an orbit velocity of about $v =29.8$ km/s, where CRs are not expected to co-orbit but stay rather still, gives an anisotropy in the angular distribution. The relative change in intensity from the so-called Compton-Getting effect can be calculated with

$$\frac{\delta I}{I} = (\gamma + 2)\frac{v}{c}\cos\theta \tag{1.4}$$

with the spectral index γ, and the incident angle θ [92]. For the Earth movement around the Sun, a maximum anisotropy of about $5\cdot10^{-4}$ is expected. The Compton-Getting effect is used as a benchmark in ground-based measurements. It has already been measured in the beginning of CR observations as diurnal variation in the sidereal time [93]. For the movement of the Sun within the galaxy with a speed of about 220 km/s, a maximum anisotropy of $3.5\cdot10^{-3}$ is calculated, but the Heliosphere provides an efficient shielding which reduces the amplitude.

1.4. Review of anisotropy measurements in charged cosmic rays

CRs are measured by a variety of observatories with different experimental focus. In general, one differentiates between a direct measurement of CRs, with balloon or space-based experiments, or an indirect measurement on the Earth's surface. The naming arises from the observation that charged particles that enter the Earth's atmosphere interact with air molecules and produce a cascade of particles such that only secondary particles reach ground level. From the composition of the so-called extensive air shower (EAS) the energy and incoming direction of the primary particle can be reconstructed. To some extent, also the particle and type can be reconstructed with a full shower simulation but suffer large uncertainties. First experiments of this type focused on the penetrating muon component and could only measure an incoming particle's energy. Today, most experiments of this kind have detectors on the surface, operating in an array, to measure the hadronic and leptonic component of the shower. In this way, the primary particle can be reconstructed from shower simulations. An EAS develops along the incoming direction of the primary particle in a synchronous bulk, called *pancake*. The pancake can reach a size of several hundreds of meters in diameter, depending on the primary particle's energy and type, and reaches the surface nearly synchronously. From the timing information in the surface array, the incoming direction can be reconstructed. Figure 1.17 shows a sketch of the measurement concept, with the timing information indicated
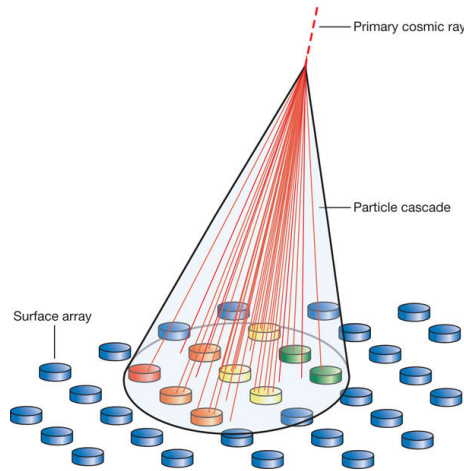
Figure 1.17.: Sketch of the measurement concept of ground-based EAS detectors, consisting of
several surface detectors operating in an array [94]. The surface array measures
the hadronic and leptonic shower component to identify the primary particle. To
improve the particle, identification the penetrating muon component of the sower
can be measured in addition by dedicated detectors underground. The timing infor-
mation is indicated by a color code from green to red, and is used to measure the
primary particle's incoming direction.

through a color code from green to red. The energy can be reconstructed similar to a
calorimetric measurement.

EAS detector arrays can cover large areas of several km^2, which results in a huge ac-
ceptance. In this way, the number of collected CRs is extremely high, even though they
cannot measure particles at lower energies where the shower gets absorbed in the at-
mosphere and does not reach the detector. They are mainly used for the measurement
of less abundant high energetic CRs above the *knee*. As detectors, water Cherenkov de-
tectors like in Milagro [95] or scintillation counters as in the Tibet array [96] are used.
In addition, the EAS can be monitored by its emission from fluorescence light by atmo-
sphere's nitrogen atoms [97], Cherenkov radiation [98] or radio waves [99]. It is common
practice to employ several of these methods in parallel in a so-called hybrid detector ar-
ray. At the moment two of the largest hybrid arrays are the Pierre-Auger observatory in
Argentina and the IceTop detector array together with IceCube at the South pole. Both
use water Cherenkov tanks as their main detector array. At the Pierre-Auger observa-
tory, fluorescence telescopes are operated in parallel. With the fluorescence telescopes,
a precise measurement of the shower can be achieved, but they can only be used during
clear dark nights, which limits the operation time, as they suffer from a background by
the full moon or other light sources.

Because of their large acceptance, ground-based detectors are suitable when it comes
to the search for anisotropies in the CRs celestial distribution, where high statistics is
necessary to recover the tiny signals. On the other hand, they are bound to a fixed spot
on the Earth's surface and cannot view the full celestial sky. A scan of a fraction of the
sky is only possible due to the Earth's rotation.

A crucial point in every analysis of the angular direction distribution of CRs is to cor-
rect for a non-uniform coverage of the celestial sky by the detector, due to operational
instabilities. In ground-based experiments, a frame can be found where the detector
operations are almost uniform. The main origin of non-uniform behavior is the zenith-
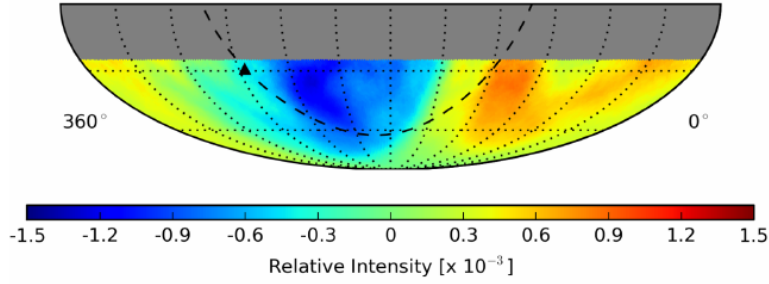
Figure 1.18.: Relative intensity in multiple adjacent declination bands from IceCube in equatorial coordinates [103]. It is to note that, even though performed in multiple declination bands, the measurement is in right ascension only, so that the map does not carry information of the complete anisotropy on the celestial sphere. In addition, it is smoothed in a 5° radius.

angle-dependent detection efficiency. If the data is ordered in sidereal time, this quantity becomes a function of declination but not a function of right ascension. The analysis has been proposed in 1975 by Linsley [100] and first adopted by Edge in 1978 [101]. The counting rate in bands of constant declination within the equatorial plane is then expanded in spherical harmonics in right ascension only [102].

It should be noticed that in the analysis in right ascension no information on the declination of anisotropy can be given. The first harmonic amplitude A_1 is then the projection of the dipole moment onto the equatorial plane and therefore of particular interest. In modern observatories with large acceptance, the analysis can be done in multiple adjacent declination bands. Figure 1.18 shows the relative intensity of multiple adjacent declination bands, performed by IceCube, in a 2-dimensional map. Plots like this one are misleading, as they give the impression of a 2-dimensional measurement. However, the measurement is done in right ascension only, so that the map does not carry information of the complete anisotropy on the celestial sphere. As a consequence, the full anisotropy cannot be inferred from these results [104]. However, an excess located at 75° right ascension, called *tail-in* anisotropy, and a deficit at 200° right ascension, called *loss-cone*, it is evident from the map. This observation could be confirmed by several experiments, and its origin is still unknown. Ground-based detectors are the only experiments which found anisotropies in the CRs arrival direction, so far.

The measured anisotropies from ground-based experiments settle at a level of 10^{-4} to 10^{-3}. For different experiments corrections related to the different latitudes and zenithal-dependent efficiencies are required to compare the measured amplitude A_1. In a naive expectation from CRs propagation, the dipole moment should point towards the galactic center, where most sources are present, and its strength should be correlated to the diffusion coefficient with energy. This simple picture is not confirmed by the measurements.

A collection of analysis in the CR arrival direction using ground-based experiments can be found in [105] and will be discussed in Chapter 5.

Direct detection experiments

Direct detection experiments can provide additional information to identify the source of the anisotropies, measured by ground-based experiments. As the name suggests, they measure the primary CR particles directly before they interact with the atmosphere. To

FOV 60⁰   FOV 15⁰   FOV 25⁰

FERMI-LAT   **PAMELA**   **AMS-02**
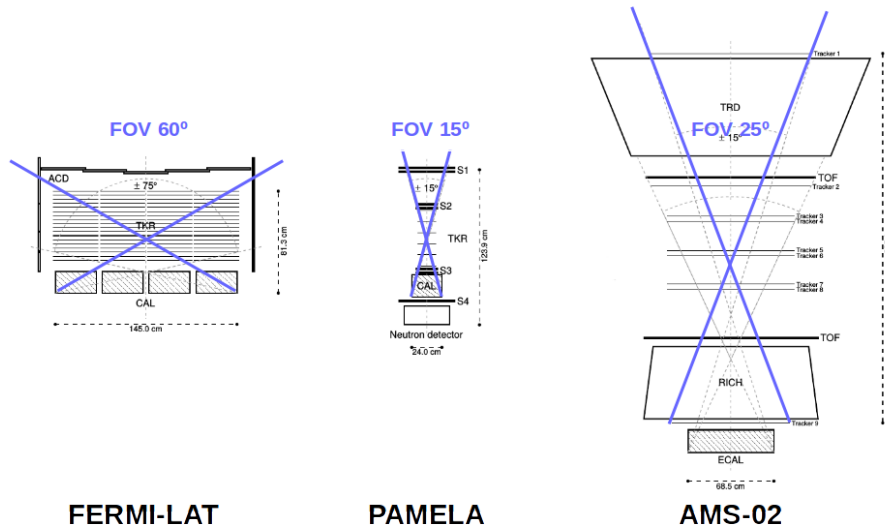
Figure 1.19.: Layout of the satellite experiments FERMI-LAT, PAMELA, and AMS-02 in real rela-
tive dimensions [8]. FERMI-LAT is a standalone satellite, designed as a gamma-ray
telescope with an electromagnetic calorimeter as main detector. PAMELA was the
first satellite-based spectrometer for direct measurement of CRs with focus on the
antimatter component and is mounted on a commercial Earth-observation satellite.
The AMS-02 detector is the newest generation spectrometers based in space aboard
the International Space Station (ISS). The detectors differ in size and field of view
(FOV), which is a fundamental ingredient for the search for anisotropies.

do so, particle detectors have to be put outside any atmospheric environment, which
can be achieved by balloon flights or satellites in space. Balloon experiments, such as
CREAM [106], have a limited measuring time and usually fly at the Earth's polar regions,
such that they cannot contribute much to the search for anisotropies. For this reason,
the focus will be on space-based experiments[4].

Due to the direct measurement of CRs, the particle recognition and energy measure-
ment are by far superior compared to indirect measurement. On a downside, they are
costly and limited in size, as they have to fit in a carrier to orbit. These factors result in a
small acceptance, compared to ground-based experiments, so their focus is on the more
abundant low energetic CRs. Even though satellite experiments have a small acceptance
and can scan only a small fraction of the celestial sky at a time, the orbit allows for an
accumulation of observation time to cover the full celestial sphere. This allows for a
full 3-dimensional reconstruction of a dipole anisotropy, compared to the ground-based
experiments, which only measure in bands of declination, as discussed. However, for
a reconstruction of the full celestial sky, any time and position dependent variations in
the operation or detection efficiencies introduce a bias which needs to be corrected. The
construction of the full map of the celestial sky for individual particles is the main task
of this Thesis.

Figure 1.19 shows three modern direct detection experiments, all based in space. The
PAMELA[5] detector which orbits Earth at an altitude of 350 to 610 km as payload on a

---

[4]The CREAM balloon experiment has been modified as a space-based detector and was installed on the
International Space Station (ISS) on August 16, 2017.

[5]PAMELA is an acronym for Payload for Antimatter Matter Exploration and Light-nuclei Astrophysics.

commercial Earth-Observation satellite [107]. The detector has several subsystems to measure all properties of an incoming particle, including the charge sign, with high precision. The detector is quite small with a height of 1.3 m. In a published analysis on the search of a dipole anisotropy in positrons, a sensitivity of the order 10^{-1} at energies of 10 GeV was reached [108]. This is two orders of magnitudes above the ground-based measurements. The number shows the problems of space-based detectors in the search for anisotropies. Even detectors with a larger acceptance, like Fermi-LAT, a standalone satellite gamma-ray telescope which is also capable of measuring electrons and positrons (but without being able to discriminate between the two), are not sensitive to the tiny signals. The motivation for a further search of anisotropies by direct detection experiments arises from the precise particle tagging, which allows for the search in dedicated CR species, and the full sky coverage. In this way a single particle might be found, where an anisotropy is enhanced, such as it could be the case for positrons originating from a pulsar point source. Such a measurement cannot be done by a ground-based experiment.

A space-borne experiment has the capabilities to scan the full celestial sky. This comes with the loss of the uniform sidereal time frame in which the anisotropy analysis was performed with the ground-based measurements. A standard analysis of these experiments is a search in so-called *relative* anisotropies. In these analyses, two independent particles with same acceptance are compared to each other. In this way, non-uniform coverage of the celestial sky, introduced by the detector, is normalized by the reference particle, which suffers the same detector effects. The ratio is expected to be flat and can be expanded into spherical harmonics. In the PAMELA study on positrons, mentioned before, electrons are used as a reference. Details on this type of studies will be given later in Chapter 3.

So far no anisotropy has been found by any direct detection experiment. Also for AMS-02, the first search for positron relative anisotropies in 2013 showed no evidence [109]. However, the detector's large acceptance, paired with the measurement of the charge sign and full coverage of the celestial sky is a promising configuration to probe the origin of the excess in the positron fraction and the hardening in the measured fluxes of protons and helium.

2. The AMS-02 Detector

The Alpha Magnetic Spectrometer (AMS-02) is a state of the art CR particle detector mounted as an external module aboard the International Space Station (ISS) since May 2011. The ISS provides AMS-02 with power, a data connection of at least 9 $^{\text{Megabit}}$/s, and a safe orbit, which makes it possible to operate a high acceptance ($\approx$0.5 m^{2}sr) spectrometer over a long time in the absence of Earth's atmosphere. The lifetime of the detector is foreseen to last until the end of the ISS mission which is currently set to 2024, but is discussed to be extended up to 2028. By achieving this lifetime, AMS-02 will be able to extend the measurements of particle fluxes to higher energies up to several TeV, further improving the understanding of CR propagation in our local environment. Also, time-dependent effects within the heliosphere can be studied in a full solar cycle for the first time.
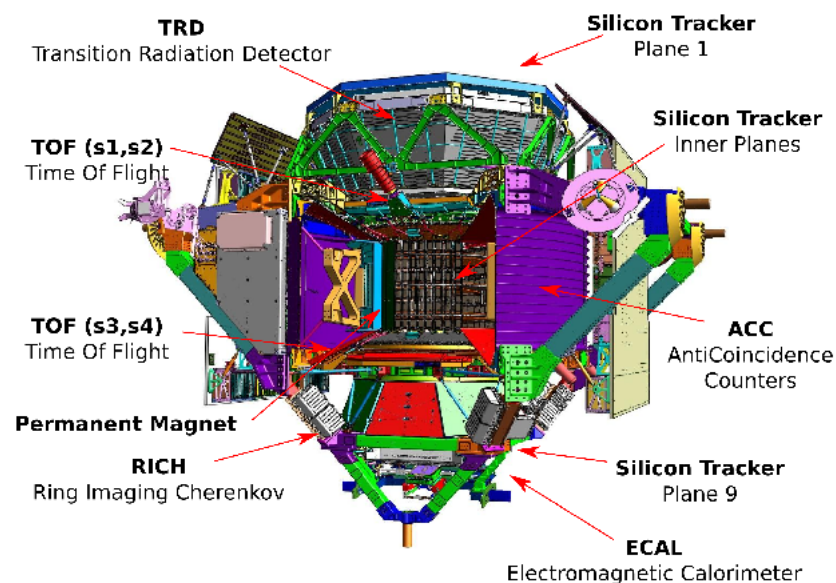
Figure 2.1.: Technical sketch of the AMS-02 detector with its main sub-detectors labelled [110]. The electronics of the data acquisition system are located outside the detector's core, on both sides for full redundancy, within the support structure (colored in green).

Figure 2.2.: Aluminum honeycomb support structure of the TRD allowing for a high acceptance space qualified detector with a weight of less than 500 kg [111].

The main goals of the experiment are the measurement of charged CRs up to Iron (Z=26) in an energy range between 0.5 GeV and a few TeV, the measurement of the antimatter component in the primary CR flux and the search for primordial antimatter. These measurements will help to understand the origin and propagation of Galactic CRs and can be used to understand the nature of Dark Matter.

The detector consists of six subdetectors which are specialized in the measurement of different particle properties. Most of the properties are measured redundantly to ensure a high particle recognition performance and energy resolution, making use of cross-calibration. From top to bottom a particle has to cross a Transition Radiation Detector (TRD), a Time of Flight (TOF) detector, a Silicon Tracker, a Ring-Imaging-Cherenkov detector (RICH) and an Electromagnetic Calorimeter (ECAL). The heart of the detector is a homogeneous magnetic field from a cylindrical permanent magnet which surrounds the main part of Tracker, referred to as inner Tracker. By measuring the bending of a particle's trajectory inside the magnetic field, the charge sign can be determined, which allows for the identification of antimatter. The concept of this configuration, back then without TRD and RICH, has been tested by a prototype during a ten days space shuttle flight in 1998, known as AMS-01.

In this chapter, the different subdetectors and their role in the measurement of CRs are introduced. Also, the challenge in operating the detector in space will be discussed for its high impact on the data-taking.

2.1. The Transition Radiation Detector

Charged particles crossing the boundary between two media of different dielectric properties emit electromagnetic radiation as a collective response of the matter surrounding their trajectories [112]. The intensity of the radiation, known as transition radiation, is directly dependent on the Lorentz factor $\gamma = E/m$ and therefore sensitive to the rest mass of relativistic particles with a given momentum [113]. As the radiated photons are X-rays with energy in the order of keV, emitted in forward direction, they can be detected with high efficiency using well-known methods such as scintillation detectors [114] or gaseous detectors [115].

In AMS-02 a transition radiation detector is used to reject the abundant high mass protons over lightweight electrons and positrons, which are much more likely to emit transition radiation, up to an energy of several hundred GeV.
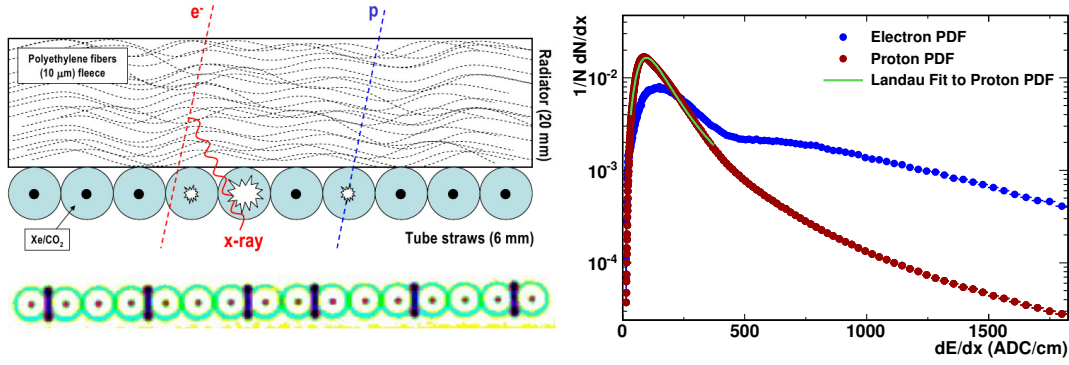
Figure 2.3.: **Left:** Sketch of a TRD module in cross-section view. In blue the trajectory of a proton crossing the radiator and leaving an ionization signal in a straw tube compared to the typical behavior of an positron which emits transition radiation as a keV photon is drawn. Below, a CT scan image of a straw tube module can be seen [110]. **Right:** The probability density functions for the energy deposit per unit path length in a single straw tube for electrons and protons of same energy. For electrons the emission of transition radiation leads to a higher expected energy deposit than for protons. A Landau function is fitted to the proton PDF to emphasize the ionization deposit following the Bethe formula.

A 0.06 $\mathrm{g/cm^3}$ polypropylene/polyethylene fiber fleece is used as radiator. Fibers are of 10 μm in diameter to ensure a high number of interfaces maximizing the number of X-ray photons. The transition radiation is detected by straw tubes, filled with xenon as absorber and CO_2 as quencher at a mixing fraction of about 90:10 [111, 116]. A 22 mm thick layer of fleece radiator placed on top of 16 parallel aligned straw tubes of 6 mm in diameter are combined to one module. 328 modules are arranged in 20 layers in an octagonal pyramidal aluminum honeycomb support structure of 80 cm in height and of 220 cm in diameter on top reducing to 120 cm to the bottom keeping the overall weight to a minimum (see Figure 2.2). The 16 central layers are aligned with the magnetic field direction and four outer layers perpendicular to it. This configuration allows for an independent three-dimensional track measurement.

The energy deposit dE by ionizing xenon atoms along the particle's trajectory dx in the straw tubes follows the Bethe relation $dE/dx \propto Z^2$. For the TRD, which is operated with high voltage of about 1400 V, the energy deposit can be measured up to helium (Z=2). For higher charged nuclei saturation of the electronics limits the resolution. By lowering the voltage, the measurement of the energy deposit could be extended up to carbon. However, this would reduce the energy resolution for protons, for which the working point is optimized. By comparing the ionization signal of protons with the transition radiation signal of electrons and positrons, the particles can be separated. The probability density functions for the energy deposit per unit path length in a single straw tube is shown in Figure 2.3 for electrons and protons together with an illustration of the measurement principle. By combining the signals of the 20 layers in a likelihood estimator, a proton to electron rejection of more than 10^3 up to 200 GeV can be achieved, as shown in Figure 2.4.

The TRD gas system adds up to a volume of about 230 liters, divided into 41 independent circuits to avoid a single point of failure. CO_2 gas is constantly lost through diffusion, and small leaks lead to a loss of xenon and CO_2. This amounts to a combined loss of
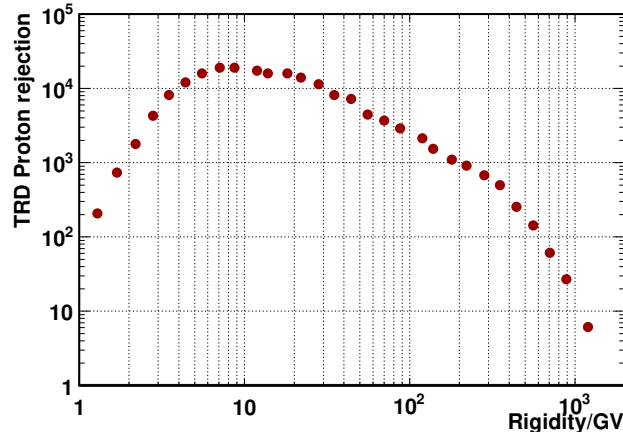
Figure 2.4.: TRD proton rejection evaluated from flight data at 90% positron selection efficiency as function of rigidity measured by the Silicon Tracker [1]. Electron and proton samples were selected using the Electromagnetic Calorimeter and the ratio of momentum over energy deposit in the ECAL.

about 4.5 $\mathrm{mbar}/\mathrm{day}$, stable since the start of AMS-02 operation [117]. These losses, and a varying temperature due to the ISS orbit and ISS operations, result in a steady change in the gas gain over time. On a daily basis, this is corrected for by lowering the high voltage, as the free path length in the gas mixture increases. On a longer time scale gas, from dedicated storage vessels, is transferred into the manifold system, the so called *Gas Refill.* Such detector operations affect the data taking, as it will be discussed in Section 3.1.

2.2. The Time Of Flight Detector

The TOF system measures the velocity of particles and rejects up-going secondaries from interactions. With its fast response and good time resolution, it serves as the main trigger for the detector. The system consists of four layers of scintillator counters located directly above and below the magnet in pairs of two, referred to as upper and lower TOF. By the energy deposit in the scintillator material, the particles charge can be estimated.

From top to bottom the layers are composed of 8-8-10-8 polyvinyl-toluene scintillator paddles of 1 cm thickness and a length varying between 117 cm and 134 cm, aligned parallel with an overlap of 0.5 cm to avoid geometric inefficiencies. For upper respectively lower TOF the two layers are aligned perpendicular to each other allowing for an x-y-resolution of the particle's penetration point. The arrangements of the paddles in upper and lower TOF is shown in Figure 2.5. Each paddle has photomultiplier tubes (PMTs), optically coupled through acrylic glass light guides, at both ends to get a time resolution nearly independent from the position of the impact point of the measured particle [118, 119].

In total 144 PMTs are connected to the 34 scintillator paddles powered in couples of two or three with applied high voltage of around 2000 V, reaching a nominal gain of 10^6. The anode signals for each counter side are summed up and are transmitted to the TOF readout electronics. Here they are compared to fixed thresholds of

- 20% of the minimum ionizing particle (MIP) signal as low threshold (LT) for a fast signal time measurement,
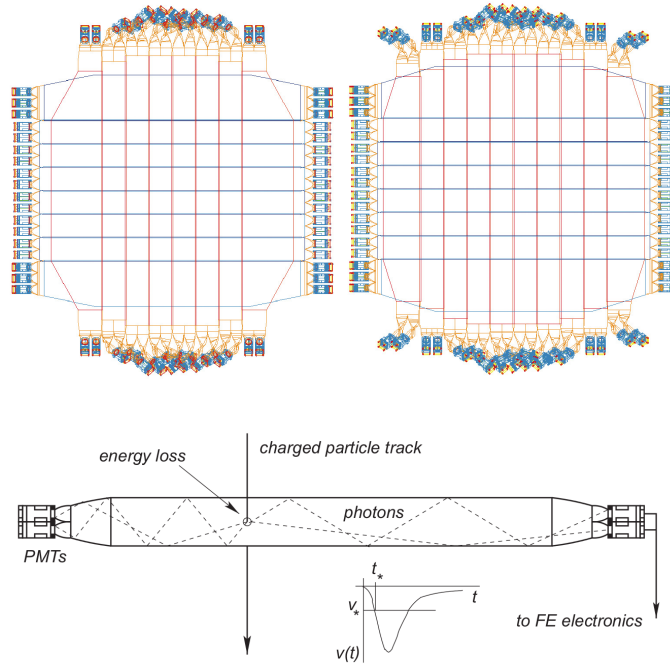
Figure 2.5.: **Top:** Sketch of the arrangement of the 34 scintillator paddles in the four planes of upper and lower TOF with PMTs at both end sides [120]. **Bottom:** Scheme of a single paddle with its principle of operation indicated [119].

- 60% of the MIP signal as high threshold (HT) for a trigger on charged particles with Z≥1 and

- a super-high threshold (SHT) of 400% of the MIP signal for a trigger on particles with charge greater Z≥2.

A cutout fraction of about 5% of the anode signals is also used for a charge measurement of low charge 1≤Z≤8 nuclei. Also, the signals of the third to last dynode of every PMT are read out independently of the anode signals and are used to extend the charge measurement to nuclei charges greater than Z≥3, where anode signals start to saturate [121]. With the combination of anode and dynode signals, the TOF is able to perform a charge measurement of nuclei up to Zn (Z=30) via $Z^2 \propto dE/dx$ using the energy deposit in every layer as shown in Figure 2.6.

The LT signals with good time resolution are used to calculate the particle's relative velocity $\beta = \frac{\Delta s}{c \Delta t}$ using the trajectory Δs given by the Tracker between the upper and lower plane. The resolution $\Delta \beta$ is about 4% for protons, improving for higher Z nuclei as shown in Figure 2.6. This precise measurement of the particle's velocity rejects upward-going particles from downward-going particles to the order of 10^9 which is essential for the charge sign measurement in the magnetic field [120].

2.3. Permanent Magnet

To identify if a particle is of matter or antimatter nature, a measurement of the charge sign is needed. For AMS-02 this is done by a magnetic field via the Lorenz-force

$$\vec{F} = q(\vec{v} \times \vec{B}) \quad ,$$
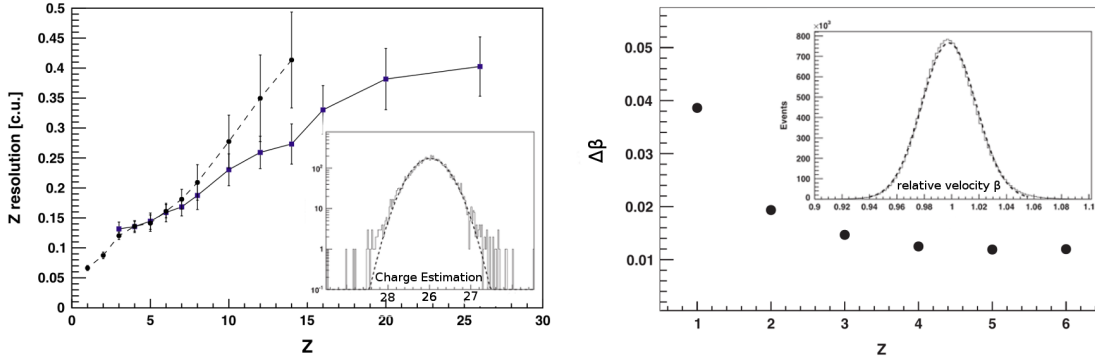
Figure 2.6.: TOF charge and velocity resolution [121]. **Left:** TOF charge resolution in charge units (c.u.) for the anode (dashed line) and dynode (solid line) estimation as function of the charge Z together with distribution of the charge estimator for iron ions (Z=26) from a single TOF counter and a Gaussian fit of the width $\sigma = 0.38$ (dashed line). **Right:** TOF velocity resolution $\frac{\Delta\beta}{\beta^2}$ as function of the particle charge Z together with the velocity distribution for helium ions with rigidity R>20 GV and a Gaussian fit of the width $\Delta\beta = 0.02$ (dotted line).

created by a permanent magnet which is the core and name-giving component of the detector. The magnet with its supporting structure alone has a weight of 2.2 tons, giving a significant contribution to the detector's total weight, strictly limited by the carrier. This example shows the challenge of designing a space-borne spectrometer. Although superconducting magnets were the state-of-the-art technique in particle physics as AMS-02 was designed, the decision towards the permanent magnet, which already has been used for the AMS-01 test flight, fell for a long lifetime and low maintenance during operation in space [122, 123]. The cooling of a superconducting magnet with liquid nitrogen would have limited the lifetime of AMS-02 to three years, much shorter than the planed 10+ years from the ISS mission.

The cylindrical magnet with an inner diameter of 1115 mm and a height of 800 mm resulting in a geometric acceptance of 0.82 m^{2}sr is composed of 6400 high-grade Nd-Fe-B blocks with a size of 5×5×2.5 cm^3 combined to 64 sectors. The resulting nearly homogeneous magnetic dipole field has a field strength of B$_x$=0.14 T defining the x-axis of the internal frame. The magnet dimensions and magnetic field configuration are shown in Figure 2.8.
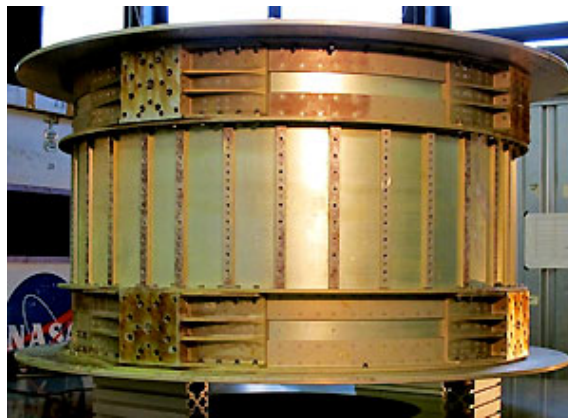
Figure 2.7.: Photo of the AMS-02 permanent magnet [110].
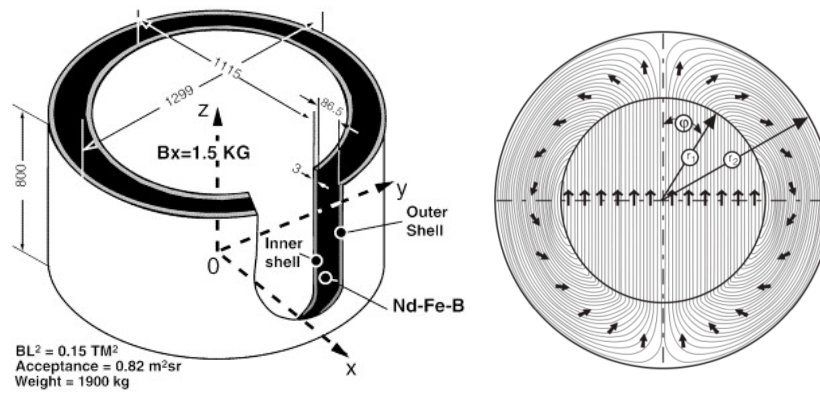
Figure 2.8.: **Left:** Technical sketch of the permanent magnet with dimensions imprinted in mm [124]. **Right:** Magnetic field in the x-y-plane of the detector's internal frame [125].
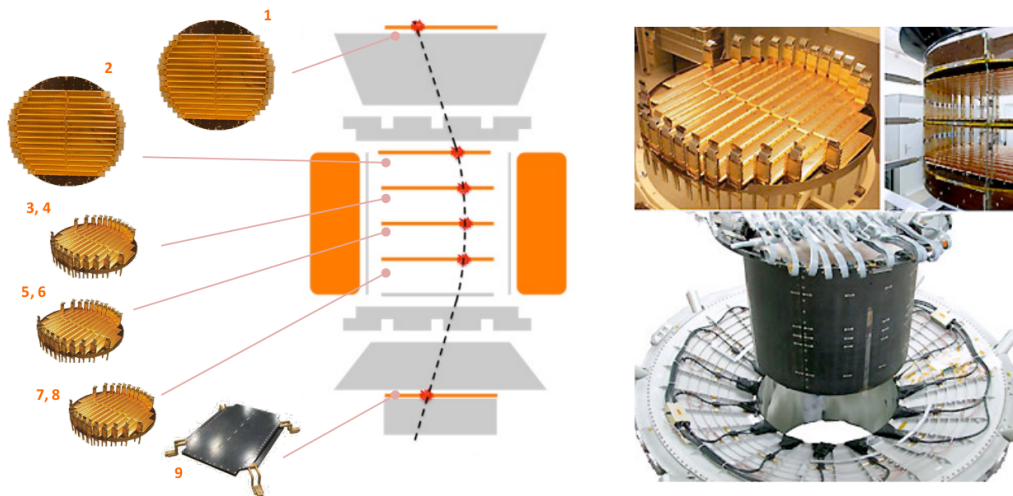
Figure 2.9.: Illustration of the positions of Tracker planes inside the detector and photos taken during the installation phase [110, 127].

The outer magnetic dipole moment is of negligible strength, as it would result in a constant torque from the interaction with the Earth's magnetic field, and the external magnetic field drops rapidly to not interfere with the detector's or space station's electronics. In total, three full-scale magnets have been build: Two for vibration and safety tests and one for the actual experiment [124].

2.4. The Silicon Tracker

To measure the trajectory of charged particles, 2284 double-sided silicon microstrip sensors are distributed in nine planes along the detector's z-axis performing a simultaneous measurement of the penetrating position and energy loss in each silicon plane. Sensors are grouped in standalone mechanical and electrical units with a common readout, and bias voltage referred to as ladders [126].

The single sensors consist of n-doped silicon wafers in the size of 72.05×41.36 mm^2 and a thickness of 0.3 mm. On one side they are covered with 2560 parallel aligned p$^+$−doped strips and on the other side 384 orthogonal n$^+$ strips separated by p-stop strips. The microstrip detectors are operated at full depletion. A charged particle passing through the detector creates electron-hole pairs in the depletion zone that induce an electric signal
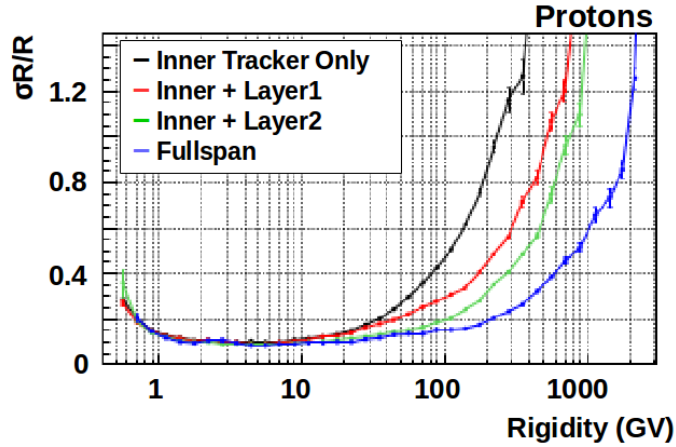
Figure 2.10.: Rigidity measurement resolution of the Tracker for protons as function of the particle's true rigidity from detector simulation [127]. Trajectories are reconstructed with four different Tracker spans with strong impact on the resolution.

in the nearby p+ and n+ strips from which 640 strips on p-side and 384 on n-side are read out in 1024 channels. By calculating the center of mass the interaction point can be reconstructed with a precision of around 10 μm in the bending and 30 μm in the non-bending direction [128].

Seven to 15 sensors glued on an Airex foam carbon reinforced support structure form one of 192 ladders, used in the nine Tracker layers, adding up to a total of about 200,000 readout channels. Six layers are installed on double layer planes inside the permanent magnet named inner Tracker, one layer directly above the magnet called layer two and two outer layers on top of TRD (layer 1) and directly above ECAL (layer 9). This configuration, pictured in Figure 2.9, allows for a maximum detectable rigidity (MDR) for protons of about 2 TV [129], where the rigidity is a measure of the bending of a trajectory in a magnetic field which is proportional to the particle's momentum divided by the absolute charge number. The sign of the rigidity also gives the charge sign. The rigidity resolution strongly depends on the constellation of hits in the nine Tracker planes, improving with hits in the outer layers one and nine in particular. The rigidity resolution with different Tracker spans is shown in Figure 2.10 for protons as a function of rigidity.

The major contribution to the rigidity resolution is given through the finite alignment of the Tracker planes which suffer from movement and deformations, caused by temperature variations in the orbit and with the solar beta angle, discussed later in Section 4.3.1.2. All this impacts the outer layers, in particular. To monitor the exact position and movement of the inner Tracker planes, a Tracker Alignment System (TAS), consisting of five laser diodes, is installed in the layer two support structure providing an inner tracker alignment on the sub-micron level. A more dynamic alignment including also the external layers is performed by interpolating the trajectory of CR protons or muons [130]. An alignment precision for the external layers of about 5 μm for layer one and 6 μm for layer nine with respect to the inner Tracker is achieved [5].

Another contribution to the Tracker performance is the noise level which depends on the operating temperature and affects mainly the inner part. A constant noise level is of particular importance for the charge measurement of the Tracker. A measured signal from a sensor is a combination of a constant offset (pedestal), the noise component and
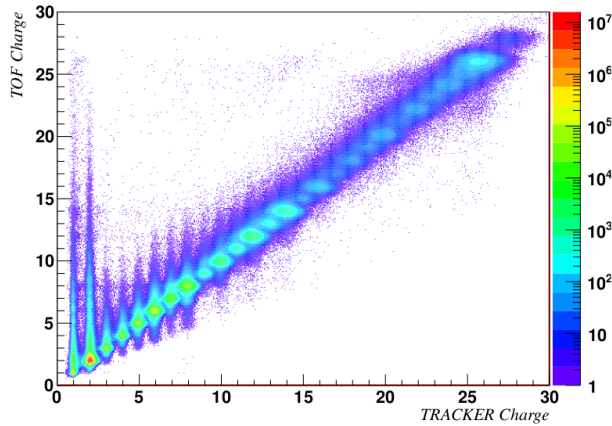
Figure 2.11: Distribution of the redundant measurement of the charge using TOF and Tracker for particles with nuclear charge up to iron (Z=26) [131].

the energy deposit by the particle itself, which is proportional to the particles charge via $dE/dx \propto Z^2$ [132]. Extracting the ionization contribution gives a second, precise charge measurement, complementary to TOF, up to iron (Z=26) as shown in Figure 2.11. The plot is a good example of redundant measurements of the same particle's properties to reduce systematics. To monitor the channel's response, a calibration is performed every 46 minutes at the equator crossing. This procedure keeps the noise level stable at around 2.9 (2.5) ADC counts for the n (p) side [128]. To maintain the operating temperature and therefore the noise level constant and homogeneous at around 10 °C and evacuate the heat emitted by the front-end electronics, an active temperature control system is required. For the AMS Tracker, this is realized in a mechanically pumped two-phase CO_2 loop system named Tracker Thermal Control System (TTCS). The system consists of two redundant fluid loops filled with CO_2 in a two-phase state, controlled by an accumulator. The CO_2 is pumped through the loops by two mutually redundant pumps in every loop to compensate for failure transporting the heat from the inside to external radiators [133]. The TTCS manages to keep the temperature of the inner Tracker stable up to a few degrees [128].

A constant noise level is of particular importance for the charge measurement received by the Tracker. A measured signal from a sensor is a combination of a constant offset (pedestal), the noise component and the energy deposit by the particle itself, which is proportional to the particles charge via $dE/dx \propto Z^2$ [132]. Extracting this ionization contribution gives a second, precise charge measurement, complementary to TOF, up to iron (Z=26) as shown in Figure 2.11. The plot is a good example of redundant measurements of the same particle's properties to reduce systematics.

2.5. The Anti Coincidence Counter

To get a clean track reconstruction for the charge determination, and to reduce the trigger rate during periods of high flux, the inner Tracker is surrounded by 16 scintillator paddles, aligned vertically with a length of 83 cm and a thickness of 8 mm, referred to as Anti Coincidence Counter (ACC) [134]. ACC is used to reject events with particles entering the detector from the side. The scintillation light is wave-shifted and guided to 16 PMTs, of which eight are located on the upper side, and eight are located at the bottom of the scintillator paddles. To use the ACC veto in the trigger logic, a fast signal processing with an inefficiency smaller than 10^{-4} is needed. However, if a highly charged nucleus produces delta electrons, which might fire the ACC, or high energy electrons
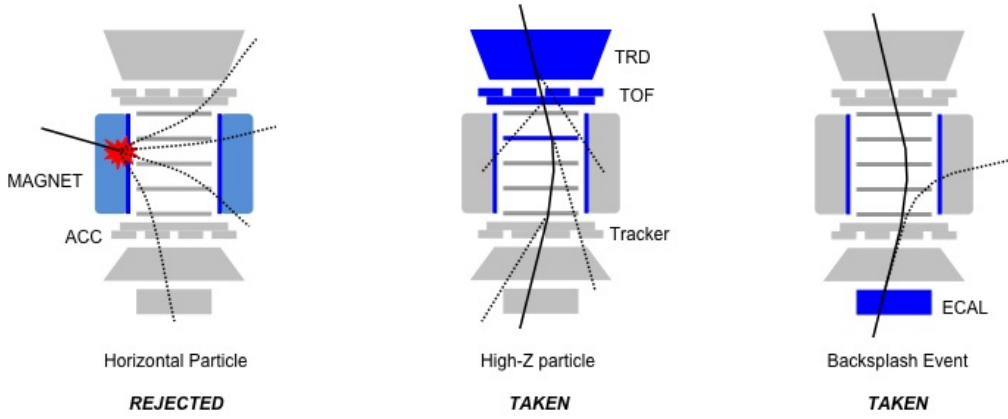
Figure 2.12.: Veto logic of the ACC for the AMS-02 particle trigger [110]. Particles which enter
                the detector horizontally are rejected to reduce false hits in the Tracker while highly
                charged particles, that produce secondaries, and events with backsplash from ECAL
                are taken.

produce back-splash from the calorimeter, the veto has to be suppressed. Hereby, the
ACC veto is set in relation to the TOF trigger signals. The role of the ACC in the trigger
logic is illustrated in Figure 2.12.

2.6. The Ring Imaging Cherenkov Detector

For the measurement of velocity and absolute charge with a focus on heavier nuclei
and isotopes, AMS-02 is equipped with a Ring Imaging Cherenkov Detector (RICH)
[135, 136].
A charged particle traversing a medium with velocity higher than the velocity of light
in that medium $\beta > c/n$ emits Cherenkov radiation due to the polarisation of the sur-
rounding material on molecular scale [137]. The light is radiated in a characteristic angle
dependent on the refractive index n of the surrounding material and the particles relative
velocity β following $\cos \theta_c = 1/(n\beta)$. The number of emitted photons is proportional to
the charge number with $n_{Ph} \propto Z^2 \sin \theta_c$.

For the AMS-02 RICH, a radiator plane of 60 cm in radius made of silica aerogel tiles
with a thickness of 2.5 cm and refractive index n≈1.050 with a cut-out central square
of sodium fluoride of refractive index n=1.33 is used. A detection plane of octagonal
shape equipped with 680 PMTs is located 47 cm below the radiator plane. The detector
plane has a central square 64 cm^2 hole, where the calorimeter is located underneath.
This configuration minimizes interactions above ECAL. The dead area in the *ECAL hole*
motivates the NaF radiator square. To maximize the photon detection sensitivity, the
conical walls between radiator and detector plane are covered with reflective mirrors as
indicated in Figure 2.13.

To get a precise measurement of the particle velocity, the aerogel refractive index needs
to be known with a precision of the order of Δn/n≤1.5×10^{-4}, depending on the tiles po-
sition. A calibration of this number on flight data is performed on proton events in [138],
giving a β resolution $\frac{\Delta\beta}{\beta^2}$ of 0.8×10^{-3} for helium and 0.5×10^{-3} for nuclei of charge Z>5.
For a correct charge measurement the number of photons has to be counted, making
the knowledge of the PMTs photon yield evaluated in [139] a major contribution to the
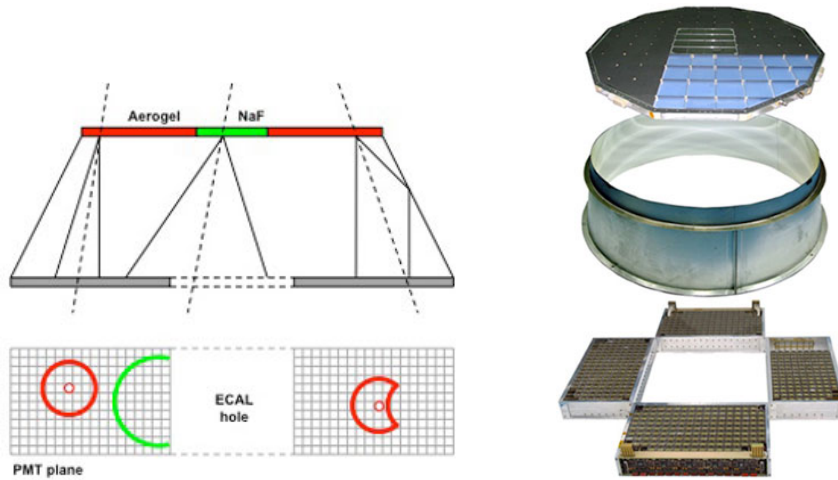
Figure 2.13.: Operation principle of the RICH (**left**) and photo of the main RICH components (**right**) [110]. Cherenkov radiation is emitted in the radiator plane in a characteristic angle dependent on the particles relative velocity β. The photons are measured by a plane of PMTs. To reduce material in front of ECAL a hole is left out in the PMT plane.
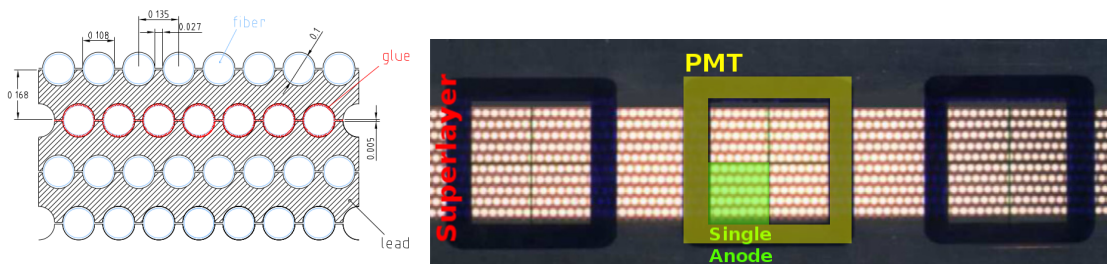
Figure 2.14.: ECAL active part structure [141]. **Left:** Technical sketch of the ECAL *pancake* with four layers of plastic scintillator fibers glued to grooved lead foils. **Right:** Superlayer with PMT indicated with the yellow box and one anode of the four-anode PMTs highlighted in green.

charge resolution. For helium, the RICH reaches a charge resolution of σ_Z/Z =0.3 and 0.5 for Z=14.

2.7. The Electromagnetic Calorimeter

The last piece in the chain of sub-detectors within AMS-02 is the Electromagnetic Calorimeter (ECAL), a lead scintillating fiber sampling calorimeter on the bottom of AMS-02 [140]. It is required to measure the energy of electrons and positrons as well as to reject protons independent of TRD.

The active part, referred to as *pancake*, is composed of grooved 1 mm thin lead foils interleaved with layers of 1 mm in diameter plastic scintillating fibers glued to the foils using optical epoxy. Eleven foils and 10 parallel aligned fiber layers are combined to one *superlayer*, pictured in Figure 2.14. A superlayer is read out by 36 PMTs with each four anodes mutually arranged on the two opposite ends of the superlayer, to read out all fibers without dead areas. By stacking nine superlayers (five in x- and four in y-direction), a three-dimensional imaging of the shower is achieved. With this configuration the *pancake* has an active area 648×648 mm^2 with a thickness of 166 mm and a
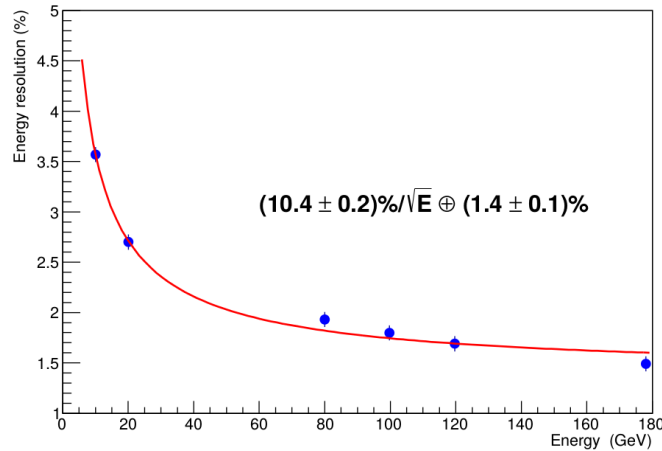
Figure 2.15.: ECAL measured energy resolution $\frac{\Delta E}{E}$ as a function of particle energy from test beam measurements on the ground [142]. Test beams with positrons were used at energies of 10, 20, 80, 100, 120 and 180 GeV. The energy resolution is better than 5% for all energies below 180 GeV. The energy resolution at higher energies and the linearity has to be monitored using the independent Tracker rigidity measurement.

weight of 496 kg, resulting in an average density of 6.8±0.2 g/cm³. This gives a radiation length X_0 of about 10 mm corresponding to a total depth of 17 X_0 and a nuclear interaction length of $\lambda \approx 0.6$. Due to the small nuclear interaction length most nuclei will only deposit energy from ionization, called a minimum ionizing particle (MIP). Electromagnetic interactions of electrons, positrons, and photons occur with high efficiency, resulting in an electromagnetic shower starting in the upper part of ECAL.

A single anode of the four anode PMTs covers an area of 9×9 mm², combining 35 fibers within half a Molière radius [143]. The resolution allows for a complete 3D shower reconstruction from which the energy after corrections for the rear and lateral leakage as well as for the anodes efficiency can be determined from 0.5 GeV up to 1 TeV. The energy scale itself and the energy resolution $\frac{\Delta E}{E}$, presented in Figure 2.15, have been calibrated using positron test beams on ground [144, 145]. The linearity in the PMT's response has been found to be under control within 1%, at least up to 300 GeV. The stability of the energy reconstruction can be monitored using the momentum measured by the Tracker and the MIP signals of proton and helium events [146].

The excellent shower reconstruction of ECAL is also necessary for its particle identification performance. Combining the lateral and longitudinal shower development, the starting point of the shower and the fraction of raw energy deposited in ECAL to the momentum, hadronic showers induced from protons can be rejected from electromagnetic showers by a factor greater than 10^4 up to an energy of 300 GeV, as shown in Figure 2.16.

Taking the center of mass of the shower energy deposit in every layer allows for a reconstruction of the shower's pointing direction with a resolution better than 1° [142]. This allows for a matching between a particle's trajectory measured by Tracker and the shower in ECAL for the correct assignment of a shower to the event. Also, it enables the ECAL for a standalone gamma ray measurement. For this task ECAL is also equipped with a standalone trigger of high efficiency and fast response, using PMTs in the second and seventh Superlayer [147]. However, it has been found beneficial for gamma ray
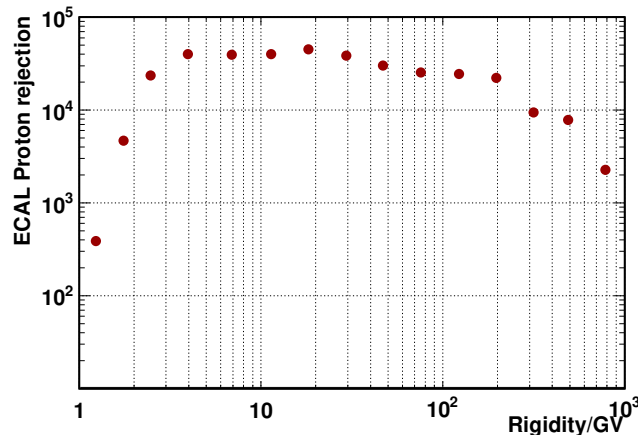
Figure 2.16.: Proton rejection as function of rigidity for ECAL and the Silicon Tracker combined, evaluated from flight data at 90% positron selection efficiency [142]. Electron and proton samples were selected using the Transition Radiation Detector.

searches to detect photons via conversions in electron-positron pairs inside the detector's material due to larger acceptance.

2.8. AMS operations and data acquisition

The AMS-02 sub-detectors create about 7 $^{GBit}/_s$ of data delivered through a total of ~300,000 channels with a maximum design-rate of 4 kHz that has to be processed in a time accuracy of at least 100 ps as desired by TOF. In addition, the system needs to work in a space environment with high temperature variations on orbit within a range of -5 to +15 °C (measured on the magnet) in the absence of cooling and under high radiation with limited power consumption of a maximum of 2.5 kW[1] and limited data transmission rate. Following these specifications, the AMS-02 Data Acquisition System (DAQ) has been designed with high redundancy in a unified chain structure as shown in Figure 2.17 [148, 149]. The communication between ~300 Digital Signal Processor (DSP) nodes is organized in a *Master-Slave* principle where data operations are instantly performed by each slave only on request of its master.

Analog signals from every channel are digitalized by sub-detector specific Application Specific Integrated Circuits (ASIC) located close to the sub-detector elements. From the ASICs, the digital data is transmitted to Data Reduction Boards (xDR[2]) where they are significantly compressed by sub-detector specific fast online data reduction and buffered into memories. Data from the TOF, ACC and ECAL fast-triggers are separated and directly processed by the Level-1 Trigger readout. On request of the trigger, the other data is shipped over to Low-Level DAQ computers JINF-x and to the Top-Level DAQ computer JINJ which serves as Level-3 Trigger and therefore is last to decide whether an event is of interest. Between DSPs, data is transmitted via a custom developed fast serial data protocol called *AMSwire*. At the end of the chain, the data is held by the Main Data Computer JMDC in a 112 GB Buffer (JBUX), enough storage for about one day of data-taking, or is directly transmitted further using ISS avionics and infrastructure. JMDC

---

[1]This is about the power consumption of a washing machine.

[2]Whereat x is a uniquely assigned letter for every sub-detector: E for ECAL, R for RICH, S for TOF and ACC, T for Tracker and U for TRD, as well as J for the Main Computers.
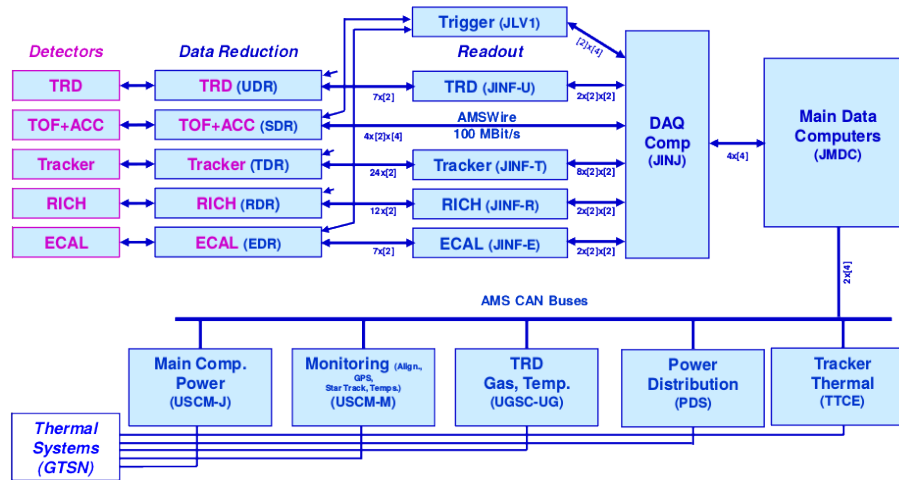
Figure 2.17.: Chart of the AMS-02 DAQ system. The five subdetectors transmit the data via their own Data Reduction Boards to Low-Level DAQ computers JINF-x and to the Top-Level DAQ computer JINJ. In the end the data is held in the Main Data Computer JMDC and transmitted to Ground. Redundancy of the different parts is imprinted at the connections. Separated and only connected via JMDC are computers for monitoring and controlling.

also manages critical detector health data in real time, incoming commands for detector operations, as well as the power distribution among the detector.

The main DAQ computers are four times redundant, twice on two opposite sides of the detector, while Low-Level and xDR boards have a redundancy of 2. The DAQ electronics is installed outside the detector inside the supporting structure on dedicated radiators to favor heat exchange with the external environment.

Within the DAQ chain, the data stream is reduced to about 10 $^{\mathrm{Megabits}}$/s which can be transferred to ground, making use of NASA's Tracking and Data Relay Satellites (TDRS) at a nominal speed of 17 $^{\mathrm{Megabits}}$/s and a duty cycle of 55 to 90%[3]. Data is transmitted via the Ku-Band in two downlinks: The so-called High Rate Data Link (HRDL) for science data and a copy of monitoring data and the Low Rate Data Link (LRDL) for housekeeping data and commanding in S-Band. In case of an unexpected connection loss, the data is on backup on a laptop inside ISS within the astronaut's grasp. With the TDR Satellites, the data arrives on ground at White Sands Complex in New Mexico, USA. Here it is forwarded within the NASA Integrated Services Network (NIS) to Marshall Space Flight Center, where the Collaborations Ground Support Computers are based. For monitoring and data reconstruction the files are then transferred to CERN's Prevessin site in France where the AMS Control Room is based in a dedicated Payload Operations and Control Centre (POCC). Despite the long journey of the data, the detector is monitored and operated in *nearly* real time 24/7.

---

[3]The data downlink is stopped for handovers between satellites, a block of the connection from the ISS solar arrays or other events.

3. The search for anisotropies with AMS-02

To search for anisotropies in the arrival direction of CRs, the particle flux in the celestial sky has to be determined with an accuracy down to the per-mille level, depending on the desired sensitivity. Irregularities in the detector operations directly affect the data taking, and introduce a time or position dependent variation in the number of measured particles, which can mimic a signal. AMS-02 is operated in a variable space environment on a hosting station with mission focused on the life support for the astronauts. The sub-detectors are subject to aging, instabilities during the orbit, and temperature variations that cannot be corrected for completely in offline calibration. Also, the detector has a finite opening angle and sees only a small fraction of the sky at a time, which leads to a non-uniform accumulation of observation time of the celestial sky, due to the ISS orbit. On top of that, the Earth's magnetic field, as introduced in Section 1.3.2, causes a natural variation in the flux of low energetic particles. The influence of the various external factors on the data taking cannot be simulated in detector Monte-Carlo simulations. The whole analysis has to rely fully on the collected data only.

All the above issues constitute a major challenge for the analysis and smart methods need to be developed. This chapter is dedicated to the introduction of the dominant effects on data taking, such as the detector's operation, the ISS orbit or the Earth's magnetic field that dominates the low energetic particle flux, and how such effects are corrected for in the analysis. To trace down if a possible source is of environmental or astrophysical origin, different coordinate systems are used. Subsequently, the tools and technical details for the analysis of anisotropies will be explained.

3.1. ISS orbit and environment

The AMS-02 detector orbits Earth aboard the ISS at an altitude of about 400 km on an orbit with inclination of 51.6° in a period of 93 minutes. The AMS-02 zenith inclination is 11° with respect to the ISS zenith. The position of the detector above Earth's surface is shown in Figure 3.1 exemplary for two orbits together with its relative abidance time, defined as the relative length of stay, integrated over five years. The plot is presented
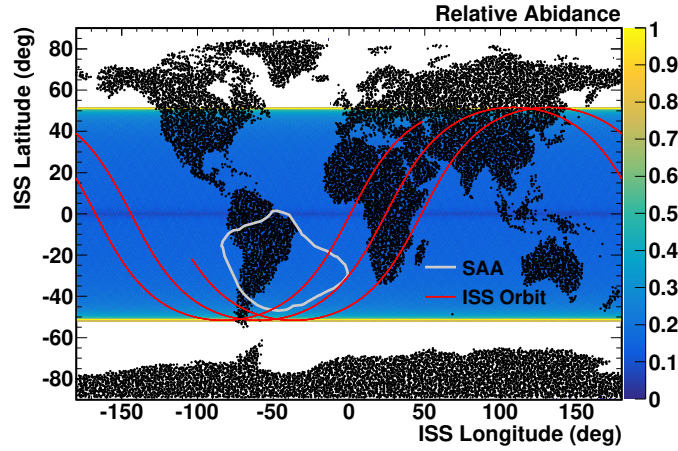
Figure 3.1.: ISS position above Earth's surface exemplary for two orbits (red line) together with its relative length of stay, referred to as abidance. The grey area marks the location of the SAA. A strong cumulation of measuring time at high latitudes is to be seen as effect of the orbit inclination.

in the Greenwich True Of Date (GTOD) system which is a natural coordinate system to describe phenomena bound to the Earth's surface as it originates in the Earth's center with the z-axis identical to the Earth's rotation axis and co-rotating x- and y-axis. A common practice is to fix the x-axis towards the Greenwich meridian at equator level. In this projection, there is a cumulation of measuring time at higher latitudes due to the ISS orbit which will perpetuate to other coordinate systems, as it will be seen later-on and also superimpose with other Earth-bound effects mainly originating from the geomagnetic field introduced in 1.3.2.

To first order, the magnetic field is a dipole field with the magnetic poles close to the Earth's Geographic Poles. Particles are deflected by the horizontal component of the dipole field, which is maximal at the equatorial region and decreases towards the poles. At lower energies (<30 GeV), particles get deflected and the flux is strongly modulated by the geomagnetic field with the magnetic latitude such that low energetic particles can only reach the detector towards the polar regions. The higher flux of the abundant low energetic particles towards polar regions increases the trigger rate and therefore the
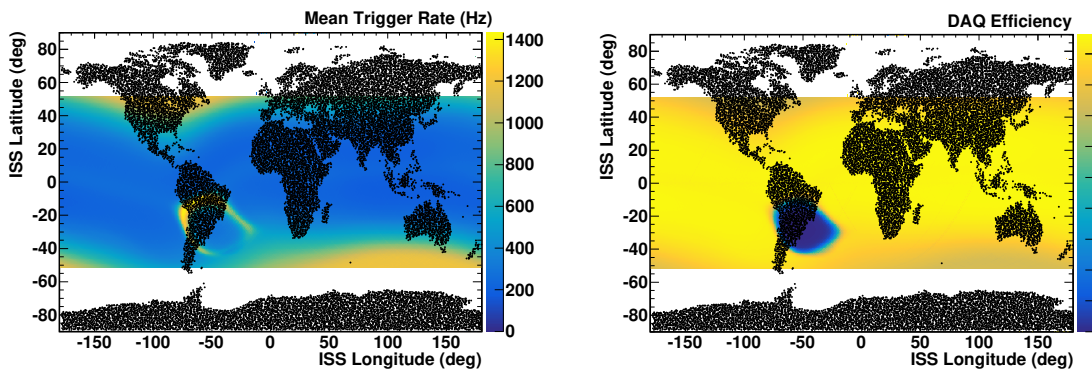
Figure 3.2.: **Left:** The mean trigger rate as function of position above Earth's surface. **Right:** DAQ efficiency as fraction of active measuring time. Both show an anti-correlated behavior: At the geomagnetic polar regions the trigger rate rises while the DAQ efficiency drops.
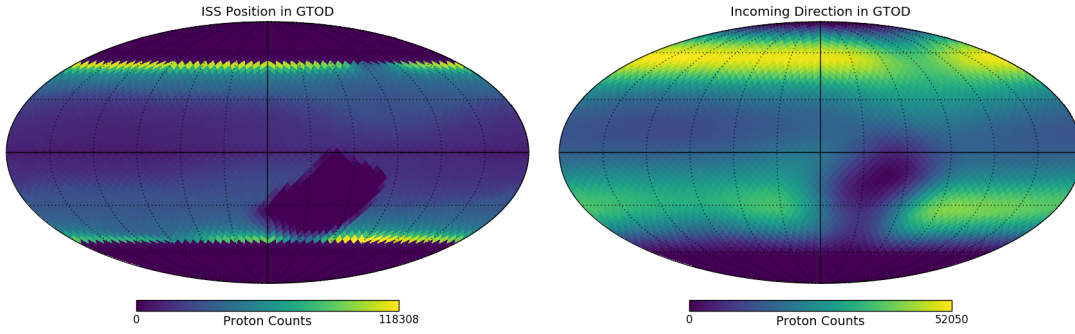
Figure 3.3.: Event counts of protons with a rigidity greater than 16 GV in GTOD plotted in Moll-weide projection. **Left:** Counts at the ISS position. **Right:** The particle's origin in the sky.

deadtime of detector electronics. Both are shown in Figure 3.2. At the South Atlantic Anomaly (SAA), where the inner Van-Allen belt reaches into the ISS orbit, trapped particles follow the magnetic field lines and reach the detector. A consequence is that the DAQ saturates and the livetime, the fraction of time in which the detector was ready to measure a new event, drops close to zero. Also the low energetic particles close to the SAA and the geomagnetic poles trigger ACC and flood TRD on top of AMS such that trigger- and particle selection capabilities decrease which affects the measurement of particles at higher energies, as well.

3.1.1. Coordinate systems

It is evident from Figure 3.1 that the orbit covers a large fraction of the Earth's surface and moreover of the celestial sky. This is a huge benefit in comparison to ground-based experiments that are located at a fixed position and therefore only scan a limited fraction of the sky as the Earth rotates. These experiments lose sensitivity for a source search in direction of the Earth's rotational axis as discussed in Chapter 1.4. Resulting measurements are then only a 2-dimensional projection of a 3-dimensional anisotropy signal. AMS-02, with its large sky coverage, is capable to measure the full 3-dimensional incoming particle distribution in the celestial sky and trace down a possible anisotropy dependent on its source in different coordinate frames. For example, if a source is of galactic origin, its signal will be enhanced in the galactic coordinate system while in other coordinate systems it might be smeared out. On the other hand, anisotropies observed in coordinate systems that are expected to be free of astrophysical signals point out systematic effects in the measurement, introduced by the detector. A similar limitation as for ground-based experiments applies to balloon experiments that are often launched at the Earth's polar regions and only cover this area. Useful coordinate systems will be introduced in the following. In general, all coordinate systems can be used to describe a position (e.g. the detector position on the Earth's surface) or an incoming direction (a pointing in the celestial sky). Figure 3.3 shows the same events in the GTOD coordinate system, that will be introduced in the next Section 3.1.1.1, at the ISS position on the Earth's surface and at the particle's origin on the celestial sphere. While for the search of astrophysical signals the particle's incoming direction, of course, is of desire, systematic effects might better be studied with the position. If not stated otherwise, all maps are shown with the particles incoming direction.

3.1.1.1. Greenwich True Of Date (GTOD) and geomagnetic coordinates

A coordinate system already introduced is GTOD which is coupled to the Earth's surface where undesired Earth-bound effects, mostly originating from the geomagnetic field, can be identified. Also single orbits of bad calibration or weak GPS signal, both from which an anisotropy might be introduced, are enhanced in this coordinate system. As for the Earth's rotation it cannot be argued that any astrophysical source of particles would reflect significantly in this coordinate system. If however any anisotropy is observed which cannot be connected to a known physical source, such as the East-West effect discussed in Section 1.3.2, it most likely will be of detector origin and needs to be found and removed from the measurement, or to be included as systematic bias. Therefore, the GTOD coordinate system serves as a control instance in the analysis. The term *True Of Date* refers to corrections on small timescales with respect to the *Greenwich Mean Time* such as Earth's precession, nutation, and polar wandering.

By tilting the z-axis by 9.5 deg, while leaving the x-axis fixed with respect to GTOD, one obtains a coordinate system aligned with the dipole axis of the geomagnetic field (geomagnetic coordinates). The x-y-plane then resembles the equator of the dipole field and the flux of low energetic particles will be constant in rings of latitude. In this way systematic biases from the external particle rate on the detector itself can be studied.

Earth-bound systems are not useful when it comes to search for an astrophysical source where celestial coordinate systems, which describe a particle's incoming direction independent from the detector position, are more handy. In this thesis, three celestial systems are used that are geared to different physical sources. A single particle's incoming direction can be expressed in all frames via simple coordinate transformations following [150]. The systems use polar coordinates projected on the virtual celestial sphere.

3.1.1.2. Equatorial coordinates

The Equatorial (EQ) system has its origin in the Earth's center and the z-axis aligned with Earth's rotation so that the x-y-plane resembles Earth's equator projected to the celestial sphere forming the celestial equator. The difference with respect to GTOD is that it is not co-rotating with Earth but fixed relative to distant stars and galaxies and thereby to possible sources. The x-axis points towards the vernal equinox where the celestial equator crosses the Earth's orbit plane called ecliptic. An illustration of the fundamental plane and the axis of the EQ system is sketched in Figure 3.4. EQ coordinates are defined as declination in direction positive towards northern latitude and right ascension eastwards along the celestial equator in longitude.
This coordinate system is the most natural for ground-based observations of the sky and consequently used in most of the published measurements discussed in Section 1.4.

3.1.1.3. Galactic coordinates

When it comes to galactic sources it is convenient to express observations in a galactic frame (GAL). The fundamental plane is the galactic one where most of the stars are located and the primary direction points towards the galactic center. The origin is set in the Sun's center of mass and the right-handed-convention is used to set the remaining axis. The fundamental directions and planes are shown in Figure 3.5. The galactic plane is tilted by 62.6 degrees with respect to the ecliptic plane. The coordinate system has been defined by the International Astronomical Union (IAU) based on the Equatorial
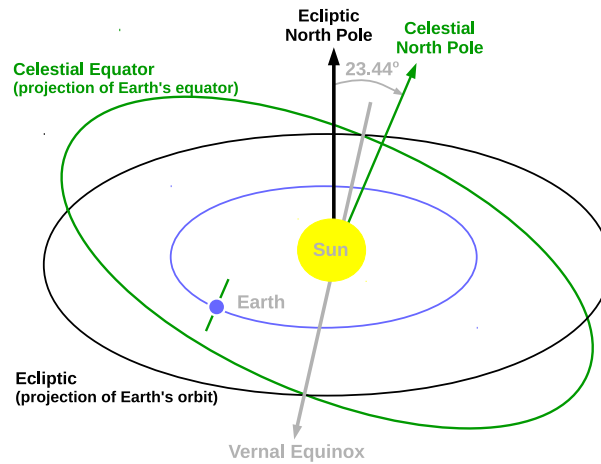
Figure 3.4.: Celestial coordinate systems with solar centered origin. The celestial plane is the projection of the Earth's equator on the celestial sphere. This plane is fixed with respect to distant stars. If the origin is moved to the Earth's center, the resulting coordinate system is the equatorial system and suited best to describe observations made from the Earth's surface.

coordinate system [151]. The galactic center has been defined using radio observations of the relative movement of neutral hydrogen (H-I regions) via the 21-cm line and kept up to date with improving observations of the galaxy. Used in this analysis is the J-2000 convention based on the observation of the radio source Sagittarius A*, which is believed to originate from a massive black hole marking the galactic center [152].

The galactic coordinate system is the most natural one for stating anisotropies in charged galactic cosmic rays as it is aligned with possible sources with the x-axis pointing towards the region with highest source density and the y-axis is aligned with the Heliosphere resulting from the Sun's movement around the galactic center. Coordinates are stated in Galactic Latitude and Longitude.

3.1.1.4. Geocentric Solar Ecliptic coordinates

To study the local particle propagation through the Sun's local magnetic field, the Geocentric Solar Ecliptic (GSE) frame is useful. As the name suggests, its origin is in the Earth's center of mass and the fundamental x-y-plane is formed by the ecliptic. The primary direction points towards the sun making the coordinate system rotate with Earth's orbit in a 1 year period with respect to Equatorial. This coordinate system is of major importance to track time-dependence due to the solar activity within a solar cycle, as it has been discussed as a source of anisotropy in Section 1.3.1. Here the evolution in time is of a major interest because of the Sun's activity cycle.

3.1.1.5. Correlation between celestial systems

It has already been argued that the different coordinate systems serve a different purpose in the analysis. Coordinate systems which are coupled to Earth's surface and are co-rotating with Earth, such as GTOD and geomagnetic coordinates, will not reveal an astrophysical source as it would be moving within the system and average out. In the following they are referred to as *signal-free* coordinate systems, as they carry no astrophysical information. It will be assumed that in these coordinate systems the sky will
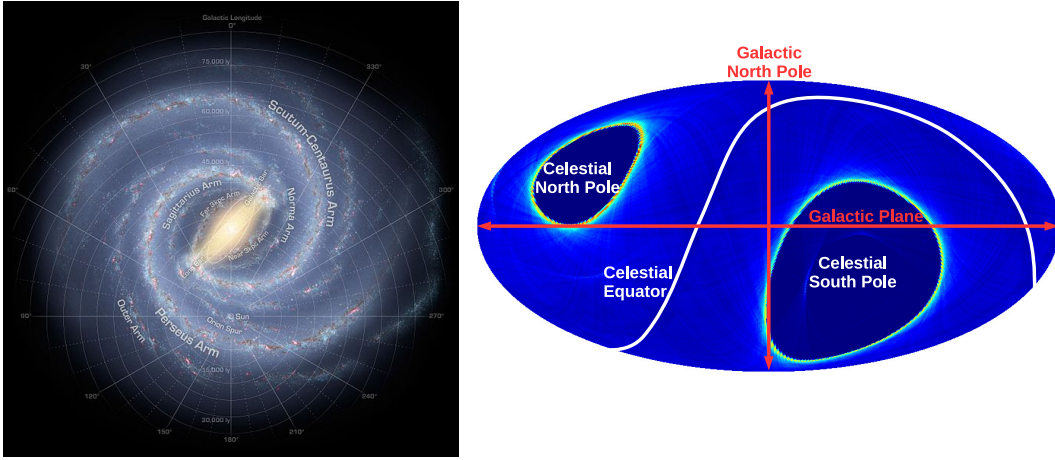
Figure 3.5.: **Left:** Artists impression of the spiral structure of the Milky Way with overlaid lattice of the galactic x-y-plane and the galactic longitude with solar origin [153]. **Right:** AMS-02 pointing direction for one year in galactic coordinates plotted in Mollweide projection. The galactic plane and North Pole are marked in red wherein the crossing point is the galactic center. The equatorial system, which is tilted with respect to GAL and shifted by one AU, is marked in white.

not show any deviation from isotropy above the East-West effect at low energies. If a deviation from isotropy is found, it must be of a systematic origin that needs to be identified and removed from the analysis. A signal in the coordinate systems EQ, GAL or GSE on the other hand could originate from different sources of astrophysical origin. The coordinate systems are therefore referred to as *analysis* coordinate systems. A summary of the different coordinate systems under study in this thesis can be found in Appendix A.

Consequently the analysis flow is the following: Check *signal-free* coordinate systems for absence of anisotropy and trace down the source, if this requirement is not fulfilled. If the systems are flat[1], a search for a physical signal can be performed in the *analysis* coordinate systems.

In order to justify this assumption, the different coordinate systems have to be uncorrelated: Signals originating in a *analysis* coordinate system have to be washed out in the *signal-free* coordinate systems as result of rotations relative to one-another. Such correlations were studied extensively in a Bachelor thesis [154], that was written to support this thesis. Artificial dipole signals were introduced in a coordinate system and it was checked if the signal survived in the other ones. For the study, the so-called *shuffling technique* was used, which will be discussed later in Section 3.2.3. The following results were found:

- Dipole anisotropies originating in the ecliptic plane of GSE are fully suppressed, up to the available sensitivity of 0.03%, in GTOD and GAL. This results from different rotation periods in GTOD (Earth's rotation of one day), GSE (Earth's orbit of one year), and GAL (fixed).

- Dipole signals induced in the GTOD equatorial plane are fully suppressed, up to the available sensitivity of 0.03%, in the *analysis* coordinate systems EQ, GAL, and

---

[1]In the following, the term *flat* is used to refer to *absence of deviation from isotropy within the statistical uncertainties.*
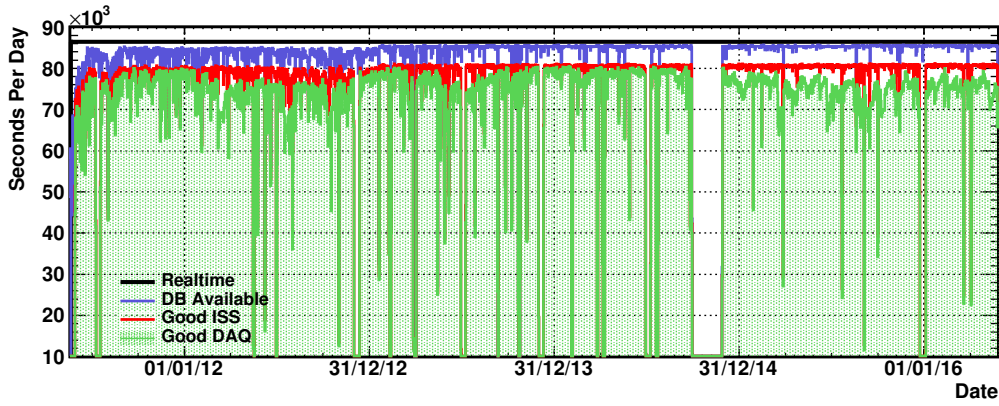
Figure 3.6.: Stability of data taking time counted in seconds in bins of one day. The black line represents the real-time, in blue only times with available GPS and position database are counted, in red times of bad ISS orientation and positions inside SAA are removed and in green times in which the detector is not in optimal state are removed. On average, the detector takes data about 90% of the time. Gaps in the data taking are mostly due to ISS conditions. The gap from beginning of October till end of November 2014 is due to a shutdown of the detector for technical reasons.

GSE.

- Dipole signals perpendicular to the ecliptic plane are fully recovered in GSE and GTOD and suppressed by a factor of ≈ 2 in GAL.

- Dipole signals along the z-axis in GAL are suppressed by a factor of ≈ 2 in GSE and GTOD, which matches the projection of the $62.6°$ tilt in the z-axis of GAL with respect to the ecliptic plane.

As a result, correlations between the coordinate systems could not be found in the x-y-planes of any kind, while signal sensitivity in z-direction is reduced due to correlations in the rotational axis among the different coordinate systems[2]. Dipoles perpendicular to the equatorial, ecliptic, or galactic plane are hard to disentangle in the different coordinate systems.

3.1.2. Stability in time

The data taking is not only affected by the outer environment as described but also by operations of the ISS and the detector itself. When a docking or an extra-vehicular activity (EVA) of the astronauts occurs or to improve the thermal environment during cold periods, the station might be reoriented from its nominal flight direction for several hours or days. If the angle between the AMS pointing direction and the vertical direction, called zenith angle, becomes too big, the data taken cannot be used in analysis. In addition, times of external actions like a video survey performed by the robotic arm are not considered when they occur inside the detector's field-of-view. Due to detector operations, some time periods are excluded from analysis, such as *Gas Refills* or calibration runs. Also smaller periods, of the order of seconds, between two runs during calibration, when no position data is available or when the detector is located inside the SAA, are removed. All factors above amount to a fraction of good data taking of about 90% time,

---

[2]An effect from the correlated z-axis of the coordinate systems will be included in the study of the systematic uncertainty, later in Section 4.3.1.2.

as visible from Figure 3.6. However it is clear that good data taking time is not uniformly distributed and can introduce a time and position variation in the measurement, if not handled correctly.

3.2. Methods for anisotropy searches

The angular distribution of events measured by AMS-02 is largely dominated by operational effects present in all frames as discussed in the previous Section 3.1. Therefore the resulting event maps, as pictured in Figure 3.3 or 4.2, cannot be used directly for the search of anisotropy signals. None of the coordinate systems is subject to equal coverage. Non-physical structures in the data need to be understood and removed in the analysis process in order to find astrophysical sources. Mathematically speaking, the hypothesis of an isotropic sky as measured by AMS-02 has to be constructed and compared to the measured data. The isotropic sky is called *reference map* and its construction is the fundamental key in the search for anisotropies.

A suitable reference map for source searches needs to provide an estimate of exposure, as speaking of the particle rate $R(t)$ measured at a certain moment, and a correct coverage of the celestial sky in the field-of-view $A(\theta, \phi)$. Both items have to be known accurately up to the level of desired sensitivity, as deviations are detected as signal. To create a reference map, approaches have been proposed in the literature such as the *shuffling technique* (Section 3.2.3) and the analysis in declination bands (described for ground-based telescopes in Section 1.4). Both were found to be not usable in the AMS-02 anisotropy analysis. It will be shown that restricting factors in the choice of reference maps for AMS-02 are the limited field-of-view, in comparison to ground-based experiments, and the dynamically changing environment of the detector. In light of these constraints, new methods to construct reference maps are needed, and were developed in this thesis.

3.2.1. Other particle species as reference

In order to keep the systematic bias from the evaluation of geometric acceptance $A(\theta, \phi)$ and particle rate $R(t)$ small, the normalization of exposure can be done to a second particle that shares the same selection properties but is of different astrophysical origin. The method, named *relative anisotropy* was first shown in [109] and also used in the Pamela analysis [108]. For positrons this could be electrons which, being their antiparticles, are measured similarly in the detector, which is used as the basis in the measurement of the positron fraction [1, 2]. They have a similar effective acceptance and, by construction, suffer the same operational effects. Only the different bending direction in the detector's magnetic field could introduce an anisotropy of systematic origin. If the same source is shared, even though the relative contribution of the source differs, one loses sensitivity. This would be the case for pulsars which would produce electrons and positrons in the same share, but since electrons are primary particles and therefore more abundant the relative contribution is smaller compared to positrons. Also in case of a signal it would not be evident if an anisotropy in the positrons or their reference particles or even an unintended local charge dependent anisotropy has been measured since only the *relative anisotropy* is measured. For the case of positrons a second choice of reference particle is available, which is protons. They carry the same charge but might not share the same effective acceptance because hadrons and leptons are subject to different processes in

the detector. Last of all, it is not possible to find a reference particle for all species as for the restrictive requirements:

- The particles need to share the same selection to conserve the acceptance $A(\theta, \phi)$ and particle rate $R(t)$.

- The reference particle needs to be more abundant than the signal particle, otherwise fluctuations in the reference map dominate the dipole signal in the signal map.

- Absence of a signal in the reference map.

The first requirement already eliminates particles of different charge, which rules out an anisotropy search in helium and higher charge nuclei. The second requirement leaves protons without any reference particle. The issue will be discussed in more detail later in Section 3.2.6. As a consequence, the proposed method only allows to construct a reference map for positrons and electrons.

3.2.2. Same particle species at different energy as reference

The flux of protons, as measured by AMS-02 [5], shows a hardening in the flux at rigidities above 100 GV. The observation could be explained by the contribution of a point source with a rigidity dependent contribution to the flux. The proton flux as measured by AMS-02 is shown in Figure 3.7. To search for anisotropies in the arrival direction of protons, the method used in the *relative* anisotropies has been adapted to be used with protons in the frame of this thesis. If the observed hardening is of a point source origin, starting to contribute for high energies, an anisotropy relative to the low energy regime, where the point source does not show up, might be measured. To probe the isotropy of protons with a reference map of the same selection, low rigidity protons are used as a reference for high rigidity signal protons, as marked in the plot. The reference sample must be of rigidity greater than the geomagnetic cutoff which modifies the particle rate $R(t)$ at rigidities below $\approx$32 GV and introduces a rigidity dependent coverage. Both will show up as deviations from isotropy. To conserve acceptance $A(\theta, \phi)$, the particles selected in the low rigidity reference and the high rigidity signal regime need to have the same geometric acceptance, which is only true if the selection efficiencies are sufficiently constant with energy. Also protons at high energies need to pass the full Tracker span, including the external layers one and nine, to get a reliable rigidity measurement. The requirement cannot be relaxed for the low rigidity reference sample, as it would change the acceptance. Finally, the sample statistics give the upper boundary of the reference sample, which is set to 80 GV, as the reference sample needs to be of higher sample size with respect to the signal sample. This issue will be discussed in Section 3.2.6.

The method only gives an anisotropy *relative in rigidity*. A possible signal which already contributes in the reference samples rigidity range will not be fully recovered. Proposed methods of *relative* source searches have in common that systematic uncertainties are hard to assess and therefore have limited significance. Consequently, an *absolute* measurement of the angular distribution of the particles incoming direction is desirable.

3.2.3. Shuffling technique

The so called *shuffling technique* has been introduced by [155] in the search for ultra-high-energy (UHE) cosmic ray point sources and applied to data from the Fly's Eye
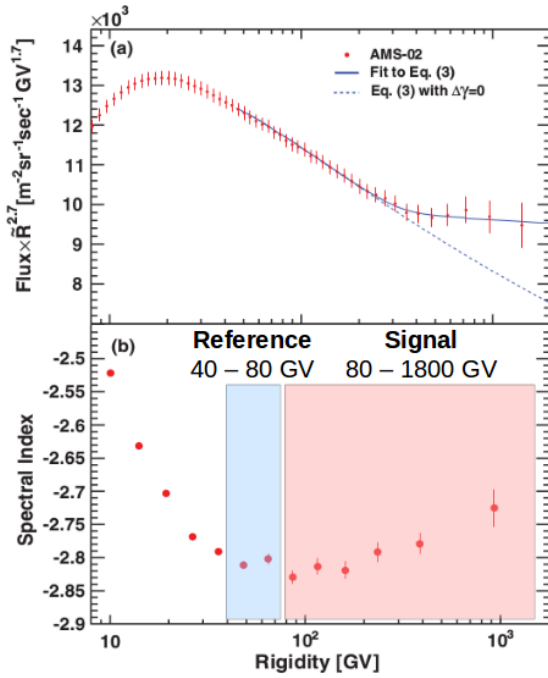
Figure 3.7: Proton flux and spectral index with rigidity as measured by AMS-02 [5]. A hardening in the spectral index is observed for rigidities above 100 GV with unknown origin. The rigidity range from 40 to 80 GV, marked in blue, is used as the reference sample for the search in anisotropy in the signal range above 80 GV. If the hardening is of a point source origin, starting to contribute at high rigidities, an anisotropy might be measured.

ground-based detector in 1990. Later on, the method has been applied in the search of large-scale anisotropies by the same experiment in [156] and by the Fermi-LAT collaboration in [157].

The expected isotropic flux of particles in celestial longitude l and latitude b is a combination of the particle rate $R(t)$, which is sensitive to time and position dependent effects introduced by the detector operation and the effective acceptance $A(\theta, \phi)$. In general, it can be calculated by

$$I_0(l, b) = \int_{t_0}^{t} R(T) \times A(\theta, \phi) dT$$

where usually the quantities are energy dependent as well. In order to preserve the rate and acceptance in the reference map, both of which are subject to large systematic uncertainties, a method based on randomizing reconstructed particle incoming directions of detected events was developed. The idea is that a list of selected events containing incoming directions (θ, ϕ) in the detector frame and the timestamp t, which corresponds to the detector's position, is created and shuffled in a way that every timestamp gets paired with a random incoming direction. From these fake events the new celestial incoming directions (l', b') are calculated. Hereby the acceptance $A(\theta, \phi)$ is covered by the list of incoming directions and the particle rate $R(t)$ is fully conserved in the list of timestamps on an event by event basis. The randomization efficiently removes the correlation from any point-source within the detector's field-of-view (FOV). The shuffling procedure can be repeated several times to produce as much statistics in the reference map as desired.

The Fly's Eye ground-based telescope has an extended FOV and the method has been developed for the search of point sources with an extent much smaller than the FOV. The AMS-02 FOV for electron and positron studies is limited by ECAL to about 25° from the instrument's zenith axis. For proton studies for which ECAL is not required, the FOV is roughly 35°. The Fermi-LAT has a much wider FOV of 60° from the instrument's zenith axis, covering about 20% of the sky at all times [157].

To study if the *shuffling technique* can be used for the search of large-scale dipole an-
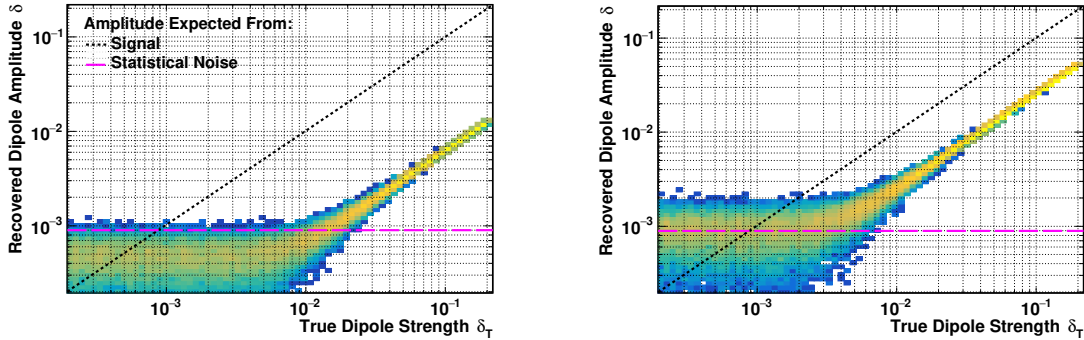
Figure 3.8.: Reconstructed dipole amplitude as function of a dipole created with varying amplitude for detectors with a flat circular acceptance with opening angle of 25°, corresponding to AMS-02 (**left**), and 60°, corresponding to FERMI-LAT (**right**). The experiments were created using a toy Monte-Carlo approach and maps were created using the *shuffling technique*.

isotropies with a limited FOV, experiments were simulated using a toy Monte-Carlo approach. The simulated experiments have a flat coverage of the sky-sphere with a constant circular acceptance within an opening angle of 25° and 60°, simulating AMS-02 and Fermi-LAT. For each, 10 million events are simulated. In a second step, dipole signals of varying amplitude are introduced. A reference map is then created using the *shuffling technique* and the dipole signal is recovered making use of the fit procedure described later-on in Section 3.2.6. The results are displayed in Figure 3.8. It is evident that even a dipole of high amplitude cannot be recovered by the fit, as it is still present in the shuffled map. The amplitude is systematically reduced by a factor of 10 for the 25° FOV and a factor of 5 for the 60° FOV. Also, the recovered dipole amplitudes in the regime of $\delta_T < 10^{-3}$, where statistical fluctuations are larger than the simulated signal, a dipole amplitude is recovered smaller than expected from the statistical fluctuations. The reasons are correlations in statistical fluctuations that are not washed out in the shuffling process for the finite binning of the maps. This has a tremendous impact on the physical result, as will be discussed later in Section 3.2.7.

In conclusion, the *shuffling technique* cannot be used for the study of large-scale anisotropies with AMS-02 and even Fermi-LAT. The problems in the application of the *shuffling technique* in the search of large scale anisotropies were first reported in [158]. In a follow-up publication on seven years of Fermi-LAT data [159], the authors address this issue, however the *shuffling technique* is still used in the analysis. The method is still useful for point-like signals, smaller than the instrument's FOV, and for simulations of signals in the celestial sky, as it has been done in Section 3.1.1.5.

3.2.4. Simulation of the isotropic sky

In the last section it was illustrated that the shuffling technique does not yield good reference maps for signal searches on scales smaller than the FOV. For this reason, in the framework of this thesis a new method to estimate the image of the isotropic sky as seen by a certain detector for a certain particle selection in a given measurement time was developed. The method was developed for and applied to the AMS-02 detector, but it can in principle be applied to any space or ground-based instrument. It has been presented for the first time in [160] and was later applied by FERMI-LAT in [159, 161].

A measurement of the particle flux $\Phi_i(\Delta E)$ for a species i is performed by measuring the number of events $N_i(\Delta E)$ in an energy bin ΔE per unit of effective acceptance $A_i^{eff}(\Delta E)$ (as a convolution of a geometrical factor quantifying the fiducial acceptance of the detector and the specific efficiencies of a given selection) and the total livetime $T_{exp}(\Delta E)$ of the detector in the measured period. The quantities are put together in the flux equation

$$\Phi_i(\Delta E) = \frac{N_i(\Delta E)}{A_i^{eff}(\Delta E)T_{exp}(\Delta E)\Delta E} \quad .$$

If the incoming particle fluxes were isotropic in nature, the measured fluxes $\Phi(\Delta E, p_1)$ and $\Phi(\Delta E, p_2)$ for any two sky pixels p_1 and p_2 would be identical. If, in addition, the detector and its sky coverage were perfectly isotropic, the terms $A_i^{eff}(\Delta E, p_1)T_{exp}(\Delta E, p_1)$ and $A_i^{eff}(\Delta E, p_2)T_{exp}(\Delta E, p_2)$ were identical, as well as the selected event numbers $N_i(\Delta E, p_1)$ and $N_i(\Delta E, p_2)$. For a real, not perfectly isotropic, detector with non-uniform sky coverage $A_i^{eff}(\Delta E, p_1)T_{exp}(\Delta E, p_1) \neq A_i^{eff}(\Delta E, p_2)T_{exp}(\Delta E, p_2)$ and hence the selected event numbers $N_i(\Delta E, p_1) \neq N_i(\Delta E, p_2)$.

Therefore, an estimate of the quantity $A_i^{eff}(\Delta E, p_1)T_{exp}(\Delta E, p_1)$, for a given selection and data taking period and all sky pixels, can serve as a reference map for anisotropy searches. If the incoming particle fluxes in nature were perfectly isotropic[3], the ratio map

$$R(p) = \frac{N_i(\Delta E, p)}{A_i^{eff}(\Delta E, p)T_{exp}(\Delta E, p)} \quad .$$

would be compatible with isotropy. Any deviation from isotropy in the arrival directions of cosmic rays in nature would show up as a mismatch in the map's $N_i(\Delta E, p)$ and $A_i^{eff}(\Delta E, p)T_{exp}(\Delta E, p)$ and could be detected as a signal, provided that the statistics in N_i is high enough.

In the following the quantity $A_i^{eff}(\Delta E, p)T_{exp}(\Delta E, p)$ will be called an *IsoSkyMap*. It is our current best estimate of what an isotropic sky would look like to the detector for a given particle selection in a given data taking time. The algorithm to create *IsoSkyMap* for AMS-02 is the following:

- A list of particle incoming directions (θ, ϕ) in the detector frame is created from selected particles in the energy range ΔE.

- For every second k of measuring time t, a constant number N of incoming directions is drawn randomly from this list.

- From the detector's position at the time t_k and the random incoming directions (θ, ϕ), the incoming directions in the celestial sky (l', b') are calculated for the N simulated events.

- To account for a busy trigger from the higher particle rate towards the polar regions, the simulated events are weighted by the detector's livetime at $T_{LF}(t_k)$.

- To correct for inefficiencies in the particle detection caused by increased noise from low energetic particles, the simulated events are additionally weighted with a position and time-dependent correction factor (the origin of this factor will be discussed in Section 4.3). The *IsoSkyMap* is filled with these weighted events.

---

[3]*perfectly isotropic* means that the level of isotropy is compatible with statistical fluctuations.

The number of incoming directions drawn per second needs to be bigger than the number of particles actually measured per second $N/s \gg R(t)$. In comparison to the *shuffling technique* discussed in Section 3.2.3, the algorithm does not conserve the number of events, but the particle rate. The approach excludes correlation between the data sample and the reference map, as it has been demonstrated to be the case in the *shuffling technique*. It is clear that for each pixel the systematic uncertainty in the estimate of the *IsoSkyMap* need to be smaller than the statistical fluctuations in $N_i(\Delta E, p)$.

3.2.5. Significance

In order to compare the measured data to the reference, any deviation has to be stated in a statistically reliable way. For this, the significance S as proposed by Li & Ma in [162], derived using a maximum Likelihood ratio test, is used. The method has been developed for the explicit observation of source regions with a Gamma-ray telescope. A source is stated as excess in the comparison to an off-source region that defines the background. In such experiments, the observation time in the on- and off-source regions is highly asymmetric which causes an inaccuracy in the construction of residuals, as used in a Chi-square test. In the case of a CR particle experiment, the observation time is the same for the signal and reference map of choice. However, the particle counts can be highly asymmetric due to the different flux of reference and signal particle, or the large number of reference particles simulated, such that the problem of asymmetric statistical uncertainties in the signal and reference map is the same. The significance following the Li & Ma approach has been used before by FERMI-LAT and Pamela. The significance is computed via

$$S = \sqrt{2} \left\{ N_{Sig} \ln \left[\frac{1 + \alpha}{\alpha} \left(\frac{N_{Sig}}{N_{Sig} + N_{Ref}} \right) \right] + N_{Ref} \ln \left[(1 + \alpha) \left(\frac{N_{Ref}}{N_{Sig} + N_{Ref}} \right) \right] \right\}^{-1/2}$$

where N_{Sig} is the number of data counts in a pixel and N_{Ref} the expected number of counts from the reference map. In the case of on-off searches, the factor α weights the unequal observation time. In the application to the CR particle experiment, α is the ratio of total data counts to expected counts from the reference. A sign is applied to the quantity such that

$$\text{Sgn}(S) = \begin{cases} +1, & N_{Sig} > N_{Bkg} \\ -1, & N_{Sig} < N_{Bkg} \end{cases} .$$

For the isotropic case the significance follows a Gaussian distribution centered around zero with unit variance in case the isotropic hypothesis is true. Figure 3.9 shows the significance map and the distribution among the pixels for the case of two flat maps with a signal to background ratio of 10, as it is expected from the positron fraction in Figure 1.6 for positrons with electrons as reference. The significance map is flat and no structure apart from statistical fluctuations is to be seen, as expected. The significance distribution in the pixels follows a normal distribution as indicated by the fit.

The advantage of the presented significance definition, with respect to a standard residual definition, is that it is more robust against cases where pixel counts are low or when $\alpha \neq 1$, as it is expected for most of the anisotropy measurements. In analogy to the naming convention of normalized ratios from Equation 3.1, the significance between a signal and a reference map is marked with $S_{\text{Sig/Ref}}$ in the following.
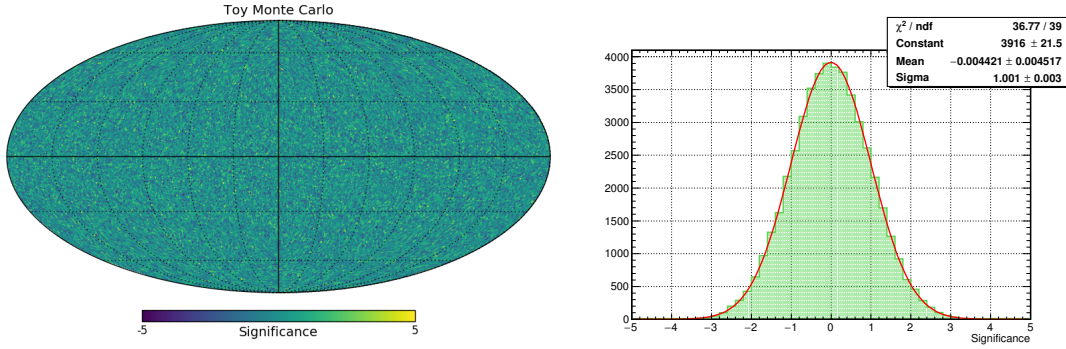
Figure 3.9.: Significance map and distribution for two flat maps. Entries for the 49152 map pixels have been drawn from a Poisson distribution with a constant mean for the signal map and 10 times the mean for the reference. The significance map is flat and no structure apart from statistical fluctuations is to be seen, as expected. The significance distribution in the pixels follows a normal distribution as indicated by the fit.

3.2.6. Multipole analysis

The angular distribution of particle incoming directions is expanded to a dipole. An astrophysical point source, in the simplest approximation, is expected to give the strongest contribution in this quantity. More complex model approximations, as for example taking the Heliosphere into account, give contributions in higher multipole components, as well. From the analysis point of view, a dipole model is good to handle and the most generalized result to state. In the case of incomplete coverage of the celestial sky an expansion to higher multipoles gives unstable results and systematic effects cannot be controlled.

The test variable is the normalized ratio $R^i_{\text{Sig/Ref}}$ of data to reference counts in a pixel i, calculated using

$$R^i_{\text{Sig/Ref}} = \frac{N^i_{Sig}}{\sum_j^{N_{\text{Pixels}}} N^j_{Sig}} \frac{\sum_j^{N_{\text{Pixels}}} N^j_{Ref}}{N^i_{Ref}} \quad , \tag{3.1}$$

with the same nomenclature as introduced in Section 3.2.5. For identical maps this ratio will be 1 for all of the pixels and in case of isotropy it will fluctuate around $\langle R \rangle \approx 1$. In case of a dipole signal the distribution will be directly proportional to the signal. To extract this information, a fit with spherical harmonics templates using a likelihood minimization is performed.

As spherical harmonics are designed to be a complete set of orthogonal functions defined on the unit sphere, they build a basis to describe spherical distributions. In spherical coordinates they are defined in longitude $\phi \epsilon [0, 2\pi]$ and latitude $\theta \epsilon [0, \pi]$ as

$$Y_l^m(\phi, \theta) = \sqrt{\frac{2l + 1}{4\pi} \frac{(l - m)!}{(l + m)!}} P_l^m(\cos \theta) e^{im\phi} \tag{3.2}$$

in degree $l = 0, 1, 2, ...$, which roughly corresponds to the angular scale of $\frac{180°}{l}$, and order $m = 0, \pm 1, \pm 2, ..., \pm l$. The set of functions $Y_l^m(\phi, \theta)$ are eigenfunctions of the angular part of the Laplace operator. $P_l^m(\cos \theta)$ denote the associated Legendre polynomials as canonical solutions of the general Legendre equation. As the spherical harmonics functions
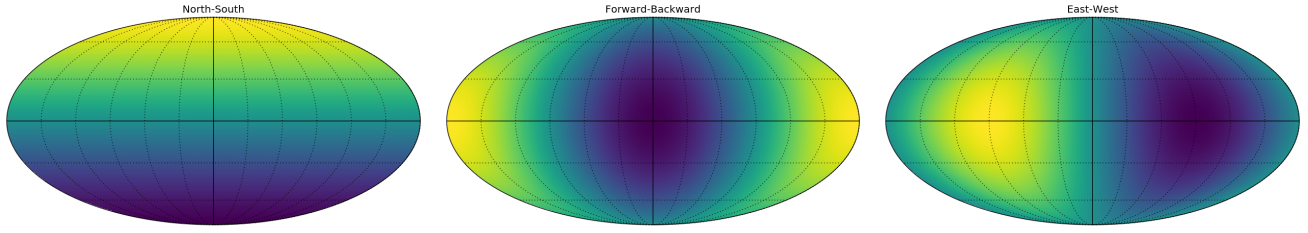
Figure 3.10.: Representation of the real spherical harmonics $p_{x,y,z}(\phi,\theta)$ in Mollweide projection. From left to right p_z, in the following referred to as north-south (NS) direction, p_x, in the following referred to as forward-backward (FB) direction, and p_y, in the following referred to as east-west (EW) direction are shown.

$Y_l^m(\phi,\theta)$ form a Hilbert space, any function on a unit sphere $f(\phi,\theta)$ can be expanded as linear combination

$$f(\phi,\theta) = \sum_{l=0}^{\infty} \sum_{m=-l}^{l} a_l^m Y_l^m(\phi,\theta) \tag{3.3}$$

of them with the expansion coefficients a_l^m. A dipole is described in the first degree $l = 1$, the $l = 0$ term gives an constant offset, the isotropic component, and thus can be disregarded for an expansion in the normalized ratio, where the normalization is fixed to 1 by construction. The three remaining spherical harmonics used in the expansion are

$$Y_1^{-1}(\phi,\theta) = \sqrt{\frac{3}{8\pi}} \sin(\theta) e^{-i\phi} \quad ,$$
$$Y_1^0(\phi,\theta) = \sqrt{\frac{3}{4\pi}} \cos(\theta) \quad , \tag{3.4}$$
$$Y_1^{+1}(\phi,\theta) = -\sqrt{\frac{3}{8\pi}} \sin(\theta) e^{i\phi} \quad .$$

These are complex functions, which is nether desirable nor needed for a physical measurement of a simple particle ratio. The basis of the coordinate system can be rotated in a way, such that

$$a_l^{-m} = (-1)^m a_l^{m^*}$$

and the complex spherical harmonics can be rotated in a way that the expansion coefficients become real. The real spherical harmonics are found to be

$$p_x(\phi,\theta) = \sqrt{\frac{1}{2}} \left(Y_1^{-1}(\phi,\theta) - Y_1^{+1}(\phi,\theta) \right) \quad ,$$
$$p_y(\phi,\theta) = i\sqrt{\frac{1}{2}} \left(Y_1^{-1}(\phi,\theta) + Y_1^{+1}(\phi,\theta) \right) \quad , \tag{3.5}$$
$$p_z(\phi,\theta) = Y_1^0(\phi,\theta) \quad .$$

The three real spherical harmonics for $l = 1$ are shown in Figure 3.10 in Mollweide projection. Following the notation from GTOD the real spherical harmonics can be translated into direction of north-south (NS) for p_z, forward-backward (FB) for p_x and east-west (EW) for p_y.

In the following steps, the coefficients a_l^m in Equation 3.3 are rewritten in the new basis using Equations 3.5 and re-normalized to match a dipole description. The transformation translates to

$$\begin{pmatrix} d_1 \\ d_2 \\ d_3 \end{pmatrix} = \begin{pmatrix} \sqrt{\frac{1}{2}}(a_1^{-1} - a_1^{+1}) \\ \sqrt{\frac{1}{2}}(a_1^{-1} + a_1^{+1}) \\ a_1^0 \end{pmatrix} \quad , \tag{3.6}$$

with a normalization to dipole components of

$$\rho_{NS} = \sqrt{\frac{3}{4\pi}} d_3 \quad \rho_{FB} = \sqrt{\frac{6}{4\pi}} d_1 \quad \rho_{EW} = \sqrt{\frac{6}{4\pi}} d_2 \quad . \tag{3.7}$$

The dipole amplitude in this basis is given by

$$\delta = \sqrt{\rho_{NS}^2 + \rho_{FB}^2 + \rho_{EW}^2} \quad , \tag{3.8}$$

with unit normalization as constructed from Equation 3.1. The dipole amplitude δ is a real value which is positively defined and smaller 1 with the given normalization of R_i

$$0 \leq \delta \leq 1 \quad .$$

With the quantities in Equations 3.7 and 3.8 and multipole templates from Figure 3.10 the normalized ratio R_i of signal to reference map can be expanded to a dipole using a likelihood template fit procedure, which will be discussed in the next Section 3.2.6.1. In principle, the whole procedure can be expanded to higher orders $l > 1$ for the search of multipoles. The expansion up to $l = 2$ has been used to check the stability of the first order $l = 1$ result, without any impact found.

3.2.6.1. Likelihood fit

In order to fit the multipole templates, derived in previous Section 3.2.6, to the ratio R_i a likelihood fit procedure is used.
The ratio R_i is evaluated in bins of equal area on the celestial sphere. For this purpose, the HEALPix[4] framework, developed and provided by NASA for studies of the CMB, is used. As the name suggests the software package provides an equal area pixelation on a sphere in rings of latitude in a hierarchical structure such that four pixels can be grouped together to rebin in a lower order. Additionally, tools for spherical harmonics transformations are provided; the multipole templates, shown in Figure 3.10, are created using HEALPix tools. In this work, all celestial sky maps are created in the HEALPix binning and plotted in Mollweide projection. The structure of the HEALPix binning on a sphere is illustrated in Figure 3.11.

The task of the fit procedure is to find the combination of the real expansion coefficients

$$R_i^{Exp} = 1 + d_1 p_x + d_2 p_y + d_3 p_z \quad , \tag{3.9}$$

where R_i^{Exp} is the modeled ratio in a pixel i, which best describes the data. The same quantity on the data is given in Equation 3.1. In the analysis, the fit procedure has to be

---

[4]HEALPix is an acronym for Hierarchical Equal Area isoLatitude Pixelation of a sphere.
    HEALpix website: http://healpix.sourceforge.net
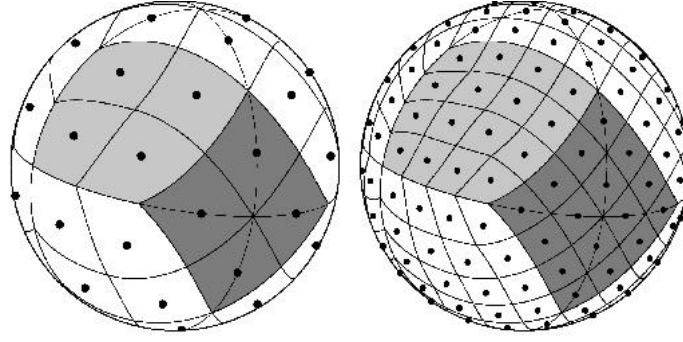
Figure 3.11.: Illustration of the HEALPix binning on the surface of a sphere divided in 48 (**left**) and 192 (**right**) pixels [163].

stable even for cases with low pixel counts especially for the signal component, due to the low positron flux in particular and unequal exposure in general. As a consequence, the fluctuations in the ratio R_i are large and the uncertainty on the ratio σ_{R_i}, which only depends on the available number of events in the given pixel, is poorly estimated. A Chi-square fit, which minimizes the sum of quadratic differences over all pixels

$$\chi^2 = \sum_{i=1}^{N_{Pixels}} \frac{\left(R_i - R_i^{Exp}\right)^2}{\sigma_{R_i}^2} \quad , \tag{3.10}$$

is not robust against the large fluctuations of R_i. An advantage would be that it is model independent. In a master thesis associated with this work [164], a modification to the Chi-square method is applied in a way, that the intermediate model estimation of the variance

$$\sigma_{R_i}^2 = R_i^{Exp\,2} \left(\frac{1}{N_{Sig}^{i,Exp}} + \frac{1}{N_{Ref}^i} \right) \tag{3.11}$$

is estimated in an iterative process. The number of expected signal particles in a pixel $N_{Sig}^{i,Exp}$ is taken from the best model estimation from the previous fit step

$$N_{Sig}^{i,Exp} = R_i^{Exp} N_{Ref}^i \frac{N_{Sig}}{N_{Ref}} \quad . \tag{3.12}$$

Equation 3.11 is derived from a simple Gaussian error propagation under the assumption that the pixel counts in the signal and reference map are not correlated. To be precise, this assumption is not exactly true as both quantities are measured by the same detector in the same environment. But if the detector measures incoming particles with high efficiency, the pixel counts are close to nature where CRs are arriving the detector independently to our best knowledge.

If a model for the probability distribution of events in a pixel is already involved for the prediction of the variance, a likelihood fit can be even more robust for its independence of the quadratic difference which is highly fluctuating for low statistics. In a likelihood fit procedure, the product of likelihood probabilities

$$\mathcal{L}(d_1, d_2, d_3) = -\log \left(\prod_{i=1}^{N_{Pixels}} f(R_i | R_i^{Exp}) \right) \tag{3.13}$$
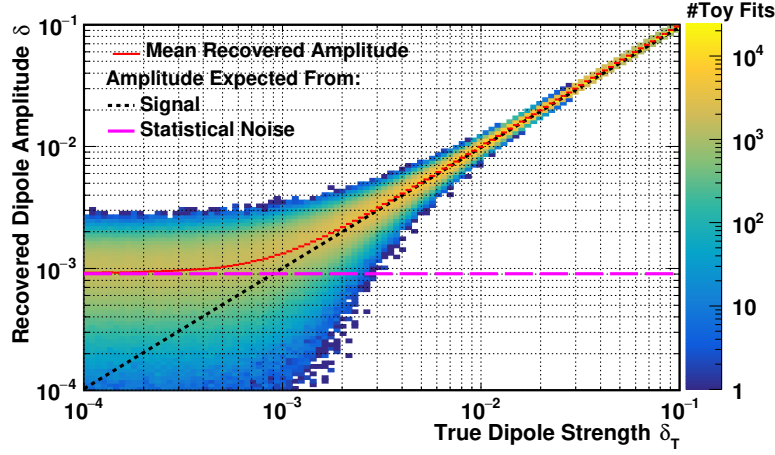
Figure 3.12.: Recovery of a dipole as a function of an induced dipole with varying strength. The maps were created by drawing events following a Poisson distribution. The red line is the mean recovered dipole amplitude, while the black dashed line gives the expectation for a perfectly recovered dipole signal. The magenta dashed line marks the expectation from statistical fluctuations, as it will be studied in Section 3.2.7. A dipole signal can be recovered down to the level of 10^{-3} with the proposed fit procedure, for a simulated sample size of 10 million events. At low signal amplitude the statistical fluctuations in the event map dominates the signal and a natural limitation is reached.

is minimized, where $f(R_i|R_i^{Exp})$ is the probability density function (PDF) to measure the ratio R_i under the assumption of the expected ratio from the model. A priori, this function is not known and has to be modeled. Using the assumption of uncorrelated pixels the ratio R_i is a ratio of a Poisson distribution for the low signal counts N_{Sig} and a Gaussian distribution for the high reference counts N_{Ref} in a pixel, which is the Gamma-distribution with the PDF

$$f(x, k, \theta) = \frac{\theta^k}{\Gamma(k)} x^{k-1} e^{-\theta x} \quad \text{for } x > 0. \tag{3.14}$$

$\Gamma(k)$ denotes the Gamma-function and the parameters are defined as

$$k = \frac{R_i^{Exp\,2}}{\sigma_{R_i}^2} \qquad \theta = \frac{\sigma_{R_i}^2}{R_i^{Exp}} \qquad .$$

Using Equation 3.14 as the PDF in the likelihood minimization, a robust estimation of the expansion coefficients, and consequently the dipole components is achieved.

In cases of sufficient number of events the likelihood fit procedure has been compared to a model independent Chi-square fit with good agreement, but during the analysis process cases where the available number of events in a map was low that even the likelihood fit did not converge in a stable minimum were observed. To understand the general properties of the fit procedure, maps with a dipole have been simulated and fitted to a flat simulated reference. The maps were created by drawing entries from a Poisson-distribution to create maps filled with 10 million events and 10 times this number for the reference map. A ratio of N_{Sig} to N_{Ref} of 10 corresponds to most applied scenarios in this thesis, in good approximation. The number of events can be compared to the
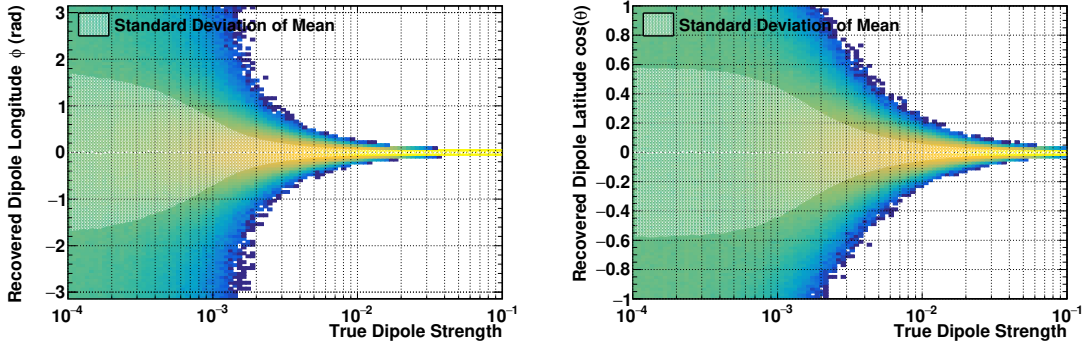
Figure 3.13.: Recovery of the direction in latitude (**left**) and longitude (**right**) of a dipole with varying strength in forward-backward direction ($\cos(\theta) = 0$, $\phi = 0$). The white shaded area marks the standard deviation around the mean. In case of a purely random direction, a standard deviation of $\sigma_{\cos(\theta)} \approx 0.58$ for the longitude and $\sigma_\phi \approx 1.81$ for the longitude is expected from the quantiles of a flat distribution. Both values stay below this limit, even for dipoles weaker than $\delta_t = 10^{-3}$.

proton counts at a middle range analysis rigidity of 80 GV. In most applications, e.g. for electrons and positrons, the number available events is lower. The impact of the available events on the analysis will be discussed in Section 3.2.7. Dipoles have been created in Forward-Backward direction, on a flat map the direction is invariant under rotations, and amplitudes ranging from 10^{-4} to 10^{-1}. The reconstructed dipole amplitude, calculated from Equation 3.8, is shown in Figure 3.12 as function of the created dipole amplitude.

It can be seen that the fit is able to recover the dipole amplitude up to a strength of order 10^{-3} where the mean recovered dipole strength, plotted in red, starts to deviate from the expectation and converges toward the expectation from the statistical noise. It has been investigated that this also holds for the non-uniform coverage of the sky maps measured by AMS-02. Figure 3.13 shows that not only the amplitude, but also the correct direction is recovered up to this limit. In the region where the mean recovered dipole amplitude flattens, the statistical fluctuations in the map overcome the dipole signal and dominate the fit. This depends only on the available events in the map with lower statistics, which is why $N_{Ref} \gg N_{Sig}$ is needed. If this condition is not fulfilled, the statistical properties of the reference map will dominate the fit result and lead to misinterpretation.

It is evident that even if the dipole amplitude can no longer be reconstructed, the probability for the fit to converge in the correct direction is still higher than the purely random expectation. This characteristic has been noted since the beginning of the usage of the multipole expansion technique in the 1970s and is used in the analysis of many ground-based experiments [105]. A more detailed study can be found in [165].

From Figure 3.12 it can be concluded that a limit on the recovery of a dipole is of statistical origin, in the following called sensitivity. The recovered dipole amplitude will not be zero in case of absence of anisotropy but will give a result $\delta > 0$, based on statistical fluctuations. As fit parameters, the expansion coefficients which enter the calculation of the limit in Equation 3.8 are Gaussian distributed around their true value. In case of isotropy the coefficients distribution is centered around zero with a width dependent on the available number of signal events, without any correlation. In this case the reconstructed dipole amplitude is a squared sum of three Gaussian distributed fit values all scaling with $\sqrt{N}$ and therefore scaling with $\sqrt{N}$ by itself. The dipole amplitude δ can-
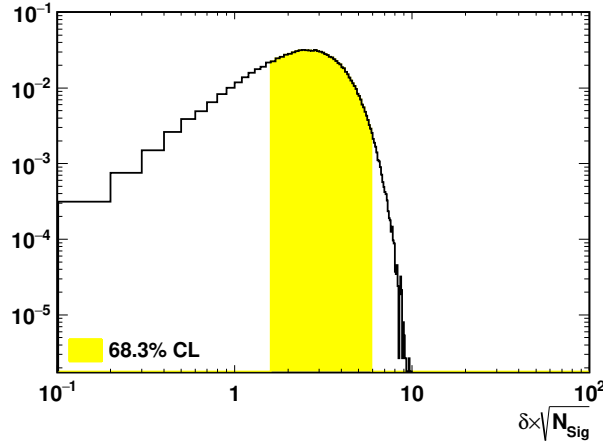
Figure 3.14.: Distribution of the recovered dipole amplitude δ in case of isotropy, scaled with the number of signal events $\sqrt{N_{Sig}}$. The yellow band marks the two-sided 68.3% confidence interval around the mean. The distribution has been created using 2,500,000 toy Monte-Carlo maps and gives the expectation on the result under the isotropic hypothesis.

not reach values smaller than zero and a number larger than zero is stated also for the isotropic case.

Possible sources of anisotropy are only expected to give a weak dipole, such that the understanding of the null hypothesis of isotropy is of major importance in the interpretation of results. In this case an upper limit on the dipole amplitude, to exclude models with an anisotropy stronger than the quoted limit, is of physical interest.

3.2.7. Limit on the dipole amplitude

To get an estimate of the δ distribution in the isotropic case, a toy Monte-Carlo study is performed. Similar to the approach used to study the dipole recovery in Figure 3.12, two maps are created and fitted with the dipole model. Here both maps are flat but the condition $N_{Ref} \gg N_{Sig}$ still holds. The distribution of recovered dipole amplitudes of the isotropic case is shown in Figure 3.14. The dipole amplitude has been scaled with $\sqrt{N_{Sig}}$ to make it independent of the sample size. The distribution is asymmetric, always greater than zero and peaks at a value δ_{Max}. The yellow band marks the two-sided 68.3% confidence interval around the mean and will be referred to as isotropic expectation in the following. This region gives the expectation of the dipole amplitude scaled with the available number of signal events. To get a handle on the interpretation of the reconstructed dipole amplitude, this isotropic expectation will be shown together with the fit results.

In most cases no signal above the statistical noise is expected and an upper limit on the dipole amplitude is stated as physical result. Quoting an upper limit simply on quantiles of the discussed isotropic distribution would be misleading. A correct way to set the limit has to take the fit result and possible correlations into account, even if they are only of statistical nature.

Assuming nature yields a true, but unknown, dipole amplitude δ_T. Then an experiment will measure a value δ around δ_T within the experiments sensitivity. If the measurement
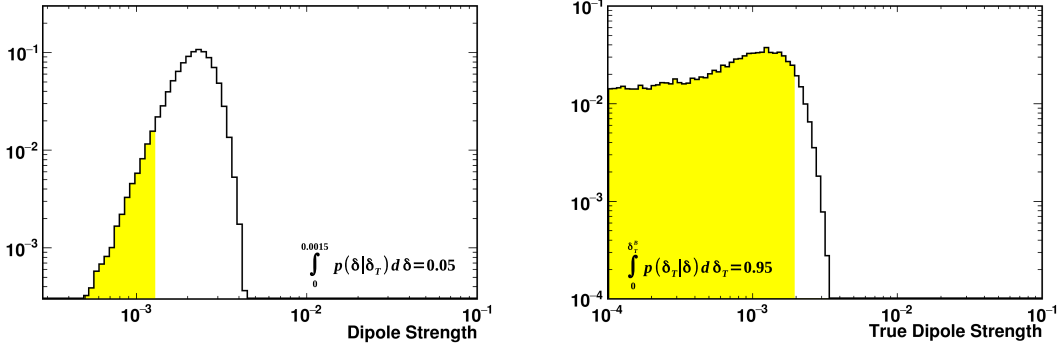
Figure 3.15.: Neyman and Bayesian construction of the upper limit on the dipole strength at an assumed recovered dipole amplitude $\delta = 0.0015$. **Left:** Probability distribution of the dipole strength distribution where the probability of measuring $\delta < 0.0015$ is 5%, known as Neyman construction. The distribution is equivalent to a projection onto the y-axis at an x-value of around 0.002 in Figure 3.15, which is the Neyman limit on the true dipole amplitude $\delta_T^N \approx 0.002$. **Right:** Probability distribution of the dipole strength under the assumption of a measurement of an unknown true quantity with finite sensitivity, known as Bayesian construction with flat prior. The Bayesian limit on the true dipole amplitude $\delta_T^{B,95}$ corresponds to the 95% quantile of the distribution called credible interval.

could be repeated N times, a distribution of δ would be measured, identical to the projection onto the y-axis in a small slice around δ_T on the x-axis in Figure 3.12. Since only a single measurement of δ is performed, the upper limit δ_T^N at a confidence level of 95% is defined by searching the δ_T on the x-axis where the distribution of δ on the y-axis, gives a probability of measuring a dipole amplitude smaller than δ of 5%. The condition

$$\int_0^\delta p(\delta|\delta_T^N)d\delta = 0.05$$

is fulfilled. The construction is shown on the left-hand side of Figure 3.15 and is called Neyman construction. In this approach, δ_T^N is determined by the single measurement δ and the choice of a quantile in the distribution of hypothetical measured δs.

An alternative approach is to exploit the fact that, given a single measurement δ, the distribution of δ_T can be derived from Figure 3.12. The distribution can be constructed by a projection onto the x-axis, in small slices around δ on the y-axis. This is known as the Bayesian approach and requires an assumption on the distribution of the true dipole amplitude p(δ_T^B), which is called prior and is chosen to flat to allow for all values[5]. From the distribution of δ_T the limit is quoted from the 95% quantile, as shown on the right-hand side of Figure 3.15.

Both methods of constructing an upper limit on the dipole amplitude are equally well justified, however the choice of a prior p(δ_T^B) in the Bayes construction is not well justified and introduces a degree of freedom that is somehow subjective. The Neyman construction fails for exceptionally small signals. For this special case, a modification to

---

[5]In the case of the presented analysis, the dipole amplitude has already been restricted to $\delta > 0$, so the flat function is actually a step function at 0.
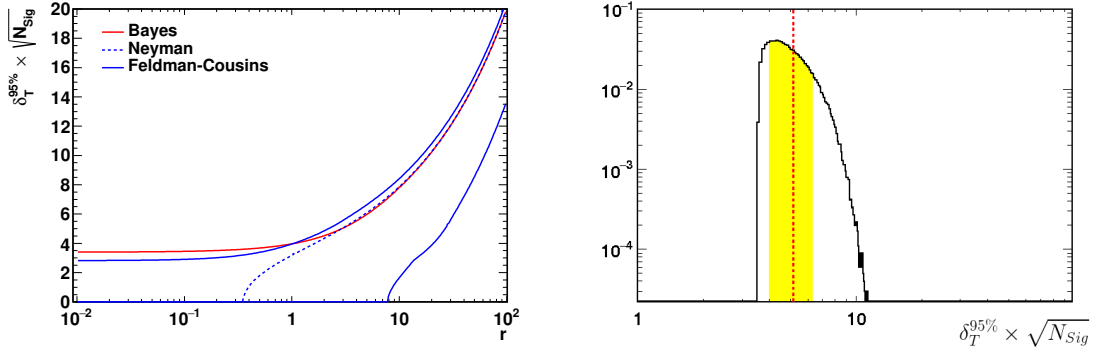
Figure 3.16.: **Left:** Comparison of methods to construct an upper limit in case of a null-result [166]. The value r corresponds to a parameter describing the fit quality $r = \frac{\delta^2}{\sigma^2}$, where σ is the fit uncertainty on the expansion coefficients. The Neyman construction (blue dashed line) fails in the construction of small signals r<1. The Feldman-Cousins construction (blue solid line) was introduced to fix this issue. In the case of large signals r>8 the null-result is rejected and a two-sided confidence level is set. The Bayesian construction (red solid line) is used in this thesis. **Right:** Distribution of the Bayesian limit $\delta_T^{B,95}$ at 95% credible interval, scaled with the included number of signal events $\sqrt{N_{Sig}}$. The yellow band marks the two-sided 68.3% confidence interval. The red dashed line marks the mean.

the Neyman construction was proposed by Feldman and Cousins in [167], which introduces an ordering principle based on likelihood ratios to set limits also on small signals. For fits dominated by high fluctuations, a two-sided confidence interval is set. Figure 3.16 shows a comparison between the three different methods of limit calculation. The value r corresponds to a parameter describing the fit quality r= $\frac{\delta^2}{\sigma^2}$, where σ is the fit uncertainty on the expansion coefficients. With the generalized function shown in Figure 3.16, the limit can be read independently from the fit result and the given number of signal events, as both can be scaled. All discussed procedures to derive a limit on a null-result are comparable in the region of $1 < r < 10$, which is the most probable result in case of isotropy. For (unphysical) small signals, the Neyman construction fails. For large signals, the Feldman-Cousins constructions rejects the null-result and sets a two-sided confidence level. In the analysis of AMS-02 data, a large fraction the fits are dominated by systematic limitations where the Feldman-Cousins construction will not reflect the intended interpretation of the data. Therefore, all quoted limits in this thesis are Bayesian at a credible interval of 95%, following an internal agreement within the AMS-02 collaboration. To account for the fact that the construction of the limit is not explicit, but has an outstanding relevance in the interpretation of the data, the appendix provides all necessary information from the fits presented in Chapter 4, such that the reader can construct an upper limit following any preferred method.

As the dipole amplitude, the limit distribution scales with sample size by $\sqrt{N_{Sig}}$. The scaled distribution of the Bayesian limit $\delta_T^{B,95}$ is shown on the right-hand side of Figure 3.16. In this way, an expectation on the physical result can be stated before the dipole fit is performed. A discussion on limits to be expected from an experiment with given statistics, can be found in [168].
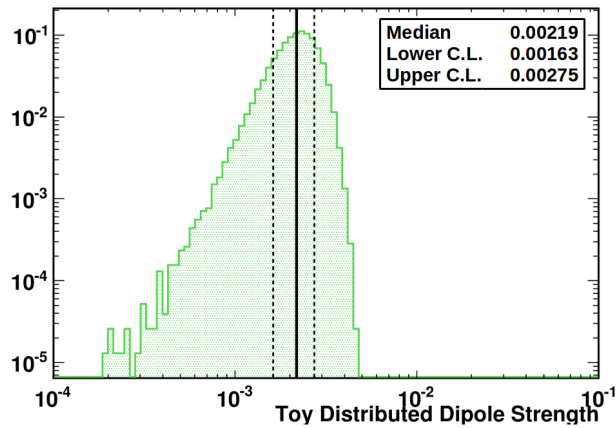
Figure 3.17.: Toy simulated distribution of a measured dipole amplitude $\delta = 0.0022$ with uncertainties on the dipole components $\sigma_{Rho} \approx 0.0015$. The distribution has been created using a multivariate correlated Gaussian distribution with widths of the fit uncertainties, a mean of the dipole components fit value and the correlation matrix evaluated in the fit. A two-sided 68.3% confidence level around the median is quoted as uncertainty on the measured dipole amplitude δ.

3.2.7.1. Uncertainty on a measured dipole amplitude

In case of a recovered dipole amplitude exceeding the isotropic expectation, the uncertainty on the dipole amplitude is of interest. In this case the three expansion coefficients might be correlated. The distribution of the measured dipole amplitude is generated by toy Monte-Carlo simulation using a multivariate correlated Gaussian distribution with widths of the fit uncertainties, a mean of the dipole components fit value and the correlation matrix evaluated in the fit. A two-sided 68.3% confidence level around the median is quoted as uncertainty as the distribution might be asymmetric, and uncertainties allowing for a negative dipole amplitude are unphysical. In Figure 3.17 an example from a fit with $\delta = 0.0022$ and $\sigma_{Rho} \approx 0.0015$ is shown.

3.3. Data sample

For the proposed analysis of positrons, electrons and protons different sets of data are selected from the first five years of AMS-02 data-taking, from May 2011 until May 2016. For the analysis of electron and positron events a selection, using ECAL and TRD to reject the overwhelming background of protons, is needed.

In the published AMS-02 particle flux analyses, as in [1–4, 15], where only the raw particle counts are of interest, a template fit in the ECAL and TRD estimators, which are discussed within this Section, is performed. However, in the analysis of anisotropies, an identification of single events is desired to efficiently use transformations between the various coordinate systems to trace down a possible source and keep systematic uncertainties to a low level. Therefore, a cut-based analysis is introduced. Template fits are still handy to estimate the purity of the selected sample over the background and its selection efficiency.

The sensitivity of the fit method, described in Section 3.2.6.1, directly scales with the size of the data sample for which a high selection efficiency in maximum acceptance
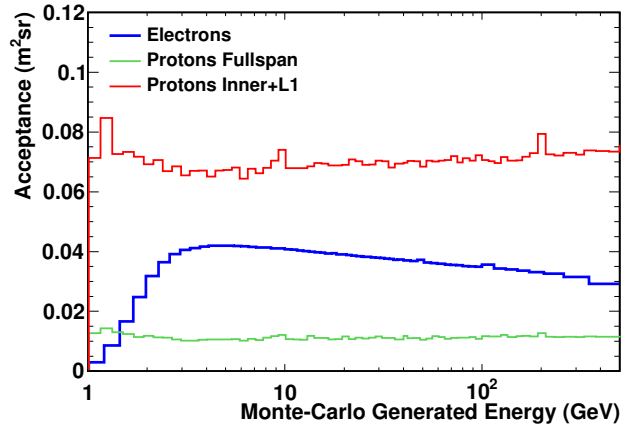
Figure 3.18.: Acceptance in m^{2}sr, evaluated from Monte-Carlo generated events, for different selections and particles. Electrons (blue) require the small ECAL to reject protons. Protons, which rely on an accurate rigidity measurement by the tracker, can be selected requiring hits in all Tracker layers (green) or by disregarding layer nine on top of ECAL (red). This comes with an increased acceptance by a factor of 4 but with worse rigidity resolution, as comprehensible from Figure 2.10.

is desired, while keeping the sample purity high. A limiting factor for the number of collected events is the relatively small acceptance of the ECAL, which is needed to reject protons over positrons and to get an accurate energy measurement. For protons on the other hand ECAL is not needed, as they are practically background-free and the momentum is measured as rigidity by the silicon tracker. As a consequence, the selection is focused on a clean reconstruction of the trajectory, which leads to a limited acceptance introduced by the external tracker layers. Figure 3.18 shows this relation, using the acceptance evaluated from Monte-Carlo generated events.

The above considerations lead to rather different sample selections of protons and leptons. A common part in the sample selection process of the two classes is the definition of the data taking time of the detector, in the following referred to as *good second*. This definition is of particular interest for the simulation of reference maps, as it directly represents the operational and environmental effect described in Section 3.1.2. The lepton selection, proton selection and definition of a *good second* will be discussed separately.

3.3.1. Electron and positron selection

The selection process of electrons and positrons can be separated into two parts: In a first step, a set of clean relativistic downward-going particles with unit charge is selected within ECAL acceptance following [169] using information from TOF, Tracker, and TRD. This dataset contains a dominant proton background among the electrons and positrons. These protons, in the following referred to as *background protons*, share the same geometric features as the electrons and positrons and therefore can be used as reference particles, as discussed in Section 3.2.1. In a second step, the identification of the particles involving TRD, ECAL and the Silicon Tracker is done. The trigger conditions for electrons and positrons will be discussed in a dedicated Section 3.3.3.

Only events with a good fit of the particle's trajectory, using only the inner Tracker layers two to eight, are considered. This trajectory is used as a starting point, from

where the sub-detector's reconstructed physical objects are connected to the particle. A good fit requires at least three hits on the six inner layers with a fit of the trajectory with normalized chi-square of less than 10, separately in the bending and non-bending projection. If more than one of these trajectories have been reconstructed in an event, it is not taken into account to avoid secondary particles from interactions, or a second primary cosmic ray.

A charge selection is done, making use of the two upper and lower TOF planes and the available hits in the inner Tracker. A two-sided cut is applied for the charge estimator by the Tracker to be $0.7 < Q_{\text{Trk}}^{\text{inner}} < 1.5$, as the charge resolution is high for charge one particles. For the upper TOF, a charge cut of $Q_{\text{TOF}}^{\text{upper}} < 1.8$ is applied to reject nuclei which can produce delta electrons that might be confused with primary electrons. For the lower TOF, a charge cut of $Q_{\text{TOF}}^{\text{lower}} < 2.0$ is applied to reject events with backsplash from ECAL.

The particle's relative velocity $\beta = v/c$ and its direction of crossing is determined by the TOF timing information. To ensure a good TOF reconstruction, a hit is required in all of the four TOF planes. Relativistic downward-going trajectories are selected in $1/\beta$ where the distribution is approximately Gaussian at $0.8 < 1/\beta < 1.2$.

The particle's reconstructed trajectory is required to pass ECAL in a fiducial volume, which is defined to be within of one cell from the border. The trajectory should also match the reconstructed shower's barycenter of the energy deposit, by 3.6 cm, or 2 PMT distance, at maximum in x-projection and 7.2 cm in the bending projection. As the shower shape in ECAL is used to distinguish between hadronic and leptonic showers, it is important that the correct shower reconstruction is matched to the particle and any leakage in the shower development is small.

The other sub-detector, specialized for rejecting proton background, is the TRD on top of the detector. In order to get a reliable estimate, at least 9 hits with a threshold of 15 ADC counts are required to be picked up along the extrapolated trajectory from the Tracker. Following the Bethe formula the energy deposit due to ionization $dE/dx \propto Z^2$ is proportional to the charge squared, resulting in a higher ionization deposit for nuclei in the TRD confusing them with transition radiation x-rays. To normalize the energy deposit by the path length through the gas tube dX^{Tube}, the Tracker track as best estimate of the trajectory is used, which introduces unwanted correlations between the sub-detectors. From the tube spectrum, as shown in Figure 2.3, and the energy deposit per unit length dE/dX^{Tube} the probability $P_Z(\hat{E})$ of a hit to be caused by a particle of type Z can be derived. The tube spectrum depends on the energy $\hat{E}$ which is measured by ECAL. The probabilities of the N^{TRD} clustered hits are combined in a geometric mean

$$\mathcal{L}_Z(\hat{E}) = \sqrt[N^{\text{TRD}}]{\prod_{k=1}^{N^{\text{TRD}}} P_Z^k(\hat{E})}$$

and put into a likelihood ratio

$$LR_{e/Z}^{\text{TRD}} = -\log\left(\frac{\mathcal{L}_e(\hat{E})}{\mathcal{L}_e(\hat{E}) + \mathcal{L}_Z(\hat{E})}\right)$$

to reject either protons $LR_{e/P}^{\text{TRD}}$, or residual helium $LR_{e/He}^{TRD}$ from the electron or positron hypothesis. On the helium estimator, a cut of $LR_{e/He}^{\text{TRD}} < 0.7$ is applied. $LR_{e/P}^{\text{TRD}}$ is used in the particle identification process discussed in the following.
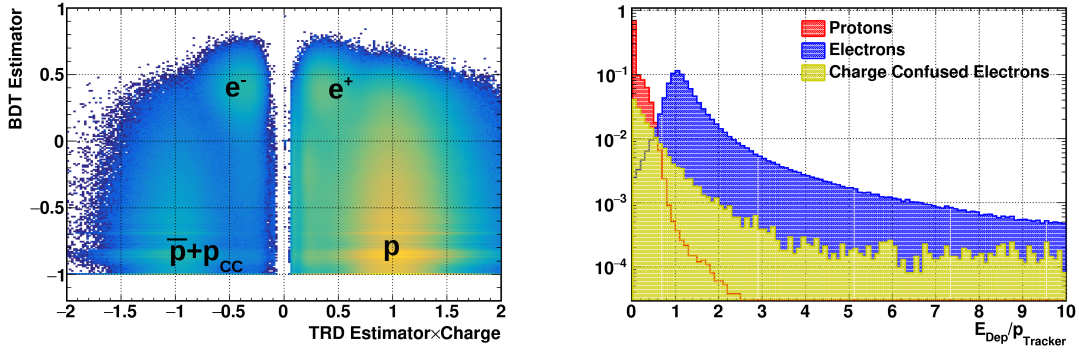
Figure 3.19.: Variables used in the particle identification of a sample of unit-charge particles already preselected in a rigidity range of 8 to 20 GV. **Left:** BDT^{ECAL} compared to $LR^{TRD}_{e/P}$, multiplied by the charge sign from the Tracker. Populations of protons in the lower-right, positrons in the upper-right and electrons on the upper left, are visibly by eye among antiprotons and charged confused protons on the lower-left. **Right:** $E_{\mathrm{Dep}}/p_{\mathrm{Tracker}}$ distribution for an electron and proton selection by TRD, ECAL and charge sign. Electrons peak at 1 while protons barely deposit a fraction of their energy. Also the distribution of charge-confused electrons, selected from a Monte-Carlo simulated sample is shown with a peak towards low values and a large tail towards higher values of $E_{\mathrm{Dep}}/p_{\mathrm{Tracker}}$. The variable is used in the analysis to reject protons and charge-confused events.

For the identification of electrons, positrons and *background* protons in the unit charge sample, further cuts are applied using variables of ECAL, Tracker and the TRD likelihood ratio as already introduced. For particle identification by ECAL, 44 variables describing the shower shape are combined in a multivariate analysis tool called *ECAL boosted decision tree BDT^{ECAL}*. Another powerful variable, combining Tracker and ECAL, is the fraction of energy deposited in ECAL E_{Dep} and the momentum measurement by the Tracker p_{Tracker}, equal to the rigidity measurement for charge one particles. While electromagnetic showers are absorbed efficiently in the lead layers, a proton most likely will not start a shower and only deposit a small amount of energy by ionization in the scintillating fibers. A hadronic shower will not be fully absorbed and thereby only deposit a small fraction of its energy within ECAL. This results in a $E_{\mathrm{Dep}}/p_{\mathrm{Tracker}}$ ratio close to zero for protons and peaking at $E_{\mathrm{Dep}}/p_{\mathrm{Tracker}} \sim 1$ for electrons and positrons, as showed in Figure 3.19. Since the Tracker's momentum resolution is finite, the width of this peak increases towards higher energies decreasing the rejection power of this cut. Also, the variable is sensitive to *charge-confusion*, the reconstruction of the wrong charge sign from secondary particles in the Tracker, or just by its finite resolution. In this case, the Tracker rigidity is underestimated and an upper cut of $E_{\mathrm{Dep}}/p_{\mathrm{Tracker}} < 5$ is applied to reduce charge-confusion. Figure 3.19 shows the relevant quantities for the particle identification in the unit charge sample.

Combining the introduced quantities, efficient particle identification with high purity can be achieved with the following cuts:

Electron:

- Negative sign of charge by $\tilde{R} < 0$.

- TRD electron like $LR^{\mathrm{TRD}}_{e/P} < 0.6$.
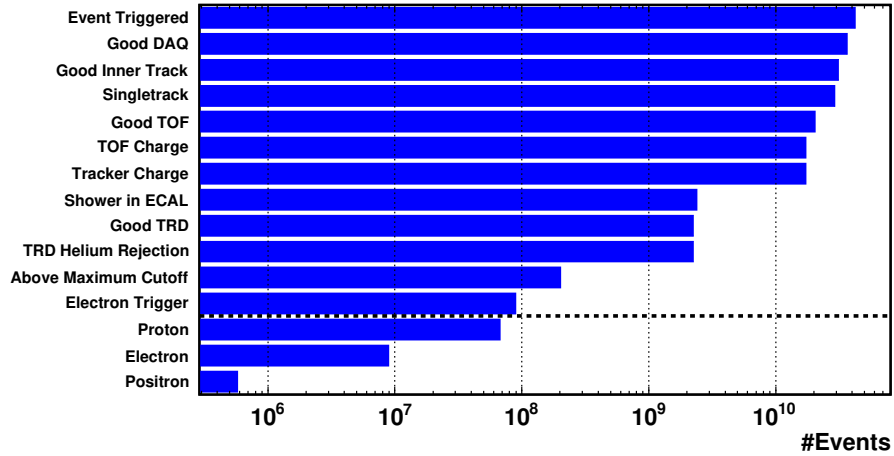
Figure 3.20.: Counted events at the different stages of the unit-charge sample selection, starting from events with available DAQ, TOF and Tracker reconstruction. Above the black dashed line, a clean relativistic downward-going set of particles with unit charge is selected within ECAL acceptance. In the following, the sample is divided in *background* protons, electrons and positrons by TRD, ECAL and Tracker.

- ECAL electron like $BDT^{\mathrm{ECAL}} > 0$.

- Full energy deposit in ECAL $E_{\mathrm{Dep}}/p_{\mathrm{Tracker}} > 0.6$.

Positron:

- Positive sign of charge by $\tilde{R} > 0$.

- TRD electron like $LR^{\mathrm{TRD}}_{e/P} < 0.6$.

- ECAL electron like $BDT^{\mathrm{ECAL}} > 0$.

- Full energy deposit in ECAL $E_{\mathrm{Dep}}/p_{\mathrm{Tracker}} > 0.6$.

Proton:

- Positive sign of charge by $\tilde{R} > 0$.

- TRD proton like $LR^{\mathrm{TRD}}_{e/P} > 0.6$.

- ECAL proton like $BDT^{\mathrm{ECAL}} < 0$.

- No energy deposit in ECAL $E_{\mathrm{Dep}}/p_{\mathrm{Tracker}} < 0.6$.

In Figure 3.20 the event counts after each selection step are shown, starting from events with an DAQ, TOF and Tracker reconstruction available.

In order to validate the selection, the efficiency and purity of the particle identification cuts have been studied using methods from [170]. The number of events selected in the cut-based approach is compared to the one obtained with a template fit analysis. Here the shape of the discussed selection variables is compared to templates of pure signal or background shape. By construction, the template fit analysis counts all available events. Figure 3.21 shows the selection efficiency for electrons with the ECAL energy. The selection has an efficiency of >80% up to 70 GeV, decreasing to 40% at 300 GeV. The break in the selection efficiency originates from the decreasing Tracker resolution with impact
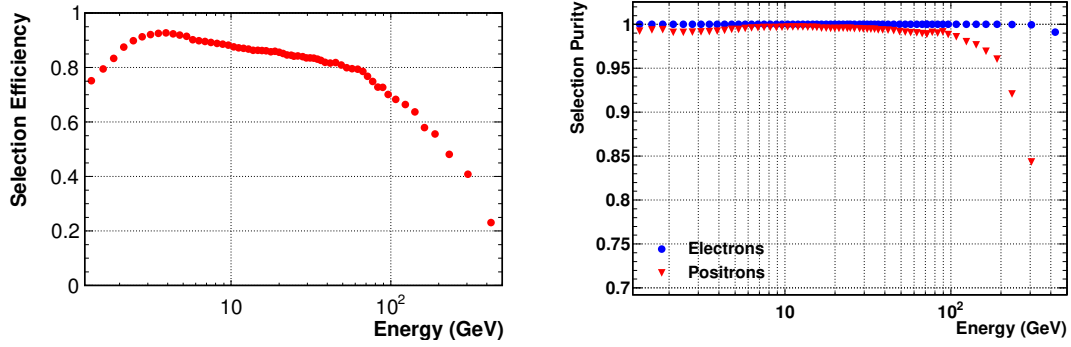
Figure 3.21.: Selection properties of the cut-based selection, determined by the template fit method, as function of ECAL energy. **Left:** Selection efficiency of electrons in the cut-based analysis approach. The break in the selection efficiency originates from the decreasing Tracker resolution with impact on the $E_{\text{Dep}}/p_{\text{Tracker}}$ variable and the decreasing TRD proton rejection. **Right:** Purity of the positron and electron selection. The plots show that a pure sample of electrons and positrons can be selected with high efficiency up to 100 GeV.
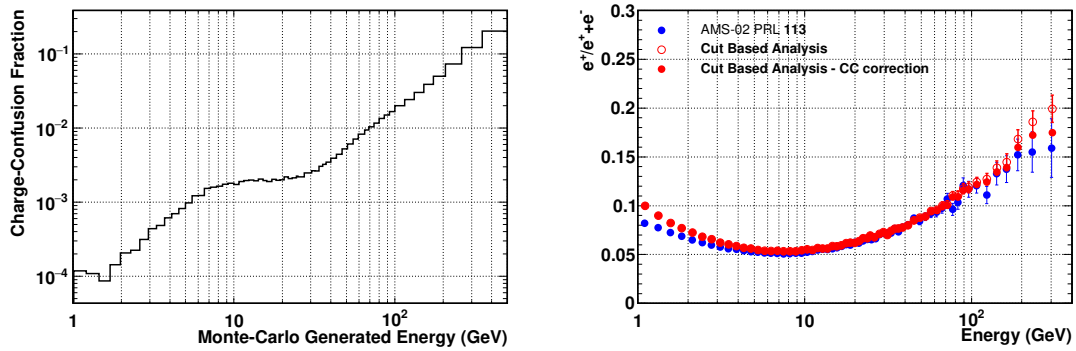
Figure 3.22.: Positron fraction compared to the official AMS-02 publication in [2]. **Left:** Charge-confusion calculated from Monte-Carlo simulated electron events. **Right:** Positron fraction result, before and after charge-confusion correction. The cut-based analysis is able to reproduce the official result, obtained with an optimized analysis strategy.

on the $E_{\text{Dep}}/p_{\text{Tracker}}$ variable. Also the TRD proton rejection decreases with energy as shown in Figure 2.4. The efficiency in the selection of positrons is taken to be identical. The purity of the selection of positrons and electrons is shown aside and is stable above 95% up to 200 GeV. Towards higher rigidities the purity of the positron sample decreases for a growing proton contamination without the additional charge discrimination from the Tracker, compared to electrons.

To further study the quality of the selection, the positron fraction is produced and compared to the result published in [2]. The result is shown in Figure 3.22, with good agreement after a charge-confusion correction has been applied. The charge-confusion correction is calculated from Monte-Carlo simulated electron events, counting the fraction of wrongly reconstructed positively charged events with generated energy in the analysis binning. Deviations in the low energy regime below 10 GeV are due to the extended measuring period with changing solar modulation.

Charge-confusion cannot be removed on a single event basis with acceptable efficiency.
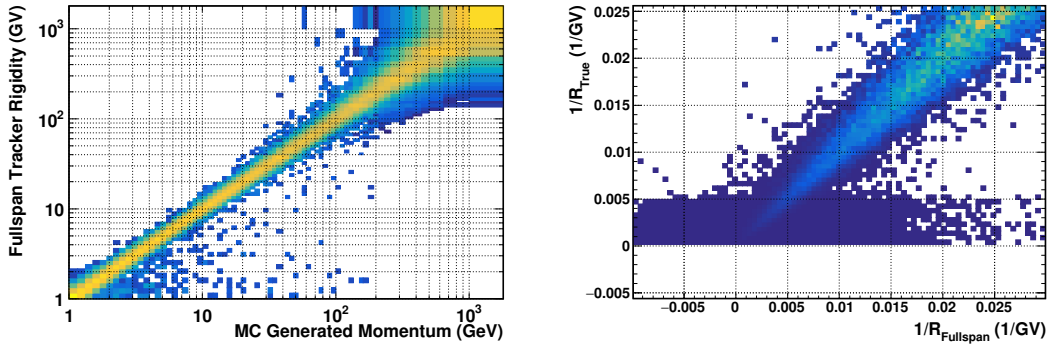
Figure 3.23.: Quality of rigidity reconstruction in the Tracker studied with Monte-Carlo. The flux of Monte-Carlo events has been weighted to match the proton flux measured by AMS-02 [5]. **Left:** Reconstructed fullspan tracker rigidity as function of generated momentum, normalized to 1 in slices along the x-axis. Towards higher energies the rigidity is reconstructed with less precision and events migrate between the bins. **Right:** Inverted fullspan tracker rigidity as function of the inverted generated momentum. In the rigidity reconstruction the track curvature is fitted, as the inverse of the rigidity, making the inverted rigidity Gaussian distributed. Towards higher rigidities the width of the distribution allows for a fit of the curvature with negative charge sign, referred to as spillover.

In the anisotropy analysis, where events are selected in a cut based approach to preserve single event information, charge-confused electrons form a background contamination in the positron sample that affects the upper limit. The treatment of such a background will be addressed in Section 4.3.3.

With the cut based approach, a pure sample of electrons and positrons can be selected with high efficiency, without losing single event information, such as the timestamp and incoming direction which are required for a directional analysis.

3.3.2. Proton selection

The selection of protons follows the analysis presented in [5]. As protons are the most abundant species, they are basically free of any background in a positive unit charge sample, where the contributions from positrons and pions are tiny. The charge can be measured accurately, to reject higher charged nuclei dominated by helium. Consequently, the selection focuses on a high event and reconstruction quality.

Again, the event reconstruction starts using the trajectory reconstructed by the inner Tracker. For this, at least three hits in the planes three to eight are required giving an inner track fit with a normalized chi-square of less than 10 separately in the bending and non-bending plane. Additionally, a hit in x and y-direction is required on Tracker plane two to stabilize the track finding, improving the rigidity resolution and the interpolation of the trajectory to plane one. With an efficiency of $\approx 70\%$, this requirement is one of the most restricting. In TOF a hit in all of the four layers is required within a restricted time of 10 ns for the upper and 4 ns in the lower TOF planes, reducing wrongly clustered hits from interactions above the detector and the TRD. Only relativistic down-going protons with $\beta > 0.3$, as measured by TOF, are taken into account. Events with interactions in the detector's core are removed by a cut on the lower TOF charge of $0.5 < Q_{\text{TOF}}^{\text{lower}} < 3.0$. The charge selection is performed by the Tracker, for the higher resolution compared
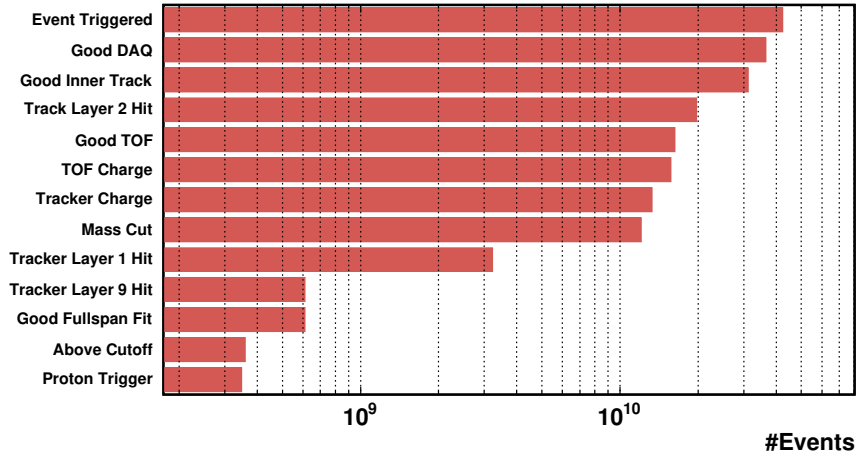
Figure 3.24.: Available events at the different stages of the proton selection, starting from events with DAQ, TOF and Tracker reconstruction available.

to TOF for single charged particles, applying a cut of $0.7 < Q_{Trk} < 1.5$. To remove a small background of low energetic pions produced in the upper part of the detector, the particle's mass, determined by combining the velocity measured of TOF with the rigidity measurement of the tracker, is required to be greater than 0.5 $^{GeV/c^2}$. The efficiency of this requirement is $\approx$100% above 2 GeV.

Finally, as the rigidity resolution is the main contributing uncertainty in the measurement of protons, only events with x-y-hits in the external Tracker layers one and nine are used. To ensure that clustered hits on the track belong to the primary particle, the trajectory as reconstructed by the inner Tracker, is required to pass inside a fiducial area in range of 62.14×47.40 cm^2 in x and y distance from the center on layer one and 33.0×29.5 cm^2 from the center inside layer nine. Also hits in the outer layers should match the unit charge hypothesis with a reconstructed charge of $0.6 < Q_{Trk}^{L1,L9} < 1.9$. The resulting track fit in the range of Tracker layer one to nine is then used for the rigidity measurement. The fit's normalized chi-square is required to be less than 10 in the bending direction. On the right-hand side in Figure 3.23, the rigidity resolution matrix, obtained from Monte-Carlo simulated events, is shown. The rigidity resolution is the dominating systematic uncertainty in the proton analysis.

The number of particles after each step in the proton selection is shown in Figure 3.24. The requirement of a so-called *fullspan* track reconstruction demanding a hit in the outer Tracker layers one and nine, decreases the sample size significantly. However, dropping these requirements would decrease the rigidity resolution down to a level where an analysis of the events is no longer practical. To validate the selection, the proton flux has been calculated. A comparison with the AMS-02 publication is shown in Figure 3.25. A reasonable agreement between the fluxes is achieved, considering the different timescale and the missing unfolding of the rigidity scale to correct for migration between bins in rigidity. Various ingredients are involved in the calculation of a flux, not all of which are relevant in the search for anisotropies. To prevent a bias in the flux calculation, the proton selection has also been validated internally with other groups working on the proton selection.
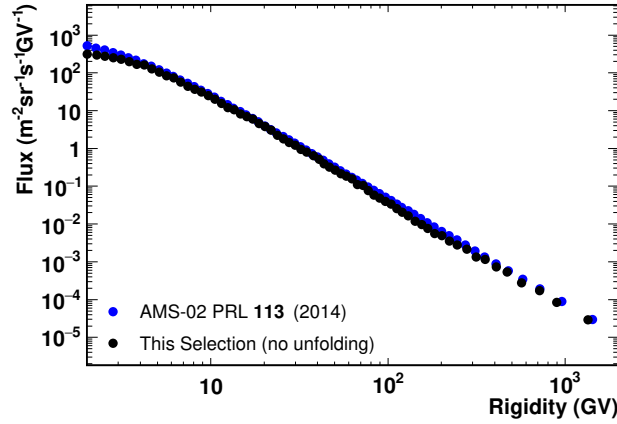
Figure 3.25.: Comparison of the AMS-02 proton flux from 2014 [5] with the flux calculated from the data sample used in this analysis. Deviations at rigidities below 10 GV can be explained by time-dependent solar modulation. For rigidities above 100 GV unfolding plays a role, which has not been applied here.
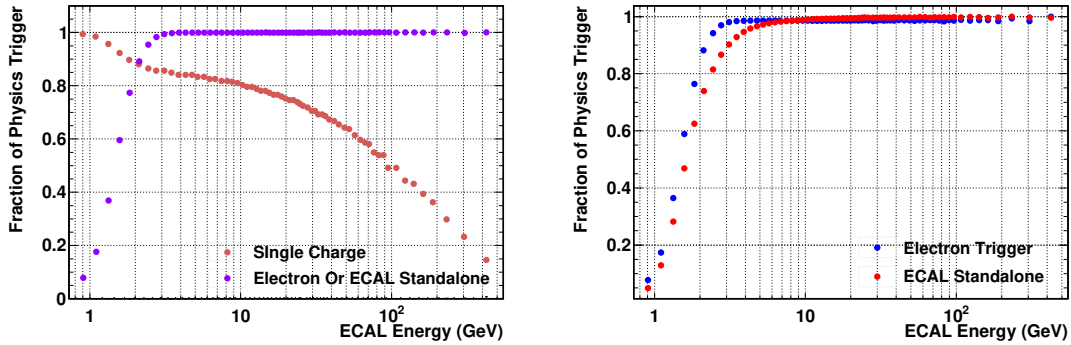
Figure 3.26.: Trigger conditions with ECAL energy, on a selected electron sample with *physics trigger*. **Left:** Fraction of electrons events with single charge trigger and electron or ECAL standalone trigger. All electron events have the ECAL trigger fired above 10 GeV. **Right:** Fraction of electrons events with electron or ECAL standalone trigger. Both trigger conditions are equally efficient. The quantity is not equivalent to the trigger efficiency, where *unbiased trigger* are counted.

3.3.3. Trigger Efficiency

As discussed in Section 3.1, the trigger rate is a major external influence on the detector's operation, making the trigger efficiency an important part of the selection. An introduction to the AMS-02 DAQ system has been given in Section 2.2. CR particles are recorded by the detector under six different *physics trigger* conditions (using abbreviations introduced earlier in Section 2.2):

- Single charge: 4/4 (HT) TOF planes, no ACC

- Ion: 4/4 (SHT) TOF planes

- Slow ion: 4/4 (SHT) TOF planes with delay

- Electron: 4/4 (HT) TOF planes, and ECAL energy deposit above threshold

- ECAL standalone: ECAL energy deposit above threshold and shower axis within FOV
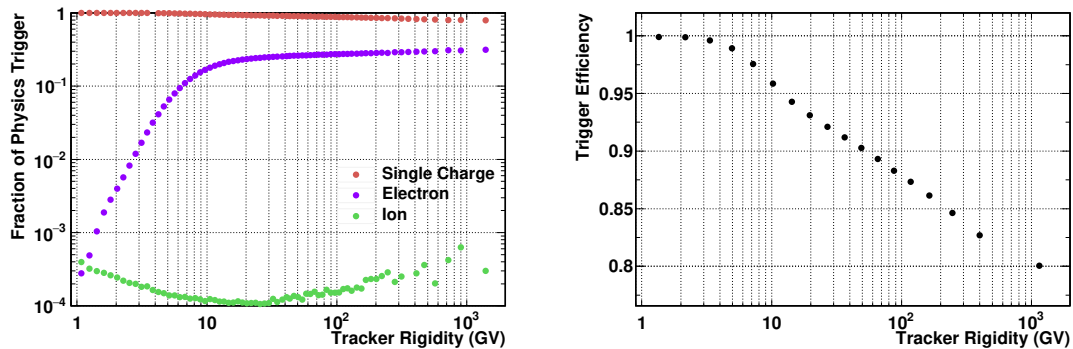
Figure 3.27.: Proton trigger as function of Tracker rigidity. **Left:** Fraction of proton events with single charge trigger, electron or ECAL standalone trigger or ion trigger. The single charge trigger is dominating. **Right:** Proton trigger efficiency using the single charge trigger only. The efficiency is greater than 80% up to 2 TeV. In order to minimize transitions in the trigger conditions during orbit, only the single charge trigger is used.

In addition, two so-called *unbiased trigger* conditions with loose selection are defined to measure the trigger efficiency directly from data. Both are prescaled in order not to saturate the DAQ:

- Unbiased charge: 3/4 (HT) TOF planes, prescaled by a factor of 100

- Unbiased ECAL: ECAL energy deposit above threshold, prescaled by a factor of 1000.

Figure 3.26 shows the fraction of electron events with *physics trigger*, which are triggered by the dedicated electron or ECAL standalone trigger, or the other trigger conditions. It is evident that the electron and ECAL standalone trigger are sufficient to trigger electrons above an energy of 10 GeV. The combination of the trigger conditions gives a high efficiency of 100% above 10 GeV. Therefore, other *physics triggers* are not taken into account in the electron and positron selection. In the selection of *background* protons, the same trigger requirements are taken in order not to introduce any systematic bias.

Having an efficient ECAL trigger is beneficial, as ECAL is located at the bottom of the detector, where most low energetic particles are already absorbed. As a consequence, ECAL is not sensitive to the external particle rate and shows a stable performance during orbit.

For protons the single charge trigger is the dominating one, as visible from Figure 3.27. Using only the single charge trigger, a trigger efficiency greater than 80% up to 2 TeV is achieved. During orbit, when the external particle rate rises, ACC is more likely to give a veto and the trigger conditions change. In order to avoid transitions between different trigger conditions, introducing instabilities with the position, only the single charge trigger is used. The dependence of the trigger efficiency with the external particle rate will be covered in Section 4.3.1.1.

3.3.4. Good second definition

The evaluation of time intervals in which the detector is in nominal operation condition, is of major importance as any deviations of nominal operations directly reflect in
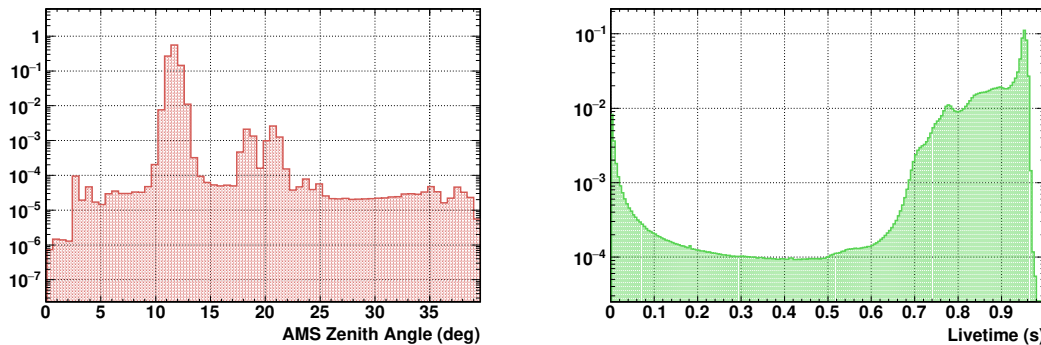
Figure 3.28.: AMS zenith angle (**left**) and livetime (**right**) distributions. The zenith angle peaks at 11 deg, as AMS-02 is slightly tilted with respect to the ISS. A cut on zenith angle smaller than 40 deg is applied. The livetime is given by the fraction of time in one second, in which the DAQ was ready to record an event. Seconds with livetimes smaller than 0.5 s are removed in the analysis.

the measured particle rate and might be detected as a signal. Time periods in which known external activities affect the data-taking, such as EVAs, material from the station crossing the detector's field-of-view or detector activities, such as calibration runs or TRD gas refills, are marked as bad runs directly during the data-taking and are removed. However, not all non-nominal operations happen on run basis and are tagged as bad, so a good second definition from offline data is applied on top. Within the AMS software, all relevant information concerning the detector operations, independently of single event triggers, is contained in a *real time information* (RTI) database. The database is organized in steps of seconds, which therefore is the minimum time resolution available. Position data is gathered by a GPS receiver installed aboard the detector [171] and the orientation is given by an ISS database maintained by NASA. Event timestamps are tagged by the JMDC time which is synchronized with the GPS time once per day. The RTI database is organized in JMDC time as well. For every second of data-taking, the RTI database, the GPS database and the ISS orientation has to be available and marked as good. Missing database information mainly results form the time in-between two runs and from rapid unforeseen changes in the operation of the ISS such as reboosts, where the signal to GPS satellites might get lost. These seconds amount to about a 5% loss of data taking time.

For the detector's orientation in space two variables are taken into account. One is the angle of the AMS pointing direction with the zenith, which is tilted by about 11 deg with respect to the ISS in nominal operation. If the station is rotated, which regularly happens for docking maneuvers, the Earth's atmosphere enters the detector's field-of-view. These time periods are identified by a zenith angle greater than 40 deg. The distribution of the AMS zenith angle is shown in Figure 3.28. In a second step, a hard cut on the ISS orientation, stated in yaw, pitch and roll, is applied. It has been found to eliminate some defective orbits not removed by the zenith angle requirement.

A good alignment of external Tracker layers is defined by comparison of two independent alignment methods to not differ more than 35 μm in Tracker layer one and not more than 45 μm for layer nine.

To remove events where the DAQ is close to saturation from low energetic particles, which mainly happens at the magnetic polar regions, a livetime cut of 0.5 seconds is applied. The livetime per second is determined by sampling the status of the DAQ in
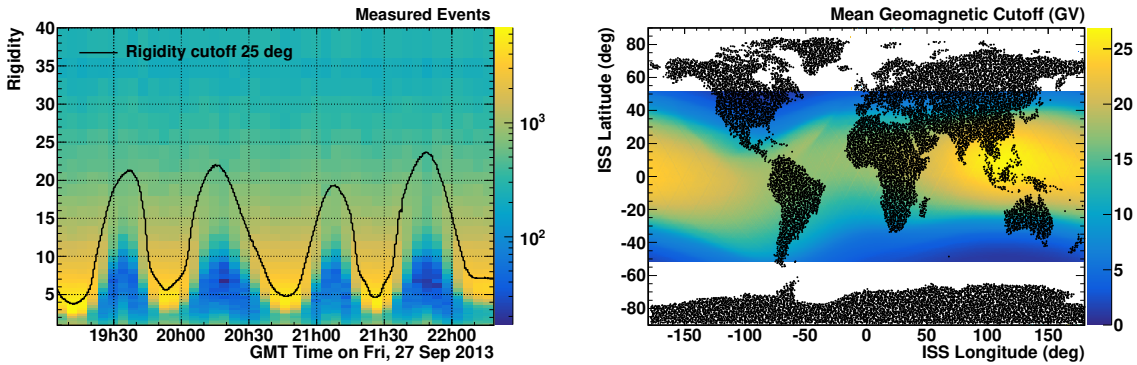
Figure 3.29.: **Left:** Time evolution of the rigidity distribution of measured events for two orbits. The black line shows the rigidity cutoff. At rigidities close to zero, trapped particles can be seen. **Right:** Mean geomagnetic cutoff for an opening angle of 25° with the position above Earth's surface.

small steps of 20 ns. In addition seconds spent inside the SAA are removed by a geometric definition as plotted in Figure 3.1.

An outstanding role of the definition on *good seconds* is taken by external factors from the Earth's magnetic field, entering the selection process as a rigidity and position dependent cutoff, and its deformations from solar events, which affect the TRD performance. Both items will be discussed separately in the following paragraphs.

3.3.4.1. Geomagnetic cutoff

Low energetic particles are shielded by Earth's magnetic field and cannot reach the detector depending on its position. The small number of events still measured are produced by interactions in the upper atmosphere and trapped in the geomagnetic field [172]. Particles of this type can be removed from the sample by introducing a position and time-dependent geomagnetic rigidity cutoff.

For each second of data taking, imaginary particles inside the detector's FOV are traced back in the IGRF-11 dipole model of the geomagnetic field [173]. Particles which cannot escape the magnetic field during a propagation time of 10 seconds are considered to be trapped and the maximum energy of such particles is called maximum rigidity cutoff [174]. A factor of 1.2 is applied on top of this value to ensure that only primary particles are measured in a certain second. Events with reconstructed rigidity below the maximum cutoff are not considered. In Figure 3.29, the measured time evolution of particle rigidities is plotted for two orbits with the maximum cutoff value for positively charged particles within a 25 deg FOV and the mean cutoff for the ISS position. In this way, the rate of particles is modulated at rigidities below 30 GV and a time-dependence is introduced that directly affects angular direction studies: Reference maps for rigidities below the maximum cutoff at around 30 GV will differ in their coverage of the sky. For the fullspan proton selection, the cutoff is calculated with a FOV of 25 deg and positively charged particles. For the lepton studies the maximum cutoff out of positive and negative charged particles in the same FOV is applied.

3.3.4.2. TRD performance

The pressure from the solar wind deforms the Earth's magnetic field and compresses it on the day side. In periods of high solar activity, the deformation increases up to a
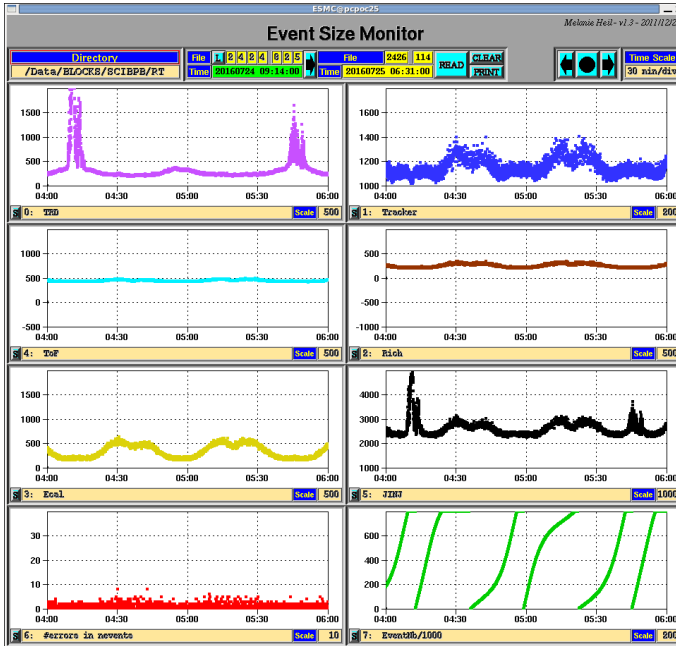
Figure 3.30: Screenshot from the POCC event size monitoring screen. It can be seen that the TRD event size (purple) rises in periods of ≈90 minutes. The other sub-detectors, Tracker (blue), TOF (cyan), RICH (brown) and ECAL (yellow) are not sensitive to this rise: The event size stays flat.
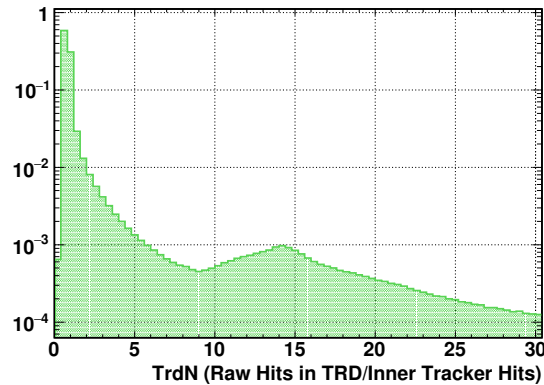
Figure 3.31.: Distribution of the TRD performance variable *TrdN* among seconds of data taking. The variable peaks at 1, as expected, and a second population at TrdN=14 is observed. These seconds, of high TRD occupancy, are desired to be removed by the requirement.

level where low energetic particles, in the lower MeV energy range, reach the detector. These deformations, on a short time scale of hours to days, are not contained in the magnetic field models and therefore not reflected in the applied geomagnetic cutoff. As the particles get absorbed in the upper AMS-02 material, they are not triggered as events and do not show up in the livetime or the Tracker. However, TRD on top is flooded with particles and loses its reconstruction capabilities. Figure 3.30 shows a screenshot of the monitoring program of the event sizes of the data produced in the different sub-detectors in the POCC. The monitoring shows a clear peak-like rise in the TRD event size in a period of one orbit. The event size of the Tracker and TOF do not show the peak and only follow the usual orbit variations. During SAA orbits, a rise is present in these variables as well. The presented screenshot was the first time that the effect, introduced above, has been observed and linked to to the analysis of the absolute anisotropies.

As TRD is involved in the track finding selection efficiencies drop, which leads to a decrease in the particle rate for all energies. A cut on the raw hits in TRD can be applied,
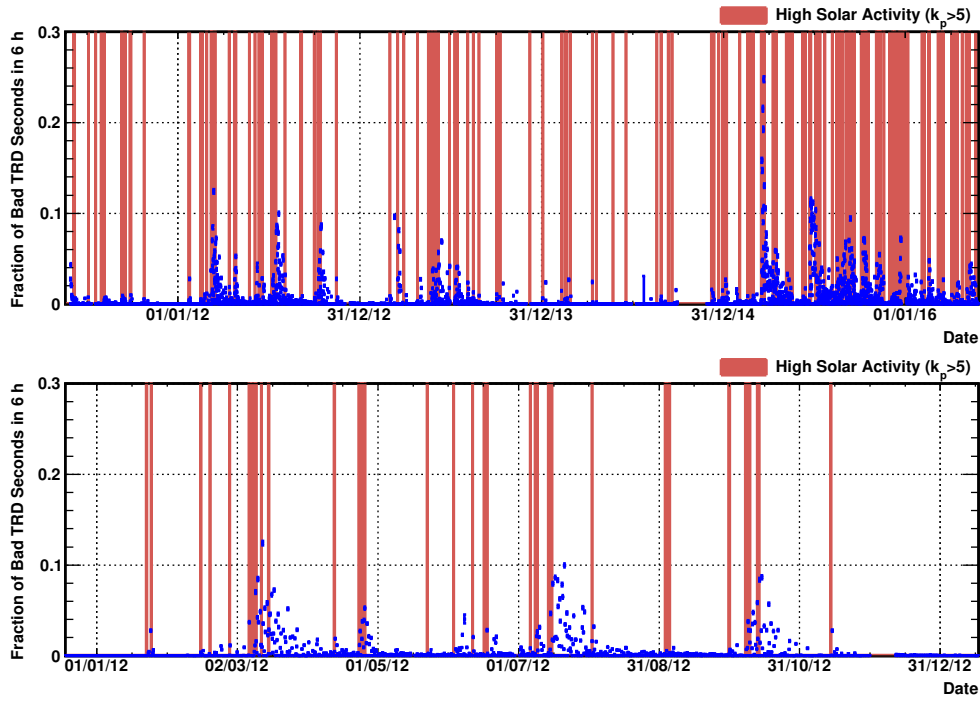
Figure 3.32.: Fractions of seconds, removed by the TRD performance cut, in a time interval of six hours, correlated to time periods of high solar activity (red) for the full operation time **(top)**, and the year 2012 **(bottom)**. The solar activity is stated as k_p-value, which describes the deformation of the Earth's magnetic field, ranging from 0 to 9. Values of $k_p > 5$ are considered as solar storm. The k_p-values are provided in steps of six hours by [175]. Beginning of 2014 the solar activity significantly increases.

but as this quantity is subject to natural fluctuations with the external particle flux, the cut will be inefficient and strongly time and position-dependent. The fact that this sort of events do not reach Tracker can be used to normalize the raw hits in the TRD. An observable of raw hits in the TRD divided by hits in x and y direction of the seven inner Tracker layers is constructed to reject times in which low energetic particles flood TRD. With 20 layers in TRD and 14 inner Tracker clusters, this observable peaks slightly below 1, in a clean event. The distribution of the variable, called *trdN* for normalized TRD hits, is shown in Figure 3.31. The peak at TrdN≈1 can be identified next to a broad peak at TrdN≈14, which is the population that needs to be removed in the analysis. A cut of smaller than 1.4 is applied in a 5 second average on the time interval, not on event-by-event basis. The cut removes about 2% of the events. To show that the variable is sensitive to the deformation of the Earth's magnetic field, Figure 3.32 correlates the inefficiency of the cut with the so called k_p-value. The k_p-value describes this deformation, ranging from 0 to 9, where values of $k_p > 5$ are considered as solar storm. The k_p-values are provided, as global average in steps of six hours measured by ground stations, by [175]. It can be seen that indeed, the TRD performance correlates with the deformation of the geomagnetic field. The effects on the simulated isotropic sky will be discussed in Section 4.3.1.2.

4. Results

This chapter applies the methods introduced in Chapter 3 to the AMS-02 data. Special focus will be given to the results obtained with the simulated *IsoSkyMaps* as this method has been developed in the frame of this thesis, and a measurement of a three-dimensional absolute anisotropy has never been achieved before within AMS-02 and other experiments. The measurement requires an understanding of operational and systematic effects down to the per mille level, as presented in [176], and has first been shown in [158]. The well understood relative anisotropies of positrons and electrons and the newly developed analysis of the anisotropy with rigidity in protons serve as a validation in this context. However, the results on their own are already of importance to the community and have been presented to the public in [109], [158], [177], and [178].

4.1. Relative anisotropies

In this type of analysis particles of a different species serve as a reference for the particles desired to study, as described in section 3.2.1. With AMS-02 electrons, positrons and protons can be selected within equal acceptance and selection properties, leading to the combinations of electrons and protons as a reference for positrons, and protons as a reference for electrons. As stated in Section 3.2.1, other combinations, involving higher charged nuclei, cannot be studied with this method for the different selection properties. Also, for the abundant protons, no reference particle can be found, as statistical fluctuations in the lower abundant reference particle will overlap a signal. For positrons, two choices of reference particles are considered: Electrons and protons. Both analyses are equivalent, but are subject to different systematic properties, as protons are measured differently by the detector. A systematic bias from the differing selection efficiencies and energy measurements might be introduced. On the other hand, protons are of the same charge sign as positrons. For electrons used as a reference, it is the other way around: Selection efficiencies are similar, as well as the energy measurement. But, they are of opposite charge sign, which can introduce an asymmetry in the detector and the incoming directions in the Earth's magnetic field.

Events are grouped into bins of energy measured by ECAL for positrons and electrons. For protons, the rigidity measured by the tracker is used. Results are stated in a cumulative binning at 16, 25, 40, 65, 100 GeV with an upper border of 350 GeV to maximize
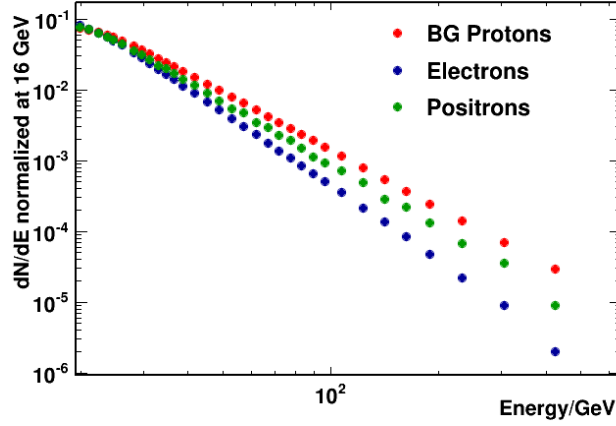
Figure 4.1.: Particle counts divided by bin width normalized to an area of one above 16 GeV of electrons (blue), positrons (green) and background protons (red). The plot points out the different spectral index in counts of the different particle species.

the sample size. In general, the distribution of incoming directions in the celestial sky is energy-dependent due to a different geometrical acceptance and magnetic field effects. The number of particles measured in a range of energy and a region in the celestial sky is the integral $\int_{E_{Min}}^{E_{Max}} \frac{dN(E,\theta,\varphi)}{dE} dE$, where $\frac{dN}{dE}$ follows a power law, in good approximation. Figure 4.1 shows $\frac{dN}{dE}$, normalized to an area of one above 16 GeV, for the three particle species, used in the relative anisotropy studies. It is evident that they have a different spectral index[1]. When comparing particles with a different spectral index to another, the integral over an energy range

$$\int_{E_{Min}}^{E_{Max}} \frac{dN_1(E, \theta, \varphi)}{dE} dE \neq \int_{E_{Min}}^{E_{Max}} \frac{dN_2(E, \theta, \varphi)}{dE} dE$$

and consequently the content in a pixel of the map, differs. Because of an energy-dependent exposure, introduced by the Earth's magnetic field, a deviation from isotropy in the *signal-free* coordinate systems is introduced with unpredictable effects on the *analysis* coordinate systems. It is desired to reduce the width of energy bins to minimize the impact of this effect, but maximizing the sample size in a bin and therefore sensitivity at the same time. To solve this contradiction, the analysis bin is divided into smaller intervals, called *layers*, which enter the likelihood fit as individual terms. The likelihood function for the expansion in the dipole components ρ from Equation 3.13, discussed in Section 3.2.6.1, becomes

$$\mathcal{L}(d_1, d_2, d_3) = -\log\left(\prod_{j(E_{Min})}^{N_{Layer}} \prod_{i=1}^{N_{Pixels}} f(R_i(dE_j)|R_i^{Exp})\right) \quad . \tag{4.1}$$

and combines the single layers in the analysis range. In this way, the width of dE in the ratio $R_i(dE)$ can be reduced, but events in all energy layers enter the fit procedure. The binning in energy used for the layers follows the one of the positron fraction analysis in [2] with a total of 35 energy layers in the full energy range from 16 to 350 GeV. The number of layers in the cumulative energy bins is contained in Table 4.1. The upper

---

[1]In Figure 1.7, the spectral index of the fluxes, corrected for the detection efficiency with different dependency on the energy for positrons and protons, is compared.
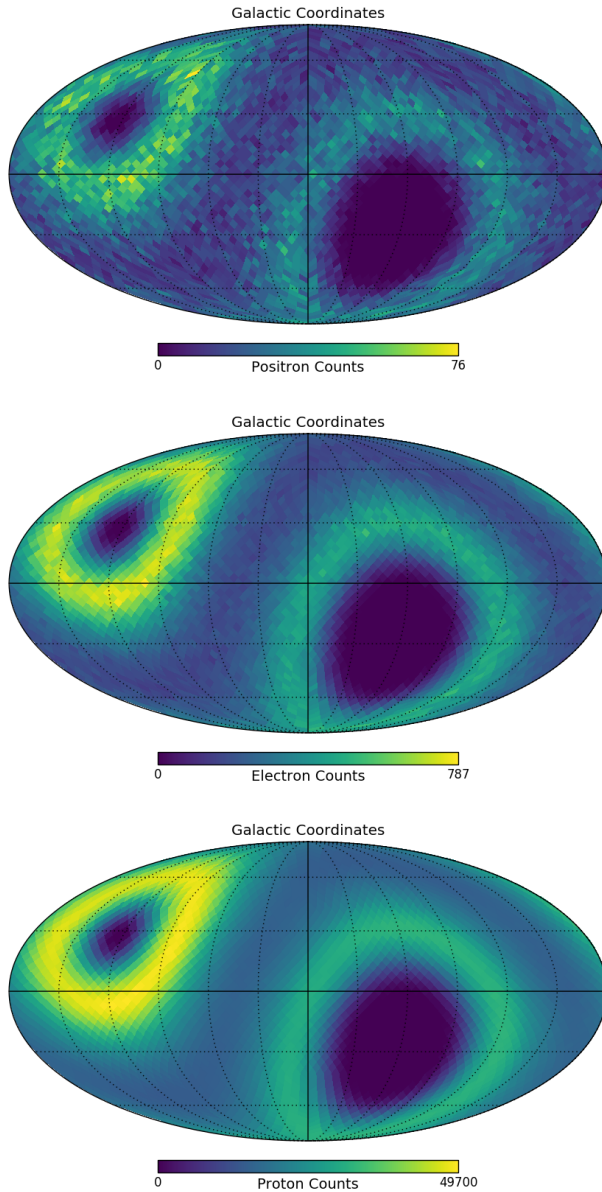
Figure 4.2: Positron, electron and background proton events (from top to bottom) selected following Section 3.3 in the energy range of 16-350 GeV in **GAL**. The N_{e^+}=69,394 positrons, N_{e^-}=913,421 electrons and ≈7 million protons are filled in maps with a resolution of 3072 pixels with a solid angle of ≈0.25 deg.

energy limit is given by the proton rejection power of the TRD which drops towards higher energies as it is evident from Figure 2.4. Towards lower energies, the geometric acceptance of the detector strongly depends on energy and the particle charge, due to the magnetic field [179]. The lower energy border of 16 GeV has been chosen accordingly, not to introduce an anisotropy in the frame of the detector.

If not stated otherwise, the data are divided into 192 HEALPix bins with a solid angle of ≈3.75 deg for the fit. For presentation, the maps are binned in a finer binning, such as in Figure 4.2, where proton, electron and positron events, in the full analysis range of 16-350 GeV, are shown in galactic coordinates.

4.1.1. Positron relative anisotropies

Using the selection described in Section 3.3 N_{e^+} ≈70,000 positrons are collected in the analysis range from 16 to 350 GeV. As reference particle, N_{e^-} ≈910,000 electrons and 7 million protons are selected in the same acceptance and energy range. The resulting

E_{Min} (GeV)	N_{Layers}	N_{e^+}	$\delta^{95\%}_{Exp}$	N_{e^-}	N_P
16	35	69,394	1.97%	913,421	67.72×10^6
25	27	34,422	2.80%	393,084	39.29×10^6
40	19	13,937	4.40%	129,017	17.99×10^6
65	13	5,401	7.06%	39,598	7.70×10^6
100	7	2,227	10.99%	13,434	3.47×10^6

Table 4.1.: Number of selected positrons and reference particles within ECAL acceptance in a cumulative energy binning with upper energy border of E_{Max}=350 GeV. N_{Layers} is the number of flux bins contained in a cumulated bin and is equal to the layers in the fit. The expected limit $\delta^{95\%}_{Exp}$ at a 95% credible interval originates from the mean of the limit distribution for the given number of positrons and is independent of the reference.

event maps in galactic coordinates for the three particle types are shown in Figure 4.2. Following the description given in Section 3.2.7, an expectation on the isotropic limit can be derived from the given number of signal particles, independently from the reference map and coordinate system, given $N_e^+ \ll N_{Ref}$ and a sufficient coverage in the coordinate system. The condition has been tested with a N_{Sig} to N_{Bkg} ratio of 10 which is approximately the value expected from the positron fraction. For the number of collected positrons in the lowest energy range, a limit on the dipole amplitude at a 95% credible interval of $\delta^{95\%}_{Exp} \approx 2\%$ is expected from the mean of the distribution shown in Figure 3.16, scaled to the appropriate sample size. However, the spread of this quantity will be large, as evident from the width of the distribution. For positrons in the full energy range, the one standard deviation interval of the expected limit ranges from 1.5% to 2.4%. The selected number of positrons together with the limits $\delta^{95\%}_{Exp}$ to be expected in case of isotropy with the available sample size are shown in Table 4.1. The number of selected reference particles are shown, as well.

A first impression of the quality of the two choices of a reference map for positrons can be derived from the significance in the GTOD coordinate system. As discussed in Section 3.1.1, this coordinate system serves as a systematic validation of effects introduced by the detector or the Geomagnetic field. Figure 4.3 shows the significance map for positron signal in GTOD coordinates with electrons and protons used as a reference for the full energy range. While the electron reference shows no features in the map, the same plot with protons as a reference reveals a deficit of positrons aligned with regions of high Geomagnetic cutoff. The significance distribution is slightly shifted towards negative values and the description with a normal distribution is not optimal with a normalized $\chi^2 \approx 1.8$. A reason for this observation might be the different rigidity measurement by the tracker for protons with respect to positrons, of which the energy is measured by ECAL. Also, the selection by TRD and ECAL might introduce some bias. Nevertheless, protons as reference are carried on to the *analysis* coordinate systems in the further analysis to get a handling of the impact of such deviations in the *signal-free* coordinate system in the *analysis* systems.

To study a point source signal of astrophysical origin, a fit to the normalized ratios R_{e^+/e^-} and $R_{e^+/p}$ of positrons to the electron and proton reference map is performed in galactic coordinates under the assumption of a dipole signal. The single fit components are shown in Figure 4.4 for both reference maps. The noise bands are given by the fit uncertainty, dominated by the number of positron counts, centered around zero. They
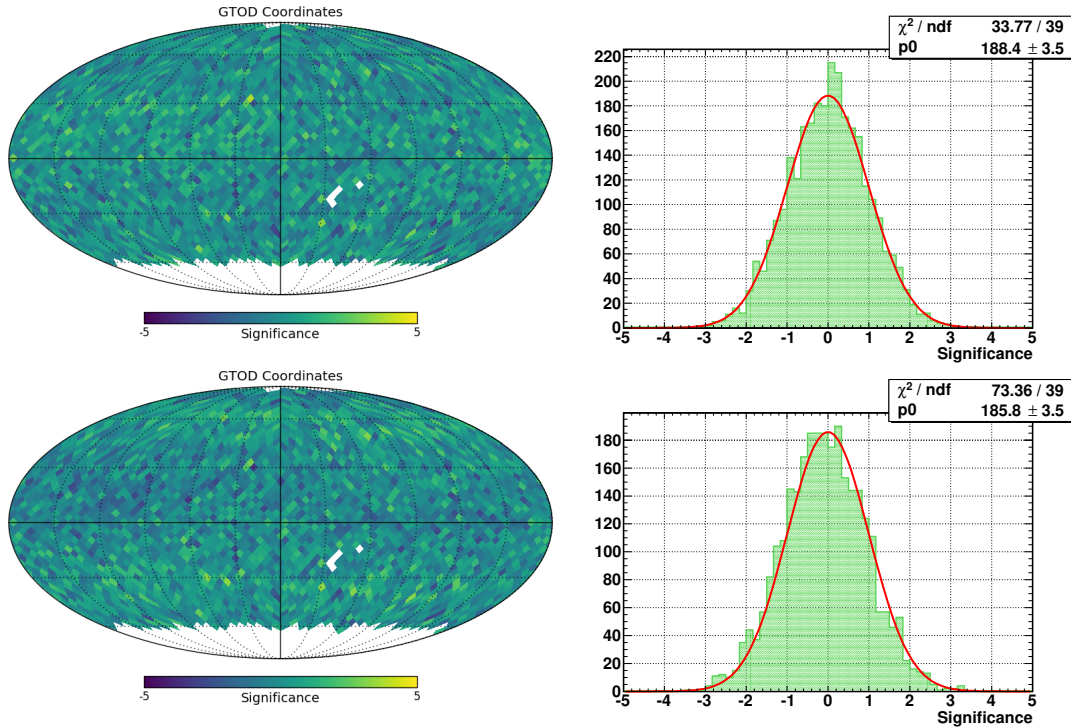
Figure 4.3.: Significance map and distribution for a positron signal in **GTOD** with S_{e^+/e^-} (top) and $S_{e^+/p}$ (bottom) for the energy range of 16 to 350 GeV. The corresponding significance distributions are shown aside, together with a Gaussian function (red line) centered around zero and width of one.

constitute the null-hypothesis of isotropy. The three dipole components are located well within the noise bands for both reference maps and all energies. At E_{Min}=16 GeV the dipole component in east-west direction exceeds the 1σ noise band by about 30%. This excess happens for both reference maps, which hints towards a feature in the positron data and not in the reference maps themselves. Even though visible by eye the deviation is not significant. Consequently, the fits are in good agreement with isotropy. The lower right of Figure 4.4 shows the three components scaled to their fit uncertainty $\frac{\rho_\alpha}{\sigma_{\rho_\alpha}}$ to enhance deviations from the isotropic expectation in units of standard deviation, exemplary for the electron reference. The one and two sigma bands are shown as gray bands. Points exceeding this area are not considered acceptable within the isotropic hypothesis. To reduce unnecessary information, the fit results will be presented in this format in the following. The numerical values of the fit results can be found in Appendix B.1.

From the three fitted dipole components, the dipole strength can be calculated using Equation 3.8. In this quantity the three squared dipole components are summated, giving an expectation greater than zero, even for the isotropic case, which makes it necessary to show the isotropic expectation for a meaningful interpretation. The uncertainty on the dipole strength is quoted as two-sided confidence interval of 68.3% from a toy Monte-Carlo simulated distribution using a multivariate Gaussian distribution with a width of the components fit uncertainty, as described in Section 3.2.7.1. The measured dipole strength can be compared to the isotropic expectation as derived in Section 3.2.7, to review the significance of a signal, or validate the statistical origin of the measurement. The isotropic expectation is shown as a band from the two-sided 68% quantile of the distribution on the left-hand side in Figure 3.14. The isotropic expectation depends only on
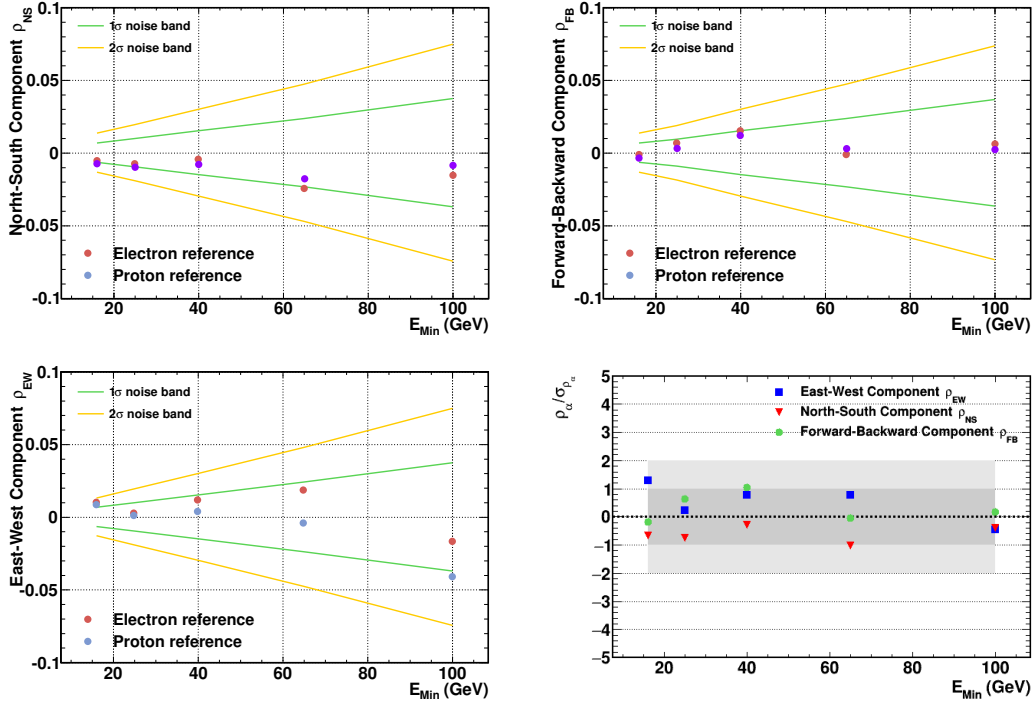
Figure 4.4.: Fit result of the dipole fit to R_{e^+/e^-} (red) and $R_{e^+/p}$ (blue) in **GAL**. The strength of the three dipole components aligned in north-south, forward-backward and east-west direction is shown with the minimum energy used in the cumulative binning with an upper limit of 350 GeV. The noise bands correspond to the fit uncertainty centered around zero, as isotropic hypothesis. The fit uncertainty of R_{e^+/e^-} is shown, but both are numerically identical. No significant excess above the standard deviation can be seen. In the bottom right, the three dipole components for the electron reference are shown in the same plot, scaled in units of the fit uncertainty. The one and two sigma range is marked in grey bands.
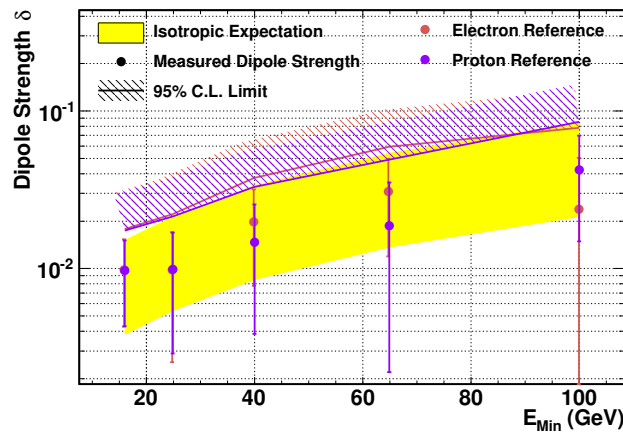
Figure 4.5.: Summary of results in the search for positron relative anisotropies in **GAL**. The reconstructed dipole strength for R_{e^+/e^-} (red) and $R_{e^+/p}$ (blue) are shown. The yellow band represents the statistical expectation of the measurement in case of isotropy, which is independent of the reference map and the coordinate system. No deviation from the isotropic expectation is found. A limit on the maximum dipole strength is stated at a credible interval of 95% using the Bayes construction (lines).

the size of the signal sample N_{Sig}, independent of reference and coordinates system. The results on the dipole strength for the positron dipole fits to R_{e^+/e^-} and $R_{e^+/p}$ in galactic coordinates are shown in Figure 4.5 together with the isotropic expectation band plotted in yellow. All points are within this yellow band meaning they match the isotropic expectation, including the fit at 16 GeV, which shows the small excess in the east-west direction. As no deviation from isotropy is found, an upper limit on the dipole strength is set to state exclusion limits on point source signals. In galactic coordinates, this is the relevant quantity to probe the pulsar hypothesis of the secondary positron population. As for all limits quoted in this thesis, the calculation follows the Bayesian construction, discussed in Section 3.2.7, but from the numbers given in the appendix, different limits can be calculated. In Figure 4.5 the limit is shown as exclusion line. Therefore, Figure 4.5 contains all relevant information on the analysis and serves as conclusion plot. For galactic coordinates, using the fit with the full sample in the maximum energy range, limits of

$$\delta^{95\%}_{e^+/e^-}(> 16 \text{ GeV}) = 1.77\%$$

for positrons with electron reference map and

$$\delta^{95\%}_{e^+/p}(> 16 \text{ GeV}) = 1.74\%$$

for positrons with proton reference map are stated at a credible interval of 95%. Both limits match the statistical expectation and are even slightly below the mean value, which was stated as expectation in Table 4.1. A reason could be correlations between the positron count map and the two reference maps, smoothing out statistical fluctuations. The isotropic result could be retrieved even though the *signal-free* GTOD coordinate system shows a small deviation from isotropy, as described from Figure 4.3. This can be understood from the discussion of coordinate system correlations in Section 3.1.1.5. However, the significance map in GTOD is the most reliable tool to enhance and study anisotropies introduced by the detector.

The same analysis, as in galactic coordinates, is performed in GSE. Because electrons and positrons are of opposite charge, differences in the propagation in the local solar magnetic field might be boosted in this coordinate system. The results are shown in Figure 4.6, without significant deviation from isotropy. The numerical result of the single fit components can be found in Table B.2, from which limits can be recalculated following any preferred method of construction. Upper limits on the dipole strength of

$$\delta^{95\%}_{e^+/e^-}(> 16 \text{ GeV}) = 1.68\%$$

for positrons over electrons and

$$\delta^{95\%}_{e^+/p}(> 16 \text{ GeV}) = 1.35\%$$

for positrons over protons are set in GSE.

Of particular interest is the development with time as the Sun's magnetic field will switch polarity expected in 2018 during the AMS-02 operational time which will affect the drifting of particles in the Heliosphere which might show up in a measurable short term anisotropy. On the other hand, the development with time is another method to find effects introduced by a change in detector operations.
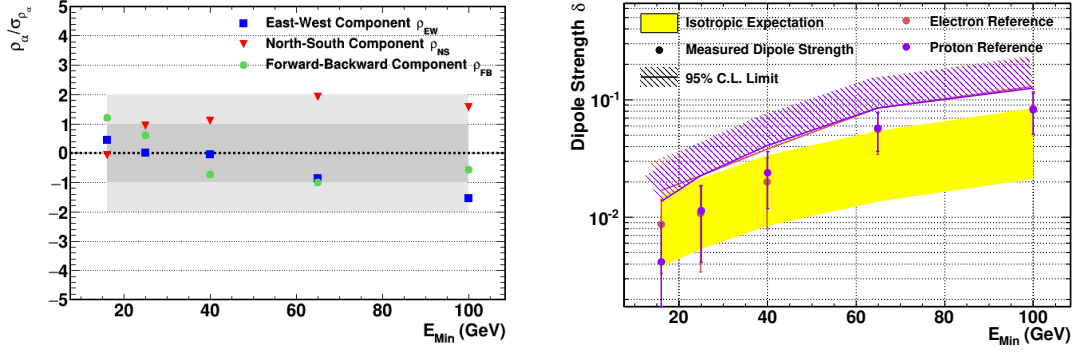
Figure 4.6.: Summary of results in the search for positron relative anisotropies in **GSE**. **Left:** Fitted dipole components of R_{e^+/e^-} scaled to their fit uncertainty. No component exceeds two standard deviations in any energy range, but the north-south component seems to be systematically shifted towards positive values. The cumulative energy binning introduces a strong correlation between the fits, which should be noted in this case. **Right:** The reconstructed dipole strength for R_{e^+/e^-} (red) and $R_{e^+/p}$ (blue). The yellow band represents the statistical expectation of the measurement in case of isotropy which is independent of the reference map and the coordinate system. No deviation from the isotropic expectation is found. A limit on the maximum dipole strength is stated at a credible interval of 95% using the Bayes construction (lines).
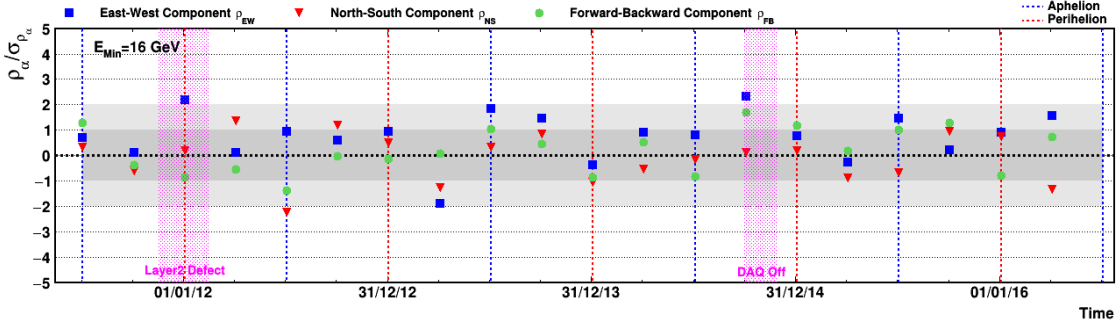
Figure 4.7.: Time evolution of the scaled dipole components in **GAL** for R_{e^+/e^-} in the full energy range from 16 to 350 GeV. The 5 years sample has been divided into 20 seasons, each of a quarter of a year. No periodic yearly variation, trend or break is visible.

Stability in time

The results shown before, are obtained over 5 years of data taking. If a source or solar activity changes its contribution to the positron flux in strength or direction during this period, a possible signal might be averaged out. To study the stability of the measurement in time, the 5 year data was divided into 20 seasons, each of a quarter of a year, defined by the Earth's elliptic orbit around the sun, namely the aphelion and perihelion. The seasonal binning starts from 20th of May 2011, 17:47:00 GMT, disregarding the first nine days of data-taking. The last season bin ends on 19th May 2016, 23:47:00 GMT being not completely covered with the available data (until 11th May 2016). The seasonal binning is shifted by 1.5 months, with respect to the astronomical seasons on Earth, where aphelion and perihelion mark the beginning of a season, instead of its center, as desired in this analysis.

Any anisotropies originating from the Earth's orbit, which could wash out in the full time period, might show up as a yearly modulation. Furthermore, a steady trend or
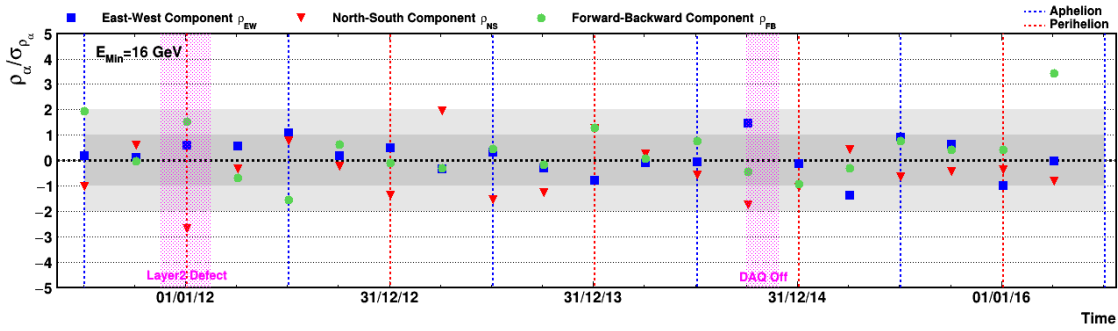
Figure 4.8.: Time evolution of the scaled dipole components in **GSE** for R_{e^+/e^-} in the full energy range from 16 to 350 GeV. The 5 years sample has been divided into 20 seasons, each of a quarter of a year. No periodic yearly variation, trend or break is visible.

break could be linked to solar activity or a change in detector operations. Of course, as the number of selected events is limited especially for positrons, this type of study is more meaningful for the analysis of more abundant particles, but it is still useful in this context as a systematic validation, of the time integrated result. The development of the three fit components using electrons as a reference with time is shown in Figure 4.7 for the lowest energy bin. No periodic yearly modulation is to be seen. Deviations of more than one sigma in fit components of a season from the constant fit line, or the zero line if they deviate, is expected naturally from fluctuations.

The time stability of the raw fit components can be found in Appendix B.1, Figures B.2 to B.6, for all analyzed energies. In Appendix B.1 also a fit of a constant to the time binned result is shown, which can serve as a control parameter for the time integrated analysis. If only statistical fluctuations, and no systematic effect is reconstructed, the constant fit value matches the time integrated result. Because of the reduced sample size in the time bins, the seasonal analysis is sensitive to effects which depend on the number of selected signal events. For positrons, where the number of events is low, the seasonal analysis cannot reproduce the time integrated result, in particular towards higher energies. For the other, more abundant, particles the seasonal analysis will be a more valuable crosscheck.

In general, to eliminate unstable fits, caused by the low sample size in a season, the fits are performed on maps with reduced pixel number of 24 HEALPix bins. A special focus should be given on the bin corresponding to fall 2014, where the detector has been shut off for about two months. This bin contains significantly fewer events than the others. Another period, during which the fit seems to be non-stable is the bin corresponding to winter 2011 in where the Tracker has been reconfigured, due to a failure of some segments in layer 2.

The development in time of the three fit components in GSE is shown in Figure 4.8 for the lowest energy bin, with the same conclusions as on the galactic coordinates. The time stability for all energies can be found in Appendix B.2, Figures B.7 to B.11. A discussion on the relative positron anisotropies will be given together with, and in comparison to, the absolute measurement in Section 4.3.

4.1.2. Electron relative anisotropy

A further relative analysis can be performed in electrons using protons as a reference sample. Because of the increased number of events by a factor of ~10 the analysis is
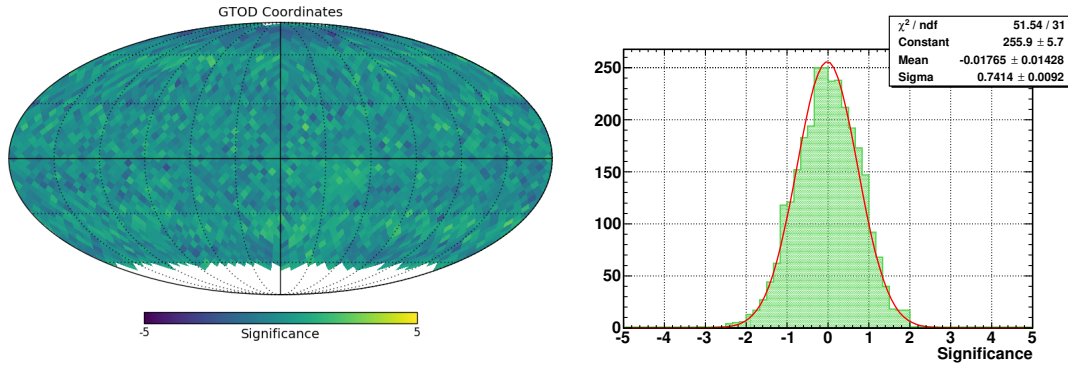
Figure 4.9.: Significance map and distribution $S_{e^-/p}$ in **GTOD** coordinates. A small deficit of electrons at the north pole, which hints towards a systematic detector or charge-dependent effect, can be identified. The significance distribution is well described by a Gaussian function (red line) slightly shifted towards negative values with an normalized $\chi^2 \approx 2$. The width is significantly smaller 1, pointing out correlations between the two maps, flattening out statistical fluctuations.

more sensitive to systematic effects than the positron to proton relative analysis. This is important to predict systematic limits in the relative positron analysis, originating for example from the tracker momentum measurement for the reference protons in comparison to the ECAL energy measurement. Possible systematic effects are searched for in the significance map in GTOD, as shown in Figure 4.9. In fact, there is a deficit of electrons, compared to the proton reference, in a region towards the north pole. In combination to the similar observation made in the significance map of positrons with proton reference the hypothesis that the difference originates from the energy measurement seems plausible. The distribution of significances does not follow a Gaussian with a width of one but is systematically compressed with a width of 0.7. However, the shape is well described by a Gaussian centered around zero and given width. This hints towards a correlation between the electron and the proton map which flattens out statistical fluctuations. Despite the observed anomalies in the GTOD coordinates, the analysis will be carried on to the *analysis* coordinates.

By itself, the search for a large scale anisotropy in electrons is relevant as they are mostly primary particles and therefore do not share the same astrophysical origin as positrons, which are pure secondaries. To understand secondary production, the primary component of CRs needs to be understood first. Electrons are more sensitive to a deviation from isotropy due to their higher abundance. A local point source, such as pulsars or the decay of dark matter, would produce electrons and positrons in the same share. Even though the relative contribution of electrons from an additional source above the primary background is lower, the analysis might still be sensitive to the source, as well.

The analysis in electrons is performed in the same cumulative energy binning as it was used in the positron analysis covering a total energy range 16 to 350 GeV, divided into smaller layers as introduced before. Table 4.2 gives the selected number of electrons and protons as a reference in the analysis binning with the limit on the dipole strength to be expected. With a factor of ≈ 13 more events, compared to positrons, a limit of factor $\sqrt{13} \approx 3.6$ smaller is expected for electrons, which gives an expected upper limit of $\delta_{Exp}^{95\%} \approx 0.5\%$ for the full energy range from 16 to 350 GeV.

E_{Min} (GeV)	N_{e^-}	$\delta_{Exp}^{95\%}$	N_P
16	913,421	0.54%	67.72×10^6
25	393,084	0.83%	39.29×10^6
40	129,017	1.44%	17.99×10^6
65	39,598	2.61%	7.70×10^6
100	13,434	4.47%	3.47×10^6

Table 4.2.: Number of selected electrons and reference protons within ECAL acceptance in a cumulative energy binning with upper energy border of 350 GeV. The expected limit $\delta_{Exp}^{95\%}$ at a 95% credible interval originates from the mean of the limit distribution for the given number of selected electrons and is independent of the reference map.
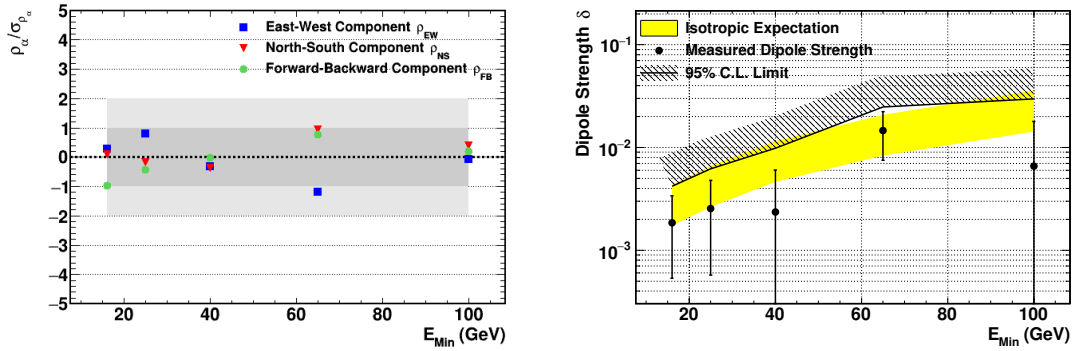
Figure 4.10.: Summary of results in the search for electron relative anisotropies in **GAL**. **Left:** Fitted dipole components of $R_{e^-/p}$ scaled to their fit uncertainty. No component exceeds two standard deviations in any energy range. **Right:** The reconstructed dipole strength for $R_{e^-/p}$. The yellow band represents the statistical expectation of the measurement in case of isotropy. No deviation from the isotropic expectation is found. A limit on the maximum dipole strength is stated at a credible interval of 95% using the Bayes construction (line).

Looking at the dipole components of the fit in galactic coordinates as shown in Figure 4.10, the measurement is in agreement with the isotropic hypothesis for all energy bins. The resulting upper limit for the dipole strength is

$$\delta_{e^-/p}^{95\%}(> 16 \text{ GeV}) = 0.42\%$$

in agreement with the expectation from the sample size mentioned before. The numerical fit values can be found in Table B.3.

In GSE, results deviate from the expected observation of isotropy. Figure 4.11 shows the three fit components of $R_{e^-/p}$ with energy, scaled to their statistical variation, in GSE coordinates. At lower energies of 16 and 25 GeV, a significant excess in negative forward-backward and east-west direction is evident. The dipole strength exceeds the isotropic expectation band with a strength of about 1%. For energies above 25 GeV the excess disappears. Here either the source of the excess disappears with energy, or the sensitivity drops below the strength of the anomaly. Consequently, no limit is set for the first two bins which disagree with the isotropic hypothesis.

Figure 4.12 shows the map of significances $S_{e^-/p}$ and their distribution for the lowest energy bin of 16 to 350 GeV in GSE. The map itself does not reveal any visible features.
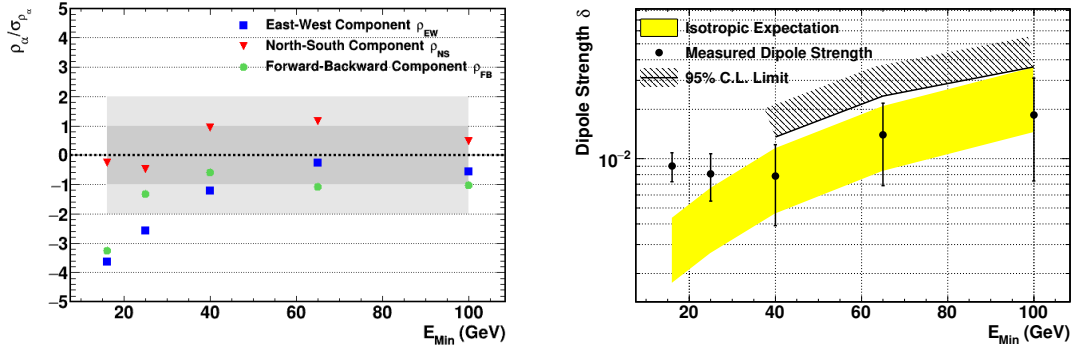
Figure 4.11.: Summary of results in the search for electron relative anisotropies in **GSE**. **Left:** Fitted dipole components of $R_{e^-/p}$ scaled to their fit uncertainty. At lower energies of 16 and 25 GeV, a significant excess in negative forward-backward and east-west direction is evident. **Right:** The reconstructed dipole strength for $R_{e^-/p}$. The yellow band represents the statistical expectation of the measurement in case of isotropy. The dipole strength exceeds the isotropic expectation band with a strength of about 1% for the lowest energies. A limit on the maximum dipole strength is stated at a credible interval of 95% using the Bayes construction (line) for bins, which are in agreement with isotropy.
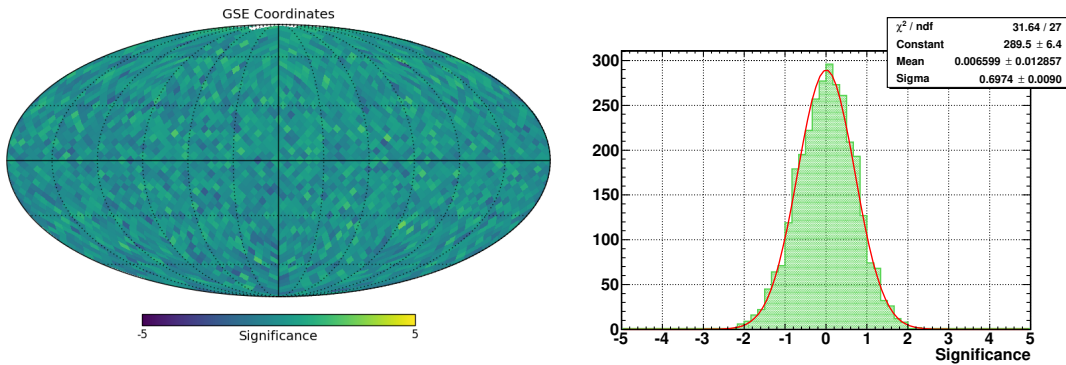
Figure 4.12.: Significance map and distribution $S_{e^-/p}$ in **GSE** coordinates. The significance distribution is well described by a Gaussian function (red line), centered around zero, with an normalized $\chi^2 \approx 1.2$. The width is significantly smaller 1, pointing out correlations between the two maps, flattening out statistical fluctuations.

The significance distribution is well described by a Gaussian centered around zero with a normalized $\chi^2 \approx 1.2$, but its width is smaller than one. At this point, the significance does not give any useful information to study the nature of the anomaly in GSE. A physical reason for the observation could be the Sun's magnetic field which might introduce a charge-dependent anisotropy by the bending of trajectories. The fact that no deviation in the north-south direction, and therefore no bending perpendicular to the magnetic field plane is observed, supports this hypothesis. A systematic effect could be introduced by variations in the detector's temperature towards the Sun. However, the significance map in GTOD hints towards a systematic limit for this type of analysis. The evidence towards a physical signal from the $R_{e^-/p}$ variable alone is not strong, for this reason. An answer can be given by studying the absolute anisotropy of electrons and protons, which will be done later in Section 4.3. A broader discussion of the different processes which might introduce such an anomaly in GSE and its impact to the galactic coordinate system will be given in Chapter 5, in the light of these absolute anisotropy studies.
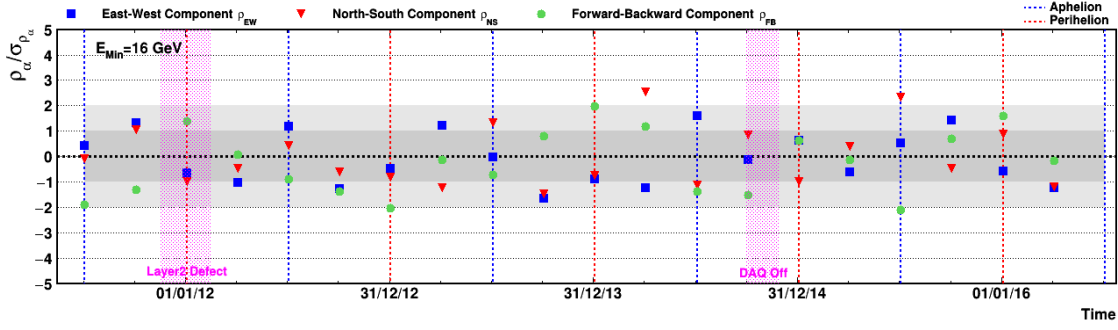
Figure 4.13.: Time evolution of the scaled dipole components in **GAL** for $R_{e^-/p}$ in the full energy range from 16 to 350 GeV. The 5 years sample has been divided into 20 seasons, each of a quarter of a year. No periodic yearly variation, trend or break is visible.
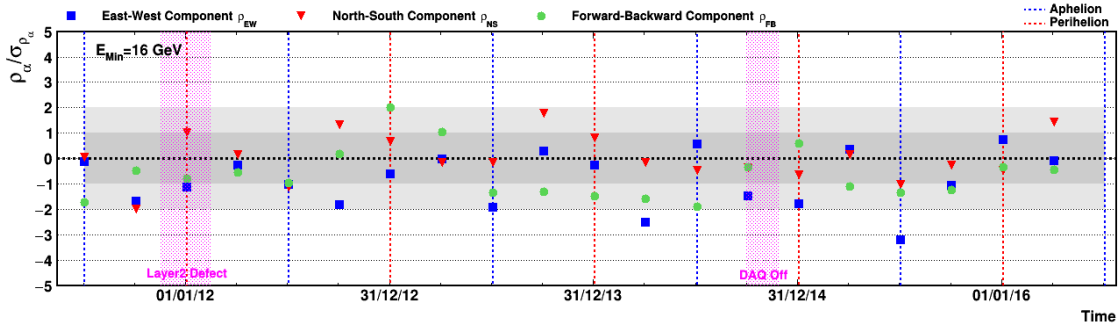
Figure 4.14.: Time evolution of the scaled dipole components in **GSE** for $R_{e^-/p}$ in the full energy range from 16 to 350 GeV. The 5 years sample has been divided into 20 seasons, each of a quarter of a year. No periodic yearly variation, trend or break is visible.

Stability in time

The analysis has been performed in the seasonal binning that has been introduced before in Section 4.1.1, to search for time-dependent structures in $R_{e^-/p}$. Figure 4.13 shows the dipole components, scaled to their statistical uncertainty, for the lowest energy bin of 16 to 350 GeV in galactic coordinates. The results for all energy ranges are shown in Appendix B.3, Figures B.12 to B.16. The analysis reveals no anomalies above expected statistical variations. Figure 4.14 shows the seasonal analysis in GSE, where an anomaly towards east-west and forward-backward has been observed. The time-dependent study confirms the constant shift to negative values in the east-west component, but the significance is decreased with respect to the time integrated fit due to the reduced sample size. In the forward-backward direction, the deviation from zero is even less visible, showing the reduced power of the time-dependent analysis. Appendix B.4, Figures B.17 to B.21, show that the dipole components fitted in the time integrated analysis can be confirmed also with the seasonal analysis for all energy bins. In the less abundant positrons, this was not possible. The observation excludes systematic sources of the anomaly with time scales larger than the seasonal binning, as it would be the case for changes in the detector operation or aging. Here a trend or break should be visible. If the anomalie's strength becomes comparable to the statistical variation, even a yearly modulation would be visible, which is not the case. A time variation on a smaller time basis, for example daily, weekly, or monthly cannot be excluded with this type of observation and will be discussed later in Chapter 5 in the view of the absolute anisotropies.
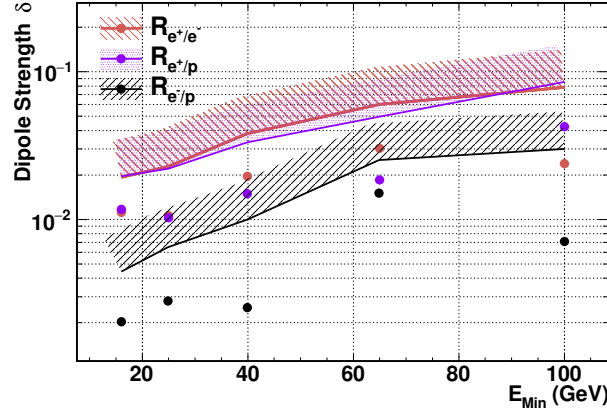
Figure 4.15.: Summary of results in the search for relative anisotropies in R_{e^+/e^-} (red), $R_{e^+/p}$ (blue) and $R_{e^-/p}$ (black) in **GAL** with minimum energy in a cumulative binning. The reconstructed dipole strength is shown with markers. No significant deviation from anisotropy has been found in any of the measurements, an upper limit on the maximum dipole strength is stated at a credible interval of 95% using the Bayes construction (lines).

Conclusion on relative anisotropies

Putting the results of relative anisotropies in positrons and electrons together, no large scale anisotropy of galactic origin could be found and limits were set, matching the expectation given from available number of signal events. Figure 4.15 shows a summary of the three observables R_{e^+/e^-}, $R_{e^+/p}$ and $R_{e^-/p}$, with the fitted dipole strength in energy and the exclusion limit for a dipole anisotropy at a credible interval of 95%. It also shows the robustness of the analysis as two independent reference maps give the same result for positrons. On the other hand observations in the electron analysis demand for a deeper understanding of the GSE system, where a deviation from isotropy is evident for low energies. Also, visible patterns in the maps of significances in GTOD could be found in cases where protons have been used as reference particle, which indicates a systematic limit of the relative analyses with growing sensitivity.

Both, anomalous observations in GSE and GTOD, motivate the need for new methods for the search of anisotropies, which will be discussed in the following Sections 4.2 and 4.3. The usage of low rigidity protons for the search of rigidity-dependent anisotropies has been developed as a validation measurement for the proton *IsoSkyMap*. It is limited to higher rigidities above the geomagnetic cutoff and is only able to detect strong energy-dependent variations in an astrophysical signal.

4.2. Low rigidity protons as reference for high rigidity protons

The analysis applied in Section 4.1 cannot be adopted to the search of anisotropies in protons or other particles for which no reference particle can be selected in equal acceptance and sufficient statistics. The measurement of the angular direction in protons is of interest to study the origin of the hardening in the flux of protons and helium at rigidities greater than 100 GV, published by AMS in [5] and [6]. To study this kind of

R_{Min} (GV)	$N_p^{Sig}(\times 10^5)$	$\delta_{Exp}^{95\%}$
80	38.44	0.26%
150	12.31	0.47%
300	3.49	0.88%
500	1.34	1.42%
1000	0.30	3.02%

Table 4.3.: Number of selected protons within full tracker range acceptance in the signal samples in cumulative binning with upper rigidity limit of 1800 GV. The expected limit $\delta_{Exp}^{95\%}$ at a 95% credible interval originates from the mean of the limit distribution for the given number of signal protons.

problems, where an energy-dependent point source contribution to the isotropic flux is assumed, the angular direction of the point source component can be set in relation to the angular distribution of arrival directions at a different energy. Of course, this kind of study is constrained to particles where no energy-dependent bias to the measurement introduced by the detector is present, which excludes electrons or positrons from the analysis due to the high energy-dependence in the TRD and ECAL selection.

The analysis is applied to protons, selected following Section 3.3.2, which is a different sample definition compared to the *background* protons used in the relative analysis of positrons and electrons. Only protons with rigidity measured in the fullspan tracker range are selected in order keep the geometrical acceptance constant for all rigidities. A limiting factor is the lower rigidity border which needs to be set high enough to be above the maximum geomagnetic cutoff from which a position-dependent modulation of the flux is introduced, as discussed in Section 3.3.4. With a safety margin, this gives a reference sample starting at 40 GV. The upper edge of the reference range is set to 80 GV, to be of comparable sample size to the full signal sample with an upper edge of 1800 GV, as used in [5]. In this range, the reference sample contains $N_{p^*}^{Ref} \approx 9.53 \times 10^6$ low rigidity protons p^* and $N_p^{Sig} \approx 3.84 \times 10^6$ high rigidity protons to search for a signal. Results are quoted in cumulative bins of rigidities above 80, 150, 300, 500, 1000 GV. Event numbers for the signal sample are given in Table 4.3, together with the limit $\delta_{Exp}^{95\%}$, to be expected in the isotropic case.

A first check to perform, before the analysis is done in the proposed way, is to search for any systematic effects in the *signal-free* GTOD coordinate system. If any variation in the detector's performance or acceptance with rigidity is present, characteristic features are expected to be enhanced in this frame. Figure 4.16 shows the significance map S_{p/p^*} in GTOD for the lowest rigidity bin with R_{Min}=80 GV and a higher one with R_{Min}=500 GV. With a bigger gap between the reference and the signal bin, any anomaly introduced by the detector should grow. The sensitivity, on the other hand, decreases with the sample size. No features from unequal acceptance or coverage are visible in either of the maps. The distribution of the significances are reasonably well described by a Gaussian distribution in shape. As already observed before, the width of the distributions is smaller 1, indicating correlations between the samples, which flatten statistical fluctuations. In fact, the significance distribution for the lower rigidity bin matches more the expected distribution. As a further check, a dipole fit has been performed in this coordinate system, as well. Even though the result has no physical meaning, the fit is more sensitive
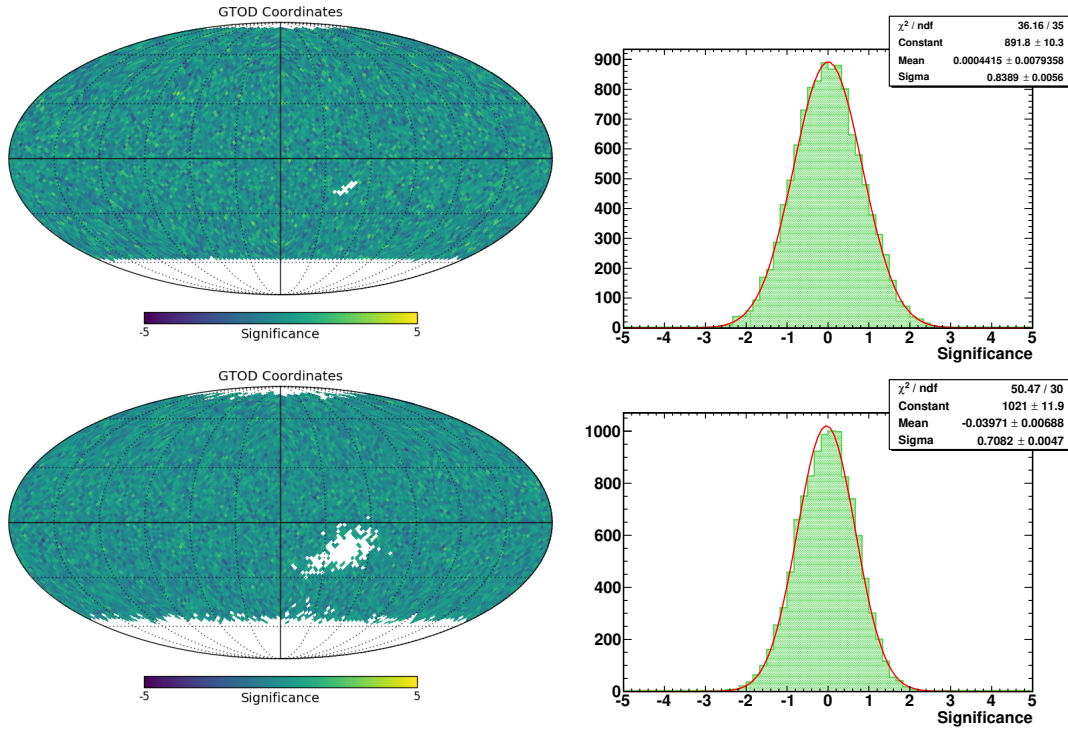
Figure 4.16.: Significance map and distribution S_{p/p^*} of protons over low rigidity protons in **GTOD** coordinates for two bins of cumulated rigidity with R_{Min}=80 GV (top) and R_{Min}=500 GV (bottom). Both maps are divided into 12288 pixels. No evidence of any anisotropy, as deficit or excess of high rigidity protons with respect to low rigidity protons can be seen. The significance distributions are reasonably described by a Gaussian function (red lines), with a normalized $\chi^2 \approx 1.00$ and $\chi^2 \approx 1.68$. Both distributions are fitted with a width smaller than 1, implying correlations between data and reference map.

to a large scale deviation from isotropy. The fitted components with rigidity scaled to their fit uncertainty are shown on the left-hand side of Figure 4.17, without significant deviation from the isotropic expectation.

The fit in galactic coordinates is shown on the right-hand side in Figure 4.17. The result is in agreement with the isotropic hypothesis for all rigidity bins. The raw fit results can be found in Appendix B.5. For the lowest rigidity bin of 80 to 1800 GeV a limit on the dipole strength in galactic coordinates of

$$\delta_{p/p*}^{95\%}(> 80 \text{ GV}) = 0.22\%$$

is set in agreement with the statistical expectation. As already mentioned, the analysis has been invented primarily as validation for the absolute result, which will be discussed in the next Section 4.3.

Also in the R_{p/p^*} observable, a fit in GSE is performed. The components with rigidity scaled to their fit uncertainty are shown in Figure 4.18 with a significant deviation from the isotropic expectation mainly in the forward-backward component pointing away from the sun. Also, east-west and north-south are deviating from isotropy, but with low significance. This is remarkable since the result in the other coordinate systems show no evidence of the presence of any signal. The anomaly is different compared to the one observed in $R_{e^-/p}$, which points in negative east-west and negative forward-backward
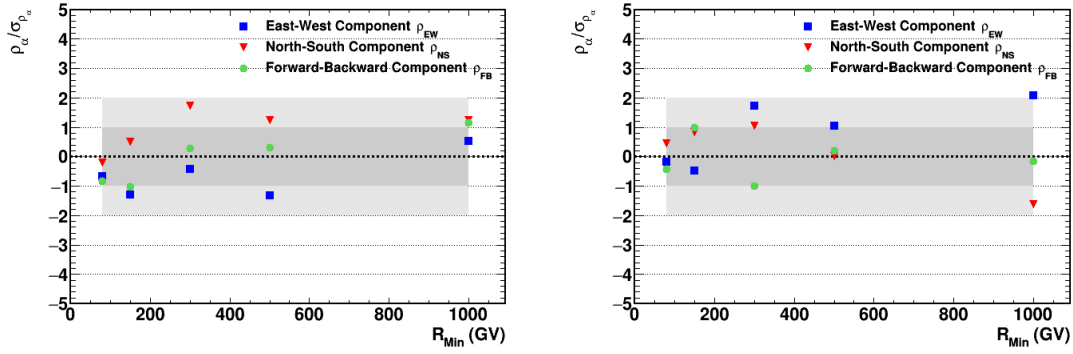
Figure 4.17.: Fitted dipole components of R_{p/p^*} scaled to their fit uncertainty in **GTOD** (left) and **GAL** (right). Both show no significant deviation from the isotropic expectation in any component.
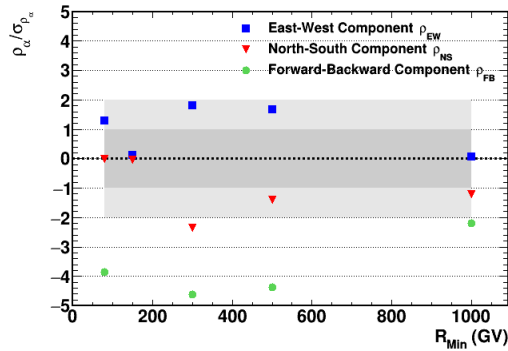
Figure 4.18.: Fitted dipole components of R_{p/p^*} scaled to their fit uncertainty in **GSE**. A significant excess above two standard deviations can be seen in mainly the Forward-Backward component pointing away from the Sun for all rigidities. At 150 GV the excess is greater than 5σ. The absolute fit values will be shown in comparison to the absolute results in Chapter 5 and can be found in Appendix B.6.

direction, but is studied at different energies. The charge sign-dependent anomaly in east-west direction, which is negative for electrons and positive for protons could arise from the Sun's magnetic field, in which the particles are bent to opposite directions. However, the presence of a dipole signal in protons would also affect the relative electron measurement where protons are used as reference. A discussion on the GSE coordinate system will be given in Section 5.1. The presence of the excess describes a dependence of the particles angular distribution on the celestial sphere in rigidity and should not be misinterpreted as an absolute signal. Also, it cannot be stated without further studies if there is an over-abundance of protons with lower energy towards the Sun or an over-abundance of high rigidity protons in direction away from the Sun. Understanding the signal in GSE requires an absolute anisotropy measurement from a simulation of the isotropic sky.

Stability in time

For the study of the time-dependence, the lowest rigidity sample from 80 to 1800 GV has been divided into the same 20 seasonal bins used before. For protons, the provided sample size is much larger than for electrons and positrons, but in this specific analysis also the minimum energy is higher. This results in a comparable sensitivity to the
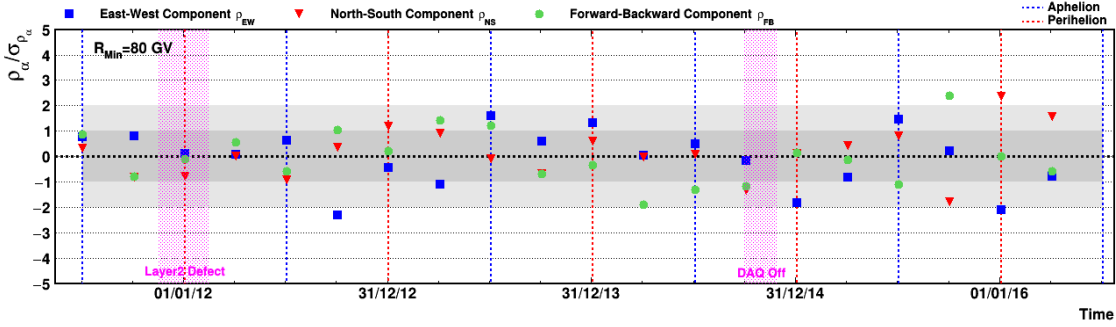
Figure 4.19.: Time evolution of the scaled dipole components in **GAL** for R_{p/p^*} in the full rigidity range from 80 to 1800 GV. The 5 years sample has been divided into 20 seasons, each of a quarter of a year.
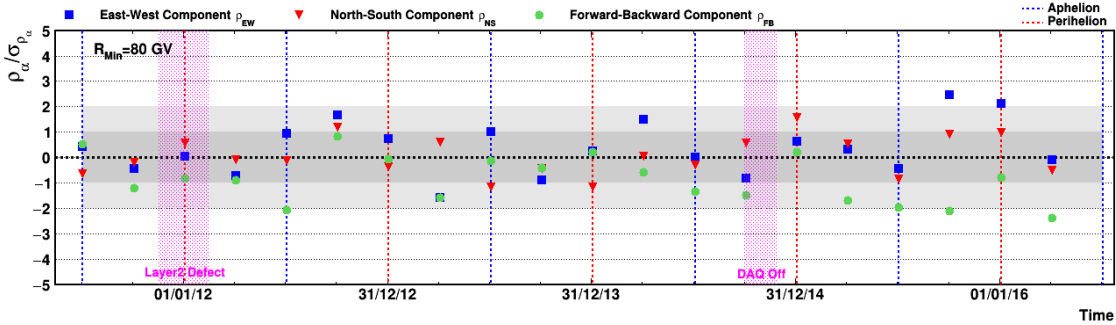
Figure 4.20.: Time evolution of the scaled dipole components in **GSE** for R_{p/p^*} in the full rigidity range from 80 to 1800 GV. The 5 years sample has been divided into 20 seasons, each of a quarter of a year.

electron time analysis. Figure 4.19 shows the time evolution of the fitted dipole components in galactic coordinates without any visible break, trend or yearly modulation. In the last year, fluctuations become huge and exceed two standard deviations. In this time period, the solar activity is higher than before, which might be an explanation. To conclude on this behavior, more data in the following time needs to be monitored. The absolute dipole components are shown in Appendix B.5, Figures B.22 to B.26. The same behavior is present in GSE, shown in Figure 4.20. The significance of the anomaly in forward-backward direction away from the sun is reduced but visible as shift. The absolute fit values with time agree with the time integrated analysis, as shown in Appendix B.6, Figures B.22 to B.26. The forward-backward direction follows a slight trend towards higher negative values in time. If this trend is assumed to be constant an increase in the forward-backward component of 0.0012/year with a variance of 0.0007/year is fitted with a normalized $\chi^2 \approx 0.079$ (in comparison of $\chi^2 \approx 0.088$ in the constant fit). A reason could be the increased solar activity in the last two years of operation, as evident from Figure 3.32.

Conclusion on the relative proton anisotropy

The search of anisotropies relative in proton rigidity shows interesting features and bears a strong motivation to further study proton anisotropies. As a first point, it is remarkable that AMS-02 is able to measure particles in a constant acceptance and efficiency over the large rigidity interval from 40 to 1800 GV, allowing for this type of analysis at all. In galactic coordinates, dipole anisotropies with a strength of more than
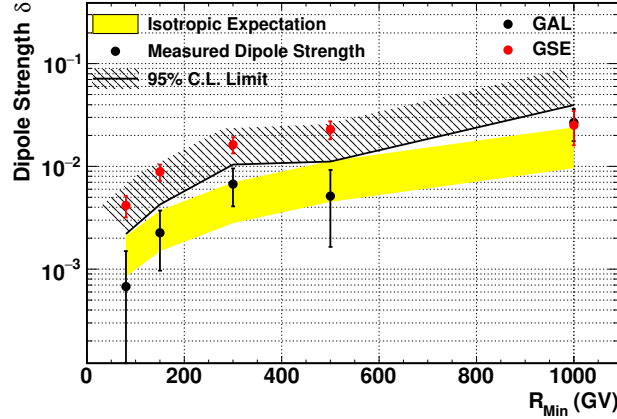
Figure 4.21.: Summary of results in the search for anisotropies in protons with low rigidity protons as reference. The reconstructed dipole strength in galactic coordinates (black points) together with the limit on the maximum dipole strength is stated at a credible interval of 95% using the Bayes construction (line). In GSE (red) the reconstructed dipole strength is larger than the expectation from the number of selected protons, which would be the same as in galactic coordinates in case of isotropy. No limit can be set. A significant signal excess is observed in mainly forward-backward direction pointing away from the Sun.

0.2% could be excluded. In Figure 4.21 the results of the search for anisotropies in protons with low rigidity protons as a reference is summarized. No evidence of a galactic dipole anisotropy could be found and a limit is set. The fitted dipole strength in GSE exceeds the isotropic expectation by more than 2σ. A detailed discussion of this result will be given in the light of absolute proton anisotropies in Chapter 5.

4.3. Absolute anisotropies

The basic formalism to construct a reference map for the measurement of absolute anisotropies, referred to as *IsoSkyMap*, has been introduced in Section 3.2.4. The *IsoSkyMap* is our best estimate of what an isotropic sky would look like to AMS-02 for a given particle selection and data taking time. In the description, the need for a position and time-dependent correction factor to account for unstable detector performance has been mentioned, but not motivated. Without it, the created map is just the detector's livetime projected on the celestial sphere. This simple but insufficient construction is called *livetime map*. The cuts defining a *good second*, described in Section 3.3.4, were specifically chosen to ensure optimal and stable working conditions for the detector such that *livetime map* already gives good results up to some precision. Figure 4.22 shows the significance map for positrons and protons in the lowest energy bin compared to their corresponding *livetime map* in GTOD coordinates. The map of proton significance is shown in 12288, positrons in 768 HEALPix pixels. A larger binning in the positrons compensates for the lower sample size compared to protons. Both maps show structures, visible by eye, which mainly follow the geomagnetic field, as it will be shown. It will be argued that these structures originate from the non-perfect description by the *livetime map*, namely from the disregard of variations in the detector's performance with position and time.
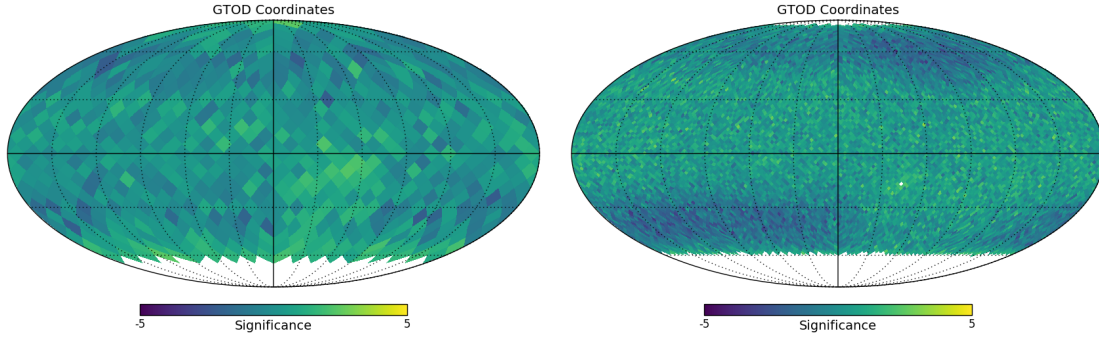
Figure 4.22.: **Left:** Significance map $S_{e^+/Livetime}$ of positrons with energy greater than 16 GeV in **GTOD**, plotted with 768 pixels. **Right:** Significance map $S_{p/Livetime}$ of protons with rigidity greater than 18 GeV in **GTOD**, plotted with 12288 pixels. Both maps show clear deviations from isotropy with similar morphology. The number of protons is much higher, making the deviations more significant and even visible in the finer binning.
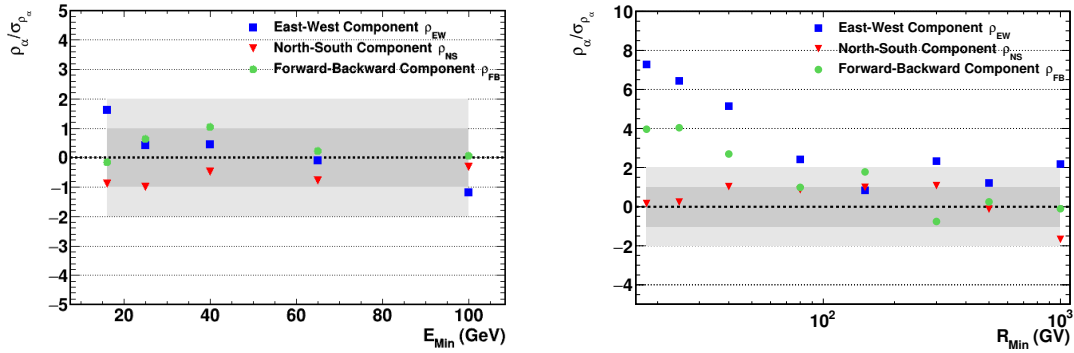
Figure 4.23.: Fitted dipole components of $R_{e^+/Livetime}$ (left) and $R_{p/Livetime}$ (right) scaled to their fit uncertainty in **GAL**. The positron fit is in agreement with isotropy, even with the usage of the *livetime map* and significant structures in GTOD. For protons the precision of the *livetime map* is not sufficient and anisotropies introduced by the detector are recovered. In the east-west component the deviation exceeds more than 5σ.

Even though the *livetime map* shows large discrepancies in the *signal-free* GTOD coordinates, its precision is already sufficient to produce results in agreement with isotropy for positrons in galactic coordinates. This is due to the low statistics in the positron sample and the fact that detector effects get washed out up to a certain degree in the galactic coordinate system, due to rotations of the detector. The fitted dipole components for the fit of $R_{e^+/Livetime}$ for positrons and $R_{p/Livetime}$ for protons scaled to the fit uncertainty in galactic coordinates are shown in Figure 4.23. The fit of $R_{e^+/Livetime}$ in the low abundant positrons already reveals an isotropic result. For the higher numbers of electrons and protons, a more precise description is needed. By artificially reducing the number of electrons to $N_{Red.}$ and fitting $R_{e^-_{N_{Red.}}/Livetime}$, one can estimate that the *livetime map* approach gives isotropic results up to a sensitivity of about 1% for electrons and positrons, which corresponds to a maximum of 120.000 events.
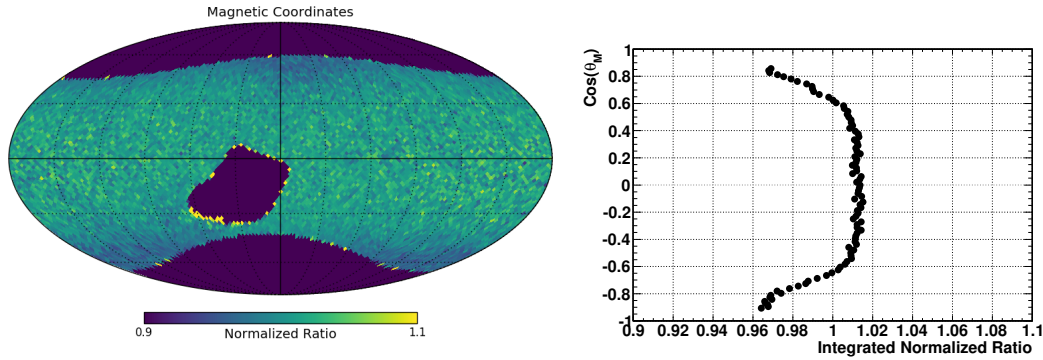
Figure 4.24.: **Left:** Normalized ratio of $R_{p/Livetime}$ at ISS position in geomagnetic coordinates for rigidities greater than 18 GV. **Right:** The same quantity as a function of geomagnetic latitude.

Rate correction for *IsoSkyMaps*

The visible structures at the north-west and the southern polar regions, seen in Figure 4.22, are expected to originate from a loss in detector performance, which is mainly dominated by the rate of low energetic particles, modulated by the geomagnetic field. To emphasize that the visible structures are indeed aligned with the geomagnetic field, the geomagnetic coordinate system is used. Figure 4.24 shows the normalized ratio $R_{p/Livetime}$ of proton counts over the *livetime map* at the detector's position in geomagnetic coordinates. The projection of the same quantity to the magnetic latitude $\cos(\theta_M)$ is shown aside.

The particle rate is expected to be constant with the detector's position at energies above the geomagnetic cutoff. Below this energy, particles get deflected by the Earth's magnetic field, and the rate of low energetic particles increases with the geomagnetic latitude. The rise of the low energetic particles flux causes the livetime per second to decrease from the high trigger rate, which is taken care of in the *livetime map*. However, also the detector's performance suffers under the increased particle rate causing efficiencies to drop. From the variation in the projected normalized ratio $R_{p/Livetime}$ on the right-hand side of Figure 4.24, an average variation in efficiencies of about 6% towards the geomagnetic poles is to be expected for protons.

A straightforward approach to address these saturation effects is to apply the $R_{p/Livetime}$ map directly as a weight for the particle rate in a second iteration at the creation of the reference map. By construction, relative differences between the *livetime map* and the data would be flattened in the *signal-free* map. In this case, the result can be biased towards isotropy, and a possible signal might be removed. To minimize such a bias, the projection on the geomagnetic latitude is applied as correction function. The idea is that the physical process causing the drop in detector performance only depends on this variable. By removing any latitudinal dependence, the external particle rate would be perfectly modeled. The usage of the geomagnetic latitude simplifies the two-dimensional position to a one-dimensional variable which is not correlated to any expected signal. The ratio function is applied in the construction of the isotropic sky map as a position-dependent weight factor. In the following, this procedure is called rate correction. The improvement with the rate correction is visible by eye when comparing Figure 4.22 to Figure 4.25. The GTOD system still is not perfectly described by the *IsoSkyMap*, as evident from the significance distribution on the right-hand side in Figure 4.25.
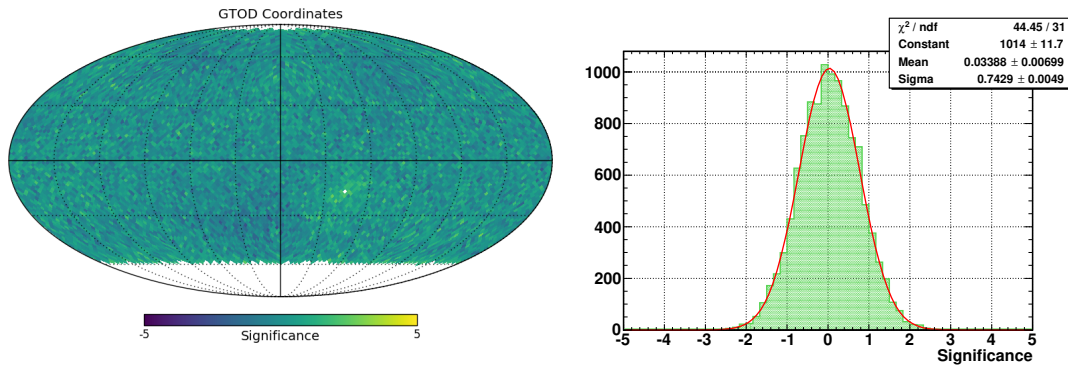
Figure 4.25.: Significance map and distribution $S_{p/IsoSky}$ of protons with rigidity above 18 GeV in **GTOD**. The difference to Figure 4.22 is evident. The significance distribution is reasonably well described in shape by a Gaussian function (red line) with a normalized $\chi^2 \approx 1.43$. The Gaussian is slightly shifted from zero and has a width smaller than one, indicating that the *IsoSkyMap* does not describe the GTOD system perfectly.

To get a handle on the performance of the *IsoSkyMap*, the high statistics protons are studied first. In this process, the precise knowledge of the correction that is applied to account for time and position-dependent variations in detector performance is the crucial point in the analysis. Only after the proton absolute anisotropy has been proven to be under control, the method is applied to electrons and positrons for which less sensitivity is needed due to the smaller sample size.

4.3.1. Proton absolute anisotropy

With the proton selection presented in Section 3.3.2, about 51 million protons with rigidity greater than 18 GeV are available in full tracker span. Due to the greater sensitivity the minimum rigidity is slightly increased, in comparison to the electron and positron analysis, to exclude influences by the east-west effect. The protons are selected in the same rigidity binning used in the flux publication [5]. The binning matches the rigidity resolution of the Tracker. In the full rigidity range from 18 to 1800 GV, the data is binned into 43 rigidity layers in the layered fit procedure described in Section 4.1. *IsoSkyMaps* are produced in the same binning and use only events from the same rigidity bin. Results are stated in a cumulative binning with maximum rigidity R_{Max}=1800 GV at the minimum rigidities of R_{Min}=18, 25, 40, 80, 150, 300, 500, 1000 GV. The number of selected events in the cumulative rigidity bins is given in Table 4.4, together with the number of layers in a bin and the limit to be expected in case of isotropy from the number of selected protons. The expected limit in the full rigidity range is $\delta_{Exp}^{95\%} \approx 0.07\%$.

The starting point of the analysis is the *IsoSkyMap* produced with the rate correction described before. In general the rate correction is time and rigidity-dependent, which means the correction function is produced for every layer in a seasonal binning. During the production of the *IsoSkyMap*, the geomagnetic latitude is read from the database and the value of the rate correction in the corresponding season and rigidity layer is evaluated. The value is used as a weight factor together with the livetime in the second. Every second N=100 incoming directions are drawn from the list of events such that $N/s \gg R(t)$ is by far fulfilled. Varying the number of events per second has no measurable effect above N>5. Also, the time and rigidity-dependence of the rate correction is of small contribution in the galactic coordinates, where such effects are washed out

R$_{Min}$ (GV)	N$_{Layers}$	N$_p^{Sig}$($\times 10^5$)	$\delta_{Exp}^{95\%}$
18	43	512.12	0.07%
25	39	314.28	0.09%
40	33	133.75	0.14%
80	23	38.44	0.26%
150	15	12.31	0.47%
300	8	3.49	0.88%
500	4	1.34	1.42%
1000	1	0.30	3.02%

Table 4.4.: Number of selected protons used in the absolute anisotropy analysis within fullspan tracker acceptance in cumulative binning with upper rigidity limit of 1800 GV. The expected limit $\delta_{Exp}^{95\%}$ at a 95% credible interval originates from the mean of the limit distribution for the given number of selected signal protons.
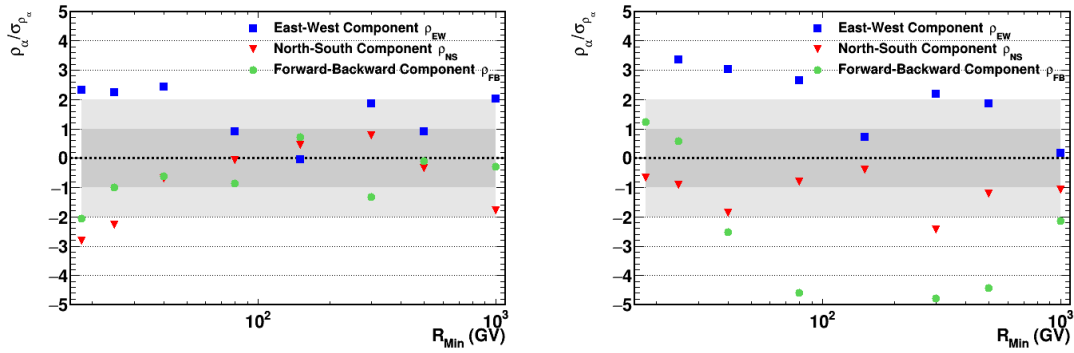
Figure 4.26.: Fitted dipole components of $R_{p/IsoSky}^{Rate}$ with rigidity scaled to their fit uncertainty in **GAL** (left) and **GSE** (right).

by the detector's movement and rotation. Still, in the case of a signal, it is desired to describe the *signal-free* coordinate systems GTOD and MAG as good as possible. In Figure 4.25, it has already been shown that the GTOD coordinate system is not described perfectly by the *IsoSkyMap*. It will be shown in Section 4.3.1.2 that remaining structures correlate with short term modulations of the geomagnetic field, which the proposed one-dimensional correction cannot cover. Figure 4.26 shows the result of a dipole fit of $R_{p/IsoSky}^{Rate}$ in galactic coordinates and GSE. For the lowest rigidity bins, where the sample size is high, significant deviations from isotropy are evident. In GSE a deviation from the isotropic expectation is observed to be even stronger.

The significance of the deviation from the isotropic hypothesis is again evident in the reconstructed dipole strength, shown in Figure 4.27, especially in GSE. Here a constant excess above the yellow band of isotropic expectation is anomalous. The main direction, however, shows a transition from mainly east-west below 80 GV, and forward-backward above. In galactic coordinates a converging of the dipole amplitude at 1‰ is evident in all rigidities with sensitivity below this level. The origin of this anomaly will be discussed in Section 4.3.1.2 The absolute fit values can be found in Appendix B.7 for the galactic coordinates, and in Appendix B.8 for GSE.

The following sections address the investigation of the results presented in $R_{p/IsoSky}^{Rate}$. As
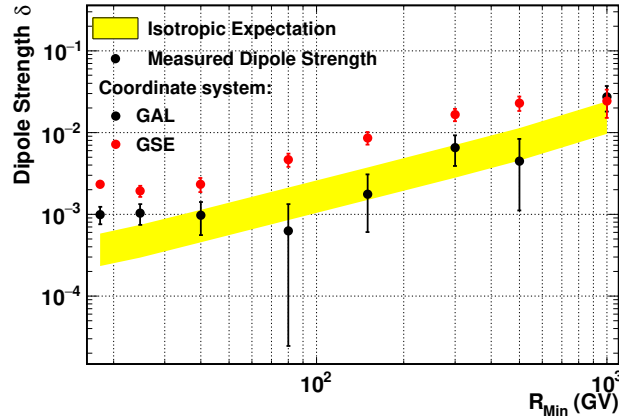
Figure 4.27.: Measured dipole strength δ with rigidity for the fit in $R^{Rate}_{p/IsoSky}$ in **GAL** (black markers) and **GSE** (red markers).

discussed, the rate correction might be biased towards isotropy and can hide or weaken an astrophysical signal. To make the *IsoSkyMap* more robust against this bias, the selection efficiencies are studied. Also, the cause of the drop in detector performance towards the geomagnetic poles can be investigated in this way.

4.3.1.1. Efficiency evaluation

The efficiencies of the cuts used in the selection of protons, described in Section 3.3.2, are evaluated as a function of the geomagnetic latitude. In a complementary approach, the trigger-rate as discussed from Figure 3.2 has been used as one-dimensional parametrization, with similar results. The variable, however, is not estimated accurately by the DAQ system, such that a model variable like the magnetic latitude is preferred for the analysis in comparison to the measured variable of trigger-rate.

To calculate the efficiency for a single cut, a control sample of the same particle type is selected using cuts which do not use measurements of the sub-detector under study. The efficiency is then calculated by applying the cut to study as last cut. This method, called *tag-and-probe*, requires a set of cuts which can select a pure sample of the particle, without introducing correlations with the cut under study. For AMS-02 this translates in the assumption that the different sub-detectors are uncorrelated, which is not true. Correlations between sub-detectors, mainly introduced in the reconstruction of physics objects, can hardly be avoided, as for example the TRD track is used to cluster hits in the Tracker layer one and two. In a flux analysis, cut efficiencies are evaluated in the calculation of the effective acceptance from Monte-Carlo simulated events and a correction factor from data, describing the same efficiency, is applied. The advantage of the *tag-and-probe* procedure is that it allows to study cut efficiencies on data, which is necessary to study position and time-dependent effects not described in Monte-Carlo simulations.

The single cut efficiencies, listed in Figure 3.24, are evaluated in 40 bins of cosine the geomagnetic latitude in the range of $\cos(\theta_M) = -1, +1$, where -1 is the southern geomagnetic pole. A bin of geomagnetic latitude forms a ring along the longitude. The *IsoSkyMap* is generated in the same layers of energy used in the fit later-on. The global value of the efficiencies does not have an impact on the normalized ratio in Equation 3.1, which means that the overall efficiency offset is not contributing to the fit, but only the
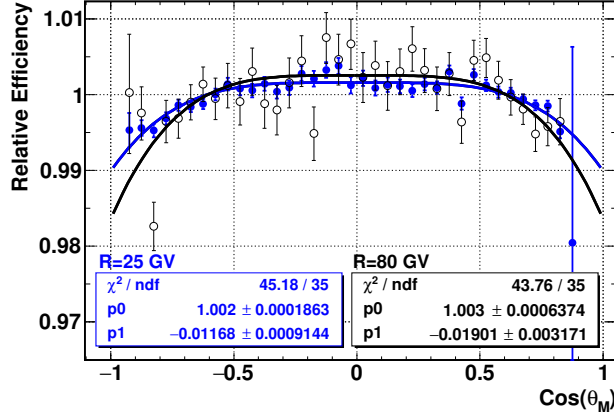
Figure 4.28.: Relative trigger efficiency, as divided by its global mean value, at rigidities of 25 (blue) and 80 (black) GV for protons as function of the cosine in geomagnetic latitude. The dependencies have been parameterized by functions $f(\cos(\theta_M)) = p0 + p1 \times x^4$ (lines) which describe the latitudinal dependence with a normalized fit χ^2 close to one. The decrease towards the geomagnetic poles originates from the increasing particle rate entering the detector, similar to the rate correction.

relative variation. The same is true for a time-dependence of efficiencies which is taken into account by producing the maps in bins of season and normalizing to the available data in this season. Figure 4.28 shows the normalized trigger efficiency of protons at 25 and 80 GV as a function of $\cos(\theta_M)$, as an example. The normalized efficiency is the efficiency in a bin of latitude divided by the global efficiency and is used in the comparison of efficiencies at different energies or for different cuts. With the normalization, the impact of the trigger efficiency at 25 and 80 GV can be compared directly, even though they are not flat as a function of energy. The dependence on the magnetic latitude is significant, and can be understood from the high rate of low energetic particles towards the magnetic poles such that the TOF trigger saturates. It becomes more likely to get an ACC veto from the multiple particles entering the detector from the side. With the normalized efficiency, several correction functions, from different cuts, can be applied independently in the creation of the *IsoSkyMap*, without changing the overall normalization.

The efficiencies in Figure 4.28 are parameterized by a function $f(\cos(\theta_M)) = p0 + p1 \times x^4$ which sufficiently describes the latitudinal dependence with a normalized fit χ^2 close to one. The parameter $p1$ describes the evolution of the latitude dependence and is called *bending parameter*. This parameter alone quantifies the latitudinal dependence of a correction function and is useful in the determination of the energy and time-dependence.

Variations of the cut efficiencies are studied separately using the pull in energy

$$P_E(cos(\theta_M)) = \frac{\varepsilon\{\Delta E, \cos(\theta_M)\} - \langle\varepsilon\{\cos(\theta_M)\}\rangle}{\sigma_\epsilon\{\Delta E, \cos(\theta_M)\}} \quad , \tag{4.2}$$

or time

$$P_T(cos(\theta_M)) = \frac{\varepsilon\{\Delta T, \cos(\theta_M)\} - \langle\varepsilon\{\cos(\theta_M)\}\rangle}{\sigma_\epsilon\{\Delta T, \cos(\theta_M)\}} \quad , \tag{4.3}$$

where $\epsilon\{\Delta T, \cos(\theta_M)\}$ is the efficiency in a single bin of magnetic latitude and time ΔT, integrated over the energy, and $\epsilon\{\Delta E, \cos(\theta_M)\}$ in energy ΔE, integrated in time.
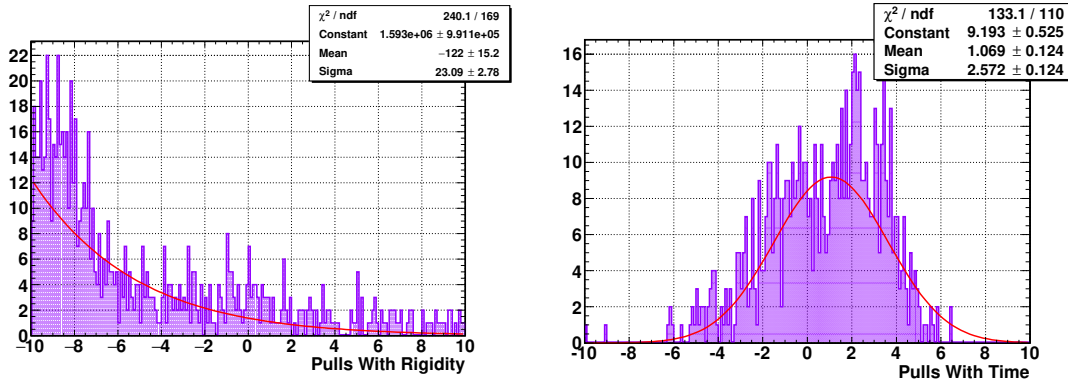
Figure 4.29.: Pull distribution for the rigidity **(left)** and time **(right)** evolution in the geomagnetic latitudinal dependence of the proton trigger efficiency. Both distributions are constructed using Equations 4.2 and 4.3. Both distributions cannot be described by a Gaussian: A variation with rigidity and time is evident.

$\langle \epsilon \{\cos(\theta_M)\} \rangle$ is the global efficiency, integrated in time and energy of the same magnetic latitude bin. The difference is normalized to the statistical uncertainty of the test quantity, as the uncertainty of the integrated one is negligible. If no dependence in time or energy in the latitude is present, the efficiencies $\epsilon\{\Delta T/\Delta E, \cos(\theta_M)\}$ fluctuate around the global mean, for every bin of latitude θ_M. In case of statistical fluctuations, the pull follows a Gaussian centered around zero with a width of one. If a time or energy-dependence is present, the pull values in every bin of latitude θ_M will be off the mean and the pull distribution is shifted from zero and has a larger width.

For protons the energy is replaced by the rigidity measurement from the Tracker. The pull distributions of the rigidity and time evolution of the proton trigger efficiency is shown in Figure 4.29. Both distributions are far from being Gaussian which means that a dependence on time and rigidity in this quantity needs to be taken into account in the analysis. A rigidity-dependence is already evident from Figure 4.28. The correction function from the trigger efficiency is created for every rigidity layer and time bin, in which the *IsoSkyMap* is produced.

All cuts in the proton selection are studied in the same manner and probed for their rigidity and time-dependence of the longitudinal dependence. The procedure also takes into account, if the global value of an efficiency is time or rigidity-dependent, which is not necessarily correlated to a variation of the latitudinal dependence with time or rigidity. Table 4.5 gives a summary of the proton cuts. A cut is described by the global average bending, quantified with the bending parameter, and whether or not the latitudinal variation depends on the rigidity or time, tested with the distribution of the pull. Most cut efficiencies vary with time or rigidity. In these cases, the bending parameter varies, which is why the average is shown. If a correction does not depend on time or rigidity, it can be calculated in a time or rigidity integrated interval to improve the precision. However, even if time and rigidity-dependence is included in the creation of the *IsoSkyMap*, the impact on the result in galactic coordinates is suppressed but is of importance in the other coordinate systems, which has already been seen for the rate correction.

Table 4.5 also shows that mainly two cuts contribute to the latitudinal dependence: The trigger efficiency and the external Tracker layer one hit efficiency. The trigger efficiency and its dependence on the external particle rate has already been discussed. For Tracker

Name of cut	Average bending parameter p_1 (%)	Dependent on	
		rigidity	time
Proton Trigger	-1.0	✓	✓
Good Inner Track	-0.1	✓	✗
Hit in Tracker Layer 2	-0.3	✓	✓
Good TOF	-0.1	✗	✗
TOF Charge	-0.1	✗	✗
Tracker Charge	-0.0	✗	✓
Mass Cut	-0.5	✗	✗
Hit in Tracker Layer 1	-1.5	✓	✓
Hit in Tracker Layer 9	-0.1	✓	✓
Good Fullspan Track	-0.2	✓	✓

Table 4.5.: Summary of the cut efficiency of protons selected in the full Tracker acceptance for the usage in the *IsoSkyMap*. The naming of the cuts follow the one used in Figure 3.24. To get an estimate of the longitudinal dependence, the average bending parameter is given in %. A ✓ marks, if the longitudinal dependence varies with rigidity or time. A ✗ marks absence of such a dependence. In these cases the correction can be calculated in a time or rigidity integrated interval to improve the precision.

layer one, which is above TRD and directly exposed to the environmental conditions, the pickup of a clean hit gets more difficult with additional noise. To improve the matching of a hit, TRD's standalone tracking capabilities are used for layer one, and also layer two hits. TRD is most sensitive to the increased rate of low energetic particles, for the large volume and its position on top of the detector. This sensitivity has been discussed in Section 3.3.4.2 and is used to identify seconds in which the geomagnetic field is disturbed. The usage of the TRD in the hit finding in Tracker layers one and two is an example where an unexpected correlation is introduced between sub-detectors.

In Figure 4.30, the combined efficiency corrections, as product of the single cut efficiencies, for protons integrated in time and rigidity above 18 GeV is plotted together with the rate correction. Variations with time and energy are small compared to the systematic difference between the rate and the efficiency approach, which differs by about a factor of two. The main reason could be the requirement of hits in tracker layer one and two where TRD is involved in the track reconstruction. This introduces a correlation between the sub-detectors and the efficiency is overestimated. Another contribution not taken into account might come from the finite rigidity resolution that cannot be studied as a function of the magnetic latitude but only on Monte-Carlo simulated data. The difference between rate and efficiency correction will be propagated as a systematic uncertainty.

Figure 4.31 shows the fit components with rigidity of a dipole fit in galactic coordinates of protons over the *IsoSkyMap* with efficiency correction $R_{p/IsoSky}^{Eff}$ in comparison to the rate corrected map $R_{p/IsoSky}^{Rate}$. The fit components for both maps are in good agreement, especially if the disagreement in the two correction functions in Figure 4.30 are remembered. This can be explained by the observation that detector effects get washed out in the galactic coordinate system to some level. The difference gives an estimate on the accuracy with which the correction function needs to be known.
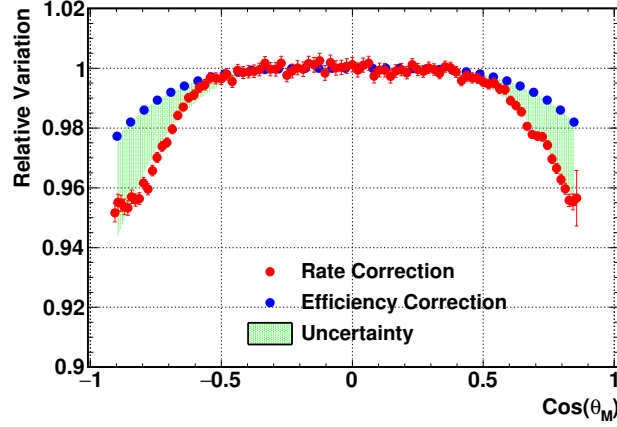
Figure 4.30.: Geomagnetic latitudinal correction for protons with rigidity greater than 18 GV obtained from the first-order rate correction (red) and the efficiency evaluation (blue). The mismatch between both methods, marked by the green area, is propagated as a systematic uncertainty.
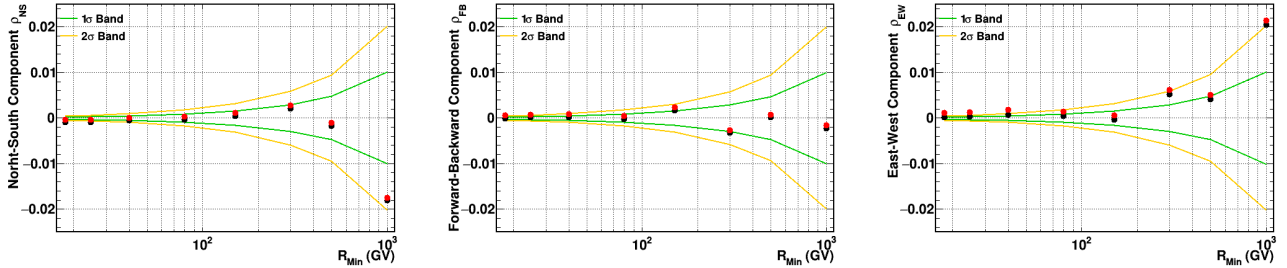
Figure 4.31.: Fitted dipole components of $R_{p/IsoSky}^{Eff}$ (red) with rigidity in comparison to $R_{p/IsoSky}^{Rate}$ (black) in **GAL**. Both fits are in good agreement.

It should be noted that both, the rate correction and the efficiency correction, alone are not robust:

- The rate correction might be biased towards isotropy and can hide or weaken an astrophysical signal present in the geomagnetic coordinate system, but the *true* correction might be smaller[2]. The rate correction would over-correct.

- The efficiency correction is blind to such an astrophysical signal, but correlations between sub-detectors, that cannot be removed, compensate for one another and a *true* correction would be larger. The efficiency correction is an underestimation.

Both points lead to the conclusion that a *true* correction function exists in-between the rate and efficiency correction. This area is marked green in Figure 4.30 and will be propagated as a systematic uncertainty. In such a study also the influence of the shape of the correction function will be investigated.

4.3.1.2. Evaluation of systematic uncertainties

To study uncertainties introduced in the construction of the *IsoSkyMap*, the stability of the result is studied under the variation of parameters which are expected to be sensitive

---

[2]Otherwise a signal would not be hidden, but enhanced.
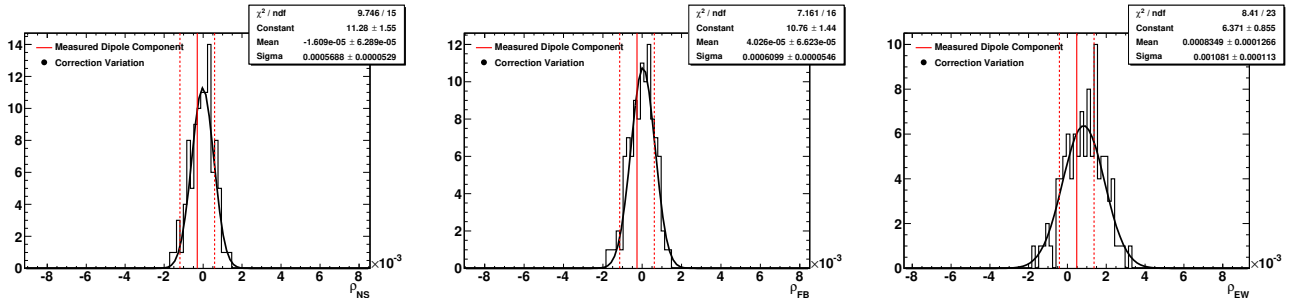
Figure 4.32.: Distributions of three dipole components ρ_α from the correction variations, for protons with rigidities greater 80 GV. The solid red line represents the fit result from $R_{p/IsoSky}^{Rate}$, with the fit uncertainty as red dashed line. The distributions are well fitted by a Gaussian function.

to systematic effects introduced by the detector. Most certainly, the biggest impact on the result will be introduced by the correction function in magnetic latitude. There is some disagreement between the two independent methods to calculate corrections, namely the rate and efficiency correction. The uncertainty, originating from the correction, has to be quantified. Also, the influence of the correction functions shape will be studied.

In addition, the stability of the fit with the cut on the TRD performance has to be investigated. The cut has been introduced to exclude seconds of a turbulent geomagnetic field, which is directly linked to solar activity. It has to be understood if this requirement alone can change the outcome of the fit results, in particular in GSE. As a third factor, the stability of the result with changing temperature has to be studied. Variations in temperature might have effects on the detector's performance, which is decoupled from the geomagnetic field and therefore not accounted for in the analysis.

For an isotropic result, it is not easy to quantify the uncertainty, originating from the discussed sources, as the variation from statistical uncertainty is large and expected to be the dominant effect. If the sample is divided to study the dependence of a single factor the sensitivity scales with the sample size and might mimic a dependence on the parameter. For the observed anomalies in GSE, the stability of the signal strength above the isotropic expectation is a valuable observation and can be tested to be stable independently of the sample size, as long as the excess is greater than the sensitivity.

Uncertainty in latitude corrections

The fundamental assumption in the proposed correction, as a one-dimensional function with the geomagnetic latitude, is that loss in detector performance is mainly dominated by the external low energetic particle rate, modeled by the geomagnetic field. However, if unforeseen environmental effects, which are not aligned with the geomagnetic field, have an influence on the performance or are cut away by specific requirements, the correction function can have breaks, an asymmetry or might be deformed in other ways. Variations alongside the geomagnetic longitude are not covered in this parametrization. Most likely, they would be washed out by the Earth's rotation, as argued in Section 3.1.1.5, at least if they persist on long timescales.

To get an estimate of the impact of the correction function on the fit result, the correction is varied within the systematic uncertainty band, shown in Figure 4.30, without any restrictive conditions. E.g., breaks or asymmetries are fully allowed, even though they
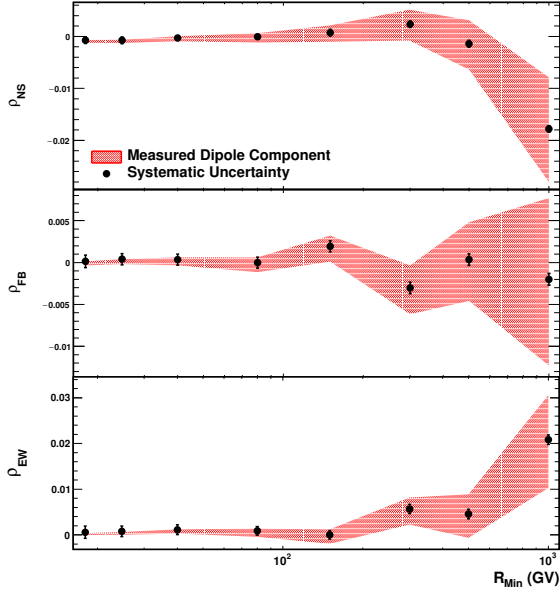
Figure 4.33: Dipole components ρ_α, from correction variation, with rigidity for protons in **GAL**. The red band represents the fit result with fit uncertainty from $R^{Rate}_{p/IsoSky}$. The black points show the mean and width of the distributions of ρ_α from the 100 simulated correction functions. The width of the distribution is stated as a systematic uncertainty on the dipole component. No shift in the position of the dipole components absolute value is observed.

would be hard to justify, from a physics perspective. In a range from -1 to 1, correction points are created in constant steps, uniformly within the systematic uncertainty band. In this way, 100 random correction functions are created. Between the points, a linear interpolation is done, in order not to smooth out breaks and kinks. From the simulated correction functions, *IsoSkyMaps* are produced and fitted to the data. From these fits, distributions of the three dipole components ρ_α are created. The ρ_α distributions from the correction variations, for protons with rigidities greater 80 GV, are shown in Figure 4.32 as an example. From the width of the ρ_α distributions, the systematic uncertainty on the dipole components is estimated. With decreasing sample size towards higher rigidities, the fit is less sensitive to the correction function and the statistical uncertainty dominates. Figure 4.33 shows a comparison of the systematic uncertainty estimation of the fit components and their statistical uncertainty for protons in galactic coordinates. The mean values of the dipole components from the correction variation do not change with respect to the fitted dipole components from $R^{Rate}_{p/IsoSky}$, which shows the stability of the $R^{Rate}_{p/IsoSky}$ result.

From the systematic uncertainty on the dipole components, the dipole amplitude expected from the finite knowledge of the correction function alone is estimated. Measured dipoles with amplitude smaller than this estimation are seen to originate from the reference map, rather than a signal in data, even if they exceed the statistical expectation. A systematic limitation of the method is quantified. The estimation of the systematic limitation is done in a toy Monte-Carlo approach: The distribution of dipole amplitudes introduced by the systematic uncertainty alone is created by drawing dipole components from a Gaussian distribution centered around zero and width of the systematic uncertainty of the component. From the distribution of dipole amplitudes the 95% quantile is stated as the systematic limitation.

The left-hand side of Figure 4.34 shows the dipole amplitudes from the absolute proton anisotropy $R^{Rate}_{p/IsoSky}$ in galactic coordinates with the systematic limitation included. The systematic limitation is found at the per mille level, and describes the sensitivity which can be reached with the proposed methods. The numerical values are quoted in Table B.7 together with the fit results and the systematic uncertainty on the dipole compo-
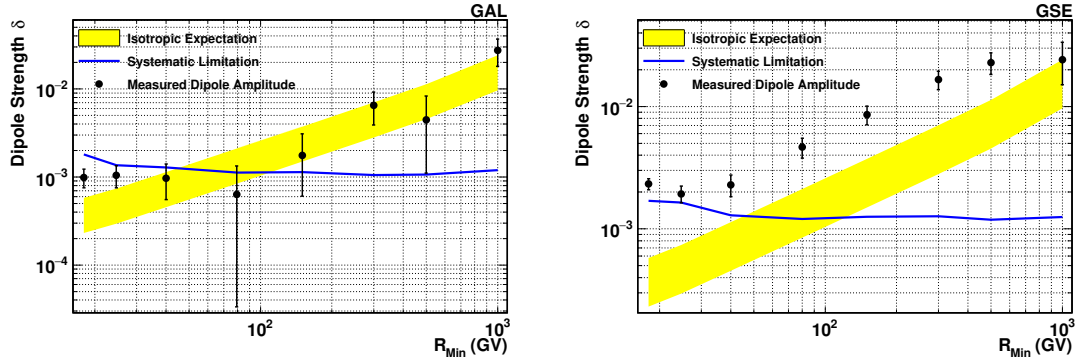
Figure 4.34.: The reconstructed dipole amplitude for $R^{Rate}_{p/IsoSky}$ in **GAL (left)** and **GSE (right)**. The yellow band represents the statistical expectation of the measurement in case of isotropy, the blue line is the estimation up to which level a dipole amplitude can be introduced by the one-dimensional correction function in magnetic latitude, quoted as a systematic limitation. In galactic coordinates the reconstructed dipole amplitude exceeds the expectation from the number of selected protons but stays below the systematic limitation. It is assumed, that no astrophysical signal is recovered, but a feature in the *IsoSkyMap*. The fit would be able to measure an astrophysical signal if it is stronger than the recovered dipole strength, such that a limit can still be constructed with the fit result. In GSE the dipole amplitude exceeds the systematic limitation. The excess cannot be explained by the reference map, an issue that will be addressed in the following Sections.

nents. Ideas to improve the analysis in order to reduce the systematic limitation will be discussed in Section 5.4.

Figure 4.35 shows the systematic uncertainty on the dipole components in GSE coordinates. The correction function affects the components differently compared to the galactic study shown before. Deviations from isotropy in positive east-west in the lowest rigidity bins, and forward-backward towards higher rigidities are not affected by the correction function in geomagnetic latitude, and persist. A conclusion on this behavior could be that a one-dimensional correction along the geomagnetic latitude is not sufficient and other effects introduced by the detector play a role. However, the measurement with the independent reference map R_{p/p^*} shows a similar anomaly, at least above 80 GV. The systematic limitation on the dipole amplitude in GSE is shown on the right-hand side of Figure 4.34, together with the dipole amplitudes from the absolute proton anisotropy $R^{Rate}_{p/IsoSky}$.

The systematic analysis of the one-dimensional correction function explains the excess of the dipole strength in galactic coordinates above the isotropic expectation to be introduced by the reference map. The anomaly in GSE is found to persist above the level of systematic limitation. The strength of the dipole increases with rigidity but not in significance. The dipole amplitude that is stated as a result describes the dipole over an isotropic component, which is normalized to one. Therefore, the dipole does not get stronger, in a sense that more particles from the dipole direction reach the detector, but only dominates more over the isotropic background,which in absolute values decreases exponentially.

In the following the stability of the measured dipole strength will be tested by varying cuts that are directly related to the Sun. In this way, a correlation to such a variable
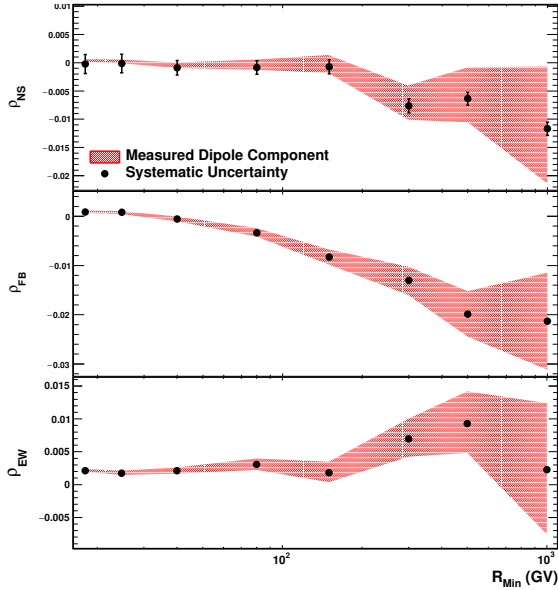
Figure 4.35: Dipole components ρ_α, from correction variation, with rigidity for protons in **GSE**. The red band represents the fit result with fit uncertainty from $R_{p/IsoSky}^{Rate}$. The black points show the mean and width of the distributions of ρ_α from the 100 simulated correction functions. The width of the distribution is stated as a systematic uncertainty on the dipole component. No shift in the position of the dipole components absolute value is observed. A deviation from the isotropic expectation in east-west and forward-backward cannot be explained by the systematic uncertainty.

might be identified to find a technical explanation for the anomaly.

TRD performance

The cut on the TRD hits normalized to hits in the inner Tracker (TrdN) has been introduced in Section 3.3.4, to remove unstable seconds where low energetic particles flood the upper part of detector and reconstruction efficiencies drop. Figure 4.36 shows the position of these seconds, which represent only 4 % of the measuring time, in GTOD. An extended cluster of bad seconds is visible south-west of the SAA and towards the poles. The distribution of the TrdN value was shown in Figure 3.31. To understand the impact on the fit result, the cut is scanned systematically from 10 to 1, removing more and more of the tail towards low TrdN values.

To understand the impact in the *signal-free* GTOD coordinate system, a dipole fit is performed in GTOD. On the left-hand side of Figure 4.37, the dipole amplitude δ is shown with rigidity for the different TrdN cuts. It can be seen that the dipole amplitude converges towards lower values, and therefore isotropy, when the cut is strengthened. The signal mainly originates from the ρ_{FB} component, as it would be expected from Figure 4.36. The fraction of removed events is small, except for TrdN<1, where the fit uncertainty is significantly increased, but the effect on the fitted dipole strength is significant. The cut used in the analysis is TrdN<1.4. Also in galactic coordinates an effect is evident. The right-hand side of Figure 4.37 shows the same study in GSE. The signal is stable among the independent subsamples with high statistical uncertainty.

The study shows that the TrdN cut is indeed efficient in removing bad seconds in which the Earth's magnetic field is deformed and low energetic particles flood the detector up to a level where the efficiency drops, with strong impact in GTOD. In GSE however, the excess is stable with the solar activity. In galactic coordinates the dipole strength increases with loosening the TrdN cut.

Solar beta angle

The solar beta angle is one of the most influencing factors on the temperature environment of a satellite. A sketch to support the explanation of β^{Sun} can be found in Figure
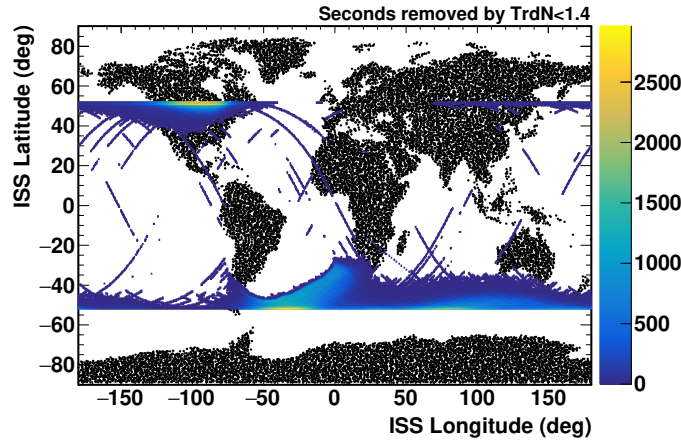
Figure 4.36.: Map of seconds with bad TRD performance, removed by a cut on TrdN<1.4. In total about 4% of measuring time are removed. It has been discussed in Section 3.3.4 that the cut is highly time-dependent. The TRD performance is mostly affected towards the polar region and around the SAA, but also some single orbits of bad TRD performance are removed.
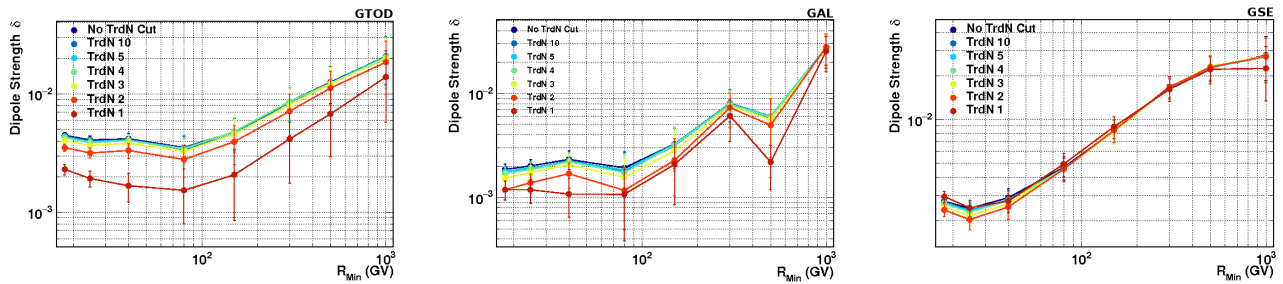
Figure 4.37.: Reconstructed dipole strength δ from the fit to $R^{Rate}_{p/IsoSky}$ with increasingly restrictive cuts on TrdN in GTOD, GAL, and GSE. In GSE, the dipole strength converges towards lower values with a stronger cut on TrdN. In GAL, the dipole strength decrees as well, but is subject to the high statistical fluctuations because no dipole signal above the statistical expectation is present, as for GTOD and GSE. In GSE the dipole strength stays constant and the dipole anomaly is recovered independently of the TrdN cut value.

4.38, together with the variation of the ISS beta angle β^{Sun}_{ISS} for one year. Being the angle between the orbit plane and the sun vector, β^{Sun} describes the fraction of time the satellite is directly exposed to the sun and from which direction. A β^{Sun} of zero means that the orbital plane is aligned with the sun vector, making the sun always shining from the side. The satellite is exposed relatively equally to the sun from all directions and spends some time shadowed by the Earth. An angle of $\beta = \pm 90°$ means that the satellite will not be shadowed by the Earth at all and will be completely illuminated from the top, or bottom direction. The ISS reaches β^{Sun}_{ISS}-angles from about -70° to +70°, as shown on the right-hand side of Figure 4.38. For AMS-02 a high negative β^{Sun}_{ISS} results in low temperatures, while an extreme positive β^{Sun}_{ISS} causes a stable and high temperature. For $\beta_{ISS} \approx 0$, the thermal interaction with the ISS is most complex.

For the alignment of the AMS-02 sub-detectors, the beta angle has the biggest impact [180]. It is obvious that this variable is correlated to the sun and might reflect in GSE. To check the stability of the result, the data was split into three independent subsamples of
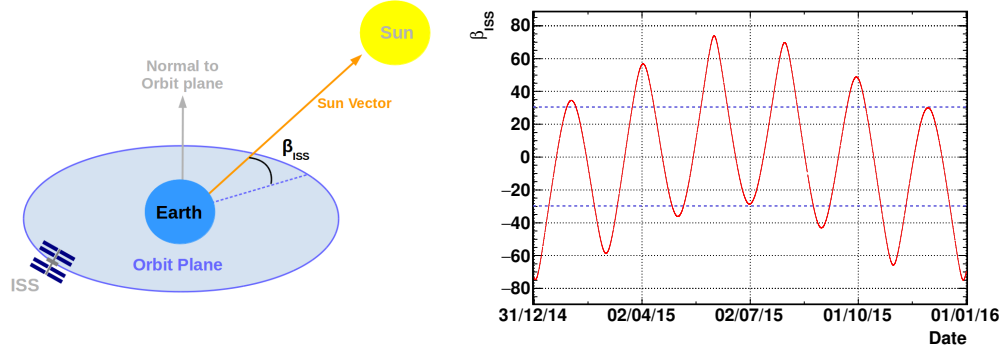
Figure 4.38.: The ISS beta angle β_{ISS}, as angle between the ISS orbital plane and the sun vector (**Left**). The beta angle is one of the most influencing factors on the temperature environment of a satellite. **Right:** ISS beta angle β_{ISS} for the year 2015. A modulation on a basis of one month can be identified, overlaid with a longterm yearly modulation. The data has been split in three independent subsamples of $\beta_{ISS}^{low} < -30$, $\beta_{ISS}^{high} > 30$ and $\beta_{ISS}^{moderate}$ in-between indicated by the blue dashed horizontal lines.

$\beta_{ISS}^{low} < -30$, $\beta_{ISS}^{high} > 30$ and $\beta_{ISS}^{moderate}$ in-between. The sample size is highly reduced, in particular for the low and high β_{ISS} subsample, but both are able to recover the anomaly. The resulting dipole strength is shown in Figure 4.39.

In conclusion, the result is stable under the strongest variations of the detector's environment described by the ISS solar beta angle and the TRD performance cut. Both are powerful studies to gain confidence in the result, which will be discussed in Chapter 5.

Discussion of AMS-02 day-night cycle

The study on the stability of the result with the solar beta angle only covers long term temperature variations on timescales of several days. To study temperature variations from the AMS-02 day-night cycle on timescales shorter than one orbit the GSE longitude can be used. The detector experiences day and night once every orbit of 94 minutes, which comes together with temperature variations up to 90 degrees on the outside of the detector, depending on the solar beta angle. Since the GSE system cannot be assumed to be *signal-free* a rate correction approach to flatten the particle rates with the day-
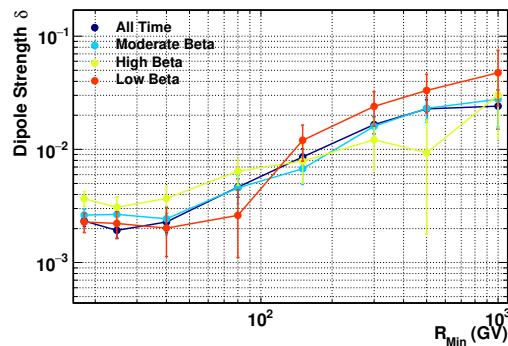
Figure 4.39.: Dipole strength δ of fit to $R_{p/IsoSky}^{Rate}(\beta)$ in **GSE**. The data has been divided in subsamples of moderate, high and low beta angle. The signal is stable among the independent subsamples with high statistical uncertainty.
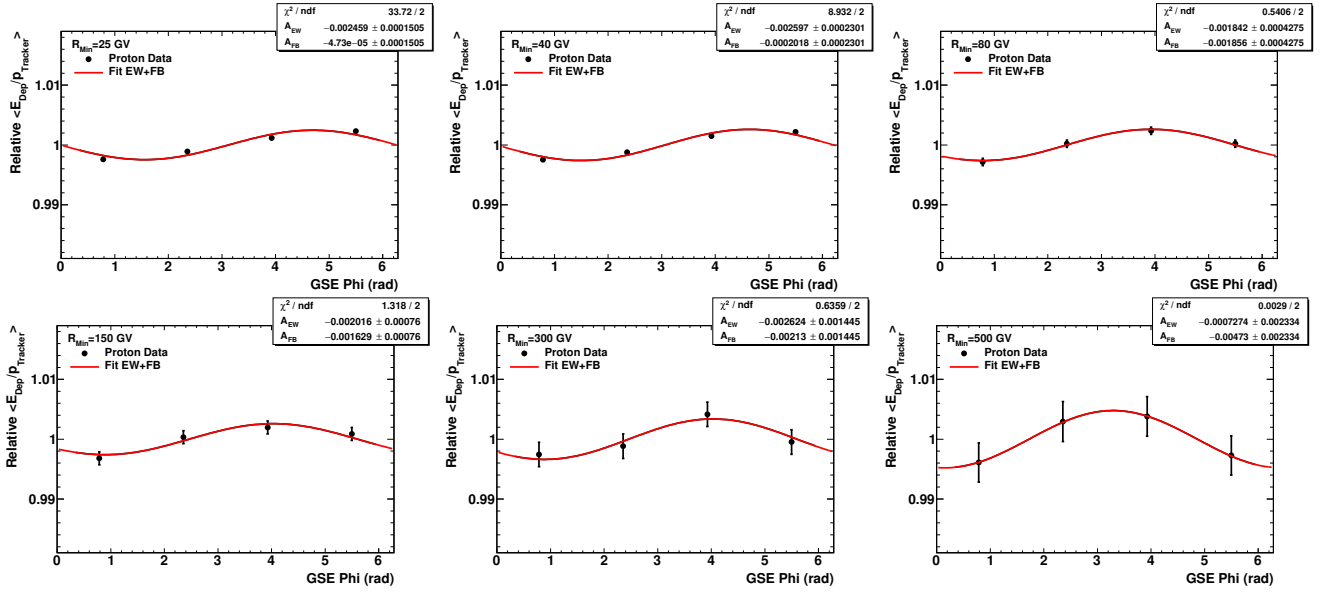
Figure 4.40.: Relative position of the mean $E_{\text{Dep}}/p_{\text{Tracker}}$ variable as a function of the GSE incoming direction projected on the equatorial plane for bins of minimum rigidity of 25, 40, 80, 150, 300, and 500 GV with a maximum rigidity of 1800 GV. The variation in GSE is significant and has been parameterized with a function $f(\phi_{GSE}) = 1 + A_{EW} \times \sin(\phi_{GSE}) + A_{FB} \times \cos(\phi_{GSE})$, equivalent to the expansion in east-west and forward-backward direction used in the dipole analysis. An approximately constant east-west variation with a strength of about 0.2 to 0.3% is evident. In addition, a variation in forward-backward direction rising with rigidity is found.

night cycle cannot be applied and variables need to be studied directly as a function of the longitude in GSE. Effects arising from the orbit are expected, but do not influence previous particle flux analyses done with AMS-02, which focused on flux measurements integrated over time. Time and orbit dependent effects were never studied in such detail as needed in the presented analyses.

In the AMS-02 proton flux analysis [5], a significant contribution to the systematic uncertainty arises from the uncertainty on the rigidity scale, which is sensitive to the alignment and the field strength of the magnet, which varies with temperature. To study the Tracker rigidity scale, the ratio of the ECAL energy deposit over the Tracker rigidity $E_{\text{Dep}}/p_{\text{Tracker}}$ for minimum ionizing particle (MIP) protons is studied as a function of the GSE longitude Φ_{GSE} projected on the ecliptic plane. The analysis sample are fullspan protons, selected following Section 3.3.2, within ECAL acceptance and less than 350 eV of energy deposit. Figure 4.40 shows the relative mean $E_{\text{Dep}}/p_{\text{Tracker}}$ as a function of the GSE longitude Φ_{GSE} projected on the ecliptic plane for six bins of minimum rigidity. The relative variation is parameterized with a function $f(\phi_{GSE}) = 1 + A_{EW} \times \sin(\phi_{GSE}) + A_{FB} \times \cos(\phi_{GSE})$. The parametrization is equivalent to the dipole expansion in east-west with $A_{EW} \equiv \rho_{EW}$ and forward-backward direction with $A_{FB} \equiv -\rho_{FB}$.

A small and constant variation in east-west direction is evident, and a forward-backward component A_{FB} rises with rigidity. The observation is interpreted as a variation of the rigidity scale with the AMS-02 day-night cycle. A shift in the rigidity scale affects the spillover fraction at high rigidities, as introduced from Figure 3.23, which directly removes particles from the analysis. A rigidity-dependent anisotropy would be introduced as observed in the fit to $R_{p/IsoSky}^{Rate}$ and R_{p/p^*}. In Figure 4.41 the comparison between the
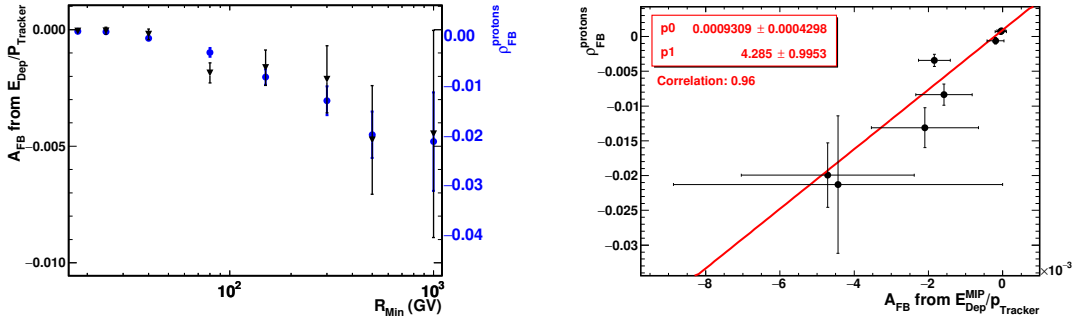
Figure 4.41.: Strength of the Tracker rigidity scale variation in GSE forward-backward direction A_{FB}, as defined in Figure 4.40, with rigidity in a cumulative binning with maximum rigidity of 1800 GV (black markers). In blue markers the result of the dipole component ρ_{FB} of $R_{p/Isosky}^{Rate}$ in GSE is shown with different y-axis, plotted in blue. Both follow the same trend in rigidity. The observation is interpreted as a shift in the Tracker rigidity scale with the AMS-02 day-night cycle which causes a deficit of high rigidity protons due to spillover.

variation in the rigidity scale A_{FB} and the GSE forward-backward component ρ_{FB} from the fit of $R_{p/Isosky}^{Rate}$ is shown as a function of the minimum rigidity. The different y-axis is equivalent to a linear transformation of the type $\rho_{EW} = \alpha + \beta \times A_{EW}$ between the Tracker rigidity scale variation and the fit components. Both variables follow the same trend with rigidity and are heavily correlated, as shown in the scattered plot on the right-hand side of the same figure.

To confirm that the observed variation in the GSE longitude is indeed introduced by the Tracker, the ECAL energy scale has to be studied separately to exclude the energy deposit as the cause of the variation. For this study, the energy deposit E_{Dep}^{MIP} of MIPs in ECAL are used. The E_{Dep}^{MIP} peak position, determines the ECAL energy scale. Figure 4.42 shows the energy deposit in eV of MIP protons, selected as background protons following Section 3.3.1, with a rigidity from 100 to 350 GeV. The distribution is parameterized by a lognormal function and peaks at around 198 eV. The position of the E_{Dep}^{MIP} peak with rigidity is shown aside. The variable is studied as a function of the GSE longitude Φ_{GSE} projected on the ecliptic plane. Figure 4.43 shows the relative position of the E_{Dep}^{MIP} peak as a function of the GSE longitude Φ_{GSE} projected on the equatorial plane for three bins of rigidity. The relative peak position is defined as the peak position in a bin of Φ_{GSE} divided by its global mean from Figure 4.42. The variation is again fitted with the same function as before with the parameters $A_{EW} \equiv \rho_{EW}$ and $A_{FB} \equiv -\rho_{FB}$. An approximately constant variation in east-west direction of about 0.27% without significant forward-backward variation is evident. In summary, a variation constant with energy in the ECAL energy scale in GSE east-west direction is found. Independently of ECAL, a variation of the Tracker rigidity scale towards higher rigidities in GSE forward-backward is identified.

Even though the correlation between the rigidity scale variation and the observed dipole components of the proton analysis in GSE is suspicious, the described study is only of a qualitative manner. To finally settle the observed anomalies in the GSE coordinate system a quantitative analysis of the observations is required. Also, a variable which allows for a separate study of the Tracker rigidity scale without using ECAL would be beneficial. For this task, the TRD could be used. The analysis in the GSE longitude emphasizes the importance of the study and understanding of several coordinate systems,
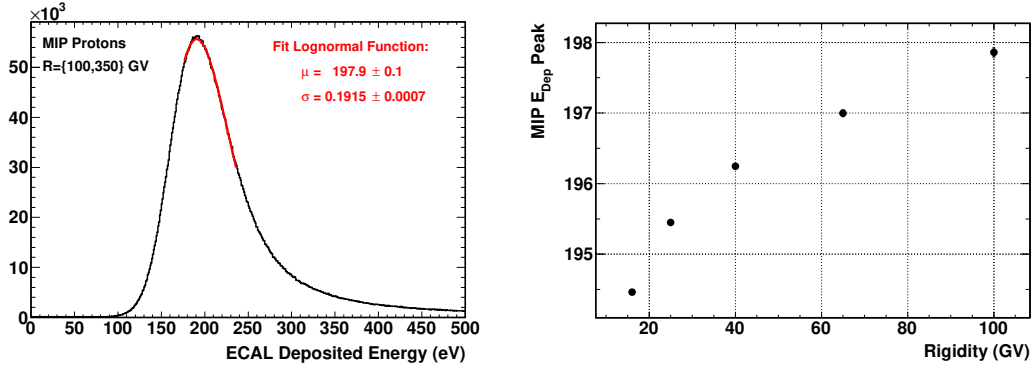
Figure 4.42.: Distribution of the deposited energy of MIP protons $E_{\mathrm{Dep}}^{\mathrm{MIP}}$ in the rigidity range from 100 to 350 GV in ECAL in eV (**left**). The distribution has been parameterized with a lognormal function to evaluate the peak position. The energy deposit, as position of the $E_{\mathrm{Dep}}^{\mathrm{MIP}}$ peak, rises with rigidity, as expected for ionization (**right**).
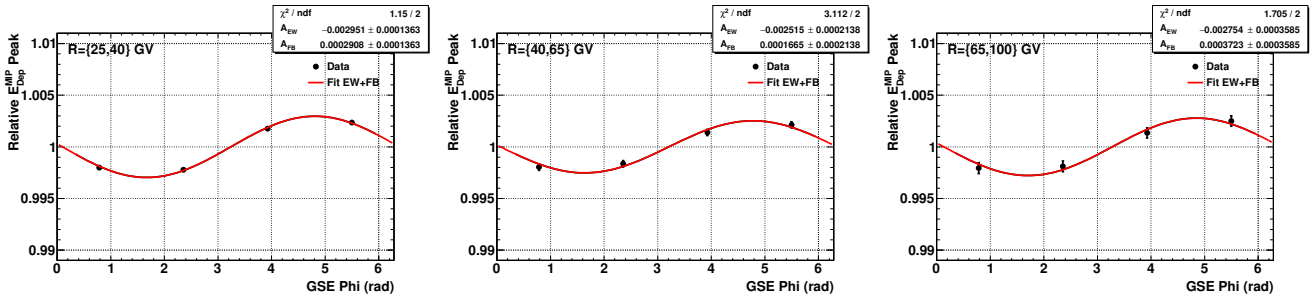
Figure 4.43.: Relative position of the $E_{\mathrm{Dep}}^{\mathrm{MIP}}$ peak, with respect to the overall value shown in Figure 4.42, as a function of the GSE incoming direction projected on the equatorial plane for rigidities of 25-40 GV, 40-65 GV, and 65-100 GV. The variation in GSE is significant. The variation has been parameterized with a function $f(\phi_{GSE}) = 1 + A_{EW} \times \sin(\phi_{GSE}) + A_{FB} \times \cos(\phi_{GSE})$, equivalent to the expansion in east-west and forward-backward direction used in the dipole analysis. An approximately constant east-west variation with strength of about 0.27% is found. In forward-backward direction no significant variation is evident. The observation is explained by a variation of the ECAL energy scale with the AMS-02 day-night cycle.

where different effects are enhanced as argued in Section 3.1.1. To get a full picture of the AMS-02 day-night cycle, the selection efficiencies need to be studied in the GSE longitude, as well. An extended quantitative analysis of the GSE longitude system is beyond the frame of this thesis.

Assuming that the transformation between the Tracker rigidity scale variation A_{FB} and the fitted dipole components ρ_{FB} from Figure 4.41 is the only source of the GSE anomaly, the forward-backward component can be corrected in the fit and a corrected dipole amplitude can be calculated. As argued, a bias towards isotropy might be introduced due to the qualitative manner of the correction. The dipole amplitude of protons $R_{p/Isosky}^{Rate}$ in GSE after correcting for the Tracker rigidity scale variation is shown in Figure 4.44. The correction removes the excess from isotropy for the higher rigidity bins. The excess in the GSE east-west component for protons at low rigidities persists. The east-west variation in the ECAL energy scale can not explain this observation since ECAL is not directly or indirectly involved in the selection of the fullspan proton sample.
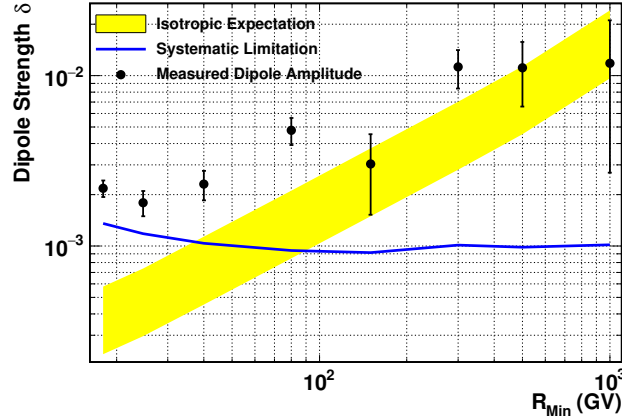
Figure 4.44.: The reconstructed dipole amplitude for $R_{p/IsoSky}^{Rate}$ in **GSE** after correcting for the Tracker rigidity scale variation. The yellow band represents the statistical expectation of the measurement in case of isotropy, the blue line is the estimation up to which level a dipole amplitude can be introduced by the one-dimensional correction function in magnetic latitude, quoted as a systematic limitation. The correction removes the excess from isotropy for the higher rigidity bins. The bin at 80 GV shows a slightly increased excess after the correction, which can be explained by a large deviation from the Tracker rigidity scale variation A_{FB} and the fitted dipole components ρ_{FB} in this bin, evident from Figure 4.41.

A dedicated study on the impact of the observed GSE dipole on the other coordinate systems, especially galactic, has been performed in [154] with the conclusion that the dipole within the ecliptic plane will not reflect in the other coordinate systems. A north-south component, which is not observed, would, however, be shared in galactic coordinates. As a conclusion, the result in galactic coordinates can be reviewed independently of GSE. A weakness in the approach used in [154] is that dipole signals of varying amplitude and direction in time are difficult to study. To include such time-dependent effects, the one-dimensional efficiency correction in the geomagnetic latitude might be dismissed in favor of a two-dimensional efficiency evaluated in the *signal* coordinate system directly. To cure the problem of low event numbers in a two-dimensional binning, the efficiency can be expanded in a dipole, or a multipole through a fit, as used in the later analysis. Methods based on this idea are currently under study but suffer from their own systematic uncertainties, and the robustness against correlations is not straightforward to justify. However, they are expected to potentially reduce the systematic limitation of the one-dimensional correction function.

Stability in time

The analysis in time for the *IsoSkyMaps* is a powerful tool to further access systematic problems in the method. Changes in the detector's operational state show up as a step in the time-dependence. In fact, many of the systematic effects that were described above were found by the time dependent analysis. Maps are produced in the same seasonal binning used before, with the five year data divided into 20 seasons. This also means that any change in the environmental conditions on a shorter time scale than a season cannot be identified.

Figure 4.45 shows the seasonal analysis in galactic coordinates for the rigidity intervals above 18 GV and above 80 GV in their scaled dipole components. In the low rigidity
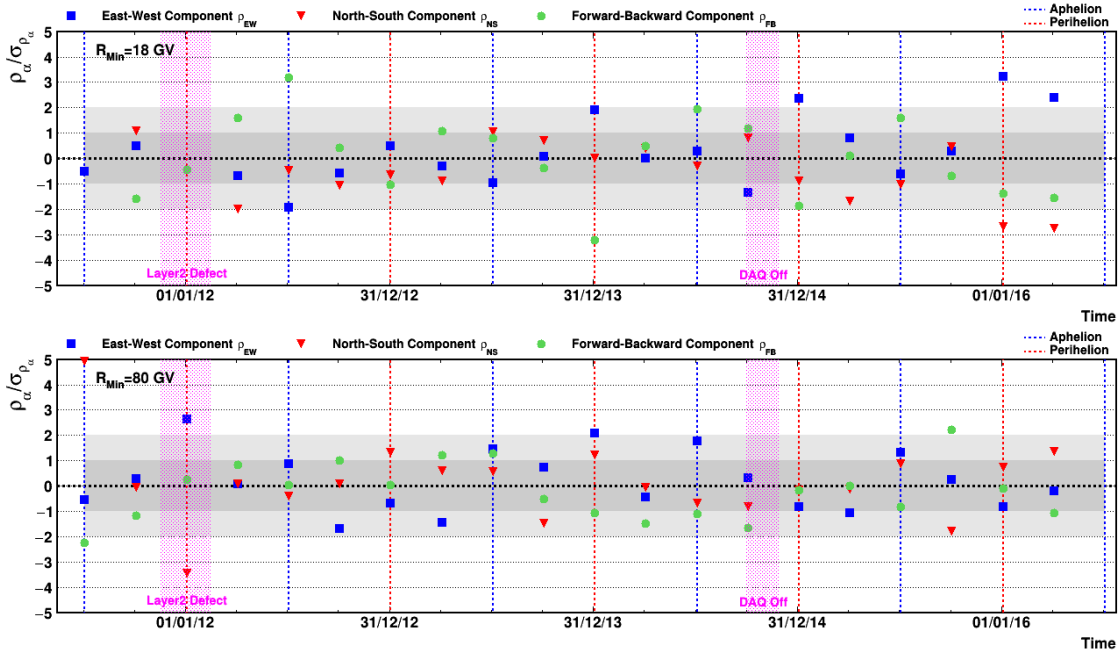
Figure 4.45.: Time evolution of the scaled dipole components in **GAL** for $R^{Rate}_{p/IsoSky}$ in the rigidity range from 18 to 1800 GV **(top)** and 80 to 1800 GV **(bottom)**. The 5 years sample has been divided into 20 seasons, each of a quarter of a year. In the first season, the detector was still in commission phase with unstable configuration which causes fit components to be off scale. In winter 2011, the defect in Tracker layer two caused a change in the acceptance. Also in this bin, fit components are off scale.

analysis, the spread around zero is found to be larger than expected. The analysis seems not to be stable at this rigidity, which is somehow expected from the systematic studies done before. For the 80 GV bin the result is more stable. Common in both analyses is an anomaly in the bin that corresponds to winter 2011. In general, in the first month of AMS-02 operations, the detector and operational conditions were not stable which is troublesome in the creation of the *IsoSkyMap*. In winter 2011 the Tracker layer two showed unstable behavior and some cells were lost, which strongly affected the acceptance, in particular. Starting 2015 the results seem to fluctuate more than before, which has already been mentioned in the seasonal analysis of the relative anisotropies. Here the Sun's activity increased which makes the environment more unstable.

In the lower rigidity ranges, also the constant fit of the seasonal analyses, shown in Appendix B.7 for GAL and Appendix B.8 for GSE in all rigidity ranges, does not reproduce the time integrated results, especially for GSE. This supports the conclusion that deviations from isotropy are of systematic origin being sensitive to the available sample size. Variations in the angular distribution of the incoming direction in GSE need to happen on smaller time scales than the one observed. Figure 4.46 shows the seasonal analysis in GSE coordinates in the same rigidity bins. The observations described in the galactic coordinate system, hold for GSE as well. High fluctuations in the 18 GV bin, in disagreement with the time integrated result, and anomalies in the 80 GV bin.

From the analysis with low rigidity protons as a reference for high rigidity for protons in GSE R_{p/p^*}, a steady trend in the forward-backward component was observed in the 80 GeV rigidity. This observation cannot be confirmed from Figure 4.46.

As the number of protons is high, the analysis was performed in a much smaller time-
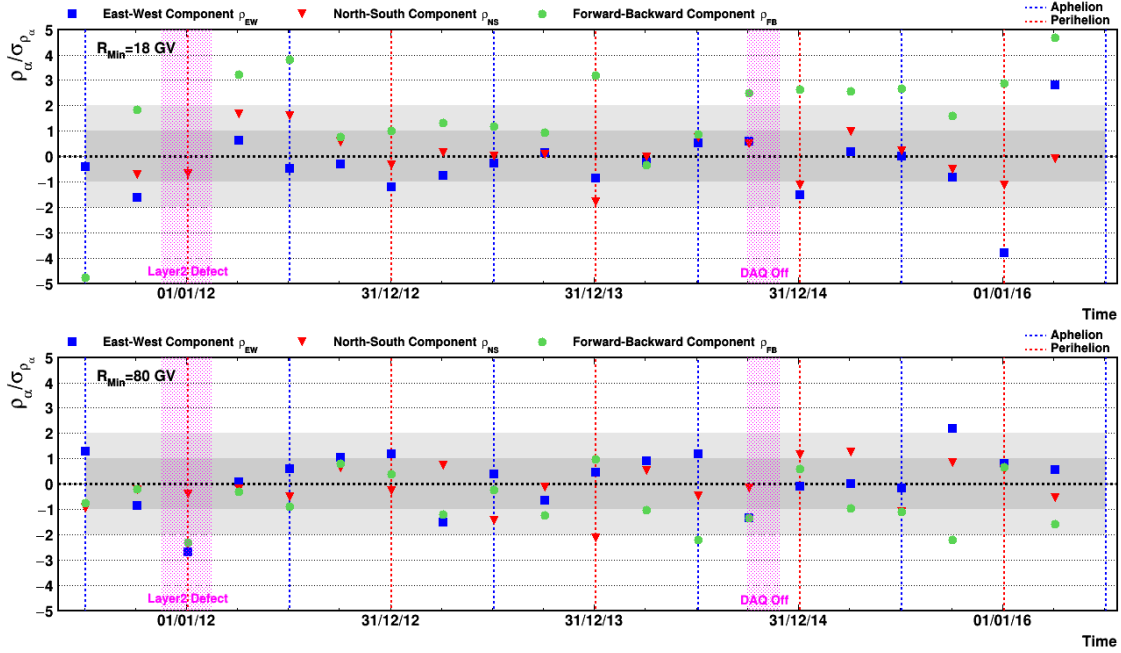
Figure 4.46.: Time evolution of the scaled dipole components in **GSE** for $R_{p/IsoSky}^{Rate}$ in the full range from 18 to 1800 GV **(top)** and 80 to 1800 GV **(bottom)**. The five years sample has been divided into 20 seasons, each of a quarter of a year. In the first season, the detector was still in commission phase with unstable configuration which causes fit components to be off scale. In winter 2011, the defect in Tracker layer two caused a change in the acceptance. Also in this bin, fit components are off scale.

binning of Carrington rotations as well. One Carrington rotation is the time in which the Sunspots circle around the Sun's surface at the equator, which takes about 27 days. The analysis shows good agreement with the seasonal analysis but does not provide additional information.

4.3.1.3. Conclusion on proton absolute anisotropies

About 51 million events with rigidity greater than 18 GV were studied in fullspan tracker acceptance. The number gives a statistically expected limit of $\delta_{Exp}^{95\%} \approx 0.07\%$ with an upper 1σ quantile of 0.09%. The fit results show a significant deviation from the isotropic hypothesis in both, galactic and GSE coordinates at the lowest rigidities. In further studies, it has been shown that a systematic limitation at the 1‰ level limits the sensitivity of the analysis. The isotropic expectation in GTOD is not fulfilled either at low rigidities where the sensitivity for systematic effects is high, because of the large number of selected protons. If the uncertainty from the correction function is included, results in galactic coordinates are in agreement with the isotropic hypothesis. The excess in GSE east-west direction persists.

For galactic coordinates, a limit is set, following the Bayes construction. The limit with rigidity is shown in Figure 4.47. For the full rigidity range above 18 GV the limit on the dipole amplitude in galactic coordinates of

$$\delta_p^{95\%}(18 \text{ GV}) = 0.13\%$$

is set. At 80 GV the analysis is not dominated by systematic effects anymore. A limit on
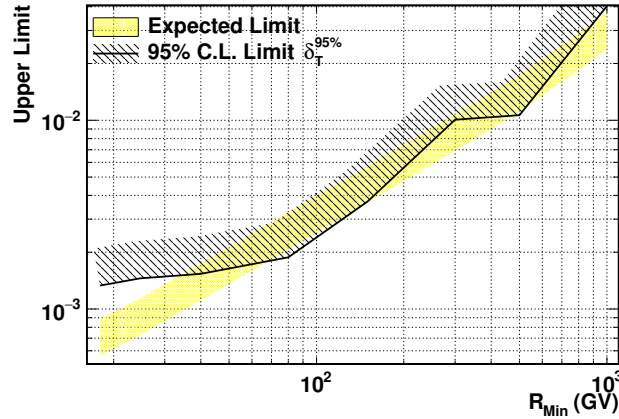
Figure 4.47.: Upper limit on the dipole amplitude for $R^{Rate}_{p/IsoSky}$ in **GAL**. For rigidities below 80 GV the limit does not reach the statistical expectation, due to the systematic limitation of the method.

the dipole strength in galactic coordinates at this rigidity the limit is set at

$$\delta^{95\%}_p(80 \text{ GV}) = 0.18\% \quad ,$$

in agreement with the isotropic expectation and the independent relative proton anisotropy.

In GSE a significant deviation from isotropy is observed, even with the systematic uncertainty included, at a strength of $\delta(18 \text{ GV}) = 0.23\%$. The signal persists under the variation of sensitive environment variables, with high impact on the detector performance. The anomaly will be investigated in a dedicated Section 5.1.

For the analysis in electrons, a sensitivity of about 0.5% is required, for positrons 2%, as suggested from the discussions in Chapter 4.1 on the relative anisotropies. The systematic limitation of the *IsoSkyMaps* from the proton study at the per mille-level is well below this requirement such that the analysis can be used for a search in electron and positron absolute anisotropies.

4.3.2. Electron and positron absolute anisotropy

The analysis in electrons and positrons is performed in the same energy layers, in the range from 16 to 350 GeV, and fits are presented at the same cumulative energy bins with the layered fit method, as it has been described for the relative anisotropies in Section 4.1. The selection is the same, such that Tables 4.2 and 4.1 are valid for this analysis, as well.

The number of positrons is low, such that a time and rigidity-dependent rate correction is not feasible. Also, the efficiencies are hard to assess. It has been shown in the introduction of this chapter, that the *livetime map* gives results in agreement with isotropy for positrons, already. To improve the result, the detector performance is studied on electrons and resulting correction functions are used for the positrons as well. In general, the analysis of the correction functions in electrons is done in the same way as for protons, starting from the evaluation of the selection efficiencies.
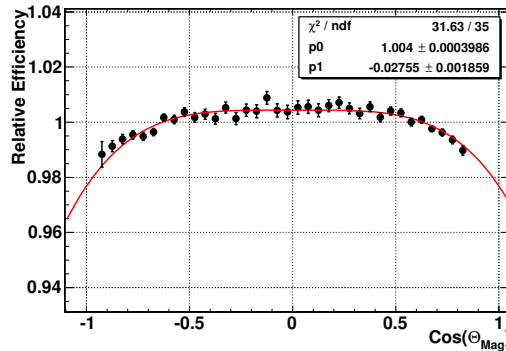
Figure 4.48.: Relative efficiency, as divided by its global value, for the single track requirement in electrons as a function of the cosine in geomagnetic latitude. The dependency has been parameterized by a function $f(\cos(\theta_M)) = p0 + p1 \times x^4$ (red line) which describes the latitudinal dependence with a normalized fit χ^2 <1. The decrease towards the geomagnetic poles originates from the increasing particle rate entering the tracker.

4.3.2.1. Efficiency evaluation

For the efficiency evaluation in electrons, the *tag-and-probe* method is used in the same way as for protons. A large difference is that for electrons a bias is introduced by the selected control sample which naturally is of reduced purity. For protons, which are the most abundant CR species, no significant background is contributing, rather than for the more rare electrons where the particle identification is of higher importance. In general, TRD cuts can be studied using a control sample selected by ECAL and vice versa.

For the protons, a strong dependence in the geomagnetic latitude originated from the trigger efficiency. The ECAL trigger used for leptons is highly efficient and robust against high particle rates, such that no contribution to the correction function is seen for the electron trigger. On the other hand, TRD is directly involved in the particle selection and is expected to be sensitive to the rate of low energetic particles. Also, the requirement for single-track events might show a strong latitudinal dependence with the increased particle rate towards the poles. Both cuts are strongly correlated through the usage of the inner Tracker track in the construction of the likelihood ratio LR^{TRD}. Hits in the TRD are clustered around this reconstructed trajectory. The correlation between these two sub-detectors will suppress the evaluated latitudinal dependence.

All cuts listed in Figure 3.20 were studied. Figure 4.48 shows the normalized efficiency with the geomagnetic latitude for the single track requirement in electrons, as an example. As it turns out, the presented single track efficiency is by far the one with the highest dependence on the magnetic latitude with a bending factor of 2%, followed by the good inner track cut. The TRD selection efficiency does not show a strong dependence on the magnetic latitude, which can be explained by the correlation to the inner Tracker, as discussed.

Possible variations in energy or time are studied separately using the pull as for protons, following Equations 4.2 and 4.3. The pull distribution for the single track efficiency is shown in Figure 4.49. Both distributions are reasonable Gaussian. Even though most of the efficiencies vary with energy or time, no significant dependence in the latitudinal behavior could be found for any of the contributing efficiencies. The observation is in
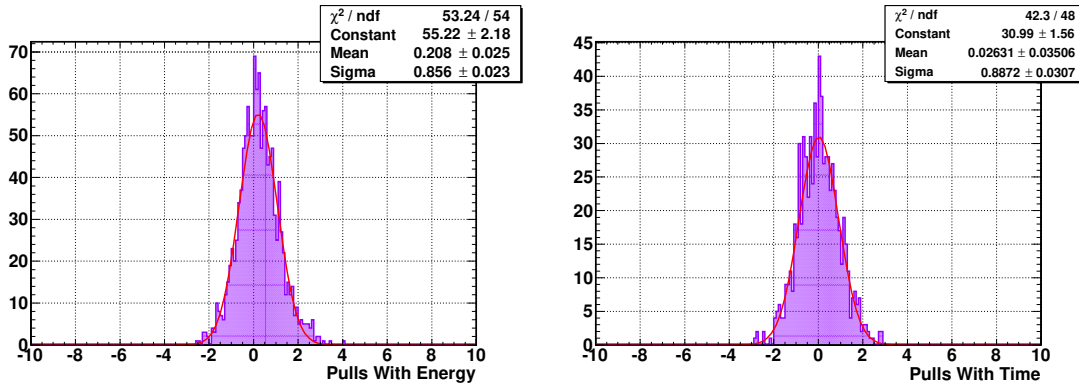
Figure 4.49.: Pull distribution for the energy (left) and time (right) evolution in the geomagnetic latitudinal dependence of the single track efficiency for electrons. Both distributions are constructed using Equations 4.2 and 4.3, and both are reasonably well described by a Gaussian (red line) distribution. Consequently no dependency in time or energy on the latitudinal correction is seen.

agreement with the estimate given by the rate correction where no significant time and energy-dependence was found as well.

The latitudinal dependence of the combined electron selection efficiencies, as product of the single cut efficiencies, is plotted in Figure 4.50 together with the rate correction from the first-order map. A significant difference in the correction methods is evident. Possible sources are the correlation of Tracker and TRD as described, or charge-confusion which is estimated from Monte-Carlo simulated data. As for the protons, the deviation, marked by the green band, will be propagated as a systematic uncertainty.
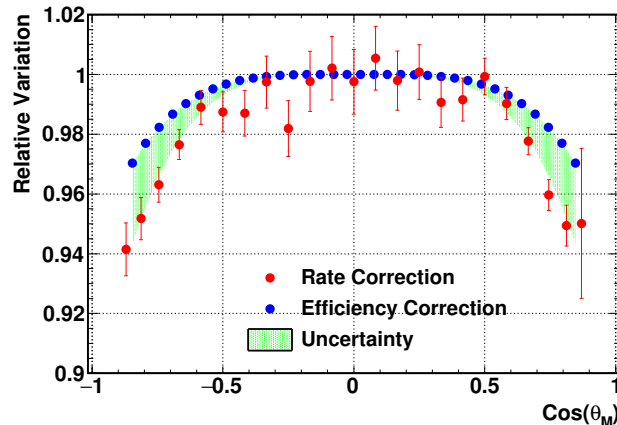
Figure 4.50.: Geomagnetic latitudinal correction for electrons with energy greater than 16 GeV obtained from the first-order rate correction (red) and the efficiency evaluation (blue). The mismatch between both methods, marked by the green area, is propagated as a systematic uncertainty.

4.3.2.2. Evaluation of systematic uncertainties

Systematic uncertainties were studied for electrons in the same way as for protons. The correction is varied within the systematic uncertainty band without any restrictive conditions e.g. on breaks or asymmetries. 100 random correction functions were created,
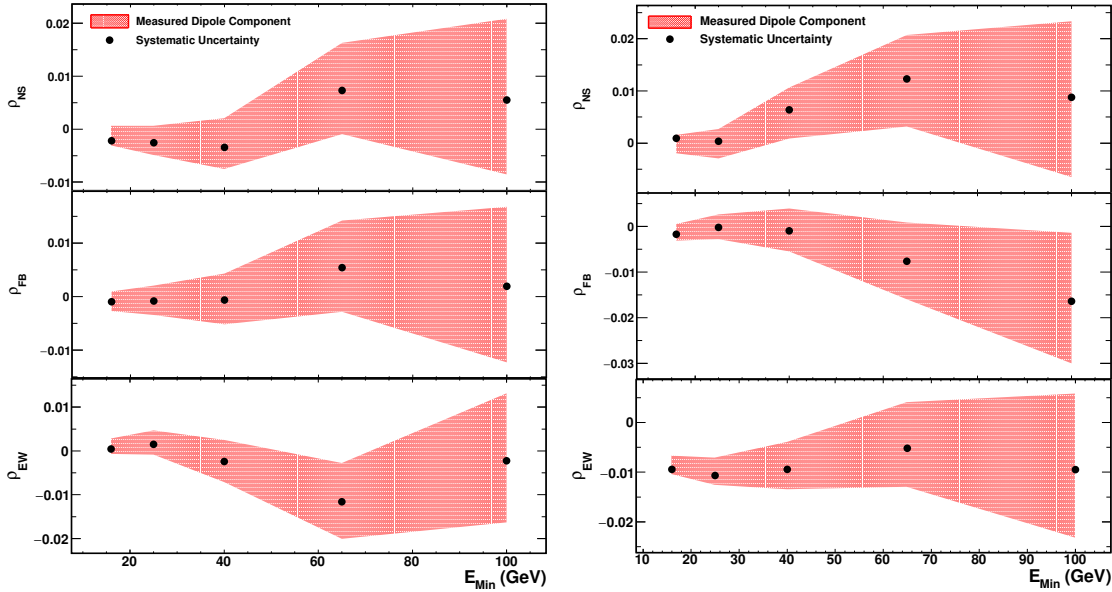
Figure 4.51.: Dipole components ρ_α, from correction variation, with energy for electrons in **GAL (left)** and **GSE (right)**. The red band represents the fit result with fit uncertainty from $R^{Rate}_{e^-/IsoSky}$. The black points show the mean and width of the distributions of ρ_α from the 100 simulated correction functions. The width of the distribution is stated as a systematic uncertainty on the dipole component. No shift in the position of the dipole components absolute value is observed.

and *IsoSkyMaps* were produced. The systematic uncertainty on the dipole components are shown in Figure 4.51 in galactic coordinates and GSE. As for protons, no shift in the absolute value of the dipole components can be seen, proving that the result is stable with the correction function. The statistical uncertainty is greater than the uncertainty coming from the correction function, where electrons are not sensitive to, over the whole energy range. Because of the low sample size, the systematic limitation is found to be even below the value for protons. The numerical values of the systematic limitation are quoted in Table B.9 and Table B.10 together with the fit results and the systematic uncertainty on the dipole components.

Figure 4.52 shows the fitted dipole components with energy of the fit in $R^{Eff}_{e^-/IsoSky}$ compared to $R^{Rate}_{e^-/IsoSky}$ in galactic coordinates. Both fits are in excellent agreement, independent of the correction function employed. Overall, the result is in good agreement with the isotropic hypothesis over the full energy range.

In conclusion, the anisotropy analysis in electrons is largely dominated by the statistical uncertainty. No systematic uncertainty has to be taken into account. The analysis has been shown in galactic coordinates, but returns the same result in GSE. Positrons are less abundant and no systematic impact has to be considered, either. The final results will be provided in Section 4.3.2.3, after the seasonal analysis.

Discussion of AMS-02 day-night cycle

In Section 4.3.1.2 the impact of temperature variations on a short timescale of one orbit from the AMS-02 day-night cycle were studied. A variation of the Tracker rigidity scale growing towards high rigidities was identified and correlated to the result of the
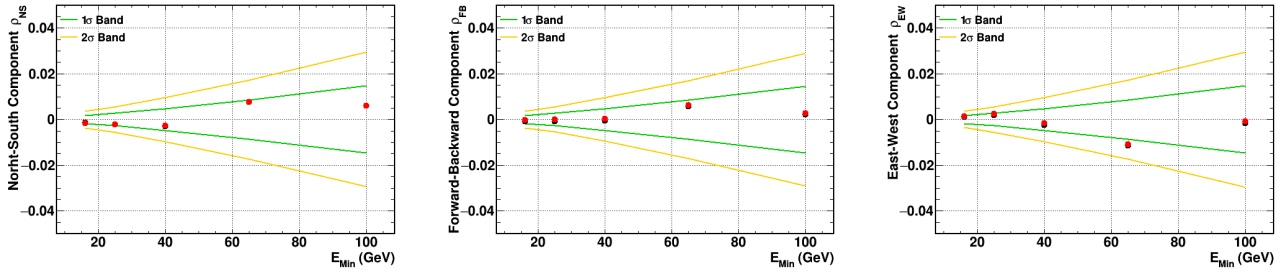
Figure 4.52.: Fitted dipole components of $R^{Eff}_{e^-/IsoSky}$ (red) with energy in comparison to $R^{Rate}_{e^-/IsoSky}$ (black) in **GAL**. Both fits are in good agreement with each other, and the isotropic hypothesis.
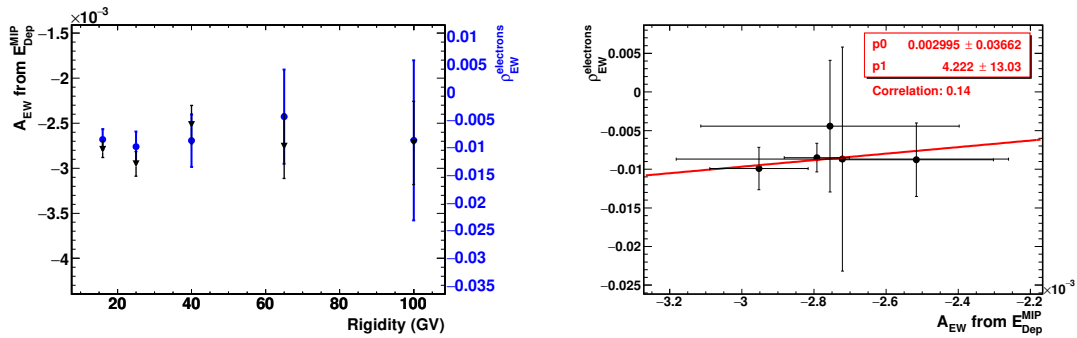
Figure 4.53.: Strength of the ECAL energy scale variation in GSE east-west direction A_{EW}, as defined in Figure 4.43, as a function of rigidity (black markers). The variation is approximately constant with the rigidity at a level of 0.27%. In blue markers the result of the dipole component ρ_{EW} of $R^{Rate}_{e^-/Isosky}$ in GSE, and as a function of ECAL energy in GeV, is shown with different y-axis. The variation in the ECAL energy scale can explain the deviation from the isotropic expectation for electrons in GSE east-west direction.

dipole fit in GSE for protons. In the same study, an approximately constant variation of the ECAL energy scale in GSE east-west direction of about 0.27% without significant forward-backward variation was found. The variation was parameterized with a function $f(\phi_{GSE}) = 1 + A_{EW} \times \sin(\phi_{GSE}) + A_{FB} \times \cos(\phi_{GSE})$, equivalent to the multipole expansion of the data in east-west and forward-backward direction used in the dipole analysis. Figure 4.53 shows the ECAL energy scale variation A_{EW} as a function of rigidity, overlayed with the fit component ρ_{EW} from the dipole fit to $R^{Rate}_{e^-/Isosky}$ in ECAL energy. The different y-axis is equivalent to a linear transformation of the type $\rho_{EW} = \alpha + \beta \times A_{EW}$ between the ECAL energy scale variation and the data which is emphasized with the linear fit to the scattered plot on the right-hand side of Figure 4.53. The correlation factor is small, as expected for a constant shift. The observation can explain the small GSE east-west offset in the fit to $R^{Rate}_{e^-/IsoSky}$.

Stability in time

For the seasonal analysis, only the lowest energy bin at 16 GeV has sufficient events. Figure 4.54 shows the results of the seasonal analysis for the absolute electron study in GSE and galactic coordinates. Fluctuations are large but show no evident pattern. The anomalies in winter 2011 and at the end of the five years data-taking period, discussed
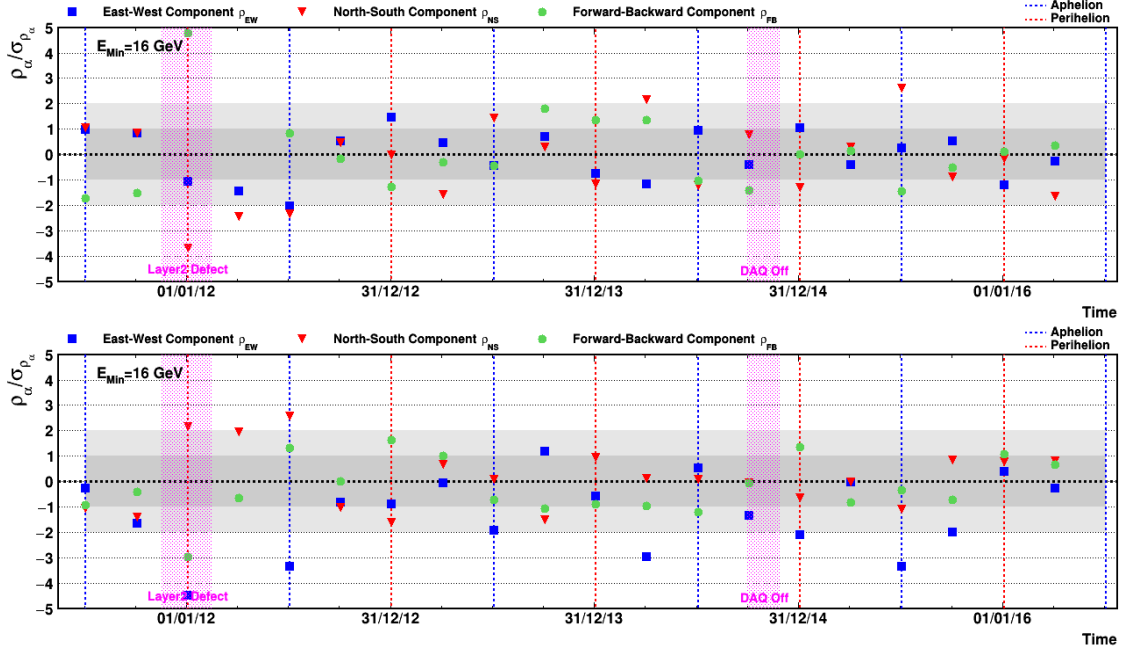
Figure 4.54.: Time evolution of the scaled dipole components in **GAL** (top) and **GSE** (bottom) for $R^{Rate}_{e^-/IsoSky}$ in the full range from 16 to 350 GeV. The 5 years sample has been divided into 20 seasons, each of a quarter of a year.
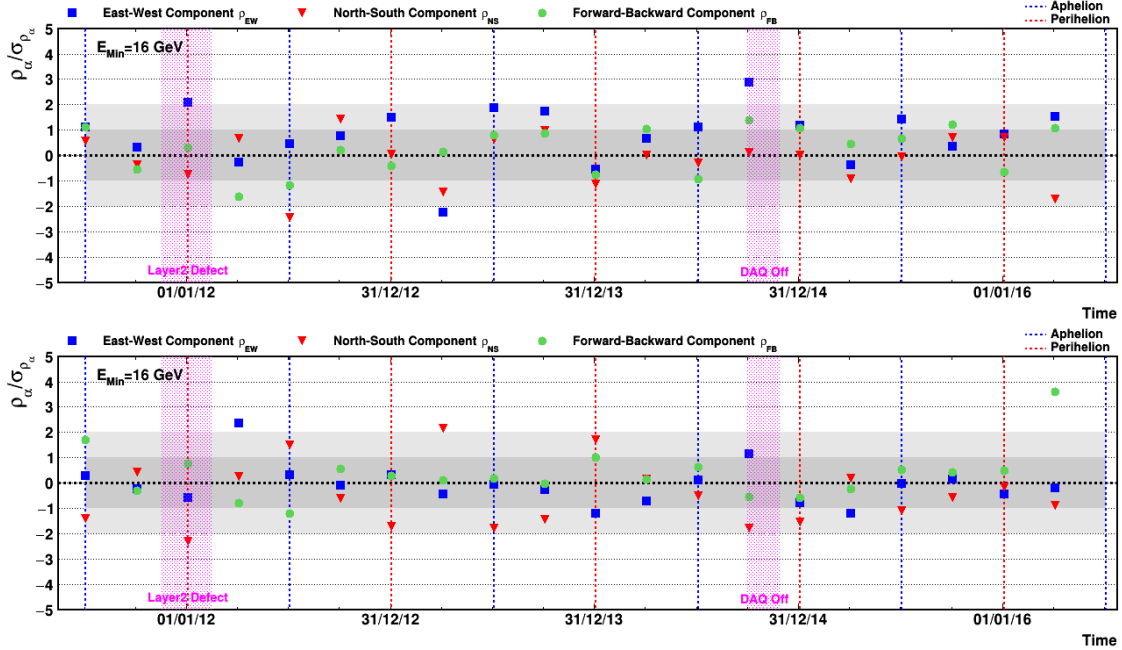
Figure 4.55.: Time evolution of the scaled dipole components in **GAL** (top) and **GSE** (bottom) for $R^{Rate}_{e^+/IsoSky}$ in the full range from 16 to 350 GeV. The 5 years sample has been divided into 20 seasons, each of a quarter of a year.
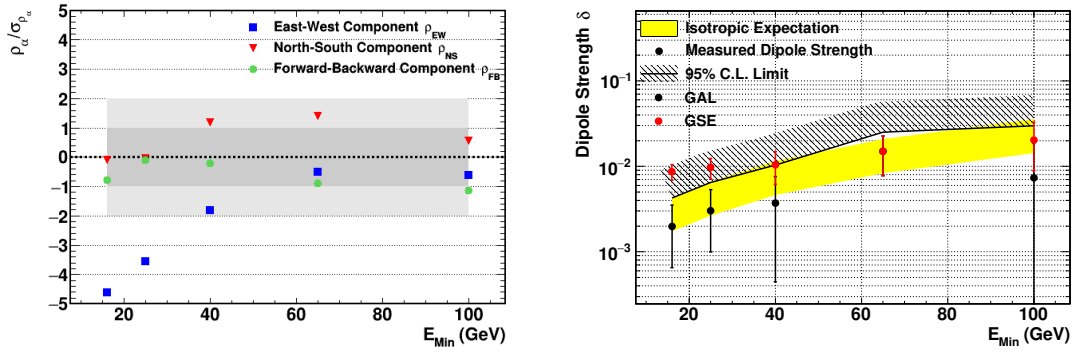
Figure 4.56.: **Left:** Fitted dipole components of $R^{Rate}_{e^-/IsoSky}$ with energy, scaled to their fit uncertainty, in **GSE**. An excess in negative east-west direction is evident for the lower energy bins. **Right:** The reconstructed dipole strength for $R^{Rate}_{e^-/IsoSky}$ with energy in **GAL** (black markers) and **GSE** (red markers). The yellow band represents the statistical expectation of the measurement in case of isotropy which is independent of the reference map and the coordinate system. In GAL no excess above the isotropic expectation can be seen. A limit on the maximum dipole strength is stated at a credible interval of 95% using the Bayes construction (black line). In GSE, an excess above the isotropic expectation is significant for the first two energy bins at 16 GeV and 24 GeV.

previously, are present in the electron seasonal analysis as well. In GSE a shift in east-west towards negative values is seen to be constant with time with a large spread.

In positrons, the seasonal analysis is shown in Figure 4.55 for GSE and galactic coordinates, without anomalous behavior. The sensitivity to this variable, however, is low due to the small number of events in a seasonal bin. The seasonal analysis in positrons can be seen more as a cross-check than to carry physical information.

4.3.2.3. Conclusion

The adaptation of the *IsoSkyMap* method, which has been successfully used on protons, to the 900 thousand electrons in the energy range of 16 to 350 GeV, revealed no unforeseen problems. Corrections along the geomagnetic latitude were applied to the electron selection without major difficulties in the rate or the efficiency evaluation. Both are in excellent agreement with each other, and with the isotropic hypothesis in galactic coordinates, as it has been shown in Figure 4.52. Figure 4.56 shows the fitted dipole components of $R^{Rate}_{e^-/IsoSky}$ with energy, scaled to their fit uncertainty, in GSE coordinates. A significant deviation from the isotropic expectation in negative east-west direction is seen for the first bins, decreasing in significance with energy. The anomaly observed in the absolute analysis $R^{Rate}_{e^-/IsoSky}$ is in agreement with the relative analysis $R_{e^-/p}$, shown in Figure 4.11.

The measured dipole strength for the absolute analysis $R^{Rate}_{e^-/IsoSky}$ is shown on the right-hand side of Figure 4.56. In galactic coordinates no deviation from the isotropic expectation is evident and a limit on the dipole anisotropy of galactic origin of

$$\delta^{95\%}_{e^-}(> 16 \text{ GV}) = 0.42\%$$

is set. This result is in good agreement with the statistical expectation and matches the
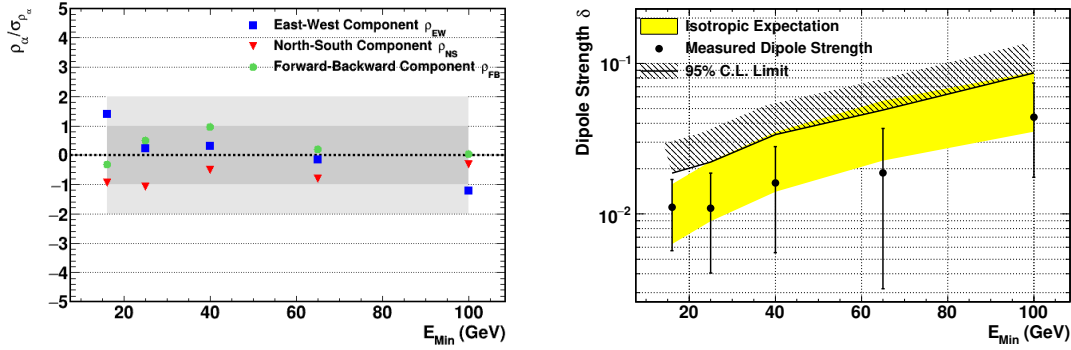
Figure 4.57.: Summary of results in the search for positron absolute anisotropies $R^{Rate}_{e^+/IsoSky}$ in **GAL**. **Left:** Fitted dipole components of $R^{Rate}_{e^+/IsoSky}$ scaled to their fit uncertainty. No component exceeds two standard deviations in any energy bin. **Right:** The measured dipole strength. The yellow band represents the statistical expectation of the measurement in case of isotropy. No deviation from the isotropic expectation is found. A limit on the maximum dipole strength is stated at a credible interval of 95% using the Bayes construction (line).

outcome of the measurement in relative anisotropy. The numerical values of the fit in $R^{Rate}_{e^-/IsoSky}$, can be found in Appendix B.9.

The GSE coordinate system shows the significant deviation decreasing with energy. No limit is set. A discussion of this anomaly will be given in Chapter 5.1. The numerical values can be found in Appendix B.10.

The corrections obtained from electrons is also applied to the positron *IsoSkyMap*, as effects introduced by the detector will be the same for both the particle species. The results in galactic coordinates are shown in Figure 4.57 with the dipole components, scaled to their fit uncertainty, and the measured dipole strength together with the upper limit. No deviation from the isotropic hypothesis is found. An upper limit on the dipole strength is set to

$$\delta^{95\%}_{e^+}(> 16\,\mathrm{GV}) = 1.87\%$$

comparable to the result obtained in the relative anisotropies, and expected from the number of selected positrons. Without any correction applied the limit on a dipole anisotropy in positrons was $\tilde{\delta}^{95\%}_{e^+}(> 16\,\mathrm{GV}) = 1.95\%$, which also matches the expectation. Numerical fit results of the analysis in $R^{Rate}_{e^+/IsoSky}$ in galactic coordinates can be found in Appendix B.11.

The result of the analysis of $R^{Rate}_{e^+/IsoSky}$ in GSE is shown in Figure B.12, without significant deviation from isotropy. An excess in this coordinate system could be useful in the interpretation of the excess seen in electrons at lower energies, and the protons, where a transition from east-west at lower rigidities to forward-backward above 80 GV. However, with a strength of 1% in electrons, the sensitivity in positrons is not high enough. From the analysis, an upper limit on the dipole strength in GSE is set to

$$\delta^{95\%}_{e^+}(> 16\,\mathrm{GV}) = 1.66\%$$

in the full energy range for positrons. The observation of this coordinate system in the future might reveal interesting insights on the propagation of charged particles in the heliosphere.
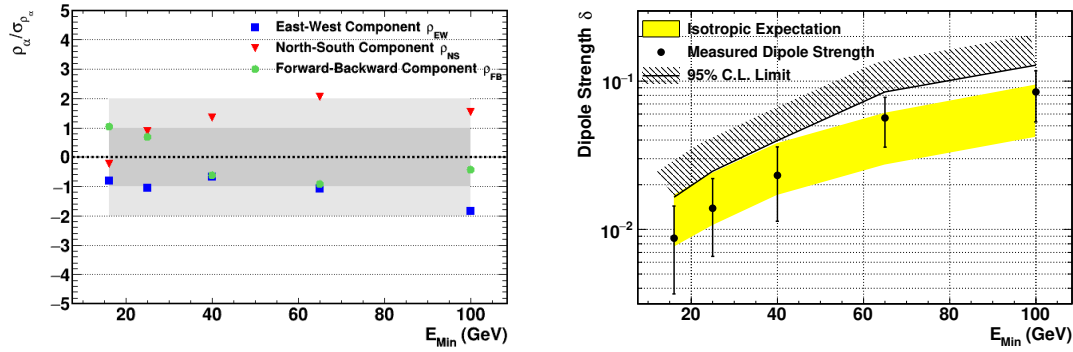
Figure 4.58.: Summary of results in the search for positron absolute anisotropies $R^{Rate}_{e^+/IsoSky}$ in **GSE**. **Left:** Fitted dipole components of $R^{Rate}_{e^+/IsoSky}$ scaled to their fit uncertainty. No component exceeds two standard deviations in any energy bin, but the north-south component seems to be systematically shifted towards positive values. **Right:** The measured dipole strength. The yellow band represents the statistical expectation of the measurement in case of isotropy. No deviation from the isotropic expectation is found. A limit on the maximum dipole strength is stated at a credible interval of 95% using the Bayes construction (line).

4.3.3. Treatment of background

The *IsoSkyMap* method provides reference maps in any celestial system with a sensitivity down to the per mille level. Above this level, the outcome of the analysis is determined by the the data only. If the data sample is contaminated with background of any kind, the upper limits that are quoted under the assumption of a pure sample of a defined set of particles, are too optimistic. Background contamination could be particles of a different species (e.g. protons in the positron sample) or from the same species at a different energy (e.g. low energetic protons migrating into the analysis bin). To produce meaningful limits, which can be used by theorists, the results need to be corrected for background, which is present in the data sample.

To account for background, the purity $p_{Layer} = \frac{N_{Sig}}{N_{Sig}+N_{Bg}}$, as fraction of pure events N_{Sig} in the selected sample contaminated with background N_{Bg}, for every fit layer of the data sample is calculated and propagated to the dipole fit as a weight factor in the Likelihood function in Equation 4.1:

$$\mathcal{L}(d_1, d_2, d_3) = -\log\left(\prod_{j(E_{Min})}^{N_{Layers}} p_{Layer} \cdot \prod_{i=1}^{N_{Pixels}} f(R_i(dE_j)|R_i^{Exp})\right) \quad . \tag{4.4}$$

In Section 3.3 the selection of protons, electrons, and positrons was described and the main sources of background were discussed. For protons, which can be selected with high purity because of their high abundance, the main contamination are protons of a different rigidity than the measured one which migrate into the analysis because of the finite tracker resolution. In a flux analysis, the bin-to-bin migration is treated by unfolding the flux, a statistical method which translates the measured rigidity to the true rigidity of a set of particles, using the resolution matrix shown earlier in Figure 3.23. For the anisotropy analysis, the unfolding procedure cannot be applied straight-forward and the migrated events are treated as background in the analysis bin. From the resolution matrix, the purity of a rigidity layer is constructed as the probability $p(\tilde{R}_{Ana}|R)$, that an
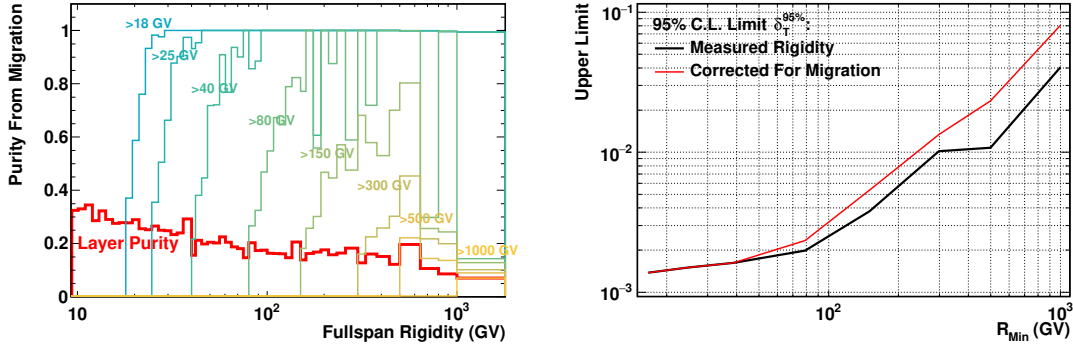
Figure 4.59.: Effect of bin-to-bin migration originating from the finite Tracker resolution on the dipole analysis of protons. **Left:** Purity of the proton sample from bin-to-bin migration. The red line gives the purity $p(\tilde{R}|R)$ of migration between the single rigidity layers, as the fraction of events where the rigidity is measured within the same rigidity bin as the true rigidity, determined from Monte-Carlo. The rigidity bins suffer a high contamination from the neighboring bins which gives only a low purity. Migration between layers in the analysis range does not affect the analysis sample and can be disregarded. This gives a purity for every rigidity layer and analysis bin $p(\tilde{R}_{Ana}|R)$ as the probability of an event to be of a true rigidity $\tilde{R}_{Ana}$ within the analysis bin, when measured with rigidity R. Because of the large analysis range, the purity approaches one for the layers in rigidity. **Right:** Degradation of the upper limit with correction for contamination from bin-to-bin migration. The effective number of events in the analysis range is decreased which causes the limit to increase.

event with a measured rigidity R has a true rigidity inside the bin of analysis $\tilde{R}_{Ana}$. In the two-dimensional resolution matrix from Figure 3.23, slices in y, along the x-axis are normalized to an integral of one to represent a probability density for a true rigidity $\tilde{R}$, in case of the measured rigidity R: $p(\tilde{R}|R)$. Events migrating within the analysis bin from one rigidity layer to another, are not counted as background, because in the construction of the limit the purity of the whole analysis sample is relevant, not the purity of a single layer. The purity $p(\tilde{R}_{Ana}|R)$ is the quantile

$$p(\tilde{R}_{Ana}|R) = \int_{R_{Min}}^{R_{Max}} p(\tilde{R}|R)d\tilde{R} \tag{4.5}$$

for every analysis bin and rigidity layer. On the left-hand side of Figure 4.59 the purity from migration for the layers in rigidity for every analysis bin is shown. To study migration effects, the Monte-Carlo spectrum is re-weighted to the measured AMS-02 proton flux [5]. The higher weight of low rigidity MC proton events, compared to the lower weight at high rigidities for the large rigidity-dependence of the flux, results in a high weight of migration events. This is the cause for the large fluctuations of the purity, as seen in Figure 4.59.

The right-hand side of Figure 4.59 shows the effect on the upper limit on the dipole amplitude for the fit in $R^{Rate}_{p/IsoSky}$. As to be expected, the limit weakens by accounting contamination in the sample. The degradation, defined as the factor by which the limit weakens, increases towards higher rigidities. The numerical values are presented in Table 4.6. The degradation reaches up to a factor of 2.

For electrons and positrons the purity from proton contamination has been shown in Figure 3.21 to be above 99% up to 100 GeV. A migration effect from the ECAL energy

R_{Min} (GV)	$\delta_p^{95\%}(R_{\mathrm{Min}})$ (%)	$\delta_p^{95\%}(\tilde{R}_{\mathrm{Min}})$ (%)	degradation
18	0.133	0.134	1.01
25	0.145	0.148	1.02
40	0.154	0.162	1.05
80	0.188	0.225	1.20
150	0.371	0.530	1.43
300	1.008	1.339	1.32
500	1.067	2.318	2.17
1000	4.030	8.073	2.00

Table 4.6.: Degradation of the upper limit on the dipole amplitude for protons from bin-to-bin migration. The limit weakens due to contamination from bin-to-bin migration which causes events of falsely reconstructed rigidity to migrate into the analysis bin.

E_{Min} (GeV)	$\delta_{e^+}^{95\%}$ (%)	$\delta_{e_{CC}^+}^{95\%}$ (%)	degradation
16	1.87	1.90	1.02
25	2.21	2.27	1.03
40	3.37	3.55	1.05
65	4.90	5.25	1.07
100	8.64	9.55	1.11

Table 4.7.: Degradation of the upper limit on the dipole amplitude for positrons from charge-confusion. The limit weakens due to charge-confused electrons entering the analysis.

resolution are negligible, as discussed in [1]. This results in a background free selection of electrons. For positrons a contamination from charge-confused electrons is present, as discussed from Figure 3.22. The charge-confusion is determined by Monte-Carlo as a function of energy. To calculate the purity p_{CC} from the fraction of charge-confused events f$_{\mathrm{CC}}$, the fraction of charge-confused electron events in the positron sample is calculated

$$p_{\mathrm{CC}} = 1 - \frac{\mathrm{N}_{e^-}}{\mathrm{N}_{e^+}} \cdot f_{\mathrm{CC}} \quad . \tag{4.6}$$

The purity is shown in Figure 4.60 with energy, aside with the evolution of the limit when charge-confusion is taken into account. The numerical values are presented in Table 4.7. The degradation reaches up to a factor of 1.1, less than for protons.

In this section a method to treat background contamination in the search for dipole anisotropies was introduced. Background contamination decreases the sensitivity for a signal and limits are set too optimistically if not taken into account. In published analyses on the search of a dipole anisotropy, as in [108, 157, 159, 161], such effects are not discussed.
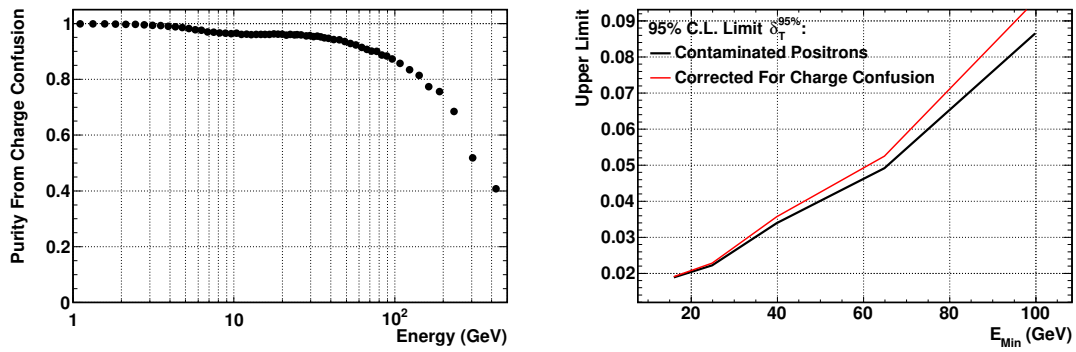
Figure 4.60.: Effect of contamination from charge-confused electrons on the dipole analysis of positrons. **Left:** Purity of the positron sample, taking contamination from charge-confused electrons into account. The purity is defined as $(N^+ - N^- \times p_{cc})/N^+$, where N^+ is the number of positrons, and N^- is the number of electrons in a layer weighted by the charge-confusion probability p_{cc} shown in Figure 3.22. **Right:** Degradation of the upper limit with correction for electron contamination from charge-confusion. The effective number of events in the analysis range is decreased which causes the limit to increase.

5. Discussion

This chapter is dedicated to a discussion of the results obtained in the previous Chapter 4. Measurements with the *IsoSkyMap* will be discussed with respect to their plausibility and significance with a comparison to independent methods in relative anisotropies and results published by other experiments. Furthermore, an outlook on anisotropy searches with AMS-02 and future experiments will be given.

5.1. Dipole anomaly in GSE

Fit results in GSE show a significant deviation from isotropy for protons in both, the relative and absolute, analysis. Towards higher rigidities, a variation in the Tracker rigidity scale with the AMS-02 day-night cycle has been identified as the cause of the deviation in GSE forward-backward. To study if an additional bias is introduced in the construction of the *IsoSkyMap*, or if the deviation originates only from the data, the dipole components of the fit to R_{p/p^*} and $R_{p/Isosky}^{Rate}$ are compared, in the overlapping rigidities above 80 GV. For fits below 80 GV, there is no analysis available to cross-check the results of the absolute proton measurement. The comparison is shown in Figure 5.1 for galactic coordinates and in Figure 5.2 for GSE. For the comparison the fit components of the relative proton analysis R_{p/p^*} have been shifted by the small deviations in the reference sample p^*, which is not perfectly isotropic, as it is measured with the $R_{p/Isosky}^{Rate}$. With this small
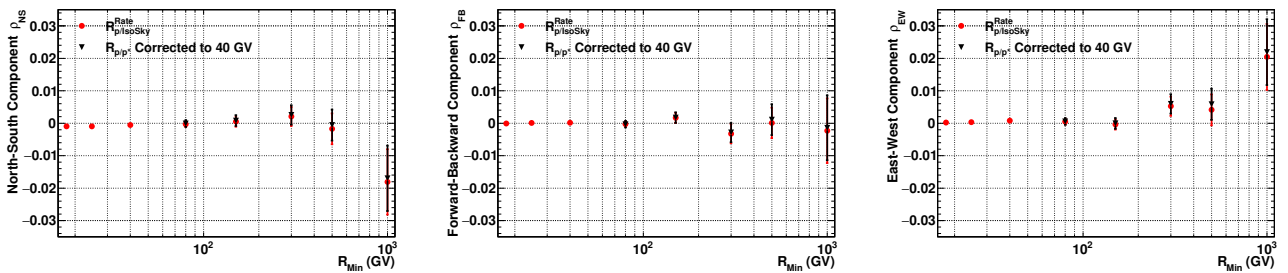
Figure 5.1.: Comparison of the dipole components obtained from the fit to $R_{p/Isosky}^{Rate}$ and R_{p/p^*} in **GAL**. The components of the relative study R_{p/p^*} are shifted by the offset of the reference sample at 40 to 80 GV, measured with the absolute study $R_{p/Isosky}^{Rate}$.
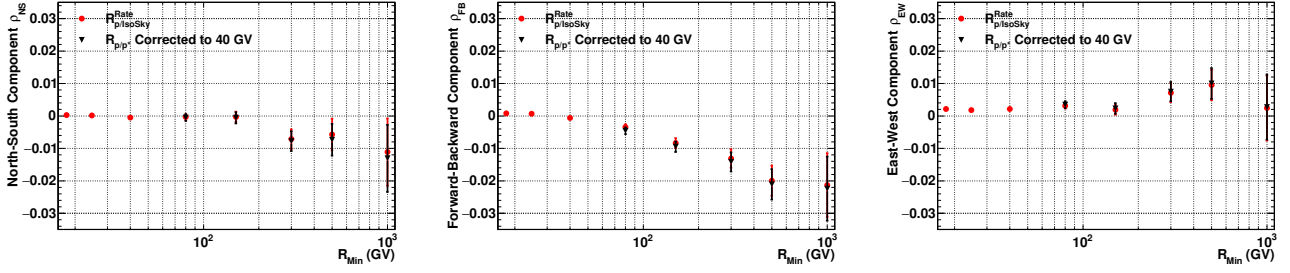
Figure 5.2.: Comparison of the dipole components obtained from the fit to $R_{p/Isosky}^{Rate}$ and R_{p/p^*} in **GSE**. The components of the relative study R_{p/p^*} are shifted by the offset of the reference sample at 40 to 80 GV, measured with the absolute study $R_{p/Isosky}^{Rate}$.

correction, both analyses are in excellent agreement with each other, even though completely independent reference maps are used. In conclusion, deviations from isotropy in protons are not introduced by the reference map, and are contained in the data.

The same comparison can be made with electrons in GSE, where a deviation from isotropy is evident in negative east-west direction for the bins at low energies. Towards higher energies, the significance decreases but a constant offset seems to persist. The ECAL energy scale has been identified as a cause of this deviation. The comparison is shown in Figure 5.3. The dipole fits in $R_{e^-/p}$ and $R_{e^-/IsoSky}^{Rate}$ show the same behavior, independently of the reference map, except for the forward-backward direction where $R_{e^-/IsoSky}^{Rate}$ tends to be more isotropic in the first two energy bins. The observation can be explained by the presence of the non-zero forward-backward component in the proton data, which is used as the reference.

The pointing direction of the dipole can be calculated from the three dipole components in the celestial sky. For GSE, the proton dipole points towards positive east-west direction for low rigidities and turns towards negative forward-backward direction, away from the Sun, for higher rigidities. For electrons, the dipole points towards negative east-west direction for low energies due to the ECAL energy scale variation, losing significance towards higher energies. The development of the pointing direction as a function of energy for electrons and protons is presented in Figure 5.4. For better presentation, the negative pointing direction is drawn in the GSE system, as both observables point away
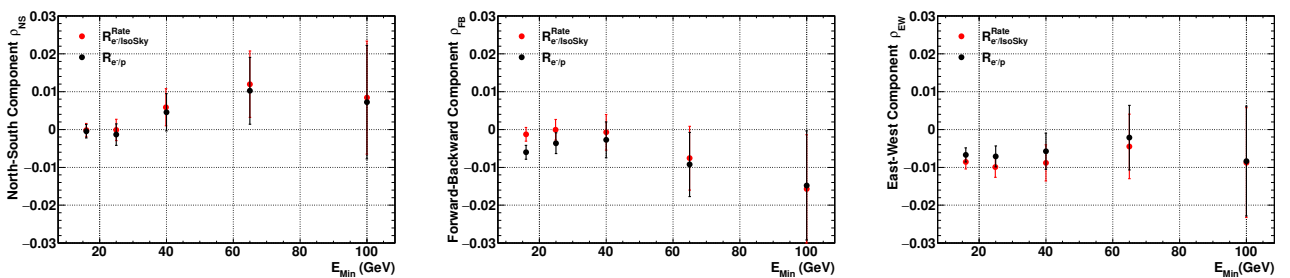
Figure 5.3.: Comparison of the dipole components obtained from the fit to $R_{e^-/IsoSky}^{Rate}$ and $R_{e^-/p}$ in **GSE**. The disagreement between the fits with the two independent reference maps in the forward-backward direction can be explained by the absolute proton measurement $R_{p/Isosky}^{Rate}$, which shows a deviation from isotropy in the proton angular distribution.
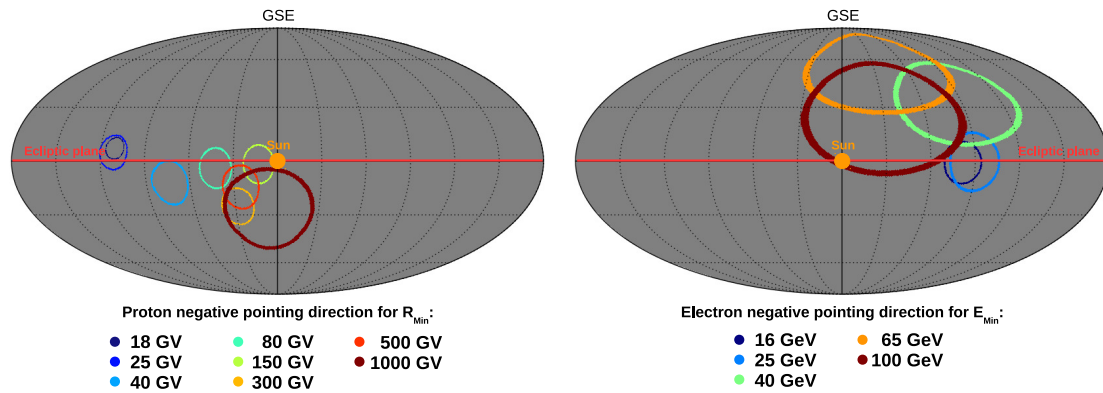
Figure 5.4.: Negative pointing direction of the measured dipole in GSE. The negative pointing direction is used to emphasize the turnover from east-west to negative forward-backward, away from the sun. The size of the circles represents the uncertainty in the direction measurement. The ecliptic plane is marked in red and the Sun's position in orange, plotted with about ten times the real opening angle in the sky. **Left:** Pointing directions for protons as a function of rigidity. The pointing direction turns from east-west towards negative forward-backward with increasing rigidity. **Right:** Pointing directions for electrons as a function of energy. The opposite pointing direction at low energies in the east-west direction for positively charged protons and negatively charged electrons is striking.

from the Sun which marks the center. The circles mark the uncertainty of the pointing direction, which has been determined in a toy Monte-Carlo approach equivalent to the one described in Section 3.2.7.1.

The dipoles pointing direction evolve along the ecliptic plane, marked in red in Figure 5.4, in which several processes could cause an anisotropy in the data to explain the observation: The Sun's magnetic field which is aligned with the ecliptic plane, the AMS-02 day-night cycle which causes variations in temperature, and the Earth's movement around the Sun.

5.1.1. Compton-Getting Effect

As discussed in the previous section, the anomaly in GSE forward-backward in protons, and GSE east-west in electrons, are most likely introduced by a variation of the rigidity and ECAL energy scale with the AMS-02 day-night cycle. So far the analysis fails to explain the east-west component in absolute protons at low rigidities. The excess exceeds the estimation of the systematic limitation, evident from Figure 4.35. As a physical interpretation, the Compton-Getting effect from the movement of the Earth around the Sun might be the source of the observed component.

Figure 5.5 shows the measured dipole strength from protons in GSE and the expected amplitude from the Compton-Getting effect. The expected amplitude of $\approx 5 \times 10^{-4}$ is just in the sensitive region, but way below the measured dipole strength. The plot also gives the projection of the isotropic expectation to 2024, which is the expected end of operation of the ISS. A significant improvement in the sensitivity search for protons is not to be expected from a longer measuring time alone, which will be addressed in Section 5.4. But it is just enough to explore the Compton-Getting regime, in the condition the remaining east-west signal will be removed. To reach the sensitivity, also the systematic limitation
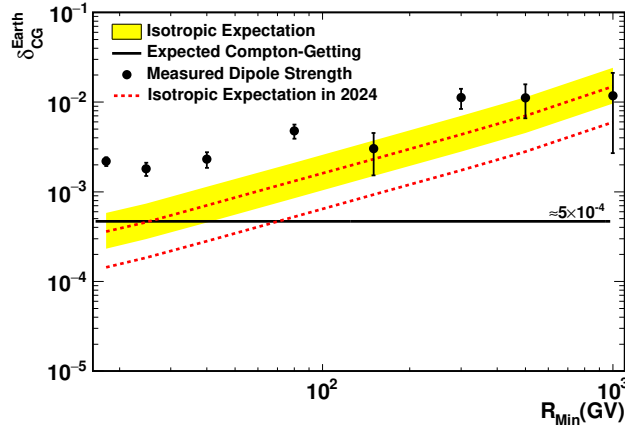
Figure 5.5.: Measured dipole amplitude from $R^{Rate}_{p/Isosky}$ in **GSE** compared to the expectation from the Compton-Getting effect by the Earth's movement on the orbit around the Sun. The Compton-Getting anisotropy is much weaker than the measured dipole amplitude. The red dashed lines show the isotropic expectation in 2024. By this time the Compton-Getting anisotropy could be measured if the current anomaly was removed. The systematic uncertainty is not included in the isotropic expectation to focus on the projection in 2024.

from the correction function has to be improved. An idea how to decrease the systematic impact of the correction function was presented in the previous section.

An east-west signal would also be expected from the bending in the Sun's magnetic field. In this case an opposite bending of the negatively charged electrons would be expected, once the sensitivity is reached. Also, such an effect would be dominant only at low rigidities. If the east-west excess is introduced by the Sun's magnetic field, a turnover in the direction will be detected as data-taking time advances, and the Sun reverses its polarity. To observe such a turnover the dipole strength and direction on a small timescale could give insights on how the Sun's magnetic field rearranges. So far, such a turnover is not observed even though the polarity has reversed in the end of 2013 [181]. A dedicated study with larger time bins and towards lower rigidities can be done with the presented methods. Also, the measurement of a similar dipole anisotropy in GSE for positrons or helium would help to identify a physical origin of the anomaly.

In case of a signal, a study including backtracing of the particles trajectories in the Earth magnetic field needs to be done, in particular at energies smaller than 100 GeV. Within AMS-02 backtracing is performed by an expert group on this subject. First results on backtracing in the GSE system show that a dipole signal can be shifted in the equatorial plane by the backtracing and a signal might be damped by some percent, dependent on the charge and energy. A signal cannot be created by the backtracing alone. From the comparison of relative and absolute anisotropies some conclusions on the impact of the backtracing can be drawn. In electrons, a reference map of different charge sign, namely protons, give the same result as the *IsoSkyMap* without any charge information, in galactic coordinates. If backtracing played a major role in the creation of a signal, a larger deviation in these two analyses would be expected. Of course, only the analysis with backtracing included can settle this issue. In this thesis, some observations on the measurement will be derived without the backtracing.
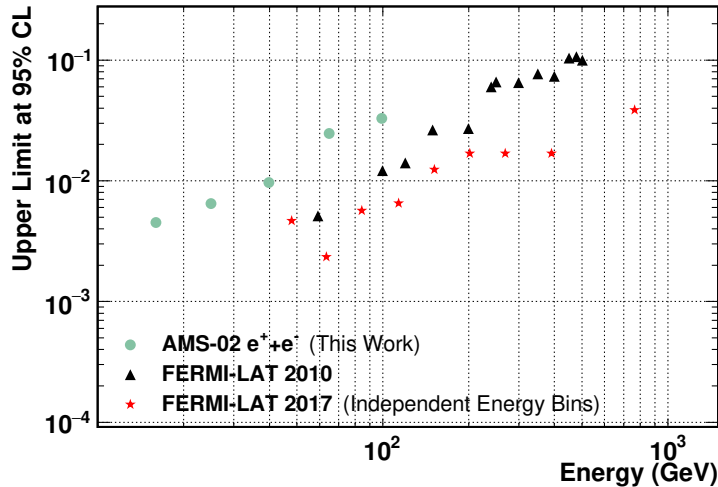
Figure 5.6.: Comparison of upper limits on a dipole anisotropy of a combined electron and positron analysis in **GAL** with results published by FERMI-LAT [157, 159]. The LAT has a much larger acceptance combined with a longer data-taking time and provides limits that are much harder compared to AMS-02 capabilities. However, the instrument is not capable of providing anisotropies of positrons only.

5.2. Comparison to previous measurements

There are a variety of experiments studying the arrival direction of charged cosmic rays at different energies. Available measurements have been introduced in Section 1.4. AMS-02 was not designed with a focus on the measurement of a large scale anisotropy, but for a precise measurement of a particles type and energy. Large ground-based telescopes, on the other hand, lack the particle identification and have a weaker energy reconstruction compared to direct CR detection experiments. The particle identification and energy reconstruction have an impact on the construction of the limit, as it was discussed in Section 4.3.3. With these qualities, the results derived in this thesis can contribute. The comparison to other experiments is split in direct CR detection experiments, in space, and indirect detection experiments on the ground.

5.2.1. Satellite measurements

For direct detection of charged cosmic rays only space-based experiments can contribute. Balloon flights usually do not cover a large fraction of the celestial sky, as they usually circle at the Earth's poles. Two satellite experiments have published studies on the search of dipole anisotropies, which are FERMI-LAT and Pamela, both introduced in Section 1.4. Pamela has similar detection capabilities compared to AMS-02, but with a much smaller acceptance and therefore low sensitivity. An upper limit on a positron dipole anisotropy of $\delta^{95\%}_{\text{PAMELA-}e^+/p}$ =0.166 in galactic coordinates is reported [108]. The study is based on 10^3 positrons in a rigidity range from 10 to 200 GV and protons are used as reference map. The PAMELA measurement is the only one directly comparable to the positron analysis presented in this thesis. The derived limit of $\delta^{95\%}_{\text{AMS-02-}e^+}$ =0.0187 at energies from 16 GeV to 350 GeV is stronger by a factor of 10. A comparable result was derived with three independent reference maps.

FERMI-LAT is not a spectrometer and therefore lacks the particle identification capabilities of AMS-02 and PAMELA. In particular, the experiment is not able to distinguish
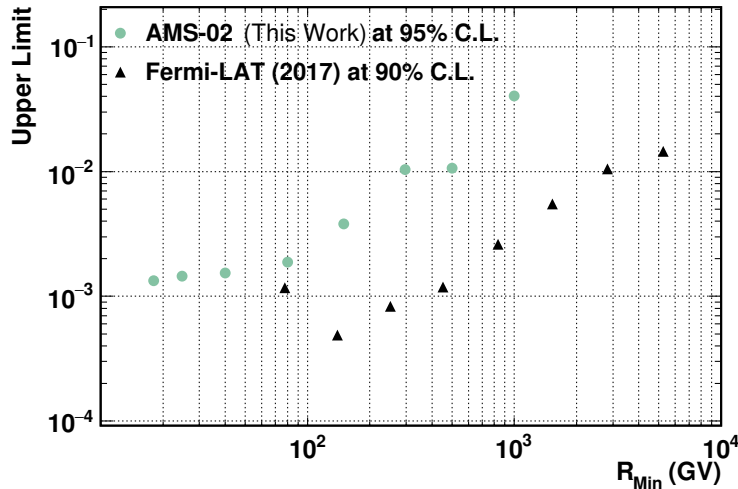
Figure 5.7.: Comparison of upper limits on a dipole anisotropy of protons in **GAL** with results published by FERMI-LAT [161]. The LAT has a much larger acceptance combined with a longer data-taking time and provides limits that are much stronger compared to AMS-02 capabilities. With AMS-02 a lower energy regime can be accessed.

between electrons and positrons. FERMI-LAT, however, has a much larger acceptance. Limits on a dipole anisotropy in a combined analysis of electrons and positrons were reported in [157] and [159]. In both publications, the *shuffling technique*, as presented in Section 3.2.3, was used to evaluate the reference map. The *shuffling technique* cannot be used to search for a large-scale anisotropy. Considering this issue, first presented in 2015 [158] and [160], a rate based method is used in [159], similar to the *livetime maps* discussed in Section 4.3. Figure 5.6 compares the FERMI-LAT results as a function of energy to AMS-02. For the comparison, a combined fit $R^{Rate}_{(e^-+e^+)/IsoSky}$ in electrons and positrons has been performed on the AMS-02 data with minor improvement compared to the electron analysis. Limits from FERMI-LAT are stronger by a factor of nearly 10, due to the high acceptance and longer data-taking time. On the other hand, the LAT is not capable of providing clean positron or electron anisotropies which are more sensitive observables for the search in astrophysical sources.

In a recently presented analysis, the angular distribution of protons, measured with the FERMI-LAT, was studied using the rate-based reference map [161]. The telescope orbits the Earth with a smaller inclination angle of 25.6°, compared to the ISS inclination of 51.6°, and therefore does not reach the polar regions where a correction for the high exposure of low energetic particles is needed. In this case the *livetime map* is similar to the *IsoSkyMap*, where such a correction is applied, and a reference map is more straightforward to construct.

Because of the large acceptance, 160 million events with an energy larger than 78 GeV could be analyzed, a factor of 40 compared to the 4 million events at rigidities larger than 80 GV, used in the presented analysis. The measurement of protons with an electromagnetic calorimeter requires sophisticated analysis. Despite the effort, the energy resolution for protons measured with FERMI-LAT is of only 20% to 40% at a confidence interval of 68.3% in the range from 50 GeV to 10 TeV [182] and a sample contamination of low energetic protons is present. The finite energy resolution and background worsens the true limit on the dipole amplitude, as discussed in Section 4.3.3. Even though

the available number of events is much larger with FERMI-LAT, an analysis by AMS-02 provides a the better momentum resolution with impact on the upper limit, which so far is not discussed in the FERMI-LAT analysis.

A comparison of the upper limit on the dipole anisotropy in galactic coordinates from FERMI-LAT, compared to the AMS-02 results is shown in Figure 5.7. As expected from the sample size, FERMI-LAT is able to set much stronger limits on a dipole anisotropy, but has a large deviation from isotropy in the lowest energy bin that is most likely caused by a systematic influence. In the presented state, the FERMI-LAT analysis also suffers large systematic effects in the quadrupole moments of the expansion.

For both observables, leptons and protons, the FERMI-LAT is able to set stronger limits for the large acceptance and the stable environment. The importance of the AMS-02 analysis presented in this thesis is the detailed understanding of possible environmental effects that affect the search for large scale anisotropies. The analysis sets limits which are best understood and therefore have a value for the community, even though they are not the strongest. The thesis suggests a road to follow for future analysis by FERMI-LAT, other planned space-based detectors, and the ground-based telescopes where new methods to create reference maps are needed to exploit the full detection power of the instruments. Some have already been used, as in the FERMI-LAT rate-based reference maps.

5.2.2. Ground-based measurements

The searches for anisotropies performed by ground-based detectors is fundamentally different from the presented analysis done with direct detection experiments. Ground-based detectors have a huge acceptance but poor particle reconstruction capabilities in the energy and incoming direction measurement, as well as poor particle identification. Also, ground-based experiments measure particles at much higher energies.

A natural limitation comes from their fixed position on the Earth's surface, which comes with a limited coverage of the celestial sky. The high sensitivity, from the huge acceptance, requires high precision knowledge of the reference. For this reason, ground-based analyses are not able to recover a full three-dimensional dipole anisotropy, but only its projection on the equatorial plane, as described in Section 1.4. The dipole amplitude, projected on the equatorial plane is called A_1. In fact, ground-based telescopes were able to find anisotropies in CRs. A variety of measured A_1 are shown on the left-hand side of Figure 5.8, compared to the proton analysis presented in this thesis. For this comparison, the proton analysis has been performed in equatorial coordinates and the projection of the amplitude recovered in the three-dimensional dipole fit, onto the equatorial plane, is calculated. It should be noted, that the result is in agreement with isotropy and should not be confused with a measurement. A direct detection experiment, with limited acceptance compared to ground-based detectors, can contribute if a measured dipole has a significant component perpendicular to the equatorial plane. Also, the superior energy resolution would allow for a better reconstruction of a signal: If a dipole signal at some energy is washed out for the bad energy measurement, the true dipole amplitude could be larger than the one reconstructed.

It has been noted in Section 3.2.6.1 that the angular direction of a dipole anisotropy can be recovered with a higher probability than the dipole amplitude. Many of the ground-based analyses use this characteristic of a spherical harmonics expansion to quote their
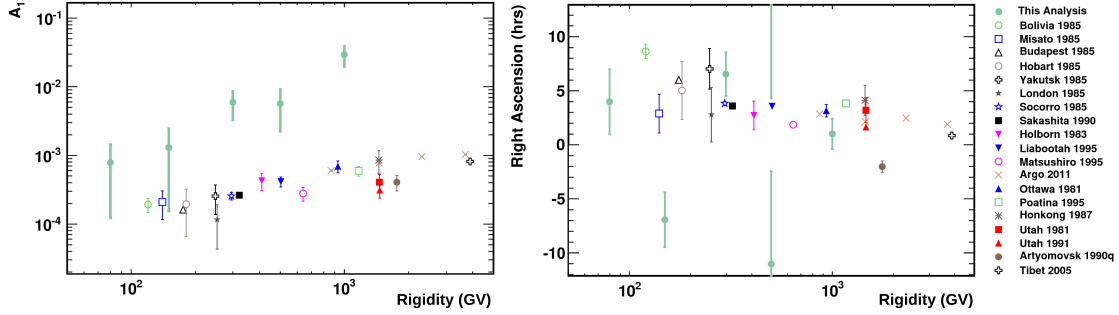
Figure 5.8.: Comparison of the measured A_1 and the right ascension by ground-based experiments, collected in [105], with the AMS-02 $R_{p/Isosky}^{Rate}$ proton analysis above 80 GV expressed in the same quantities. The AMS-02 A_1s are comparable with isotropy and should not be confused with a measurement. **Left:** The measured A_1, the dipole amplitude projected on the equatorial plane. Corrections to the amplitudes related to the different latitudes and zenithal-dependent efficiencies of the different experiments are not applied. **Right:** The right ascension measurement. The reconstructed direction in the presented analysis seems to match the given right ascension from the ground-based detectors better than an isotropic random distribution.

measurement. To boost the sensitivity with a search optimized for the measurement of a predominant direction, the proton analysis is performed in independent bins of rigidity, rather than the cumulative binning. Only rigidities above 80 GV are considered in this analysis, not to be affected by the Earth's magnetic field. Recovered directions are then compared to the one provided by the ground-based measurements, stated as right ascension in hours. If it was shown that the direction can be recovered in right ascension, the declination measurement could be provided as additional information to the ground-based observations. The results in right ascension are shown on the right-hand side in Figure 5.8.

To state if the AMS-02 reconstructed values of right ascension follow the measurements of the ground-based telescopes, the conformity of the reconstructed direction with an isotropic expectation is tested. The distributions of reconstructed directions from the five independent rigidity bins at 80 to 150 GV, 150 to 300 GV,300 to 500 GV, 500 to 1000 GV and 1000 to 1800 GV are projected onto the right ascension axis. Direction distributions are generated from the dipole fit, using a toy Monte-Carlo method to draw from a multivariate Gaussian distribution with the fitted dipole components, their fit uncertainty, and the correlation matrix. The distribution expected for isotropy is flat. The left-hand side of Figure 5.9 shows the distribution of the right ascension for the measured data (expressed in degrees), together with the isotropic expectation H_0, and the sum of 1000 toy Monte-Carlo distributions randomly generated from isotropic fits. The sum of the isotropic simulation matches the isotropic expectation H_0, which is constant. Of course, a single right ascension distribution, consisting of five more or less Gaussian shaped direction distributions, will not be perfectly flat. The more the five independent direction distributions cluster around a predominant direction, the more they deviate from H_0.

To test if the reconstructed directions are isotropically distributed, a p-test is performed. As test-variable, the area enclosed from the right ascension distribution and the isotropic hypothesis H_0 is used, counting areas below and above H_0 as positive. The smaller the value, the closer the test-variable matches the isotropic hypothesis. The distribution of
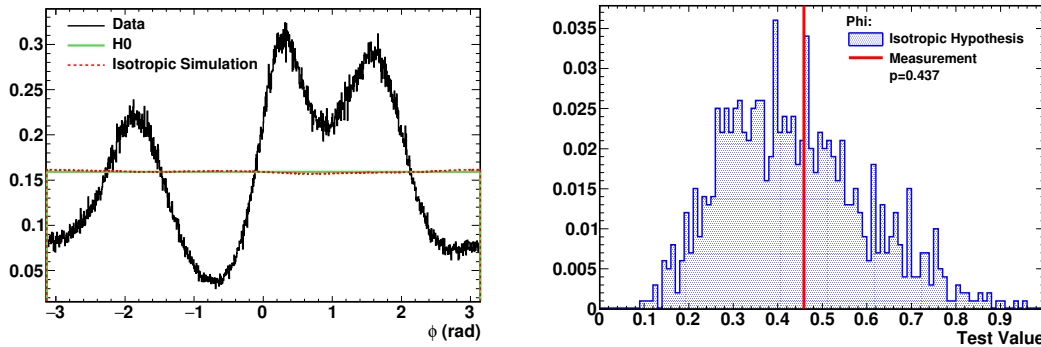
Figure 5.9.: Test on an isotropically distributed direction measurement. **Left:** Distributions of the 5 independent right ascension measurements from data, summed up in one right-ascension distribution. Also, the isotropic hypothesis H_0, which is flat, is shown and an isotropic simulation as sum of 1000 toy Monte-Carlo distributions randomly generated from isotropic fits. **Right:** Distribution of the test-variable in case of H_0, from the 1000 toy Monte-Carlo distributions randomly generated from isotropic fits. The data has a test-value of 0.459, which corresponds to a p-value of p=0.437, in good agreement with isotropy.

the test-variable in case of isotropy is created using 1000 toy Monte-Carlo right ascension distributions randomly generated from isotropic fits with the mean event number equal to the data in the rigidity bin. The p-value resembles the probability to measure a test-variable higher than the measured one in case of isotropy. If the p-value is extremely small, the isotropic hypothesis would be rejected. The right-hand side of Figure 5.9 shows the distribution of the test-variable in case of isotropy together with the test-value from data, which is 0.459. The p-value has been found to be p=0.437 in good agreement with the isotropic hypothesis. The high p-value leads to the conclusion that the AMS-02 reconstructed values of right ascension resemble isotropy and do not follow the measured direction from ground-based telescopes.

The presented method for a dipole search focusing on the direction, rather than the dipole amplitude can be a useful tool in the future if a particular source of known direction is studied.

5.3. Physics implication of the results

No excess in the dipole amplitude that could be linked to an astrophysical process has been found in the presented analysis of proton, positron, and electron data taken with AMS-02. An anomaly in GSE east-west for protons at low rigidities has to be studied further to persist with a better understanding of the GSE coordinate system and the AMS-02 day-night cycle, as well as in time. This thesis provides two important results; one for experimentalists searching for large scale anisotropies, and one for theorists modeling CR transport in the galaxy. This section aims to comment on the astrophysical impact.

The main question addresses the pulsar hypothesis as origin of the rise in the positron fraction. Various models are available, trying to explain the rise with additional local sources. All acknowledge the dipole anisotropy as a smoking gun signal for the point source origin of positrons and electrons. The models make predictions for a dipole anisotropy in positrons with strengths of the sub-percent level [42, 50], down to the per

mille level [81, 183]. Reference [81] investigates a dipole anisotropy from the electron primary production in Supernova remnants, with focus on the FERMI-LAT results, and predicts an amplitude of the order of 10^{-2}, for energies above 100 GeV. With currently available AMS-02 data, dipole anisotropies with a strength of 2% for positrons, and 0.4% for electrons with energies above 16 GeV can be excluded.

For protons, a source anisotropy of diffusing protons with high propagation distance, compared to electrons or positrons, from the galactic center direction, where the source density is higher, towards the outer galactic regions with an amplitude of the order of 10^{-4} at 100 GeV is expected [184]. In an attempt to explain the anisotropies found by ground-based telescopes, discussed in the previous Section 5.2.2, nearby SNRs were studied as local source of protons [184–186]. The amplitude of the first harmonic, projected on the equatorial plane, A_1 are stated at the level of 10^{-3} for energies above 100 GeV. In this energy range, the proton flux hardens, as measured by AMS-02 [5], which might be explained by a local source of protons. With AMS-02 data, limits on the dipole amplitude of 0.13% is set for protons above 18 GV, and 0.19% for protons with rigidities above 80 GV.

It should be noted that predictions are made for the local interstellar spectrum (LIS), outside of the Heliosphere and the local environment. The local environment has been studied in [50], with the result that a modulation of the diffusion parameter in the local bubble can boost the LIS anisotropy up to 325%, or weaken it down to 0.6%, for electrons above 16 GeV. For protons, similar numbers are stated. The impact of the Heliosphere on the arrival directions of charged CRs has been studied extensively, mostly with focus on energies above 1 TeV [85–87]. Already for these, relatively high energies, the Heliosphere could redistribute a dipole to higher multipole orders. The impact on CRs with energies of 100 GeV is even less studied. The heliosphere is fixed with respect to the galaxy on timescales of hundreds of years, such that an effect on the arrival direction would appear in the galactic coordinate system, or equally in the equatorial coordinate system. To link a dipole signal in galactic coordinates with astrophysical point sources, an extensive study of the heliosphere is needed.

In GSE, the diffusion of CRs in the local Sun's magnetic field, the Parker spiral, can be studied by searching for time dependencies. Also, the Compton-Getting effect might be observed in this frame. In fact, the excess in the GSE positive east-west component could be linked to one of these sources but needs further investigation.

5.4. Future of anisotropy searches in cosmic rays

With the increasing acceptance for the newest generation of CR detection experiments, a level of sensitivity can be explored at which the dipole amplitude (measured or excluded by an upper limit) becomes a potent observable to study the origin and propagation of charged CRs with discovery potential [187]. The precise measurements of the AMS-02 particle fluxes with unexpected features challenge the standard paradigm of CR propagation with assumption of isotropy. In this context, not only the search for pulsars as an astrophysical point source of positrons and electrons but also the measurement of anisotropies in nuclei is an important piece of information. The methods developed in this thesis provide the necessary tools for these studies. For AMS-02 this means that the search for anisotropies will be expanded towards helium, lithium and other heavier nuclei. Lithium, in particular, is an interesting observable, as it is a secondary and therefore has the potential to trace secondary production in the local environment.
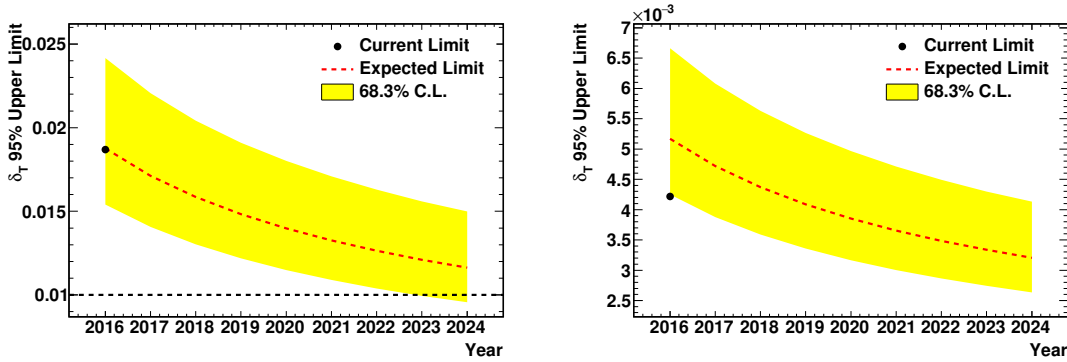
Figure 5.10.: Projection of the expected upper limit on the dipole amplitude, at E_{Min}=16 GeV, for positrons **(left)** and electrons **(right)** to the year 2024, the expected end of operation of the ISS. The current limit is shown as black marker. The current upper limit on a dipole anisotropy in electrons is found to be strong, compared to the expectation. The positron limit is in excellent agreement with the expectation. The projection assumes a linear increase in available events. By 2024 a limit of about 1% is expected for positrons and 0.3% for electrons.

AMS-02 will continue to take data up to the end of the ISS lifetime, currently expected in 2024. Compared to the five years of data analyzed in this thesis, the available number of events are projected to be more than doubled. Also, a full solar cycle will be measured continuously by 2024. The observation of changes in the anisotropy measurements in GSE, with the reversal of the Sun's polarity, might give new insights of the rearranging of the Parker-spiral.

In addition, the sensitivity of the search of anisotropies in electrons and positrons will further increase, allowing to set stronger limits in the future. Stronger limits further restrict pulsar models as origin of the rise in the positron fraction. Figure 5.10 gives a projection of the expected upper limit on the dipole amplitude for positrons and electron in the year 2024, assuming a linear increase in available events. A linear growth of data is justified from the past, shown in Appendix C. On 8th May 2017, AMS-02 measured 100 billion events [188]. By 2024 an upper limit of about 1% is expected for positrons, which will further exclude pulsar models. In electrons, an upper limit of about 0.3% is expected, which is just a minor improvement compared to the current limit of $\delta_{e_-}^{95\%}(> 16 \text{ GV}) = 0.42\%$, which is slightly stronger than expected from the sample size. Both projections are well above the systematic limitation that was estimated to be of the order of 10^{-4} and therefore can be reached with the presented *IsoSkyMap* method.

For protons, the gain in sample size from the longer measuring time is negligible, besides the fact that the measurement is dominated by the systematic limitation at the lowest energies. A projection of the isotropic expectation in 2024 has been shown in Figure 5.5. Ideas to improve the *IsoSkyMap* analysis have been given at the end of Section 5.1. A larger gain in proton events, and therefore sensitivity, can be achieved by loosening the selection. To prove the analysis concept, the well understood, fullspan selection from the flux measurement has been used. The selection is based on clean reconstructed events, rather than maximizing the number of events, because the flux measurement is largely dominated by systematic uncertainties. The analysis of anisotropies has different requirements on the event quality and rigidity resolution. If the systematic limitation can be reduced by the proposed modifications, a looser selection in Tracker layer 1 accep-
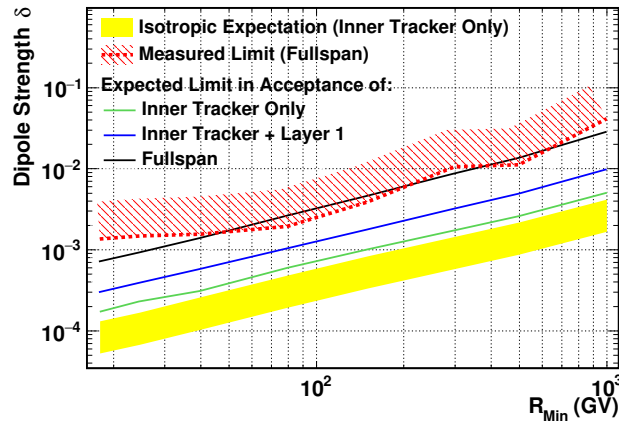
Figure 5.11.: Upper limit on the dipole amplitude for protons, to be expected with different selections. The expectation is purely based on the available number of events in a chosen acceptance. Systematic uncertainties and boundaries are not considered which will significantly affect the analysis. Also, the decreasing Tracker resolution needs to be taken into account as increasing background contamination will affect the limit, as discussed in Section 4.3.3.

tance, dismissing layer 9, or even in the inner Tracker only acceptance could improve the limit significantly, as shown in Figure 5.11. Additionally, a looser selection removes cuts that require additional corrections, as discussed in Section 4.3.1.1. Especially the hit pickup efficiency in the external Tracker layers 1 and 9 require strong corrections with large time variation and uncertainty. On the other hand, even the loosening of the Tracker layer 9 fiducial volume, from ECAL area to layer 9 area, already showed worse results from interactions in RICH. Systematic uncertainties will significantly contribute to such an analysis, which requires an extensive study on its own. Also, the increasing background contamination from bin-to-bin migration, as is was discussed in Section 4.3.3, needs to be taken into account. The decreasing purity could compensate the gain in sample size. However, with an inner Tracker only acceptance, AMS-02 could increase the sensitivity of the measured anisotropy.

Finally, more satellite experiments have started taking data in the recent years, and others are planned. ISS-Cream[1] arrived at the Space Station on August 16, 2017, to measure charged nuclei up to knee energies with large acceptance. The experiment should be able to adapt the *IsoSkyMap* method and provide sensitive measurements of the proton, helium, and lithium anisotropy, including separated by isotopes. The Dark Matter Particle Explorer (DAMPE) was launched on December 17, 2015, as a stand-alone satellite to measure high energy electrons. For the same purpose, CALorimetric Electron Telescope (CALET) has been installed on the space station in August 2015. First results have been reported recently on the flux of electrons and positrons by both experiments in [189] and [190]. Figure 5.12 gives a broad overview of currently flying and planned direct detection experiments. The experiments are plotted with their acceptance on the x-axis and expected lifetime on the y-axis. From both, the number of particles that are expected to be measured can be calculated and are shown in the plot as dashed lines. Experiments are divided into space and balloon experiments, and whether or not they have a magnet. DAMPE, CALET, and ISS-Cream are expected to collect events by at least one order of

---

[1]Short for Cosmic Ray Energetics and Mass Experiment.

magnitude more than AMS-02. The larger acceptance makes the experiments valuable for the search in CR anisotropies. However, it should be noted, that AMS-02 will stay unique in the foreseen future, as it is the only high acceptance spectrometer, capable of separating matter from antimatter, based in space.

Figure 5.12.: Overview of currently flying and planned direct detection experiments [191]. The experiments are plotted with their acceptance on the x-axis and expected lifetime on the y-axis. From both, the number of particles that are expected to be measured can be calculated and are shown in the plot as dashed lines. Experiments are divided into space and balloon experiments, and whether or not they have a magnet. DAMPE, CALET, and ISS-Cream are expected to collect at least one order of magnitude more events than AMS-02, which is the only high acceptance spectrometer based in space.

6. Summary

By the time this thesis is written, AMS-02 measured cosmic rays for seven years without any atmospheric influences. It is expected that the detector can take data up to 2024 such that by now about 50% of the total data is collected. AMS-02 results pushed forward the understanding of cosmic rays, their origin and propagation up to a level never achieved before, challenging CR propagation models. The rise in the positron fraction and a hardening in the flux of protons and helium are exciting and unexpected results that demand further studies. An anisotropy, as directional dependence in the particle's incoming directions, would provide an explicit signature to trace down the origin of these observations, if measured.

  This work provides a novel method to search for directional dependencies in particle fluxes from a simulation of the isotropic sky as it is expected to be seen by a detector, named *IsoSkyMap*. Herein the livetime, as the fraction of time in which the detector was ready to measure a new event, is projected on the celestial sphere by using incoming directions of selected events which follow the detectors geometrical acceptance without using Monte-Carlo simulated data. Inefficiencies in the detector performance, originating from an increased rate of low energetic particles towards the geomagnetic poles introduced by the Earth's magnetic field, were identified and quantified as a function of the geomagnetic latitude. The results are applied as corrections to the simulated particle rate in the *IsoSkyMap*. Corrections were obtained in two independent ways, a correction from a rate comparison in a *signal-free* coordinate system, named *rate-correction*, and directly from selection efficiencies. Differences in the strength of corrections in both methods were considered as systematic uncertainty. Undesired effects from unstable operations were studied carefully and removed in a second based definition of a *good second*. The Sun's ability to deform the Earth's magnetic field during active periods was found to be of major impact. Periods of high solar activity are identified in periods of a second, using the TRD on top of the detector and the Tracker. *IsoSkyMaps* allow for an *absolute* recovery of full three-dimensional dipole anisotropies. The measurement of, such absolute anisotropies, has never been achieved before within AMS-02 or other experiments. Different coordinate systems are used to study different impacts on the measurement, which are enhanced in a specific coordinate system. Greenwich True Of Date (GTOD) coordinates were used to identify effects introduced by the detector operation or other environmental effects. Geocentric Solar Ecliptic (GSE) coordinates are studied for the

search of solar effects, or systematic effects related to the AMS-02 day-night cycle. The search for an astrophysical source was performed in galactic coordinates, which are sensitive for the Heliosphere, as well.

The method has been applied to positrons, electrons, and protons. Data of the first five years of data taking up to March 2016 were analyzed with a total of 69,394 identified positron events and 913,421 identified electron events, in an energy range of 16 GeV to 350 GeV. For positrons, where the measurement of an anisotropy is of high interest to explain the rise in the positron fraction, the results can be summarized to:

- No sign of a dipole anisotropy of galactic origin could be found. An upper limit on the dipole amplitude for positrons is set to $\delta_{e^+}^{95\%}(>16 \text{ GV})=1.87\%$, using a Bayesian approach (see Figure 4.57).

- In GSE, no dipole anisotropy is found, either (see Figure 4.58).

- No time-dependent variation in the arrival direction of positrons is found in any coordinate system, above the statistical limitation. The measurement of the time dependence provides a systematic validation of the result.

- In a complementary search of *relative* anisotropies, comparing the positron angular distribution in the celestial sky with the one of electrons or protons, the same results were found.

With event numbers expected to be collected until 2024, the upper limit on the dipole strength can be improved to the 1% level.

For electrons, which have higher sensitivity for a dipole anisotropy because of the increased sample size, results are:

- No sign of a dipole anisotropy of galactic origin could be found. An upper limit on the dipole amplitude is set to $\delta_{e^-}^{95\%}(>16 \text{ GV})=0.42\%$, using a Bayesian approach (see Figure 4.56).

- In GSE, a constant and small excess in the negative east-west direction within the ecliptic plane was observed (see Figure 4.56). The observation can be explained by a variation of the energy scale in ECAL with the AMS-02 day-night cycle (see Figure 4.53).

- No time-dependent variation in the arrival direction of electrons is found in any coordinate system.

- A complementary search, comparing the electron angular distribution in the celestial sky with the one of protons, is in good agreement with the *IsoSkyMap* analysis. However, deviations from isotropy appear in GTOD only for the *relative* study, pointing out a systematic limitation of this sort of analysis.

- In a dedicated study of the systematic limitation of the *IsoSkyMap* method in electrons, showed no sign of any systematic limitation down to the per-mille level.

Compared to other CR experiments, the obtained limits on the dipole amplitude are weaker, which is due to the limited acceptance of AMS-02 compared to FERMI-LAT or ground-based telescopes. However, the ability to separate the analysis to specific particles or divide them by charge sign is unique among cosmic ray experiments and improves the sensitivity towards physical processes assumed to induce anisotropies.

IsoSkyMaps have also been produced for protons to search for absolute dipole anisotropies in the flux of protons, for the first time. With AMS-02, 51 million protons with rigidity from 18 GV to 1800 GV were selected. The propagation distance in the galaxy is larger for protons than for electrons or positrons, because of the smaller energy loss during propagation. This allows to investigate the source propagation from the galactic center, where the source density is higher, towards the outer galactic regions. Also, the hardening in the proton flux, measured by AMS-02, can be tested to be of point-source origin and the large number of events allows to study the limits of the *IsoSkyMap* method. The following results were found for protons:

- A limitation on the sensitivity of the analysis was identified on the per-mille level from the finite accuracy of the description of the detector performance (see Figure 4.34).

- In galactic coordinates, no excess above the systematic limitation is found and an upper limit on the dipole amplitude is set to $\delta_p^{95\%}(>18 \text{ GV})=0.13\%$, using a Bayesian approach (see Figure 4.47).

- In GSE, an excess in negative forward-backward direction, away from the sun, is found to be above the limitation from systematics towards high rigidities. The amplitude is correlated to a variation in the Tracker rigidity measurement with the AMS-02 day-night cycle (see Figure 4.41). The dipole was found, not to propagate into the galactic coordinate system, so it does not impact the search for astrophysical sources.

- To validate results, a complementary measurement of a *relative* anisotropy, comparing the angular distribution in the celestial sky of low rigidity protons with the one of protons at higher rigidity, was developed. The method only provides results above 80 GV, with excellent agreement to the *IsoSkyMap* method (see Figure 5.1 and Figure 5.2). An upper limit on a dipole amplitude in galactic coordinates is set to $\delta_{p/p^*}^{95\%}(>80 \text{ GV})=0.22\%$ with the *relative* anisotropy, compared to $\delta_p^{95\%}(>80 \text{ GV})=0.19\%$ with the *absolute* result.

- No time-dependent variation in the arrival direction of protons is found in any coordinate system.

A connection to anisotropy measurements of ground-based experiments, where an anisotropy could be found above 100 GeV, but so far could not be pinned down because of limitations from which these type of experiments suffer, is of interest and demands to decrease the upper limit on the dipole anisotropy even more in the future. This can only be achieved by absolute anisotropy measurements but have to be taken over by following experiments with higher acceptance like ISS-Cream. This work gives the recipe and sets standards for future analysis. For example, the impact of contamination in the analysis sample from background or the finite energy measurement, has not been studied in previous publications. Such contaminations can wash out a dipole signal and significantly decrease the sensitivity of the measurement.

In general, the method introduced in this thesis allows to study absolute anisotropy measurements without limitation to any particle species. In future, a measurement of the absolute anisotropy of the most abundant elements helium and lithium is of interest, since lithium is a pure secondary, while with helium a mass dependence can be studied.

Bibliography

[1] Aguilar, M. et al., *Phys. Rev. Lett.* **2013**, *110*, 141102.

[2] Accardo, L. et al., *Phys. Rev. Lett.* **2014**, *113*, 121101.

[3] Aguilar, M. et al., *Phys. Rev. Lett.* **2014**, *113*, 121102.

[4] Aguilar, M. et al., *Phys. Rev. Lett.* **2014**, *113*, 221102.

[5] Aguilar, M. et al., *Phys. Rev. Lett.* **2015**, *114*, 171103.

[6] Aguilar, M. et al., *Phys. Rev. Lett.* **2015**, *115*, 211101.

[7] Beatty, J. J.; Westerhoff, S. *Annual Review of Nuclear and Particle Science* **2009**, *59*, 319–345.

[8] Baldini, L. Space-Based Cosmic-Ray and Gamma-Ray Detectors: A Review. prepared for the 2014 ISAPP summer school, Villa Carlotta, Belgirate, arXiv:1407.7631, 2014.

[9] George, J. *The Astrophysical Journal* **2009**, *698*, 1666.

[10] Reynolds, S. P. *Annu. Rev. Astron. Astrophys.* **2008**, *46*, 89–126.

[11] Fermi, E. *Physical Review* **1949**, *75*, 1169.

[12] Drury, L. O. *Reports on Progress in Physics* **1983**, *46*, 973.

[13] Kunz, S. M. Constraints on Transport Models for Galactic Cosmic Rays and their Implications for the Anomalous Positron Abundance. Ph.D. thesis, Karlsruher Institut für Technologie (KIT), 2014.

[14] Gebauer, I. An Anisotropic Model for Galactic Cosmic Ray Transport and its Implications for Indirect Dark Matter Searches. Ph.D. thesis, Karlsruher Institut für Technologie (KIT), 2010.

[15] Aguilar, M. et al., *Phys. Rev. Lett.* **2016**, *117*, 091103.

[16] Lipari, P. *Physical Review D* **2017**, *95*, 063009.

[17] Kopp, J. *Physical Review D* **2013**, *88*, 076013.

[18] Feng, L.; Yang, R.-Z.; He, H.-N.; Dong, T.-K.; Fan, Y.-Z.; Chang, J. *Physics Letters B* **2014**, *728*, 250–255.

[19] Cirelli, M.; Kadastik, M.; Raidal, M.; Strumia, A. *Nuclear Physics B* **2013**, *873*, 530 – 533.

[20] Ibe, M.; Iwamoto, S.; Matsumoto, S.; Moroi, T.; Yokozaki, N. *Journal of High Energy Physics* **2013**, *2013*, 29.

[21] Kajiyama, Y.; Okada, H.; Toma, T. *The European Physical Journal C* **2014**, *74*, 2722.

[22] Dienes, K. R.; Kumar, J.; Thomas, B. *Physical Review D* **2013**, *88*, 103509.

[23] Bergström, L.; Bringmann, T.; Cholis, I.; Hooper, D.; Weniger, C. *Physical review letters* **2013**, *111*, 171101.

[24] Kohri, K.; Sahu, N. *Physical Review D* **2013**, *88*, 103001.

[25] Dev, P. B.; Ghosh, D. K.; Okada, N.; Saha, I. *Physical Review D* **2014**, *89*, 095001.

[26] Ibarra, A.; Lamperstorfer, A. S.; Silk, J. *Physical Review D* **2014**, *89*, 063539.

[27] Zhao, Y.; Zurek, K. M. *Journal of High Energy Physics* **2014**, *2014*, 17.

[28] Chen, C.-H.; Chiang, C.-W.; Nomura, T. *Physics Letters B* **2015**, *747*, 495–499.

[29] Jin, H.-B.; Wu, Y.-L.; Zhou, Y.-F. *Physical Review D* **2015**, *92*, 055027.

[30] Cui, M.-Y.; Yuan, Q.; Tsai, Y.-L. S.; Fan, Y.-Z. *Physical Review Letters* **2017**, *118*, 191101.

[31] Cuoco, A.; Krämer, M.; Korsmeier, M. *Physical Review Letters* **2017**, *118*, 191102.

[32] Linden, T.; Profumo, S. *The Astrophysical Journal* **2013**, *772*, 18.

[33] Mertsch, P.; Sarkar, S. *Physical Review D* **2014**, *90*, 061301.

[34] Cholis, I.; Hooper, D. *Physical Review D* **2013**, *88*, 023013.

[35] Erlykin, A.; Wolfendale, A. W. *Astroparticle Physics* **2013**, *49*, 23–27.

[36] Yin, P.-F.; Yu, Z.-H.; Yuan, Q.; Bi, X.-J. *Physical Review D* **2013**, *88*, 023001.

[37] Erlykin, A.; Wolfendale, A. *Astroparticle Physics* **2013**, *50*, 47–50.

[38] Amato, E. The theory of pulsar wind nebulae. International Journal of Modern Physics: Conference Series. 2014; p 1460160.

[39] Blasi, P. *Brazilian Journal of Physics* **2014**, *44*, 426–440.

[40] Gaggero, D.; Maccione, L.; Grasso, D.; Di Bernardo, G.; Evoli, C. *Physical Review D* **2014**, *89*, 083007.

[41] Di Mauro, M.; Donato, F.; Fornengo, N.; Lineros, R.; Vittino, A. *Journal of Cosmology and Astroparticle Physics* **2014**, *2014*, 006.

[42] Kohri, K.; Ioka, K.; Fujita, Y.; Yamazaki, R. *Progress of Theoretical and Experimental Physics* **2016**, *2016*.

[43] Cowsik, R.; Burch, B.; Madziwa-Nussinov, T. *The Astrophysical Journal* **2014**, *786*, 124.

[44] Blum, K.; Katz, B.; Waxman, E. *Physical review letters* **2013**, *111*, 211101.

[45] Kappl, R.; Winkler, M. W. *Journal of Cosmology and Astroparticle Physics* **2014**, *2014*, 051.

[46] Giesen, G.; Boudaud, M.; Génolini, Y.; Poulin, V.; Cirelli, M.; Salati, P.; Serpico, P. D. *Journal of Cosmology and Astroparticle Physics* **2015**, *2015*, 023.

[47] Evoli, C.; Gaggero, D.; Grasso, D. *Journal of Cosmology and Astroparticle Physics* **2015**, *2015*, 039.

[48] Kappl, R.; Reinert, A.; Winkler, M. W. *Journal of Cosmology and Astroparticle Physics* **2015**, *2015*, 034.

[49] F. A. Aharonian, S. V. Bogovalov and D. Khangulyan, *Nature* **2012**, *482*, 507–509.

[50] Weinreuter, A. M. On the correlation between cosmic ray arrival directions and the sources of galactic cosmic rays. Ph.D. thesis, Karlsruher Institut für Technologie (KIT), 2016.

[51] Zwicky, F. *Helvetica Physica Acta* **1933**, *6*, 110–127.

[52] Rubin, V. C.; Thonnard, N.; Ford, W. K., Jr. *APJL* **1978**, *225*, L107–L111.

[53] X-ray: NASA/CXC/CfA/M.Markevitch et al.; Optical: NASA/STScI; Magellan/U.Arizona/D.Clowe et al.; Lensing Map: NASA/STScI; ESO WFI; Magellan/U.Arizona/D.Clowe et al, Overlayed image of the Bullet Cluster. `http://chandra.harvard.edu/photo/2006/1e0657/index.html` Released: August 21, 2006, Color code: X-ray: Pink; Optical: White/Orange; Lensing Map: Blue.

[54] Fukuda, Y et al., *Physical Review Letters* **1998**, *81*, 1562.

[55] Ma, E. *Physical Review D* **2006**, *73*, 077301.

[56] Fukugita, M.; Liu, G.-C.; Sugiyama, N. *Physical Review Letters* **2000**, *84*, 1082.

[57] Dodelson, S.; Widrow, L. M. *Physical Review Letters* **1994**, *72*, 17.

[58] Bode, P.; Ostriker, J. P.; Turok, N. *The Astrophysical Journal* **2001**, *556*, 93.

[59] Baer, H.; Haider, M.; Kraml, S.; Sekmen, S.; Summy, H. *Journal of Cosmology and Astroparticle Physics* **2009**, *2009*, 002.

[60] Covi, L.; Kim, H. B.; Kim, J. E.; Roszkowski, L. *Journal of High Energy Physics* **2001**, *2001*, 033.

[61] Ade, P. and others, *Astronomy & Astrophysics* **2014**, *571*, A15.

[62] V. Sanglard et al. (EDELWEISS Collaboration), *Physical Review D* **2005**, *71*, 122002.

[63] CDMS II Collaboration and others, *Science* **2010**, *327*, 1619–1621.

[64] Angle, J et al., *Phys. Rev. Lett.* **2008**, *100*, 021303.

[65] D. S. Akerib et al. (LUX Collaboration), *Phys. Rev. Lett.* **2014**, *112*, 091303.

[66] Liu, J. and others, *Nat Phys* **2017**, *13*, 212–216.

[67] XENON Collaboration, *Phys. Rev. Lett.* **2017**, *119*, 181301.

[68] Petricca, F and others (CRESST collaboration), *arXiv:1711.07692* **2017**, XV International Conference on Topics in Astroparticle and Underground Physics, TAUP2017, submitted to Journal of Physics: Conference Series (JPCS).

[69] CMS collaboration and others, *Journal of Physics G: Nuclear and Particle Physics* **2007**, *34*, 995.

[70] Airapetian, A and others, *ATLAS detector and physics performance: Technical Design Report, 2*; ATLAS-TDR-015, 1999.

[71] Buchmueller, O.; Doglioni, C.; Wang, L.-T. *Nature Physics* **2017**, *13*, 217–223.

[72] Abercrombie, D. and others, *arXiv:1507.00966* **2015**,

[73] F. Aharonian et al. (HESS Collaboration), *Physical Review Letters* **2006**, *97*, 221102.

[74] Ackermann, M et al, *The Astrophysical Journal Supplement Series* **2012**, *203*, 4.

[75] Hooper, D.; Goodenough, L. *Physics Letters B* **2011**, *697*, 412 – 428.

[76] Vitale, V. and Morselli, A. For the Fermi/LAT Collaboration, *Nuclear Instruments and Methods in Physics Research Section A: Accelerators, Spectrometers, Detectors and Associated Equipment* **2011**, *630*, 147–150.

[77] Morselli, A.; Canadas, B. a. The Indirect Search for Dark Matter from the centre of the Galaxy with the Fermi LAT. Invited talk presented at the Workshop "SciNeGHE 2010", September 8-10, 2010, Trieste, Italy. To appear in Il Nuovo Cimento C - Colloquia on physics, arXiv:1012.2292, 2010.

[78] de Boer, W.; Bosse, L.; Gebauer, I.; Neumann, A.; Biermann, P. L. *Physical Review D* **2017**, *96*, 043012.

[79] Karle, A. et al., *Nuclear Physics B-Proceedings Supplements* **2003**, *118*, 388–395.

[80] Adriani, O. et al., *Nature* **2009**, *458*, 607.

[81] Manconi, S.; Mauro, M. D.; Donato, F. *Journal of Physics: Conference Series* **2017**, *841*, 012006.

[82] Henbest, N.; Couper, H. *The guide to the galaxy*; CUP Archive, 1994.

[83] Council, N.R. and Sciences, D.E.P. and Board, S.S. and Physics, C.S.S., *Exploration of the Outer Heliosphere and the Local Interstellar Medium: A Workshop Report*; National Academies Press, 2004.

[84] Graziani, M. Time dependence of electron and positron fluxes measured with the AMS-02 spectrometer. Ph.D. thesis, Università degli Studi di Perugia, 2015; with data from http://www.sidc.be/silso/datafiles and http://neutronm.bartol.udel.edu.

[85] Desiati, P.; Lazarian, A. *The Astrophysical Journal* **2012**, *762*, 44.

[86] López-Barquero, V.; Xu, S.; Desiati, P.; Lazarian, A.; Pogorelov, N.; Yan, H. *The Astrophysical Journal* **2017**, *842*, 54.

[87] Zhang, M.; Zuo, P.; Pogorelov, N. *The Astrophysical Journal* **2014**, *790*, 5.

[88] Weiss, N. *Astronomy and Geophysics* **2002**, *43*, 3.9–3.14.

[89] Kaase, A. Earth's Magnetosphere and Plasmasheet. NASA/Goddard `https://www.nasa.gov/mission_pages/sunearth/science/magnetosphere2.html`, Aug. 7, 2017.

[90] Smart, D.; Shea, M. *Advances in Space Research* **2005**, *36*, 2012–2020.

[91] Tsyganenko, N. *Planetary and Space Science* **1989**, *37*, 5–20.

[92] Compton, A. H.; Getting, I. A. *Physical Review* **1935**, *47*, 817.

[93] Hess, V. F. *Terrestrial Magnetism and Atmospheric Electricity* **1932**, *37*, 399–405.

[94] Pablo M. Bauleo and Julio RodrÃguez Martino, *Nature* **2009**, *458*, 847–851.

[95] Sinnis, G. and Milagro Collaboration and others, *Nuclear Physics B-Proceedings Supplements* **1995**, *43*, 141–144.

[96] The Tibet ASγ Collaboration, *Journal of Physics: Conference Series* **2008**, *120*, 062024.

[97] Abraham, J. and others, *Nuclear Instruments and Methods in Physics Research Section A: Accelerators, Spectrometers, Detectors and Associated Equipment* **2010**, *620*, 227–251.

[98] Tluczykont, M. et al., *Advances in Space Research* **2011**, *48*, 1935 – 1941.

[99] Falcke, H. et al., *Nature* **2005**, *435*, 313–316.

[100] Linsley, J. *Phys. Rev. Lett.* **1975**, *34*, 1530–1533.

[101] D.M. Edge and others, *Journal of Physics G: Nuclear Physics* **1978**, *4*, 133.

[102] Deligny, O. Cosmic-Ray Anisotropies: A Review. XXV European Cosmic Ray Symposium - eConf C16-09-04.3. 2016.

[103] IceCube Collaboration, *The Astrophysical Journal* **2016**, *826*, 220.

[104] Abdo, A and others, *The Astrophysical Journal* **2009**, *698*, 2121.

[105] Di Sciascio, G.; Iuppa, R. *On the Observation of the Cosmic Ray Anisotropy below 10^{15} eV*; Nova Science Publishers, New York, 2013; updated version of the invited review in the book "Homage to the discovery of Cosmic Rays", arXiv:1407.2144.

[106] Seo, E.-S. a. *Advances in Space Research* **2004**, *33*, 1777–1785.

[107] Bonvicini, V. a. *Nuclear Instruments and Methods in Physics Research Section A: Accelerators, Spectrometers, Detectors and Associated Equipment* **2001**, *461*, 262–268.

[108] Adriani, O. et al. *The Astrophysical Journal* **2015**, *811*, 21.

[109] Casaus, J. Determination of the positron anisotropy with AMS. Proceedings of the 33rd International Cosmic Rays Conference, Rio Janeiro, Brazil. 2013.

[110] AMS-02 website. AMS collaboration: http://www.ams02.org, 2016.

[111] Kirn, T.; Siedenburg, T. *Nuclear Instruments and Methods in Physics Research Section A* **2004**, *535*, 165–170.

[112] Artru, X.; Yodh, G. B.; Mennessier, G. *Phys. Rev. D* **1975**, *12*, 1289–1306.

[113] Jackson, J. D. *Klassische Elektrodynamik*, 4th ed.; de Gruyter: Berlin [u.a.], 2006.

[114] Nikl, M. *Measurement Science and Technology* **2006**, *17*, R37.

[115] Andronic, A.; Wessels, J. *Nuclear Instruments and Methods in Physics Research Section A: Accelerators, Spectrometers, Detectors and Associated Equipment* **2012**, *666*, 130 – 147, Advanced Instrumentation.

[116] Gast, H. Identification of cosmic-ray positrons with the transition radiation detector of the AMS experiment on the International Space Station. Proceedings, 33rd International Cosmic Ray Conference (ICRC2013): Rio de Janeiro, Brazil, July 2-9, 2013. 2013; p 0359.

[117] Heil, M. Operations and Alignment of the AMS-02 Transition Radiation Detector. Proceedings, 33rd International Cosmic Ray Conference (ICRC2013): Rio de Janeiro, Brazil, July 2-9, 2013. 2013; p 1232.

[118] Basili, A et al., *Nuclear Instruments and Methods in Physics Research Section A: Accelerators, Spectrometers, Detectors and Associated Equipment* **2013**, *707*, 99–113.

[119] Bindi, V et al., *Nuclear Instruments and Methods in Physics Research Section A: Accelerators, Spectrometers, Detectors and Associated Equipment* **2010**, *623*, 968–981.

[120] Bindi, V. The AMS-02 time of flight (TOF) system: construction and overall performances in space. Proceedings, 33rd International Cosmic Ray Conference (ICRC2013): Rio de Janeiro, Brazil, July 2-9, 2013. 2013; p 1232.

[121] Bindi, V et al., *Nuclear Instruments and Methods in Physics Research Section A: Accelerators, Spectrometers, Detectors and Associated Equipment* **2014**, *743*, 22–29.

[122] K. Lübelsmeyer et al., *Nuclear Instruments and Methods in Physics Research Section A: Accelerators, Spectrometers, Detectors and Associated Equipment* **2011**, *654*, 639 – 648.

[123] S. Ahlen et al., *Nuclear Instruments and Methods in Physics Research Section A: Accelerators, Spectrometers, Detectors and Associated Equipment* **1994**, *350*, 351 – 367.

[124] M. Aguilar et al., *Physics Reports* **2002**, *366*, 331 – 405.

[125] Duranti, M. Measurement of the Atmospheric Muon Flux on Ground with the AMS-02 Detector. Ph.D. thesis, Università degli Studi di Perugia, 2011.

[126] Zuccon, P. *Nuclear Instruments and Methods in Physics Research Section A: Accelerators, Spectrometers, Detectors and Associated Equipment* **2008**, *596*, 74 – 78, Proceedings of the 8th International Conference on Large Scale Applications and Radiation Hardness of Semiconductor Detectors.

[127] Bazo, J. In-flight operations and efficiency of the AMS-02 silicon tracker. Proceedings, 33rd International Cosmic Ray Conference (ICRC2013): Rio de Janeiro, Brazil, July 2-9, 2013. 2013.

[128] Haino, S. *Nuclear Instruments and Methods in Physics Research Section A: Accelerators, Spectrometers, Detectors and Associated Equipment* **2013**, *699*, 221 – 224, Proceedings of the 8th International Hiroshima Symposium on the Development and Application of Semiconductor Tracking Detectors, Academia Sinica, Taipei, Taiwan, December 5-8, 2011.

[129] Zuccon, P. AMS-02 Track reconstruction and rigidity measurement. Proceedings, 33rd International Cosmic Ray Conference (ICRC2013): Rio de Janeiro, Brazil, July 2-9, 2013. 2013.

[130] B. Alpat et al., *Nuclear Instruments and Methods in Physics Research Section A: Accelerators, Spectrometers, Detectors and Associated Equipment* **2010**, *613*, 207 – 217.

[131] Yan, Q. The AMS-02 time of flight (TOF) system: construction and overall performances in space. Proceedings of the 33rd International Cosmic Rays Conference, Rio Janeiro, Brazil. 2013.

[132] Vitillo, S. *Proc. 34th ICRC (Netherlands)* **2015**, *429*.

[133] G. Alberti et al., *IEEE Aerospace and Electronic Systems Magazine* **2014**, *29*, 4–13.

[134] von Doetinchem, P.; Karpinski, W.; Kirn, T.; Luebelsmeyer, K.; Schael, S.; Wlochal, M. *Nucl. Phys. Proc. Suppl.* **2009**, *197*, 15–18.

[135] Pereira, R. *Nuclear Instruments and Methods in Physics Research Section A: Accelerators, Spectrometers, Detectors and Associated Equipment* **2011**, *639*, 37 – 41, Proceedings of the Seventh International Workshop on Ring Imaging Cherenkov Detectors.

[136] Giovacchini, F. *Nuclear Instruments and Methods in Physics Research Section A: Accelerators, Spectrometers, Detectors and Associated Equipment* **2014**, *766*, 57 – 60, Proceedings of the Eighth International Workshop on Ring Imaging Cherenkov Detectors Shonan, Kanagawa, Japan, December 2-6, 2013.

[137] Grupen, C.; Shwartz, B. *Particle detectors*; Cambridge university press, 2008; Vol. 26.

[138] Gillard, W. High precision measurement of the AMS-RICH aerogel refractive index with cosmic ray. Proceedings of the 33rd International Cosmic Rays Conference, Rio Janeiro, Brazil. 2013.

[139] Giovacchini, F. In-flight determination of the AMS-RICH photon yield. Proceedings of the 33rd International Cosmic Rays Conference, Rio Janeiro, Brazil. 2013.

[140] Cadoux, F. et al. *Nuclear Physics B - Proceedings Supplements* **2002**, *113*, 159 – 165.

[141] Adloff, C. et al. *Nuclear Instruments and Methods in Physics Research Section A: Accelerators, Spectrometers, Detectors and Associated Equipment* **2013**, *714*, 147 – 154.

[142] Falco, S. D. Performance of the AMS-02 Electromagnetic Calorimeter in Space. Proceedings of the 33rd International Cosmic Rays Conference, Rio Janeiro, Brazil. 2013.

[143] Rosier-Lees, S. on behalf of the AMS02 collaboration, *Journal of Physics: Conference Series* **2012**, *404*, 012034.

[144] Cervelli, F. et al. *Nuclear Instruments and Methods in Physics Research Section A: Accelerators, Spectrometers, Detectors and Associated Equipment* **2002**, *490*, 132 – 139.

[145] Falco, S. D. *Advances in Space Research* **2010**, *45*, 112 – 122.

[146] Basara, L. Energy Calibration with MIP in space and charge measurement with AMS02 Electromagnetic Calorimeter. Proceedings of the 33rd International Cosmic Rays Conference, Rio Janeiro, Brazil. 2013.

[147] Cadoux, F. et al. *IEEE Transactions on Nuclear Science* **2008**, *55*, 817–821.

[148] Capell, M.; Cortina, E.; AMS-02 Collaboration, *International Cosmic Ray Conference* **2003**, *4*, 2173.

[149] Lebedev, A. *International Cosmic Ray Conference* **2005**, *3*, 377.

[150] Duffett-Smith, P.; Zwart, J. *Practical Astronomy with your calculator or spreadsheet*;
       Cambridge University Press, 2011.

[151] Blaauw, A.; Gum, C. S.; Pawsey, J. L.; Westerhout, G. *Monthly Notices of the Royal
       Astronomical Society* **1960**, *121*, 123–131.

[152] Reid, M. J.; Brunthaler, A. *The Astrophysical Journal* **2004**, *616*, 872.

[153] NASA/JPL-Caltech/R. Hurt (SSC-Caltech), `http://www.spitzer.
       caltech.edu/Media/releases/ssc2008-10/ssc2008-10b.
       shtml`, Version Date: 2008-06-03.

[154] Benz, B. Studies for Dipole Anisotropy Searches in the Arrival Directions of Cos-
       mic Rays with AMS-02. Bachelorthesis, Institut für Experimentelle Kernphysik
       (EKP) am KIT, 2017.

[155] Cassiday, GL et al, *Nuclear Physics B-Proceedings Supplements* **1990**, *14*, 291–298.

[156] Bird, DJ et al, *The Astrophysical Journal* **1999**, *511*, 739.

[157] Ackermann, M et al, *Physical Review D* **2010**, *82*, 092003.

[158] Gebauer, I. *Proc. 34th ICRC (Netherlands)* **2015**, *PoS(ICRC2015)408.*

[159] Abdollahi, S et al, *Physical Review Letters* **2017**, *118*, 091103.

[160] Gebauer, I. *Proc. 34th ICRC (Netherlands)* **2015**, *PoS(ICRC2015)404.*

[161] Meehan, M. and Vandenbroucke, J. and others, *Proc. 35th ICRC (South Korea)* **2017**,
       PoS(ICRC2017)170.

[162] Li, T.-P.; Ma, Y.-Q. *The Astrophysical Journal* **1983**, *272*, 317–324.

[163] The HEALPix Primer. `http://healpix.sourceforge.net`, Version
       Date: June 18, 2010.

[164] Schuckardt, D. Limits on the dipole anisotropy in the flux of cosmic ray leptons
       with AMS-02. M.Sc. thesis, Karlsruher Institut für Technologie (KIT), 2014.

[165] Deligny, O. a. Large-Scale Distribution of Arrival Directions of Cosmic Rays De-
       tected at the Pierre Auger Observatory Above 10 PeV. Journal of Physics: Confer-
       ence Series. 2014; p 012002.

[166] Mana, C. Three Lectures on Probability and Statistics. notes for the lectures on
       "Practical Statistics" at the 9th CERN Latin-American School of High Energy
       Physics, Mexico, arXiv:1610.05590, 2016.

[167] Feldman, G. J.; Cousins, R. D. *Physical Review D* **1998**, *57*, 3873.

[168] Berdugo, J and Casaus, J and Mana, C and Velasco, MA, *arXiv:1510.01221* **2015**,

[169] Vagelli, V. Measurement of the cosmic $e^+ + e^-$ Flux from 0.5 GeV to 1 TeV with the
       Alpha Magnetic Spectrometer (AMS-02) on the International Space Station. Ph.D.
       thesis, Karlsruher Institut für Technologie (KIT), 2014.

[170] Graziani, M. Time dependence of electron and positron fluxes measured with the
       AMS-02 spectrometer. Ph.D. thesis, Università degli Studi di Perugia, 2015.

[171] Zurbach, C. *Nuclear Physics B - Proceedings Supplements* **2007**, *172*, 28 – 31.

[172] Grandi, D and others, *Proc. 34th ICRC (Netherlands)* **2015**, *PoS(ICRC2015)116*.

[173] Finlay, C.C. and others, *Geophysical Journal International* **2010**, *183*, 1216–1230.

[174] Boschini, MJ and others, *Proceedings of the 33rd International Cosmic Rays Conference, Rio Janeiro, Brazil* **2013**,

[175] US National Oceanic and Atmospheric Administration (NOAA): Space Weather Prediction Center (SWPC), Station K and A Indices. `http://www.swpc.noaa.gov/products/station-k-and-indices`, Retrieved: August 21, 2006.

[176] F.K. Bindel, and others, *Proc. 35th ICRC (South Korea)* **2017**, *PoS(ICRC2017)202*.

[177] I. Gebauer, On behalf of the AMS Collaboration, *Proc. 35th ICRC (South Korea)* **2017**, *PoS(ICRC2017)186*.

[178] La Vacca, G. Search for Cosmic Ray Anisotropy with the Alpha Magnetic Spectrometer on the International Space Station. XXV European Cosmic Ray Symposium. 2016.

[179] S. Della Torre and others, Geomagnetic Effects with AMS-02. AMS internal note, 2013; INFN Milano-Bicocca.

[180] Heil, M. Measurement of the positron fraction in cosmic rays from 0.5-350 GeV with the AMS-02 detector on the International Space Station. Ph.D. thesis, Karlsruher Institut für Technologie (KIT), 2013.

[181] N. Tomassetti and others, *The Astrophysical Journal Letters* **2017**, *849*, L32.

[182] Green, D. M. Measurement of the cosmic-ray proton spectrum from 54 GeV to 9.5 TeV with the Fermi Large Area Telescope. Ph.D. thesis, University of Maryland (College Park, Md.), 2016.

[183] Pato, M.; Lattanzi, M.; Bertone, G. *Journal of Cosmology and Astroparticle Physics* **2010**, *2010*, 020.

[184] Erlykin, A.; Wolfendale, A. W. *Astroparticle Physics* **2006**, *25*, 183–194.

[185] Sveshnikova, L.; Strelnikova, O.; Ptuskin, V. *Astroparticle Physics* **2013**, *50*, 33–46.

[186] Erlykin, A.; Wolfendale, A. W. *Journal of Cosmology and Astroparticle Physics* **2013**, *2013*, 006.

[187] The Pierre Auger Collaboration, *Science* **2017**, *357*, 1266–1270.

[188] @AMSISS on Twitter. AMS collaboration: https://twitter.com/AMSISS/status/861718022259691521, 8. May 2017.

[189] DAMPE Collaboration, *Nature* **2017**, *552*.

[190] Adriani, O. et al., *Physical review letters* **2017**, *119*, 181101.

[191] Bertucci, B. Overview of direct CR measurements. International Symposium on Very High Energy Cosmic Ray Interactions (ISVHECRI). 2014.

[192] Choutko, V. for AMS Computing, Events measured by AMS-02. AMS internal, 2017.

List of Figures

Appendix

A. Overview of coordinate systems

Figure A.1.: Overview of the coordinate systems used in this thesis. Important fix points and planes are marked. The color-scale denotes the AMS-02 observation time for protons with rigidity larger than 18 GV, estimated using the *IsoSkyMap* method described in Section 3.2.4. In Geomagnetic coordinates the ISS position is shown instead of the observation time on the celestial sky.
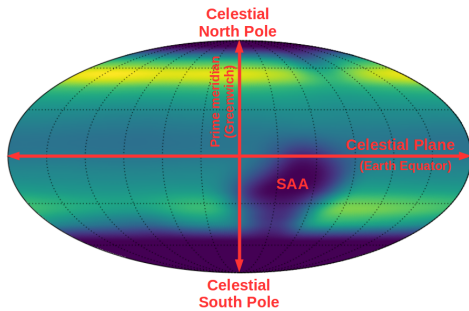
(a) **Greenwich True Of Date (GTOD):**
Bound to the Earth's surface. AMS-02 operational ffects enhanced *(Signal-free)*.
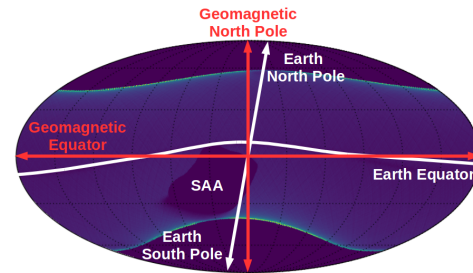
(b) **Magnetic Coordinates:**
Bound to the Earth's magnetic field. Effects from the Geomagnetic field enhanced *(Signal-free)*.
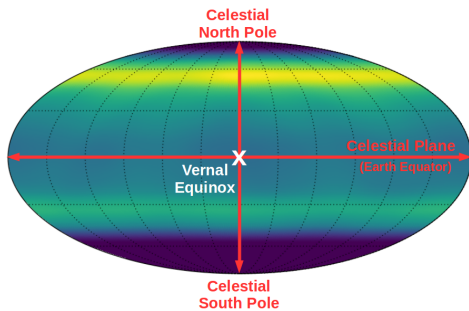
(c) **Equatorial Coordinates:**
Fixed with respect to distant stars. Used in ground-based observations *(Analysis system)*.
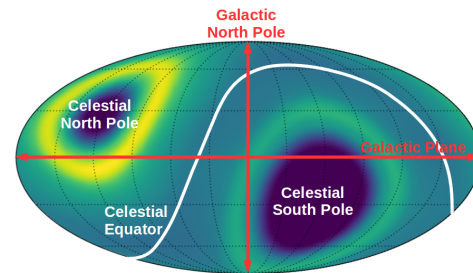
(d) **Galactic Coordinates:**
Fixed with respect to the galaxy. Most natural for galactic sources *(Analysis system)*.
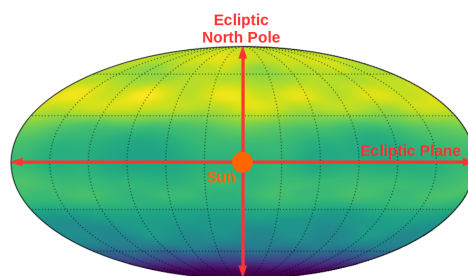
(e) **Geocentric Solar Ecliptic (GSE) Coordinates:**
Fixed with respect to the Sun *(Analysis system, but sensitive to the AMS-02 day-night cycle)*.

B. Numerical values of fit results

This appendix chapter contains the raw fit values in tables for the main results that are presented in this thesis. A detailed discussion on how the analyses are performed and noticeable deviations from the isotropic expectation, if any, can be found in the corresponding sections in Chapter 4 and the discussion in Chapter 5.

The fits, in bins of energy or rigidity for protons in the full time period are presented with the number of events in the signal and reference sample, the values of the three dipole components and their corresponding fit error, as well as the calculated dipole strength and upper limit on the dipole strength. The upper limit at 95% confidence level is constructed following the Bayesian approach described in Section 3.2.7. However, with the given values the limit can be calculated, using any approach preferred by the reader.

The number of reference events in the search for absolute anisotropies is of no physical interest and therefore is omitted. In the Tables B.7-B.12 also the systematic uncertainties on the dipole components Δ_ρ, obtained from the analysis in Section 4.3.1.2 is given, as well as the resulting systematic limitation calculated from these values. A measured dipole strength below this limitation is considered to be an artifact from the reference map.

Below the tables, the time dependent fit result in the seasonal binning is presented for all bins of energy. All three fit components are shown with error bars from the fit error. The dipole components in the seasonal binning are fitted by a constant, shown as black line, with a fit error shown as green area. The line is supposed to guide the eye for any trend or break in the time dependence. In most of the cases, the constant fit to the time dependence matches the time integrated result, showed in the comparison with the magenta dashed line that marks the time integrated result.

For the positron analysis a systematic deviation from the seasonal analysis and the time integrated analysis is found that arises from the limited statistics in the positron sample which makes the fit unstable. In the absolute protons a deviation is found for the rigidity bins where the result is dominated by the systematic limitation. As discussed, the sensitivity to artifacts in the *IsoSkyMap* is strongly dependent on available statistics.

B.1. Positron relative anisotropy - GAL

E_{Min} (GeV)	N_{Sig}	N_{Ref}	ρ_{NS}	$\sigma_{\rho_{NS}}$ (%)	ρ_{FB}	$\sigma_{\rho_{FB}}$ (%)	ρ_{EW}	$\sigma_{\rho_{EW}}$ (%)	δ (%)	$\delta^{95\%}$ (%)
16	69394	913421	-0.452	0.679	-0.128	0.673	0.853	0.663	0.974	1.774
25	34422	393084	-0.723	0.953	0.606	0.945	0.229	0.958	0.971	2.191
40	13937	129017	-0.454	1.492	1.529	1.481	1.137	1.501	1.959	3.762
65	5401	39598	-2.424	2.370	-0.139	2.352	1.815	2.388	3.031	5.912
100	2227	13434	-1.521	3.718	0.600	3.681	-1.725	3.723	2.377	7.767

Table B.1.: Fit of R_{e^+/e^-} positron relative anisotropy in **GAL**.
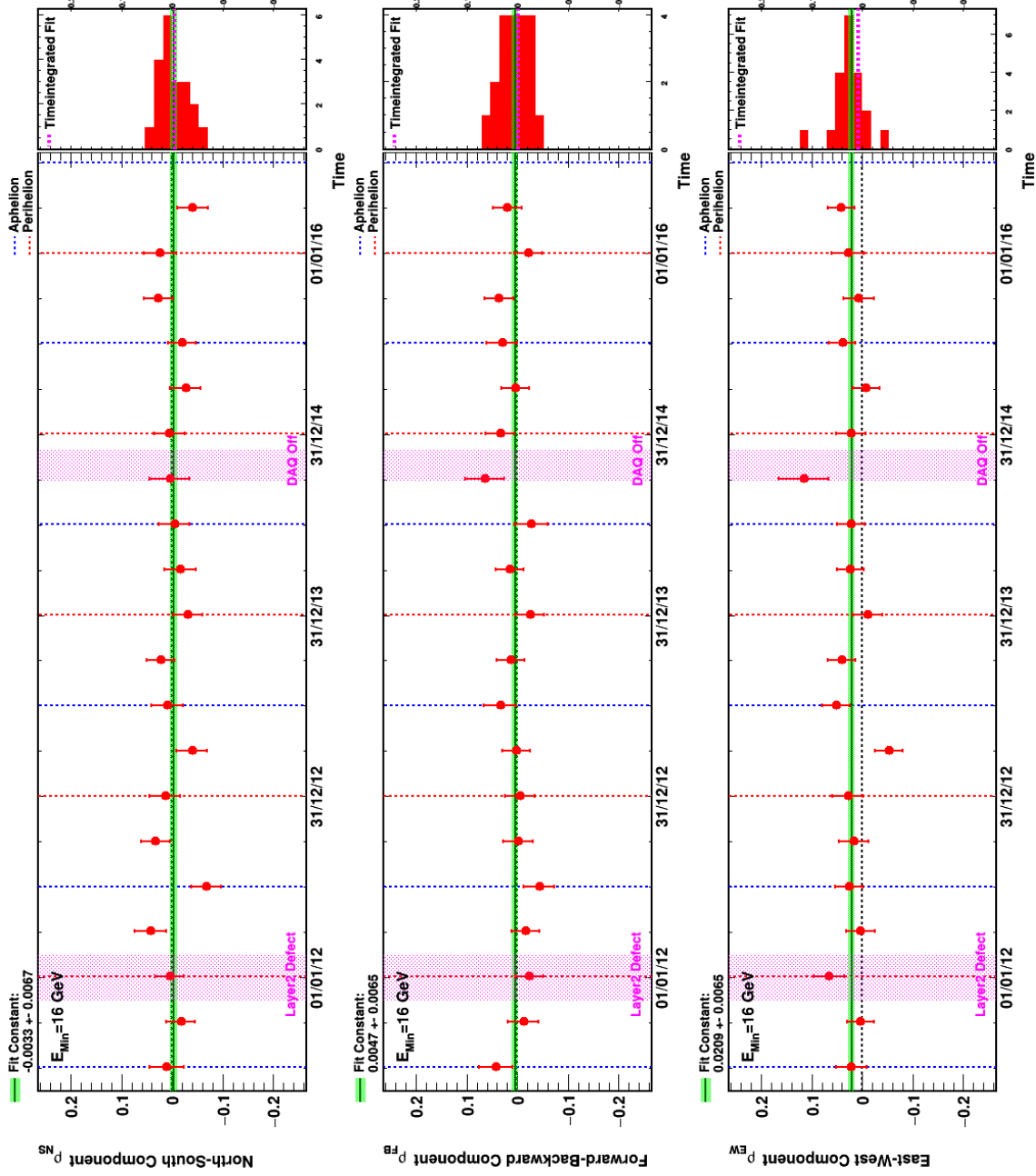
Figure B.2.: Seasonal fits of R_{e^+/e^-} positron relative anisotropy at a minimum energy of 16 GeV in **GAL**.
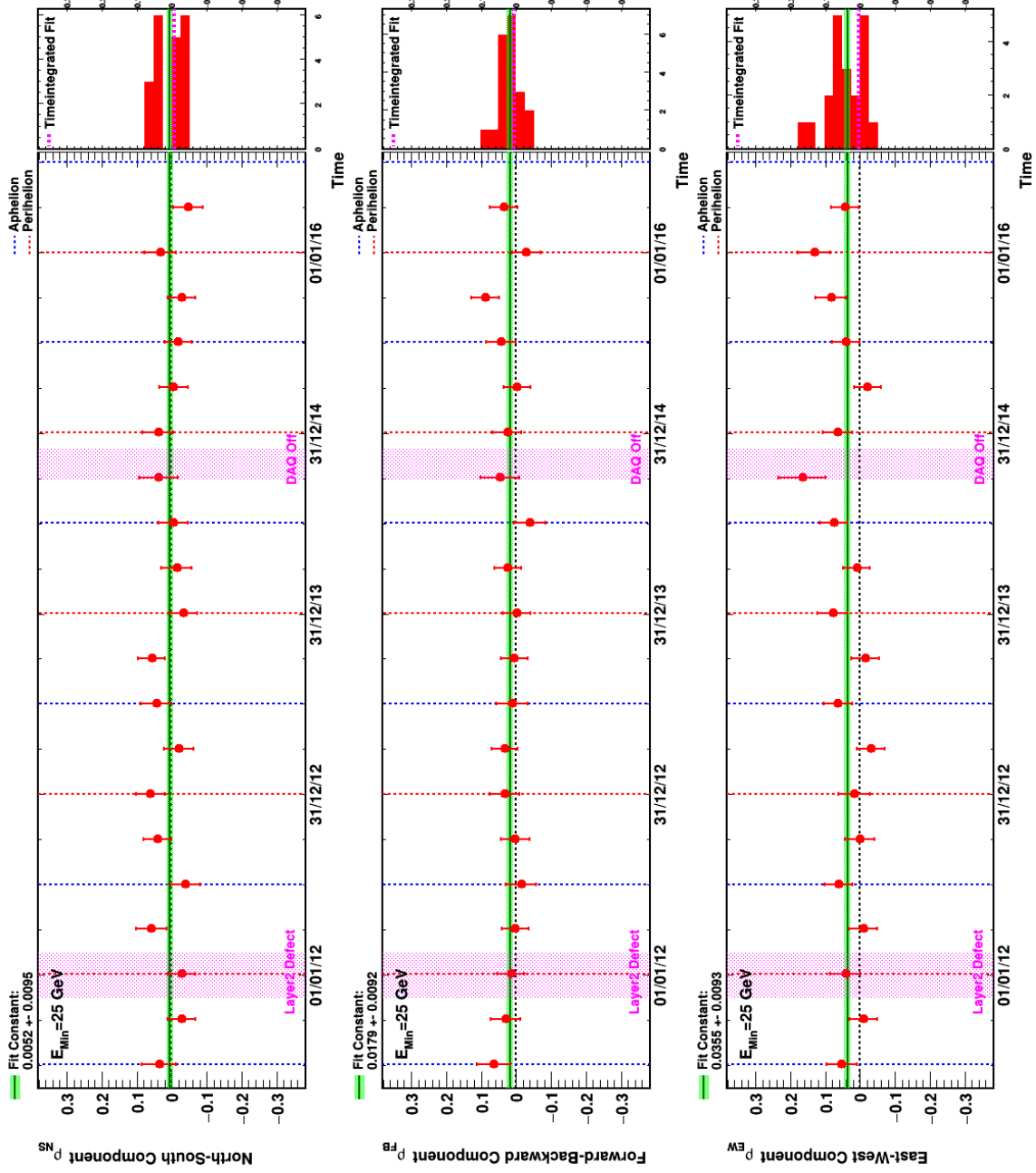
Figure B.3.: Seasonal fits of R_{e^+/e^-} positron relative anisotropy at a minimum energy of 25 GeV in **GAL**.
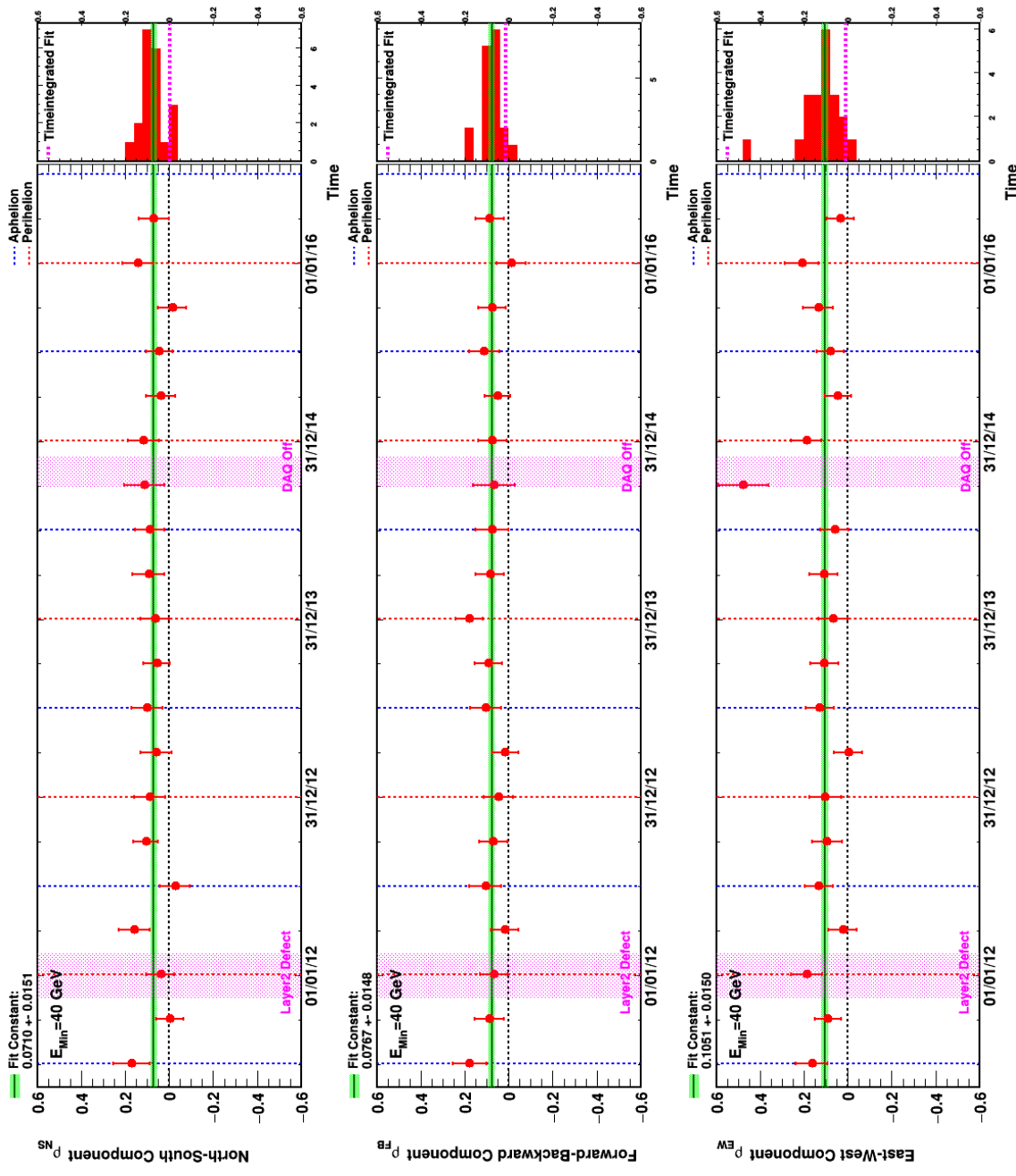
Figure B.4.: Seasonal fits of R_{e^+/e^-} positron relative anisotropy at a minimum energy of 40 GeV in **GAL**.
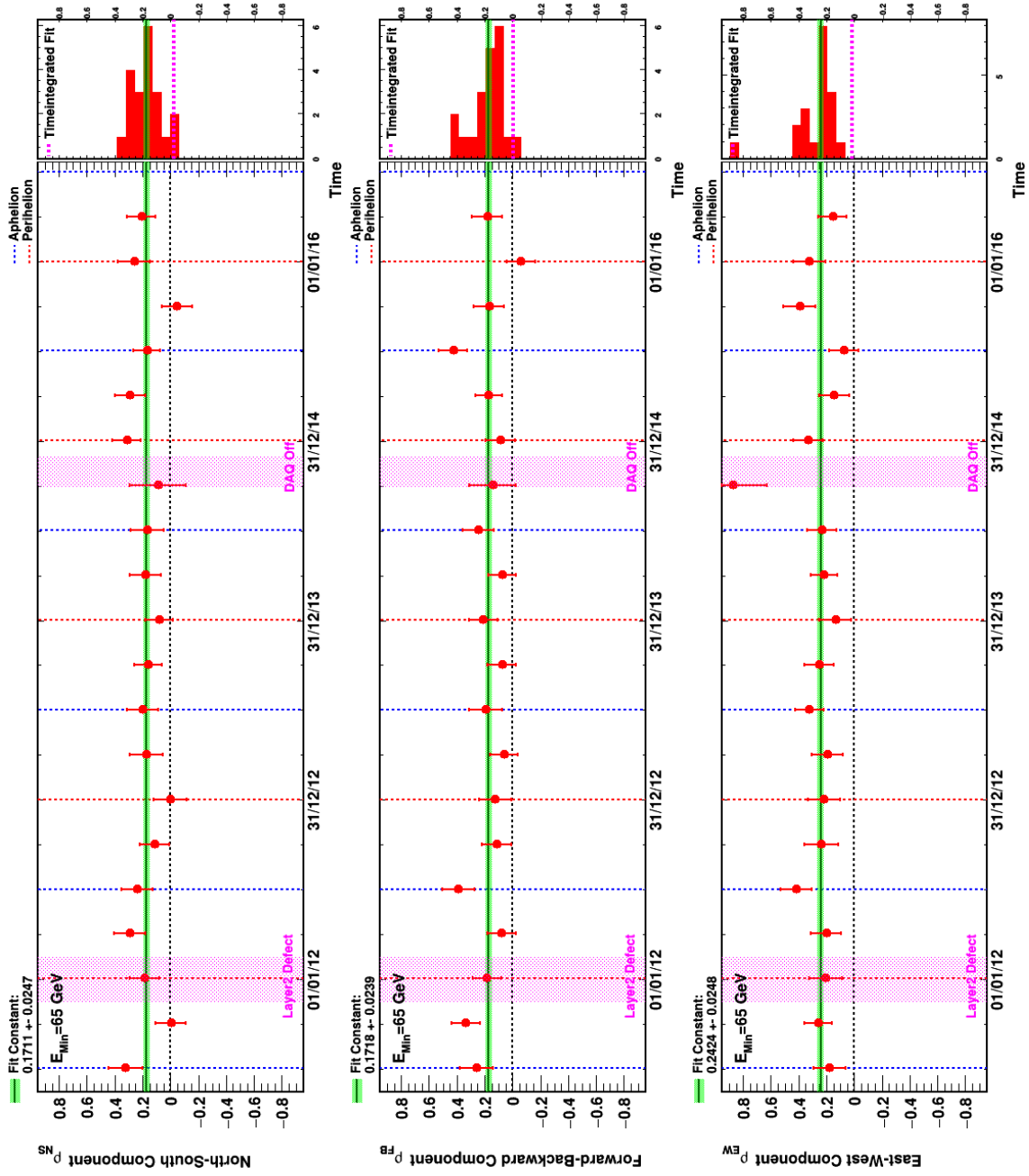
Figure B.5.: Seasonal fits of R_{e^+/e^-} positron relative anisotropy at a minimum energy of 65 GeV in **GAL**.
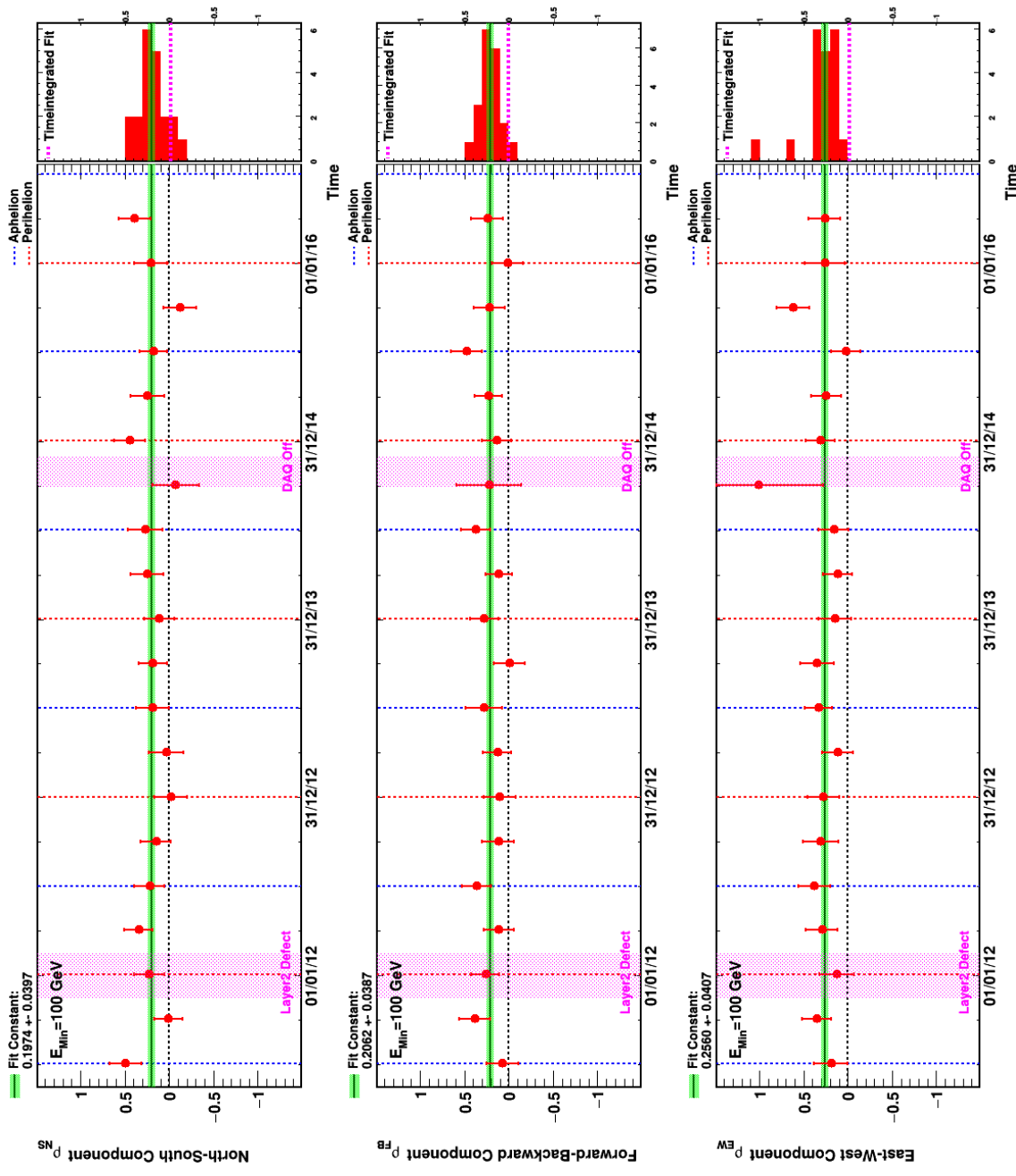
Figure B.6.: Seasonal fits of R_{e^+/e^-} positron relative anisotropy at a minimum energy of 100 GeV in **GAL**.

B.2. Positron relative anisotropy - GSE

E_{Min} (GeV)	N_{Sig}	N_{Ref}	ρ_{NS}	$\sigma_{\rho_{NS}}$ (%)	ρ_{FB}	$\sigma_{\rho_{FB}}$ (%)	ρ_{EW}	$\sigma_{\rho_{EW}}$ (%)	δ (%)	$\delta^{95\%}$ (%)
16	69394	913421	-0.043	0.658	0.808	0.675	0.302	0.678	0.864	1.678
25	34422	393084	0.915	0.972	0.567	0.934	0.015	0.942	1.076	2.261
40	13937	129017	1.677	1.520	-1.055	1.458	-0.071	1.470	1.983	3.771
65	5401	39598	4.616	2.408	-2.295	2.318	-1.993	2.339	5.527	8.427
100	2227	13434	5.842	3.740	-2.056	3.607	-5.636	3.652	8.373	12.859

Table B.2.: Fit of R_{e^+/e^-} positron relative anisotropy in **GSE**.
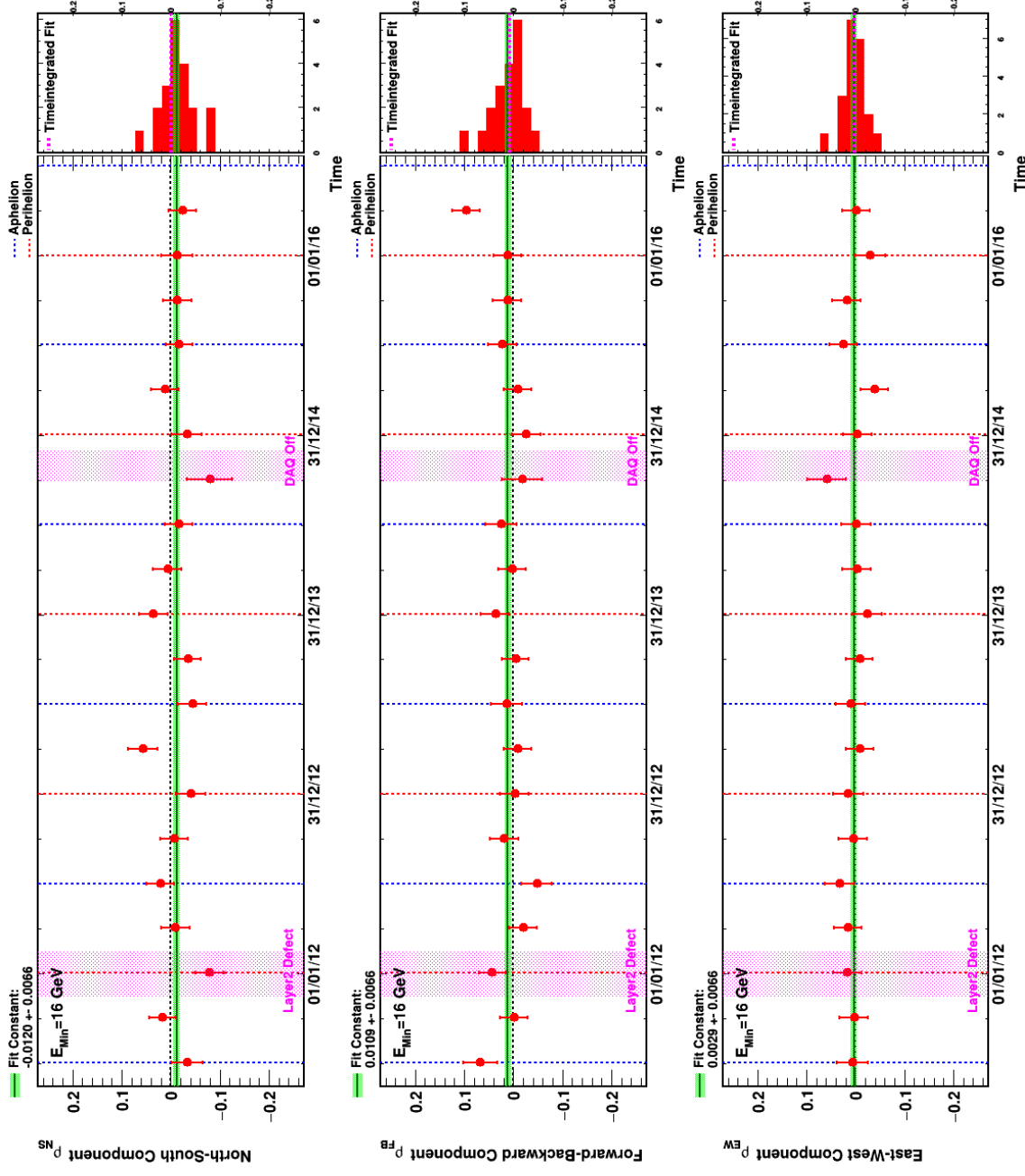
Figure B.7.: Seasonal fits of R_{e^+/e^-} positron relative anisotropy at a minimum energy of 16 GeV in **GSE**.
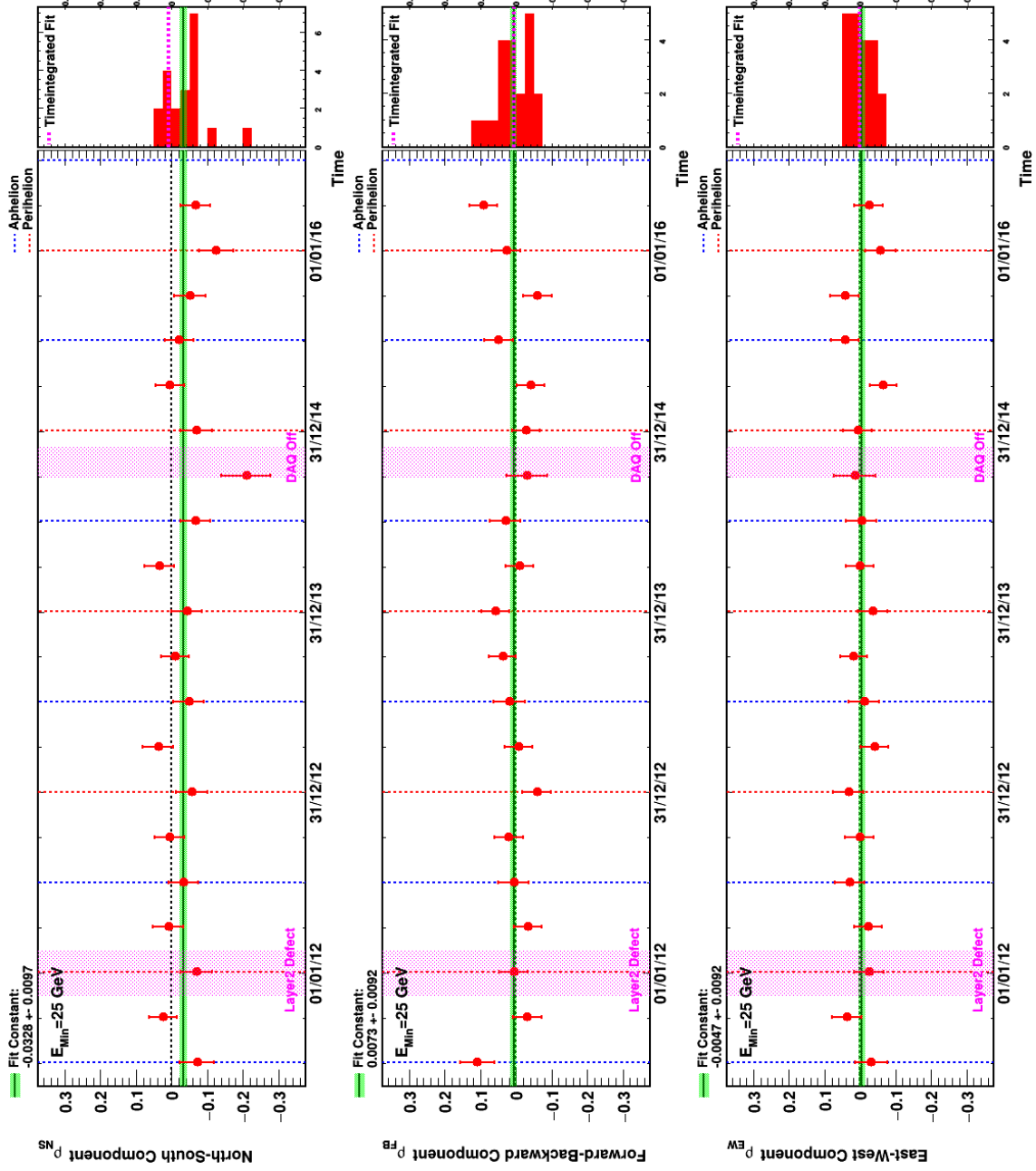
Figure B.8.: Seasonal fits of R_{e^+/e^-} positron relative anisotropy at a minimum energy of 25 GeV in **GSE**.
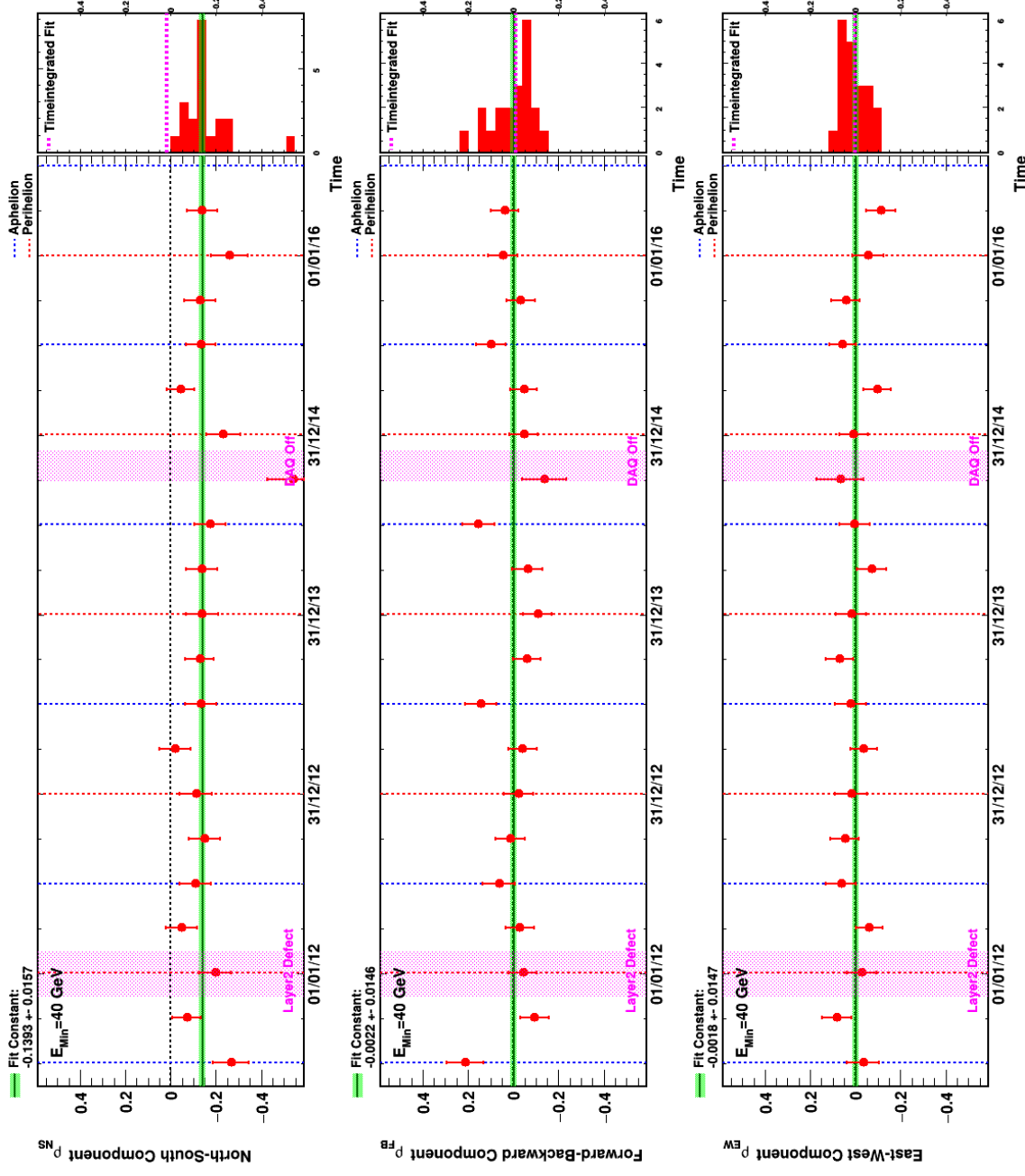
Figure B.9.: Seasonal fits of R_{e^+/e^-} positron relative anisotropy at a minimum energy of 40 GeV in **GSE**.
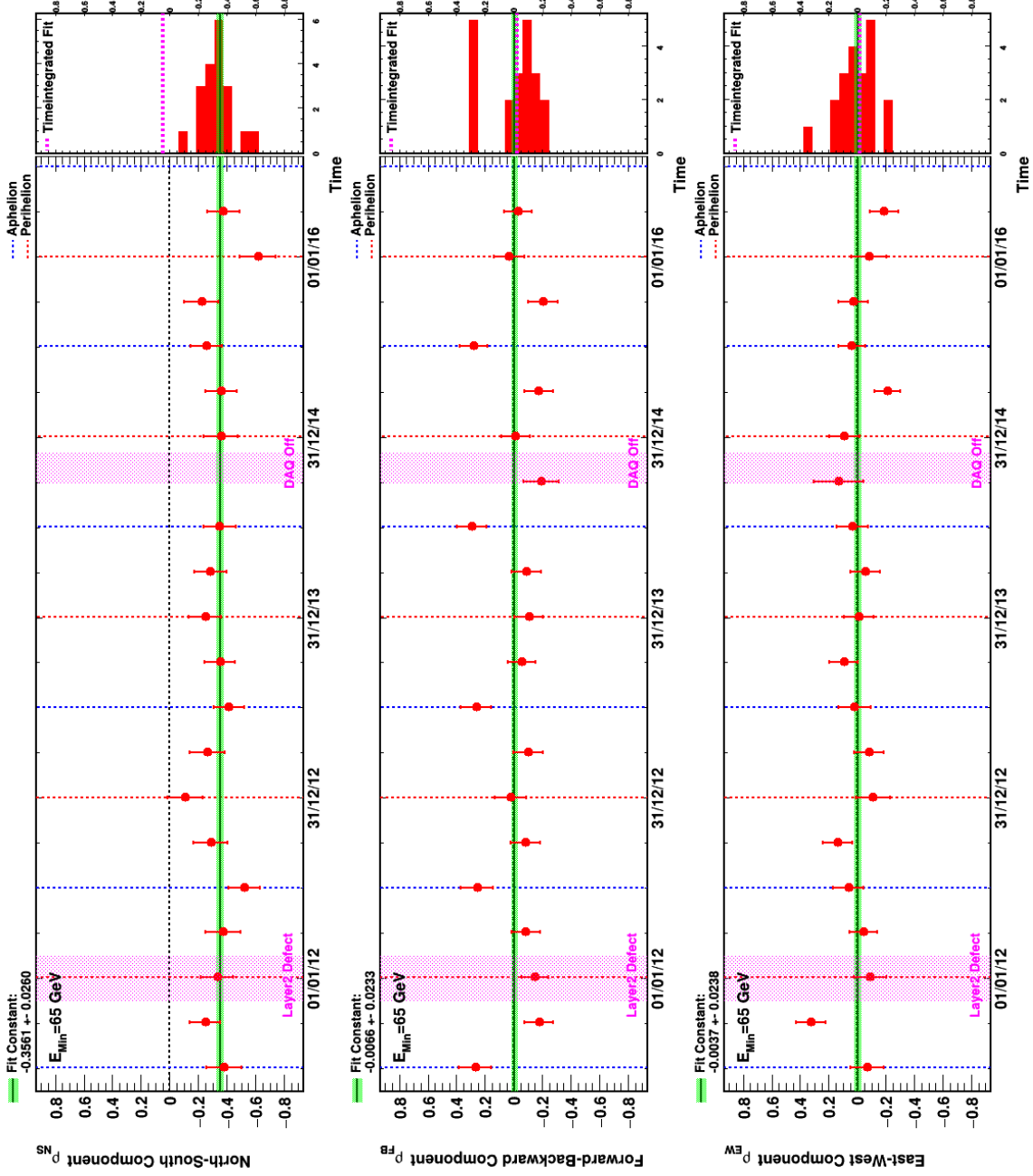
Figure B.10.: Seasonal fits of R_{e^+/e^-} positron relative anisotropy at a minimum energy of 65 GeV in **GSE**.
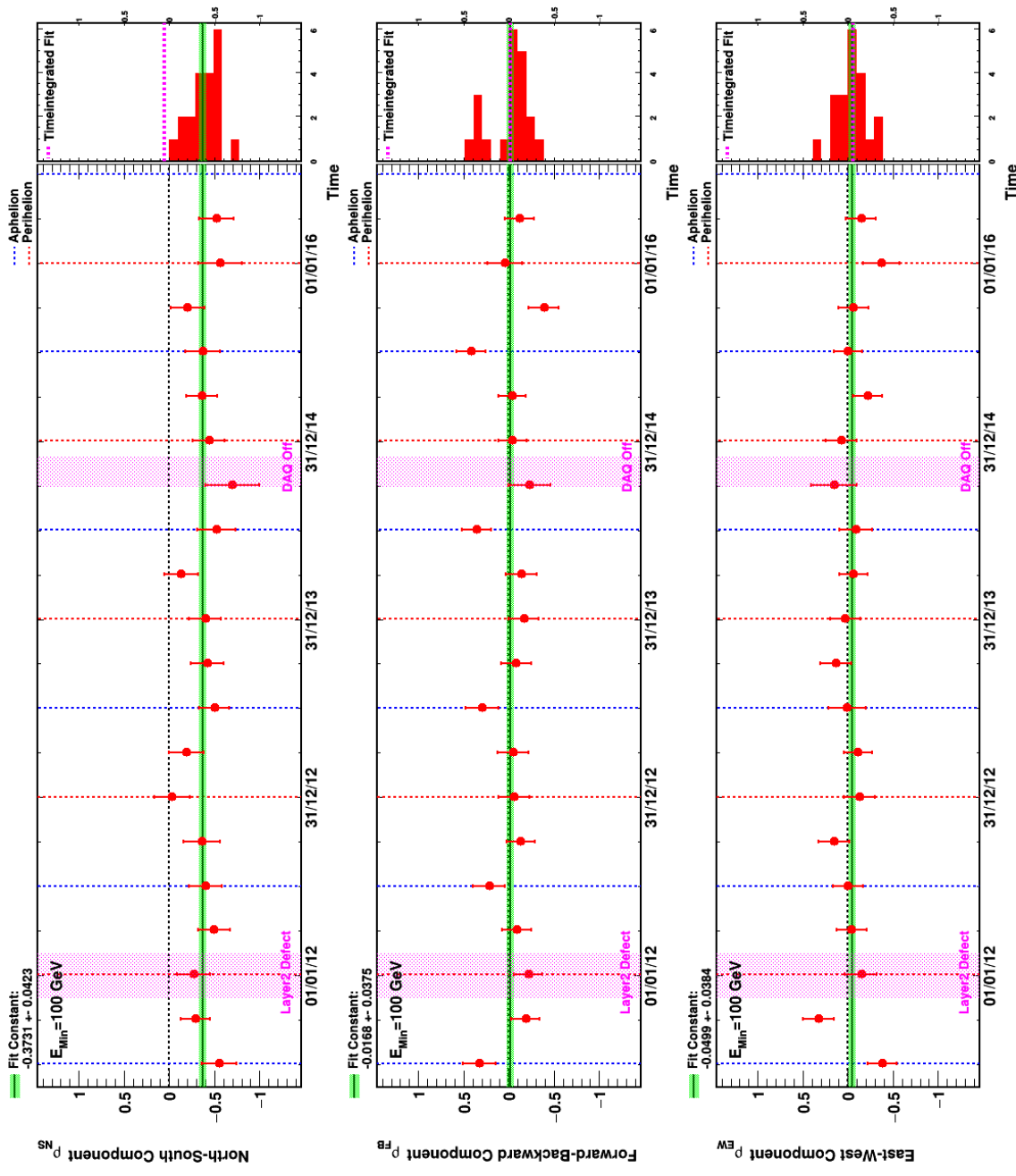
Figure B.11.: Seasonal fits of R_{e^+/e^-} positron relative anisotropy at a minimum energy of 100 GeV in **GSE**.

B.3. Electron relative anisotropy - GAL

E_{Min} (GeV)	N_{Sig}	N_{Ref}	ρ_{NS}	$\sigma_{\rho_{NS}}$ (%)	ρ_{FB}	$\sigma_{\rho_{FB}}$ (%)	ρ_{EW}	$\sigma_{\rho_{EW}}$ (%)	δ (%)	$\delta^{95\%}$ (%)
16	913421	67717500	0.015	0.185	-0.177	0.183	0.051	0.179	0.185	0.419
25	393084	39292900	-0.051	0.278	-0.116	0.275	0.220	0.279	0.254	0.620
40	129017	17992000	-0.180	0.482	-0.014	0.478	-0.150	0.484	0.235	0.981
65	39598	7702590	0.814	0.863	0.654	0.856	-1.026	0.867	1.463	2.480
100	13434	3467950	0.591	1.470	0.278	1.458	-0.092	1.478	0.660	2.976

Table B.3.: Fit of $R_{e^-/p}$ electron relative anisotropy in **GAL**.
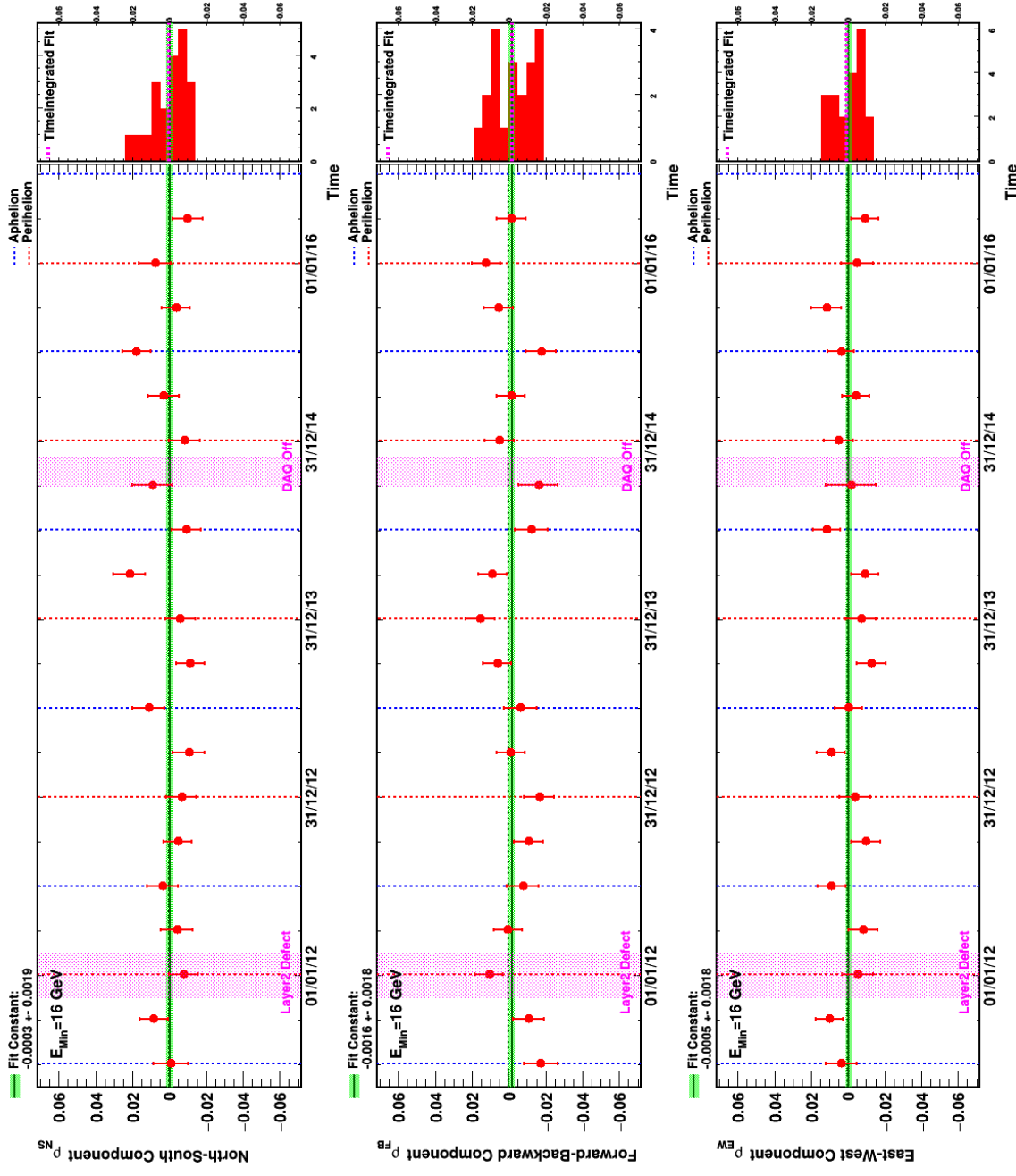
Figure B.12.: Seasonal fits of $R_{e^-/p}$ electron relative anisotropy at a minimum energy of 16 GeV in **GAL**.
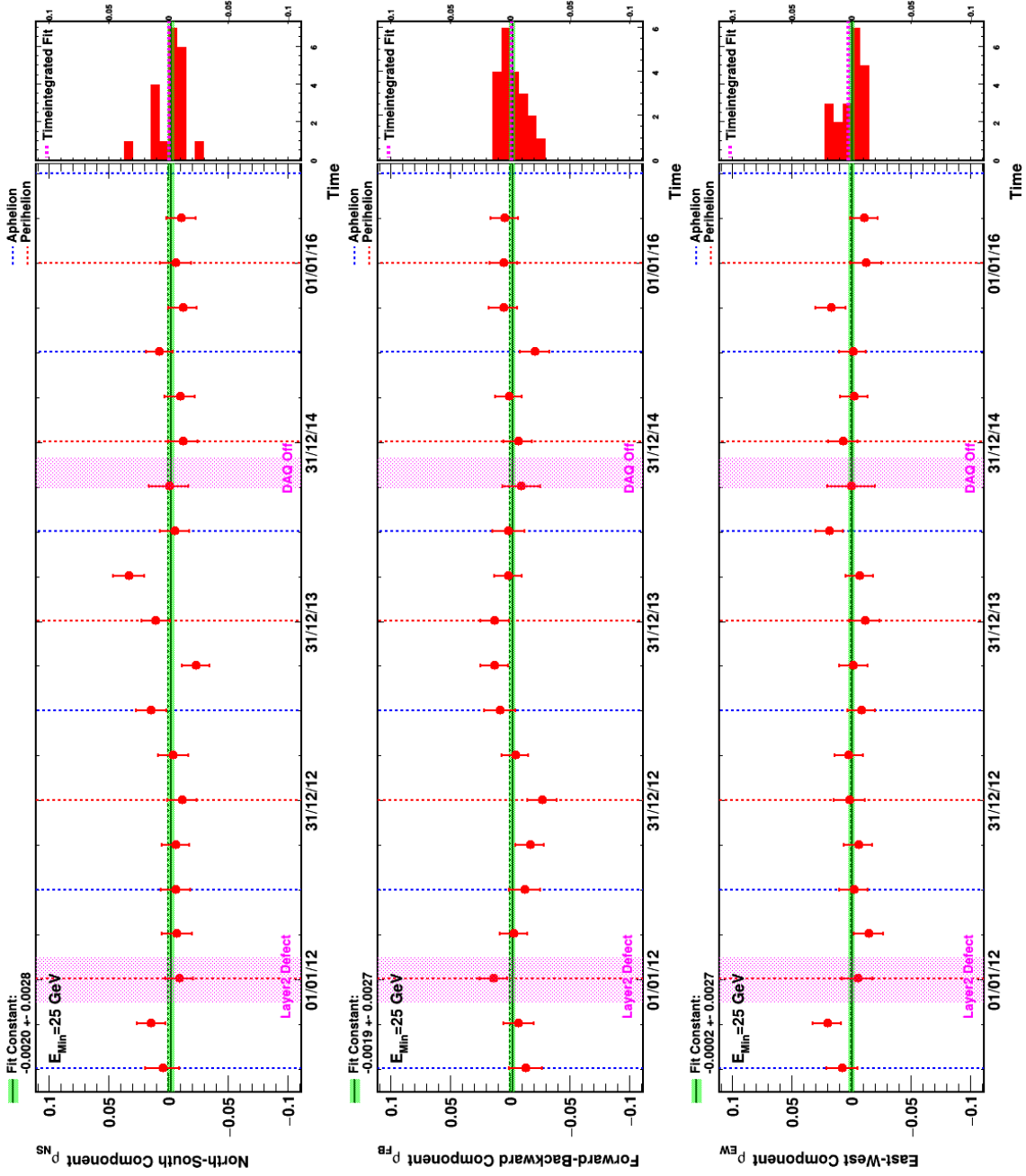
Figure B.13.: Seasonal fits of $R_{e^-/p}$ electron relative anisotropy at a minimum energy of 25 GeV in **GAL**.
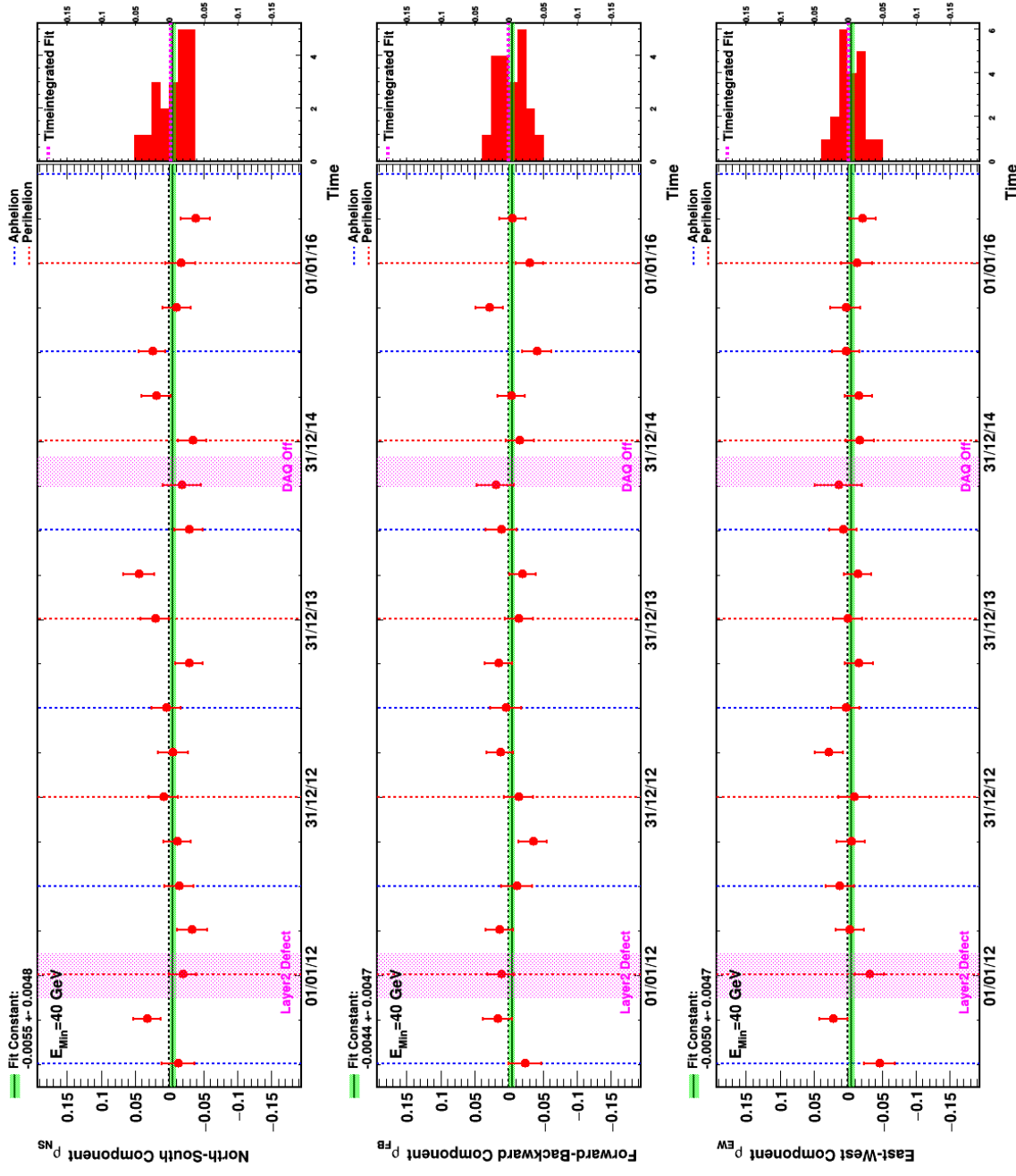
Figure B.14.: Seasonal fits of $R_{e^-/p}$ electron relative anisotropy at a minimum energy of 40 GeV in **GAL**.
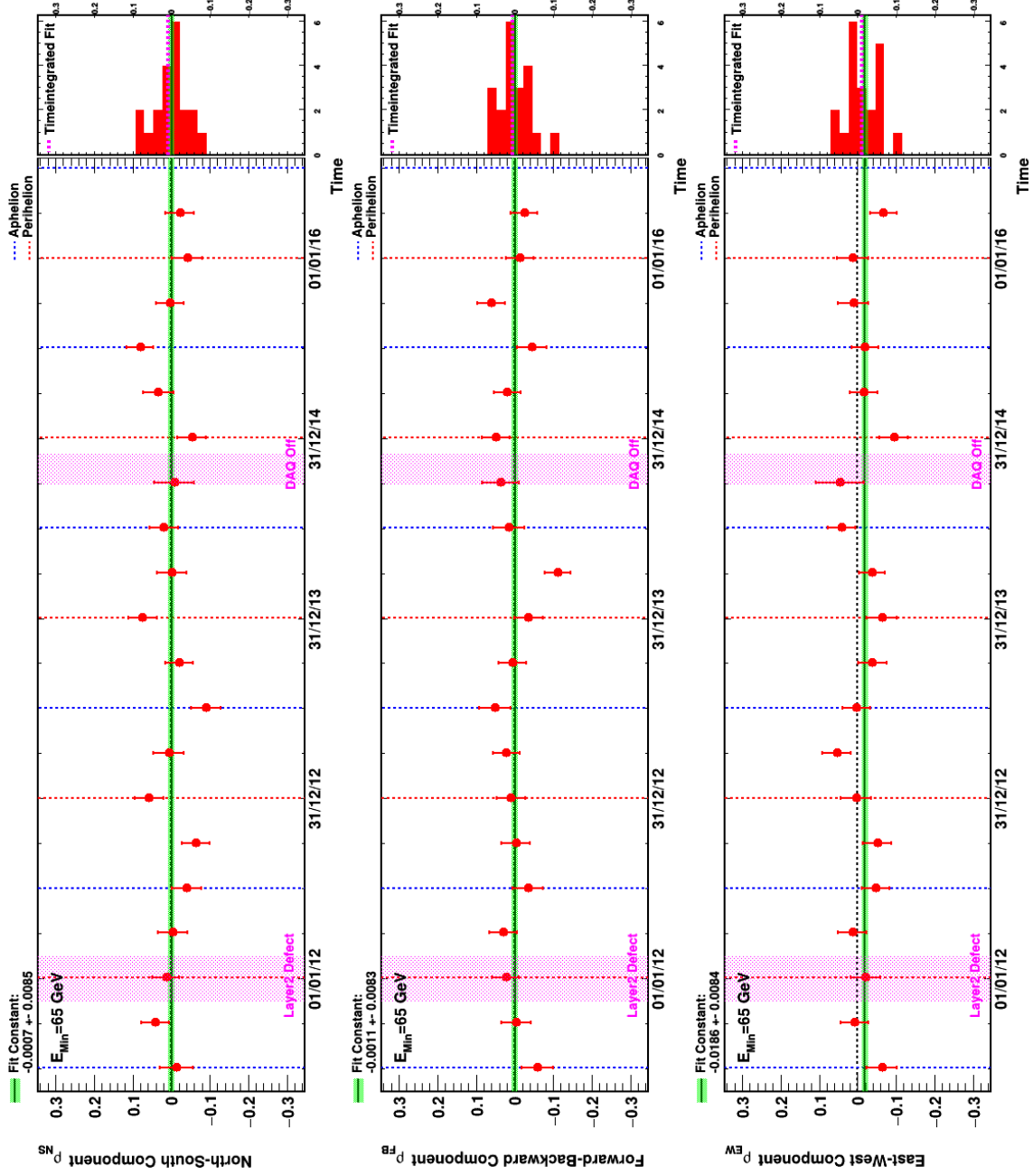
Figure B.15.: Seasonal fits of $R_{e^-/p}$ electron relative anisotropy at a minimum energy of 65 GeV in **GAL**.
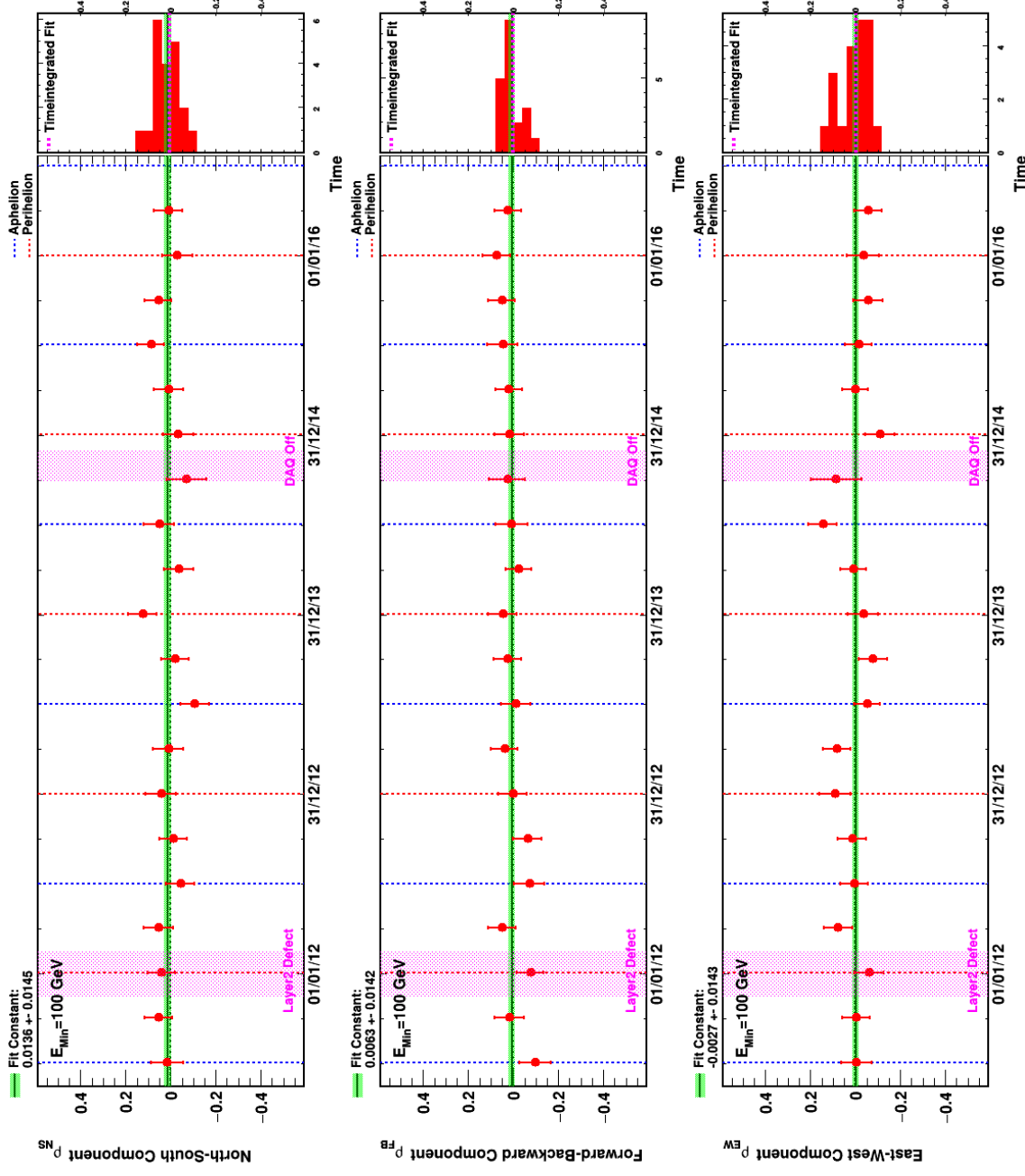
Figure B.16.: Seasonal fits of $R_{e^-/p}$ electron relative anisotropy at a minimum energy of 100 GeV in **GAL**.

B.4. Electron relative anisotropy - GSE

E_{Min} (GeV)	N_{Sig}	N_{Ref}	ρ_{NS}	$\sigma_{\rho_{NS}}$ (%)	ρ_{FB}	$\sigma_{\rho_{FB}}$ (%)	ρ_{EW}	$\sigma_{\rho_{EW}}$ (%)	δ (%)	$\delta^{95\%}$ (%)
16	913421	67717500	-0.046	0.178	-0.602	0.184	-0.672	0.185	0.903	1.170
25	393084	39292900	-0.134	0.283	-0.362	0.273	-0.710	0.275	0.808	1.171
40	129017	17992000	0.455	0.493	-0.274	0.473	-0.577	0.477	0.784	1.352
65	39598	7702590	1.022	0.880	-0.924	0.845	-0.216	0.853	1.394	2.409
100	13434	3467950	0.721	1.499	-1.478	1.439	-0.834	1.451	1.844	3.628

Table B.4.: Fit of $R_{e^-/p}$ electron relative anisotropy in **GSE**.
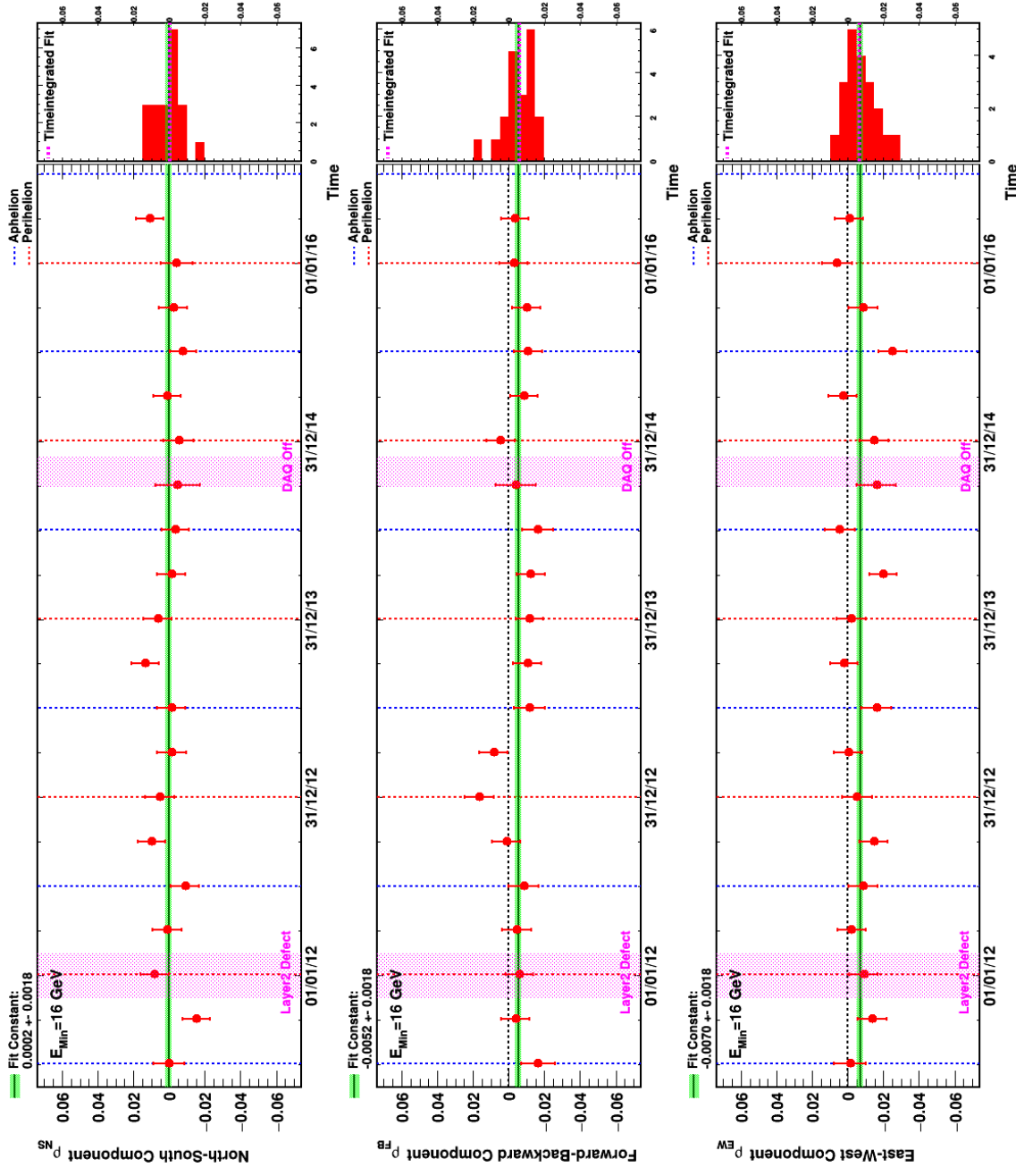
Figure B.17.: Seasonal fits of $R_{e^-/p}$ electron relative anisotropy at a minimum energy of 16 GeV in **GSE**.
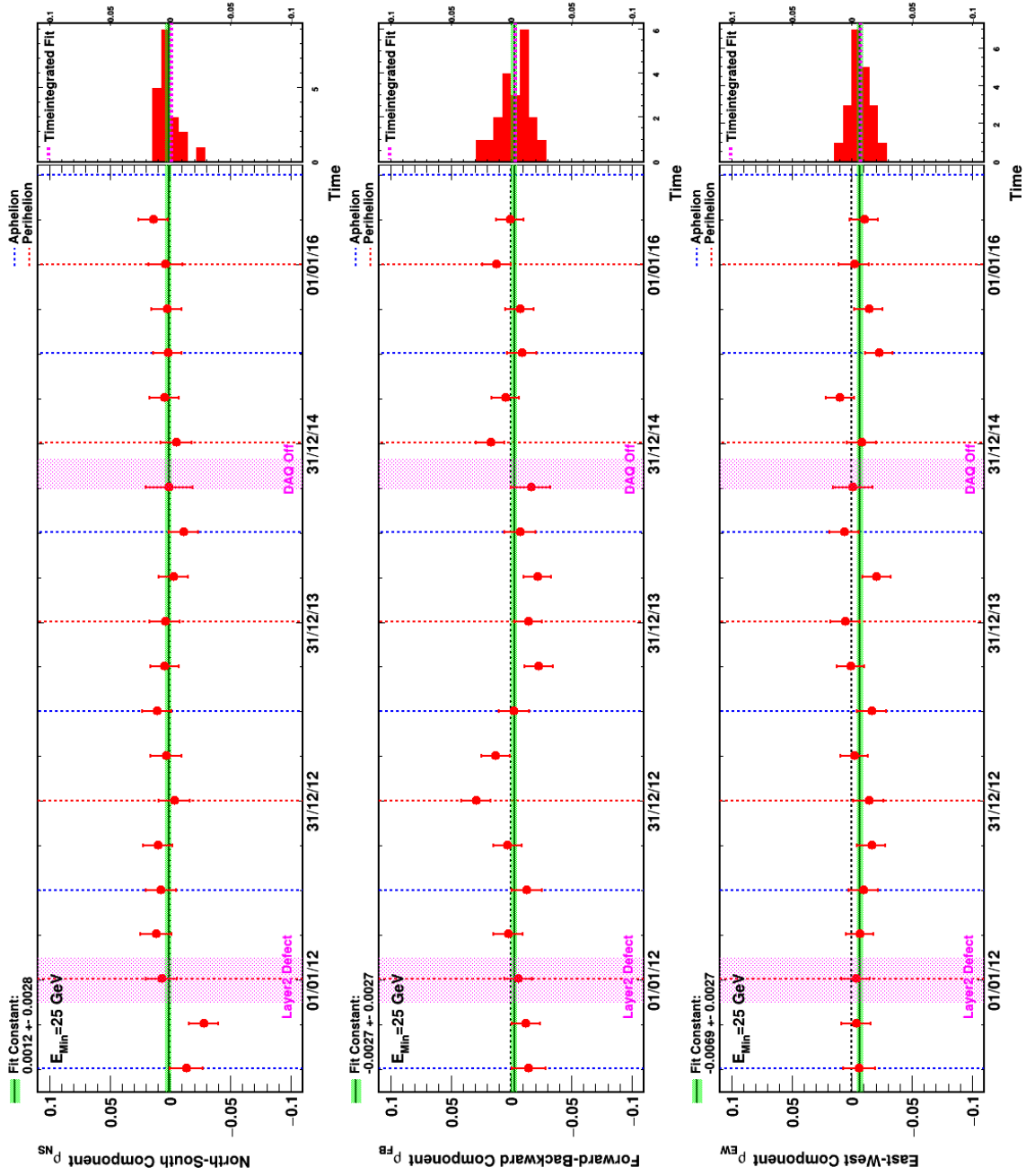
Figure B.18.: Seasonal fits of $R_{e^-/p}$ electron relative anisotropy at a minimum energy of 25 GeV in **GSE**.
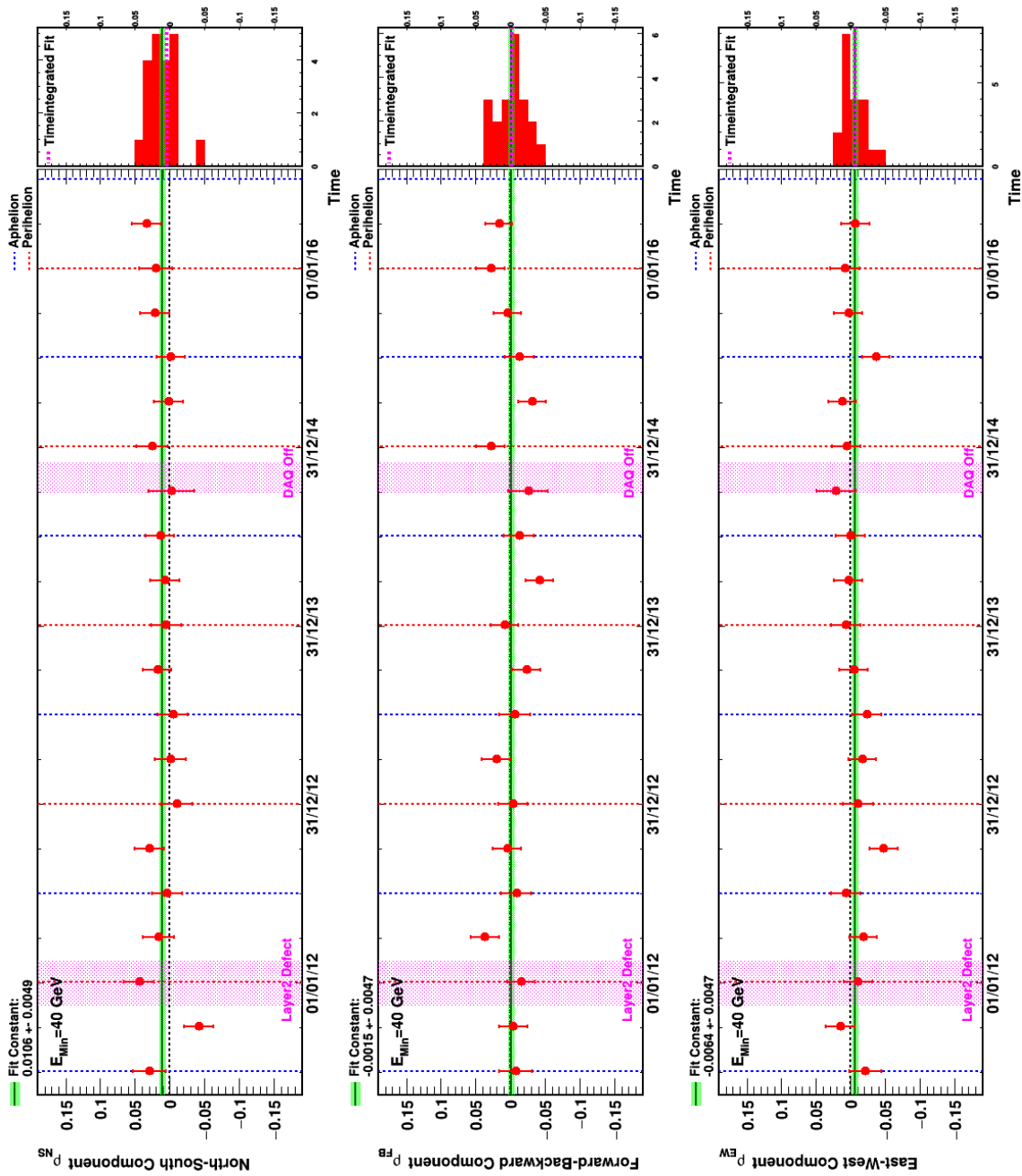
Figure B.19.: Seasonal fits of $R_{e^-/p}$ electron relative anisotropy at a minimum energy of 40 GeV in **GSE**.
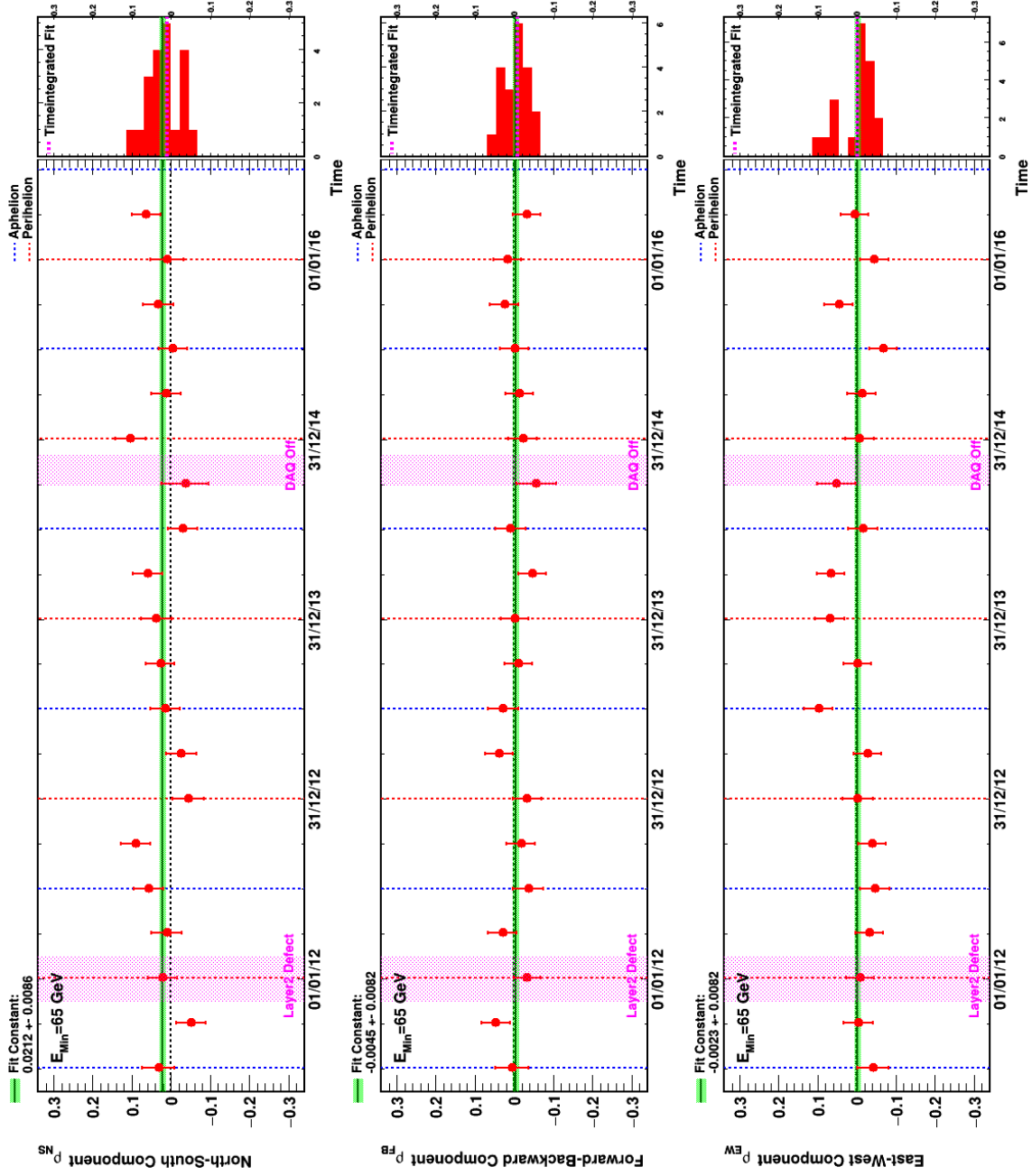
Figure B.20.: Seasonal fits of $R_{e^-/p}$ electron relative anisotropy at a minimum energy of 65 GeV in **GSE**.
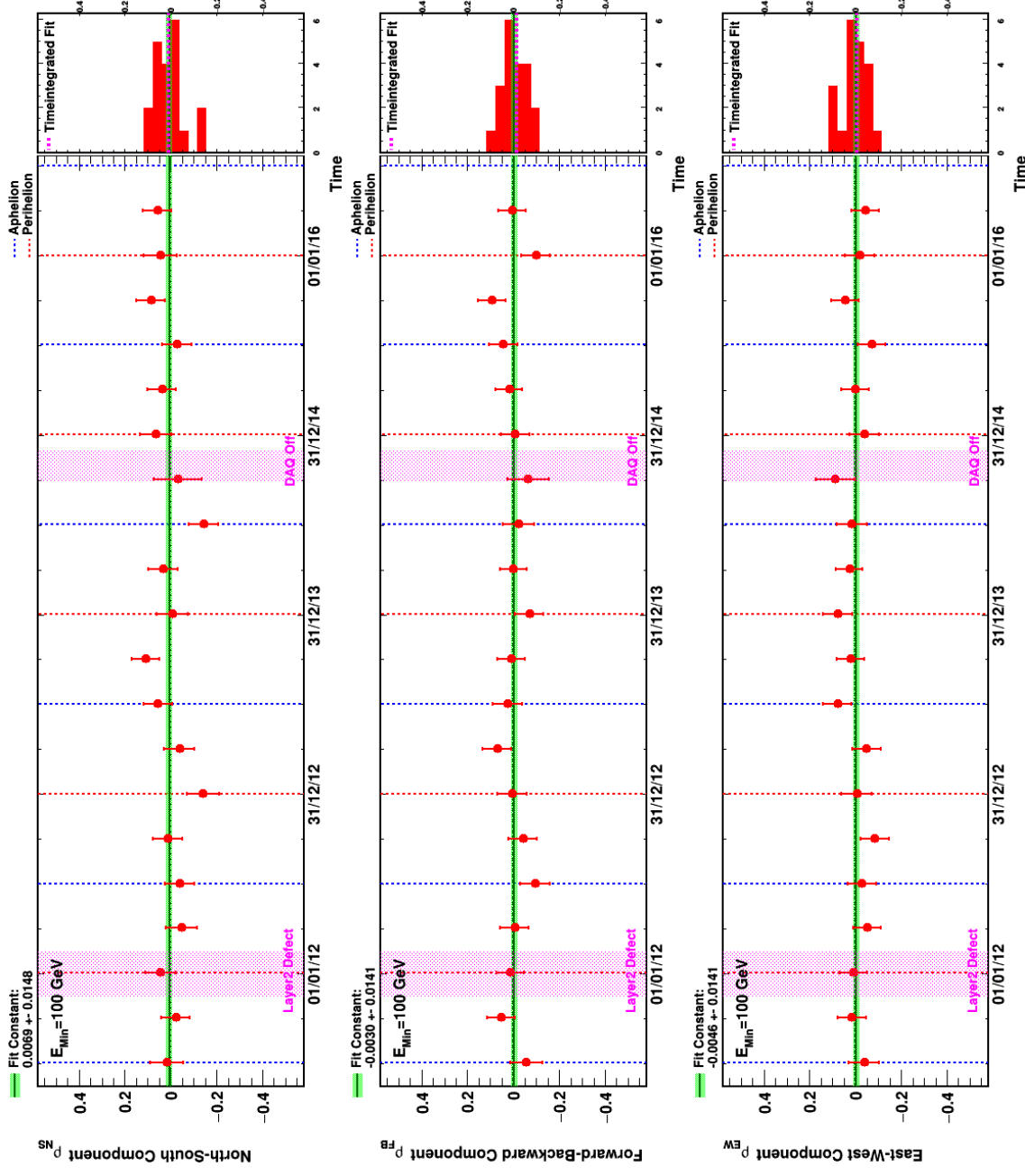
Figure B.21.: Seasonal fits of $R_{e^-/p}$ electron relative anisotropy at a minimum energy of 100 GeV in **GSE**.

B.5. Proton relative anisotropy - GAL

R_{Min} (GV)	N_{Sig}	N_{Ref}	ρ_{NS}	$\sigma_{\rho NS}$ (%)	ρ_{FB}	$\sigma_{\rho FB}$ (%)	ρ_{EW}	$\sigma_{\rho EW}$ (%)	δ (%)	$\delta^{95\%}$ (%)
80	3843860	9531050	0.048	0.105	-0.044	0.104	-0.019	0.105	0.068	0.220
150	1231090	9531050	0.138	0.167	0.161	0.165	-0.081	0.167	0.227	0.426
300	348584	9531050	0.311	0.300	-0.300	0.297	0.519	0.301	0.676	1.041
500	133946	9531050	-0.002	0.478	0.095	0.473	0.507	0.480	0.516	1.119
1000	29562	9531050	-1.641	1.011	-0.157	1.001	2.113	1.017	2.680	3.966

Table B.5.: Fit of R_{p/p^*} proton relative anisotropy in **GAL**.
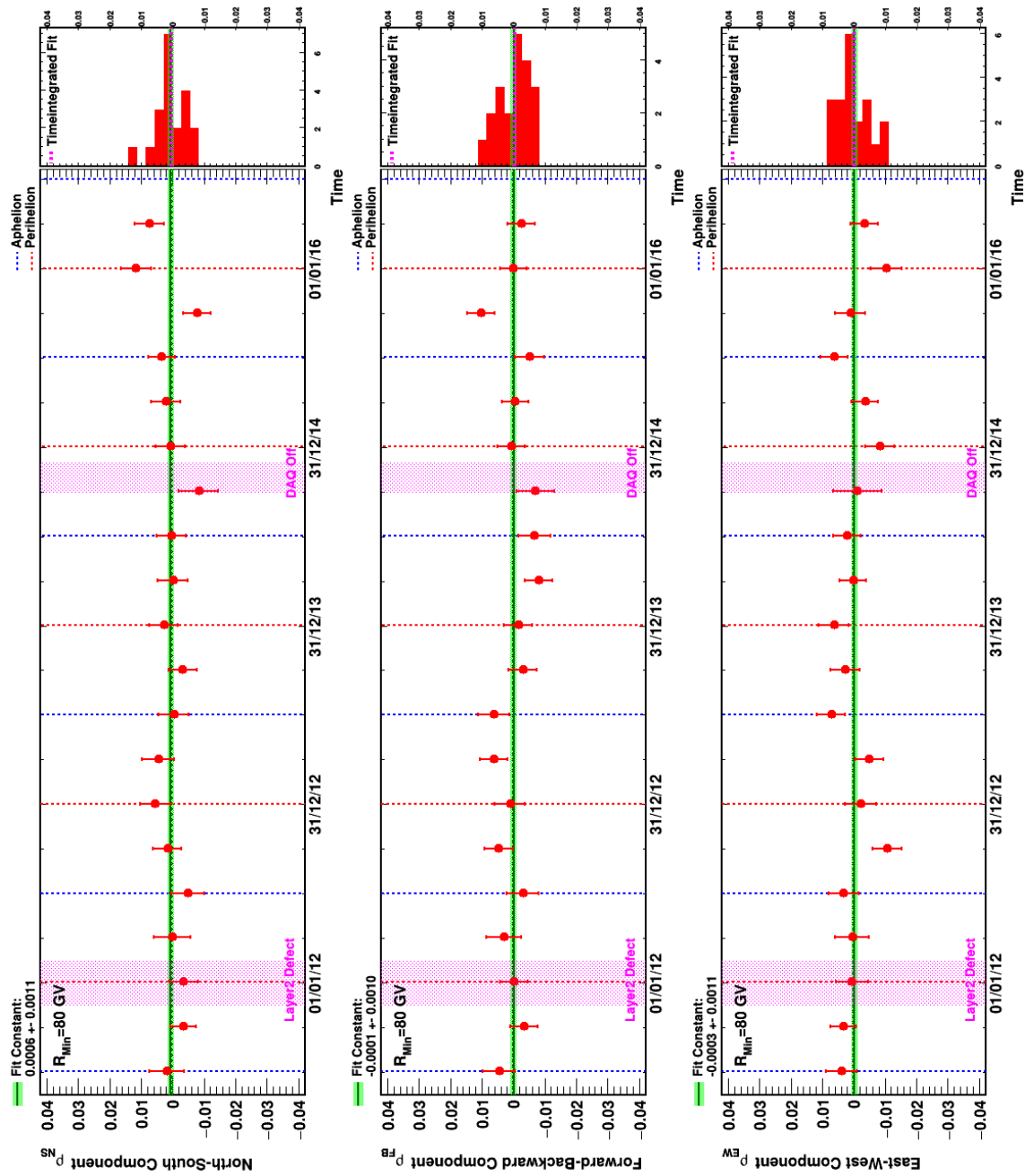
Figure B.22.: Seasonal fits of R_{p/p^*} proton relative anisotropy at a minimum rigidity of 80 GV in **GAL**.
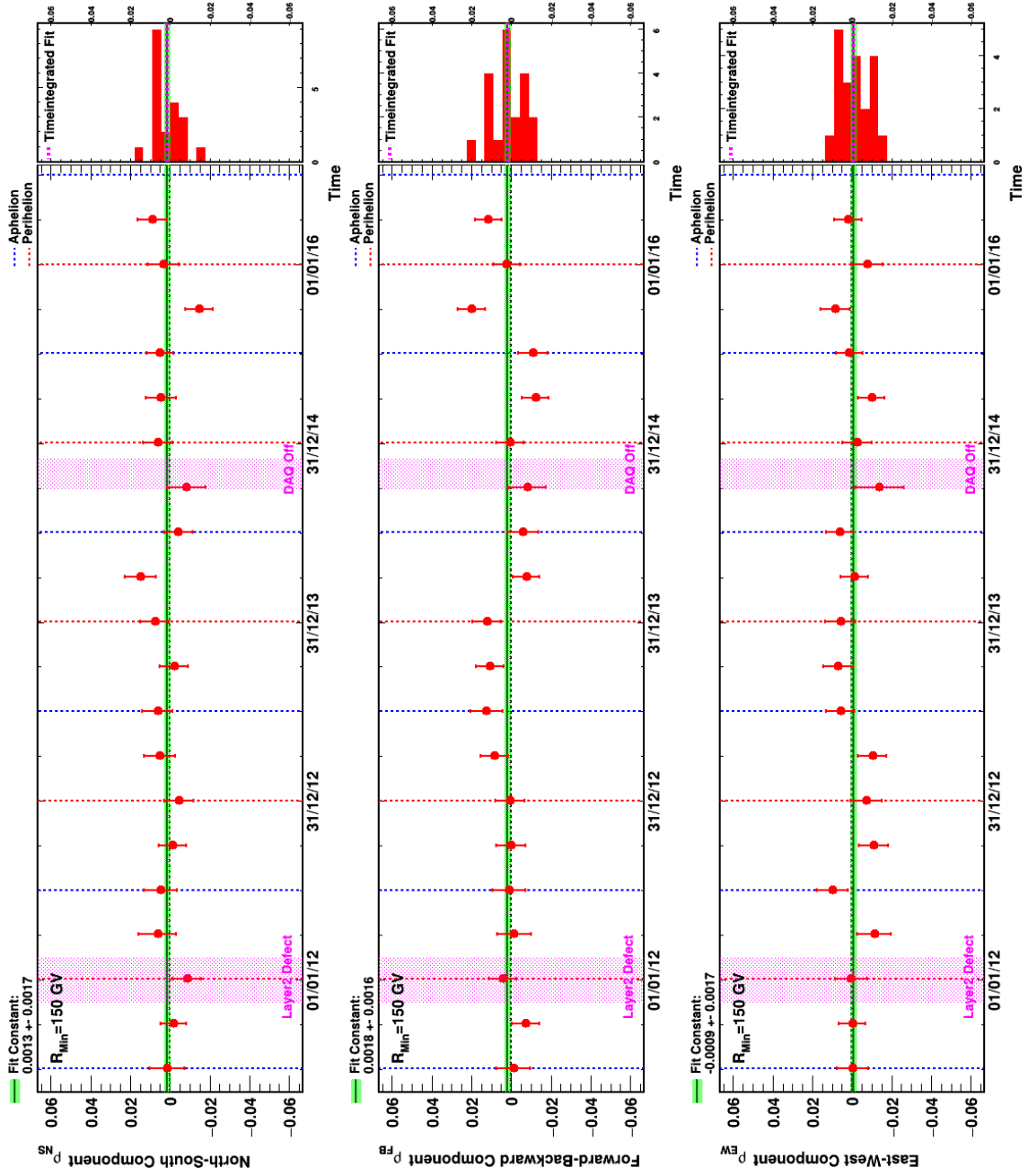
Figure B.23.: Seasonal fits of R_{p/p^*} proton relative anisotropy at a minimum rigidity of 150 GV in **GAL**.
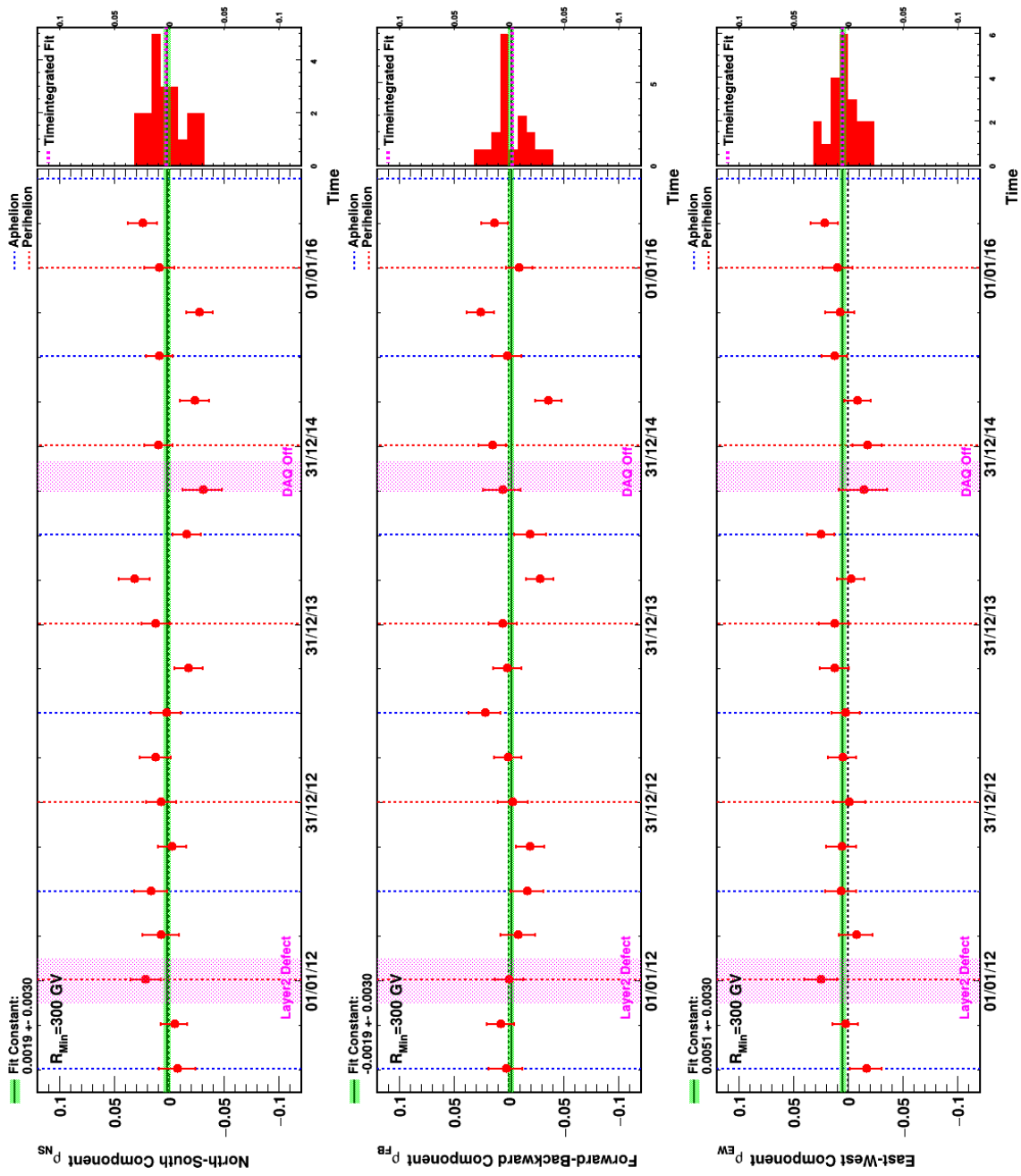
Figure B.24.: Seasonal fits of R_{p/p^*} proton relative anisotropy at a minimum rigidity of 300 GV in **GAL**.
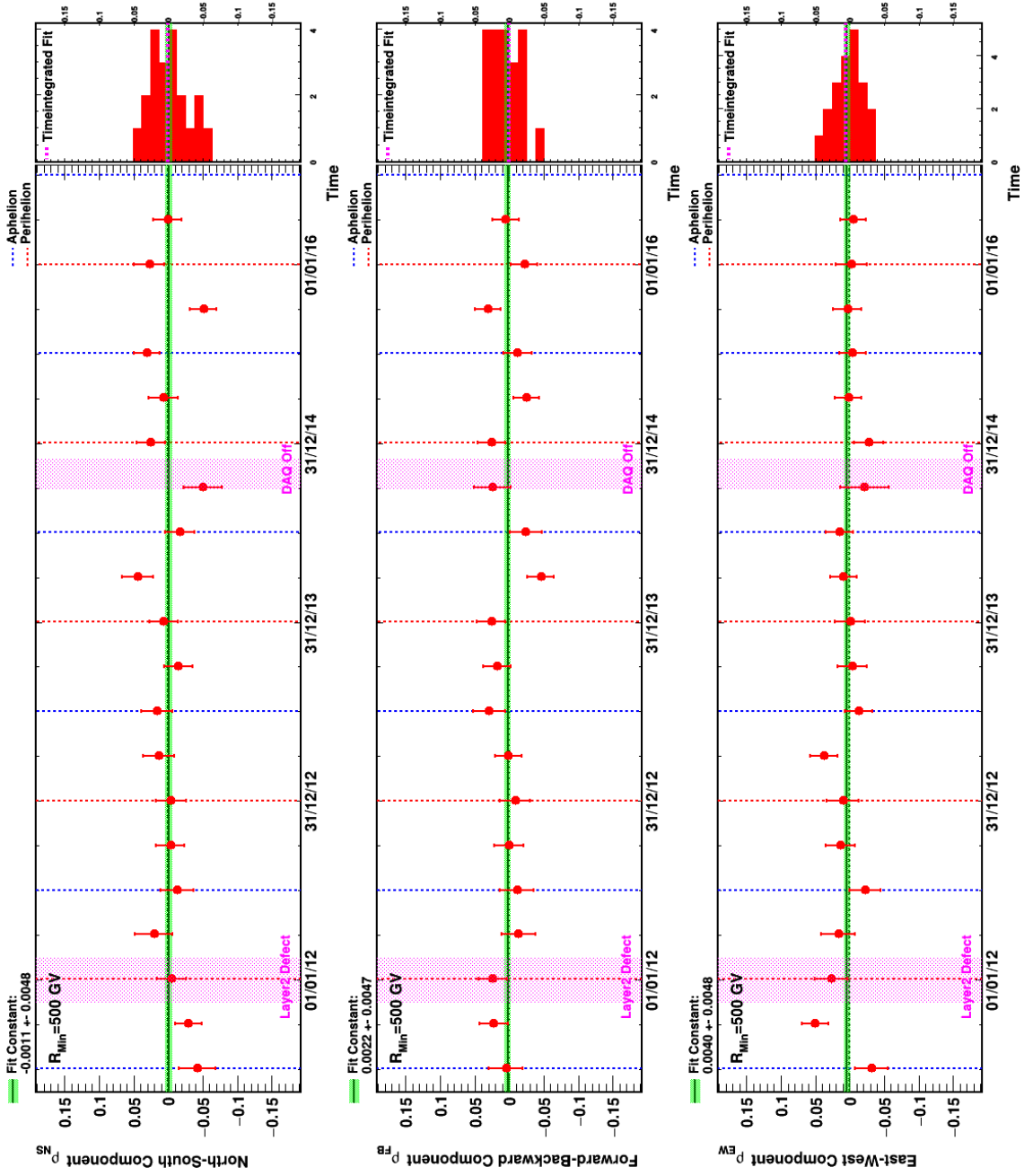
Figure B.25.: Seasonal fits of R_{p/p^*} proton relative anisotropy at a minimum rigidity of 500 GV in **GAL**.
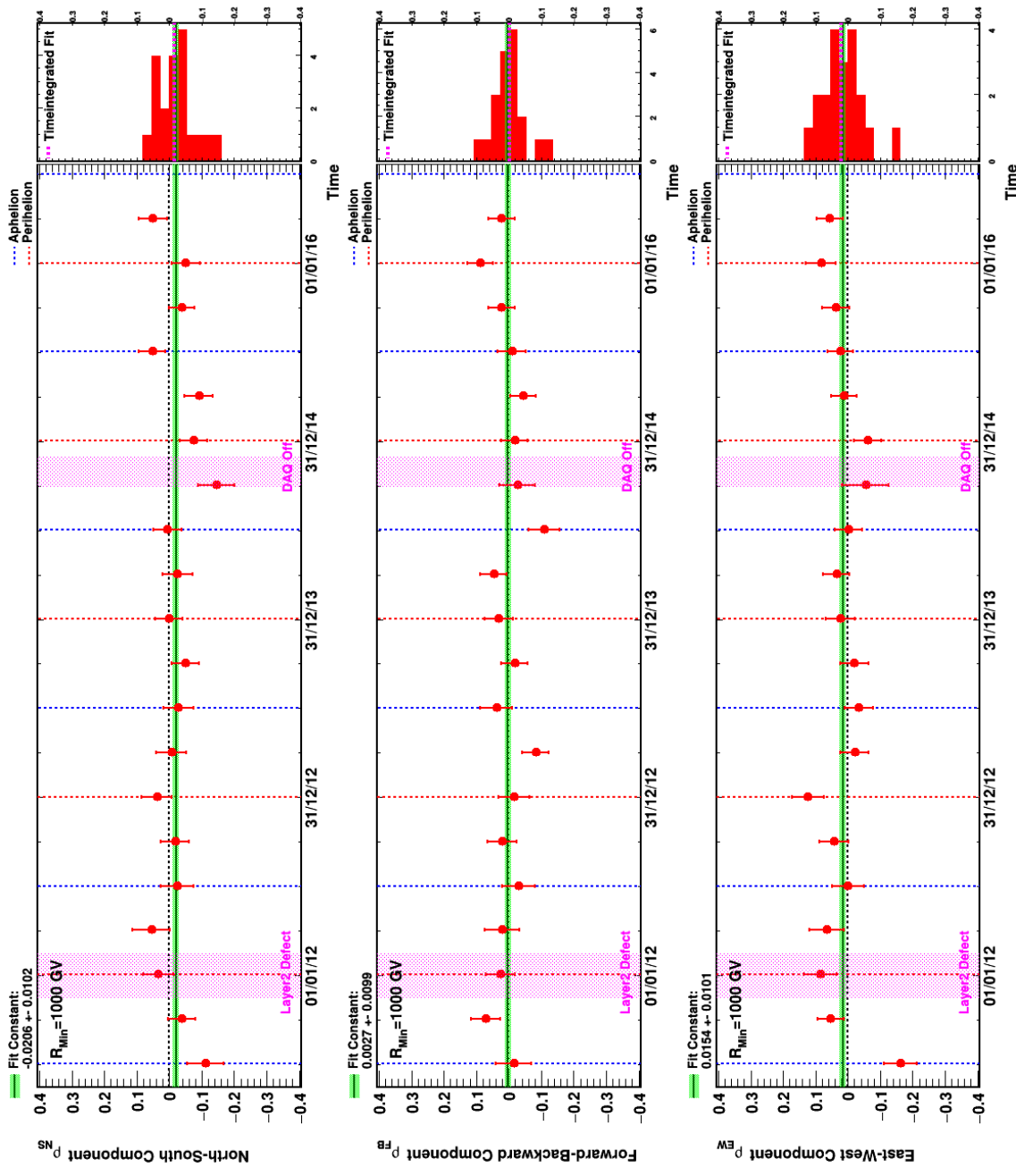
Figure B.26.: Seasonal fits of $R_{p/\bar{p}^*}$ proton relative anisotropy at a minimum rigidity of 1000 GV in **GAL**.

B.6. Proton relative anisotropy - GSE

R_{Min} (GV)	N_{Sig}	N_{Ref}	ρ_{NS}	$\sigma_{\rho_{NS}}$ (%)	ρ_{FB}	$\sigma_{\rho_{FB}}$ (%)	ρ_{EW}	$\sigma_{\rho_{EW}}$ (%)	δ (%)	$\delta^{95\%}$ (%)
80	3843860	9531050	-0.001	0.108	-0.396	0.103	0.135	0.104	0.418	0.566
150	1231090	9531050	-0.010	0.170	-0.886	0.163	0.017	0.165	0.886	1.131
300	348584	9531050	-0.729	0.307	-1.354	0.293	0.535	0.297	1.628	2.069
500	133946	9531050	-0.686	0.490	-2.046	0.467	0.786	0.474	2.297	2.990
1000	29562	9531050	-1.258	1.037	-2.181	0.988	0.057	1.002	2.518	3.781

Table B.6.: Fit of R_{p/p^*} proton relative anisotropy in **GSE**.
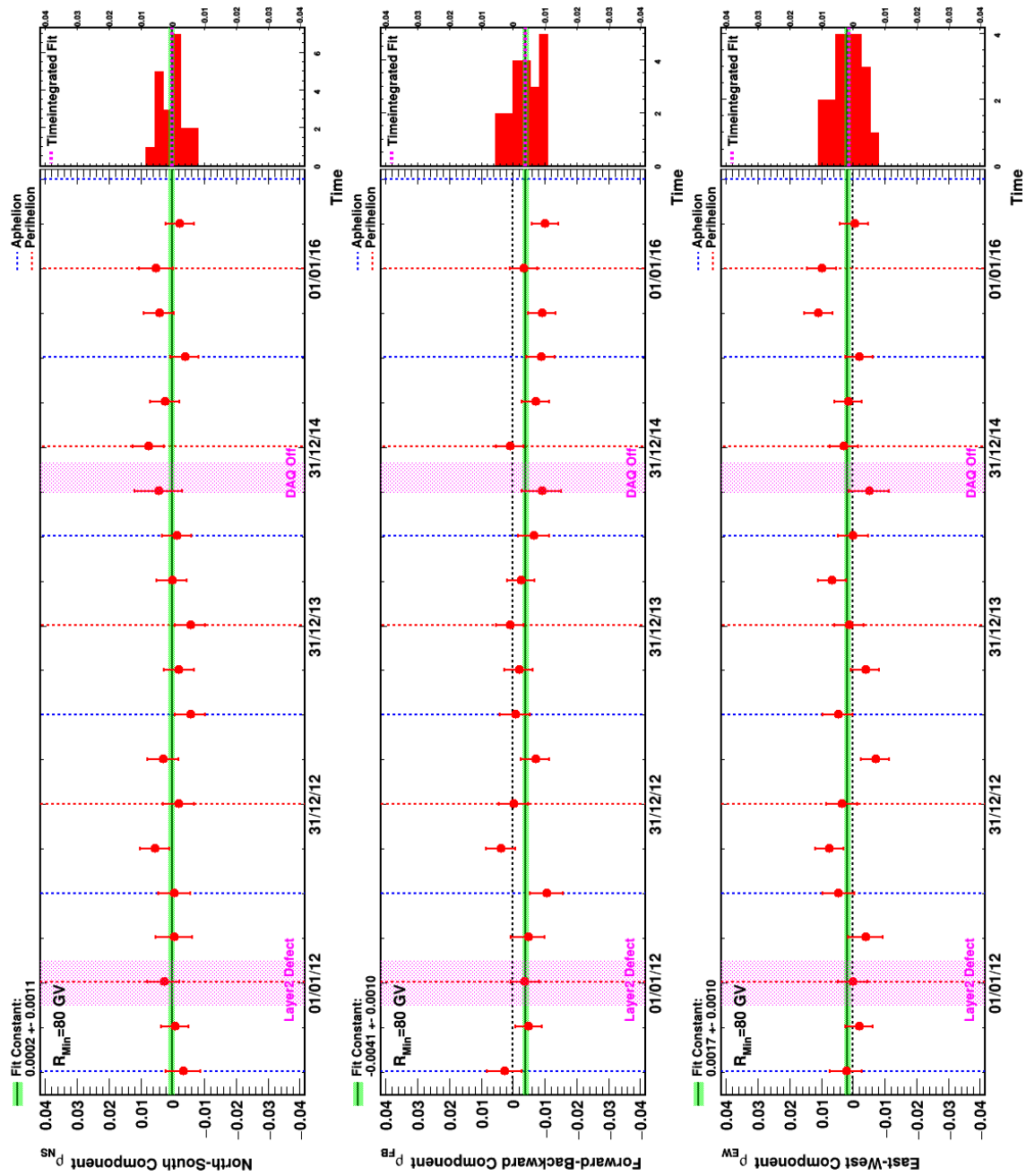
Figure B.27.: Seasonal fits of R_{p/p^*} proton relative anisotropy at a minimum rigidity of 80 GV in **GSE**.
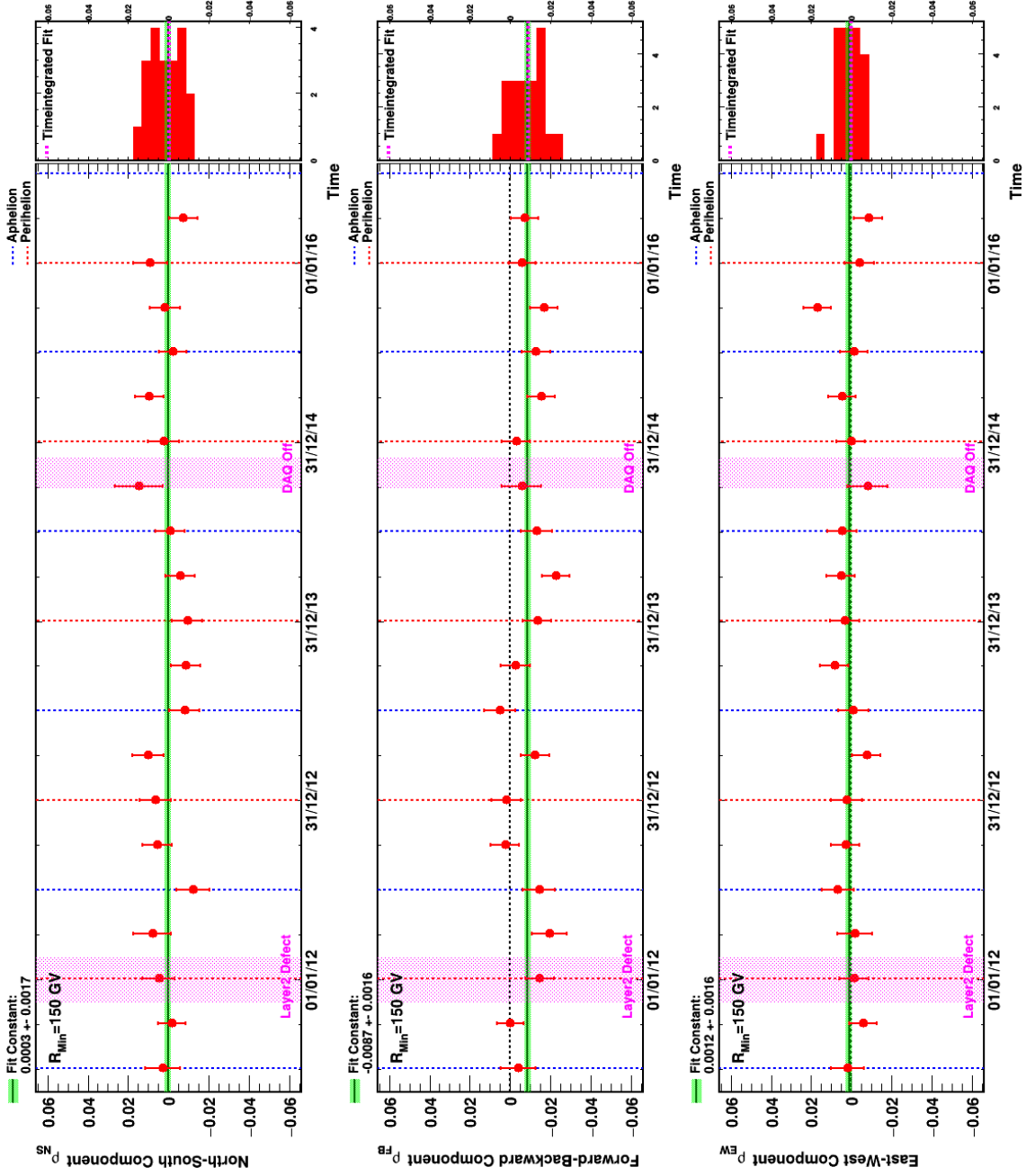
Figure B.28.: Seasonal fits of R_{p/p^*} proton relative anisotropy at a minimum rigidity of 150 GV in **GSE**.
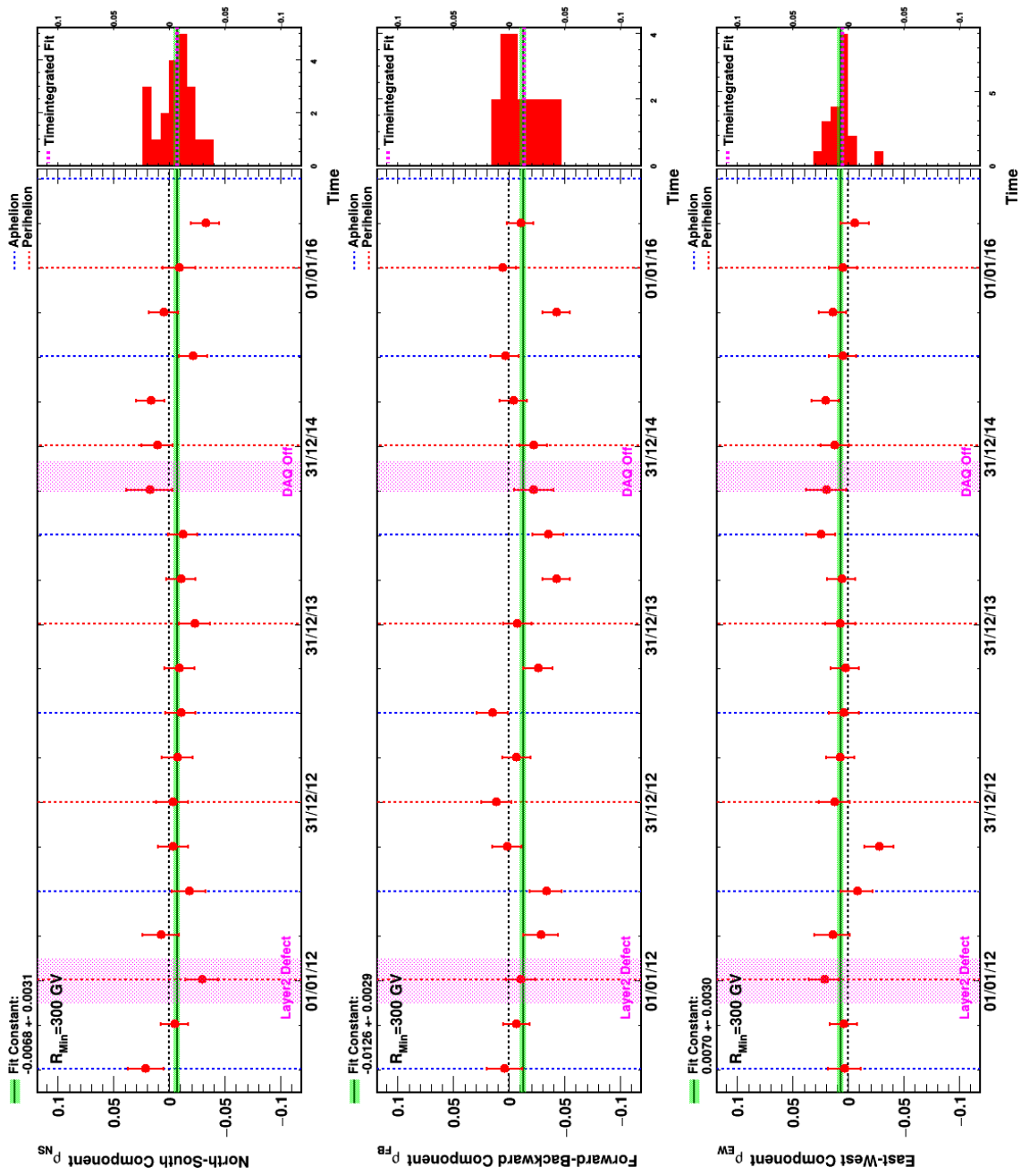
Figure B.29.: Seasonal fits of R_{p/p^*} proton relative anisotropy at a minimum rigidity of 300 GV in **GSE**.
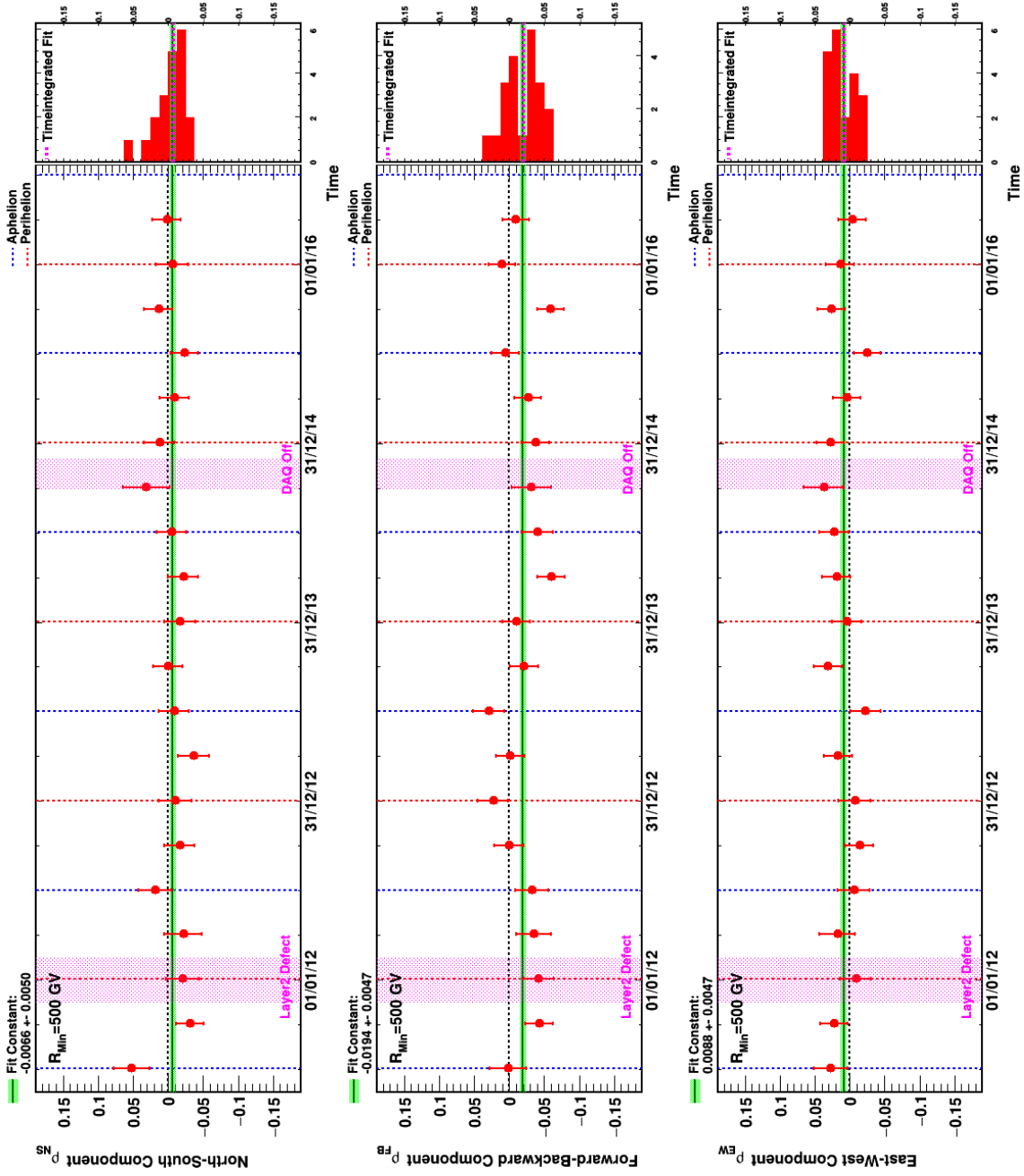
Figure B.30.: Seasonal fits of R_{p/p^*} proton relative anisotropy at a minimum rigidity of 500 GV in **GSE**.
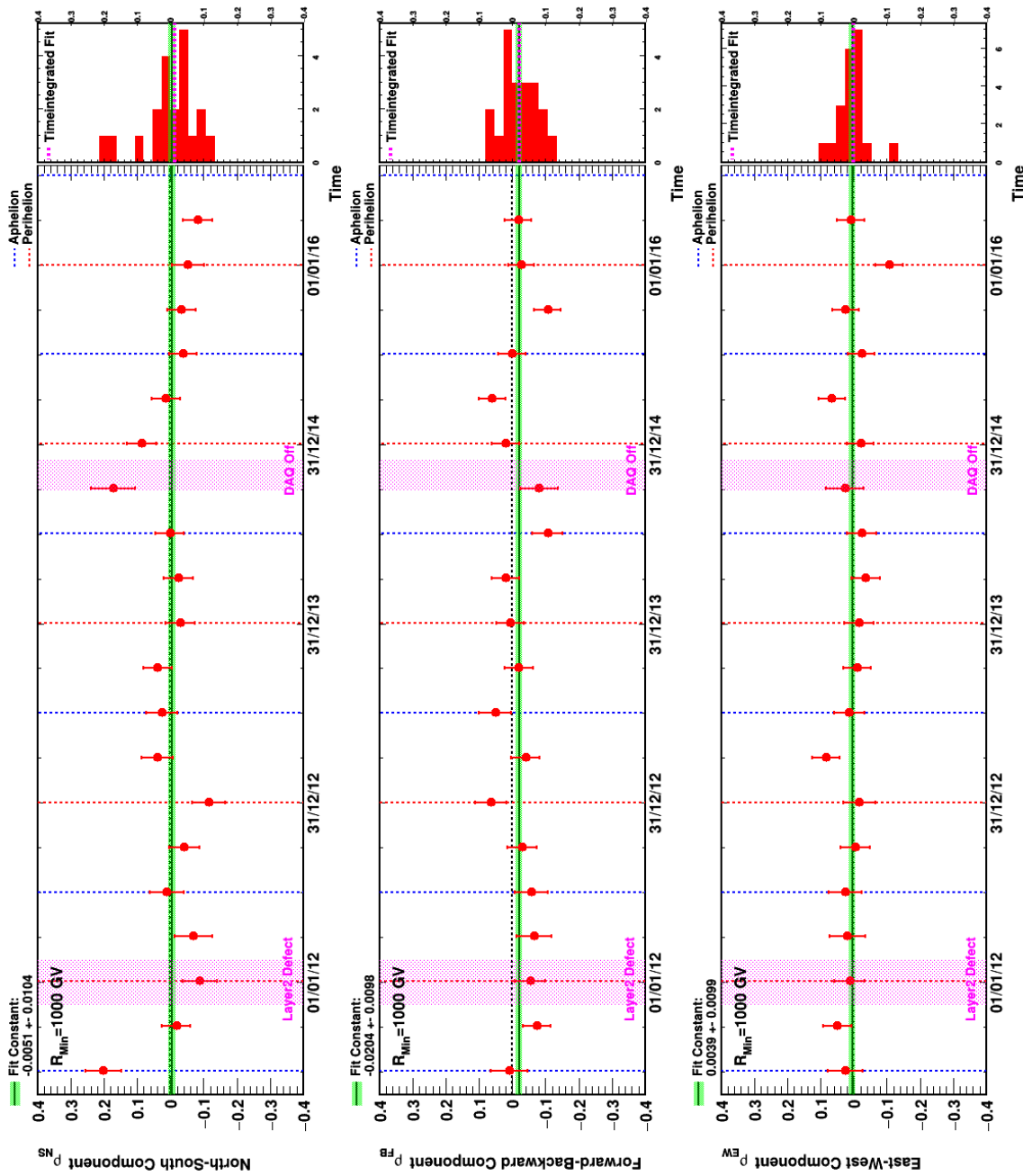
Figure B.31.: Seasonal fits of $R_{p/\bar{p}*}$ proton relative anisotropy at a minimum rigidity of 1000 GV in **GSE**.

B.7. Proton absolute anisotropy - GAL

R_{Min} (GV)	N_{Sig}	ρ_{NS}	$\sigma_{\rho NS}$	$\Delta_{\rho NS}$ (%)	ρ_{FB}	$\sigma_{\rho FB}$	$\Delta_{\rho FB}$ (%)	ρ_{EW}	$\sigma_{\rho EW}$	$\Delta_{\rho EW}$ (%)	δ	Syst. Limitation (%)	$\delta^{95\%}$ (%)
18	51211700	-0.0966	0.0244	0.0649	-0.0089	0.0241	0.0741	0.0187	0.0242	0.1339	0.0988	0.1369	0.1331
25	31428200	-0.0975	0.0310	0.0647	0.0115	0.0307	0.0675	0.0321	0.0311	0.1138	0.1033	0.1041	0.1453
40	13374900	-0.0564	0.0475	0.0573	0.0144	0.0470	0.0663	0.0775	0.0477	0.1081	0.0969	0.1125	0.1537
80	3843860	-0.0301	0.0886	0.0593	-0.0266	0.0877	0.0662	0.0477	0.0890	0.0933	0.0624	0.0919	0.1878
150	1231090	0.0477	0.1566	0.0642	0.1656	0.1550	0.0671	-0.0362	0.1572	0.0954	0.1761	0.0953	0.3714
300	348584	0.2081	0.2941	0.0637	-0.3256	0.2911	0.0684	0.5242	0.2955	0.0994	0.6512	0.0933	1.0080
500	133946	-0.1723	0.4742	0.0678	0.0108	0.4695	0.0681	0.4119	0.4764	0.1019	0.4466	0.1006	1.0666
1000	29562	-1.8099	1.0088	0.0616	-0.2305	0.9992	0.0709	2.0418	1.0150	0.1055	2.7382	0.1053	4.0304

Table B.7.: Fit of $R^{Rate}_{p/Isosky}$ proton absolute anisotropy in **GAL**.

Figure B.32.: Seasonal fits of $R^{Rate}_{p/Isosky}$ proton absolute anisotropy at a minimum rigidity of 18 GV in **GAL**.
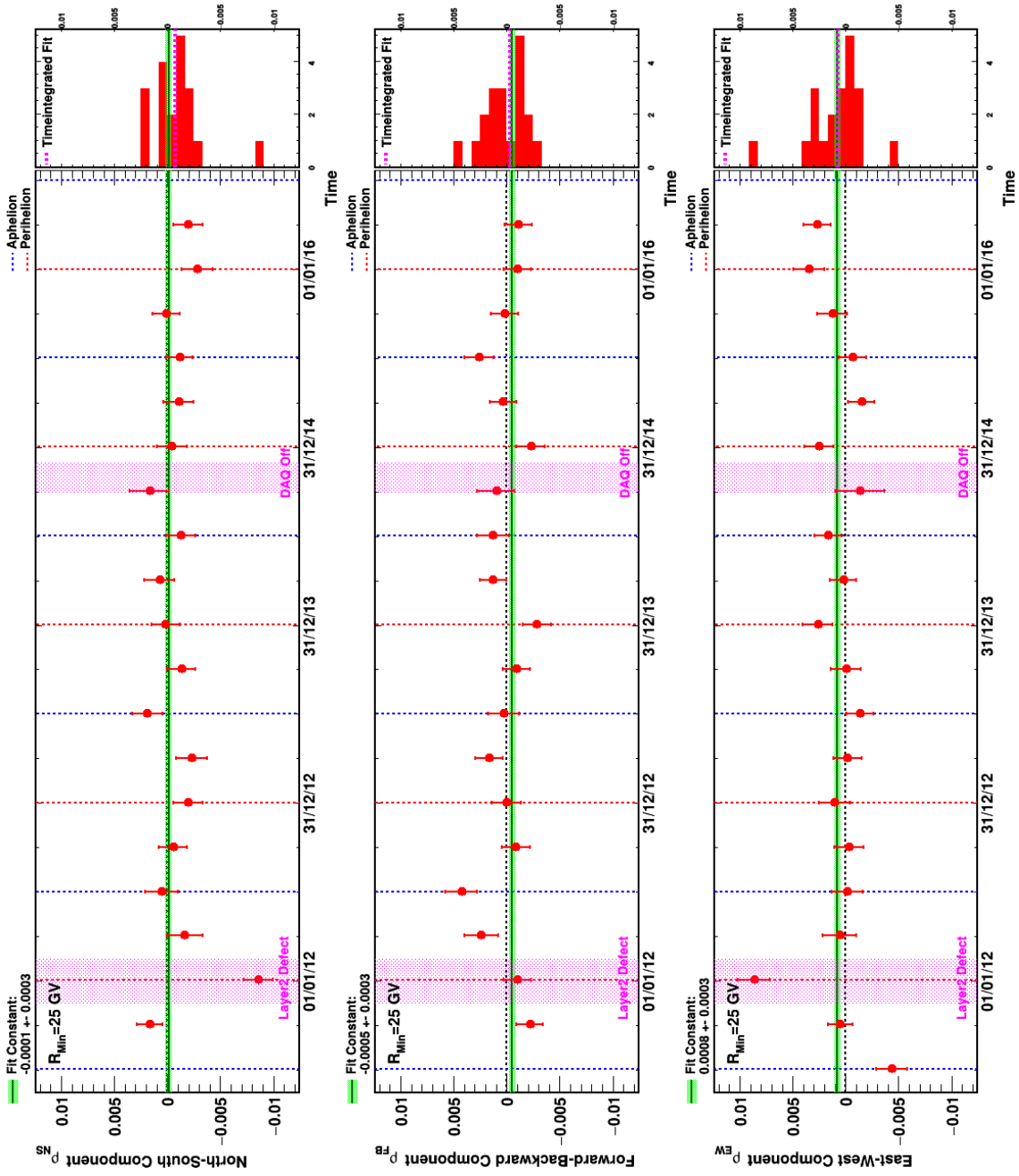
Figure B.33.: Seasonal fits of $R^{Rate}_{p/Isosky}$ proton absolute anisotropy at a minimum rigidity of 25 GV in **GAL**.
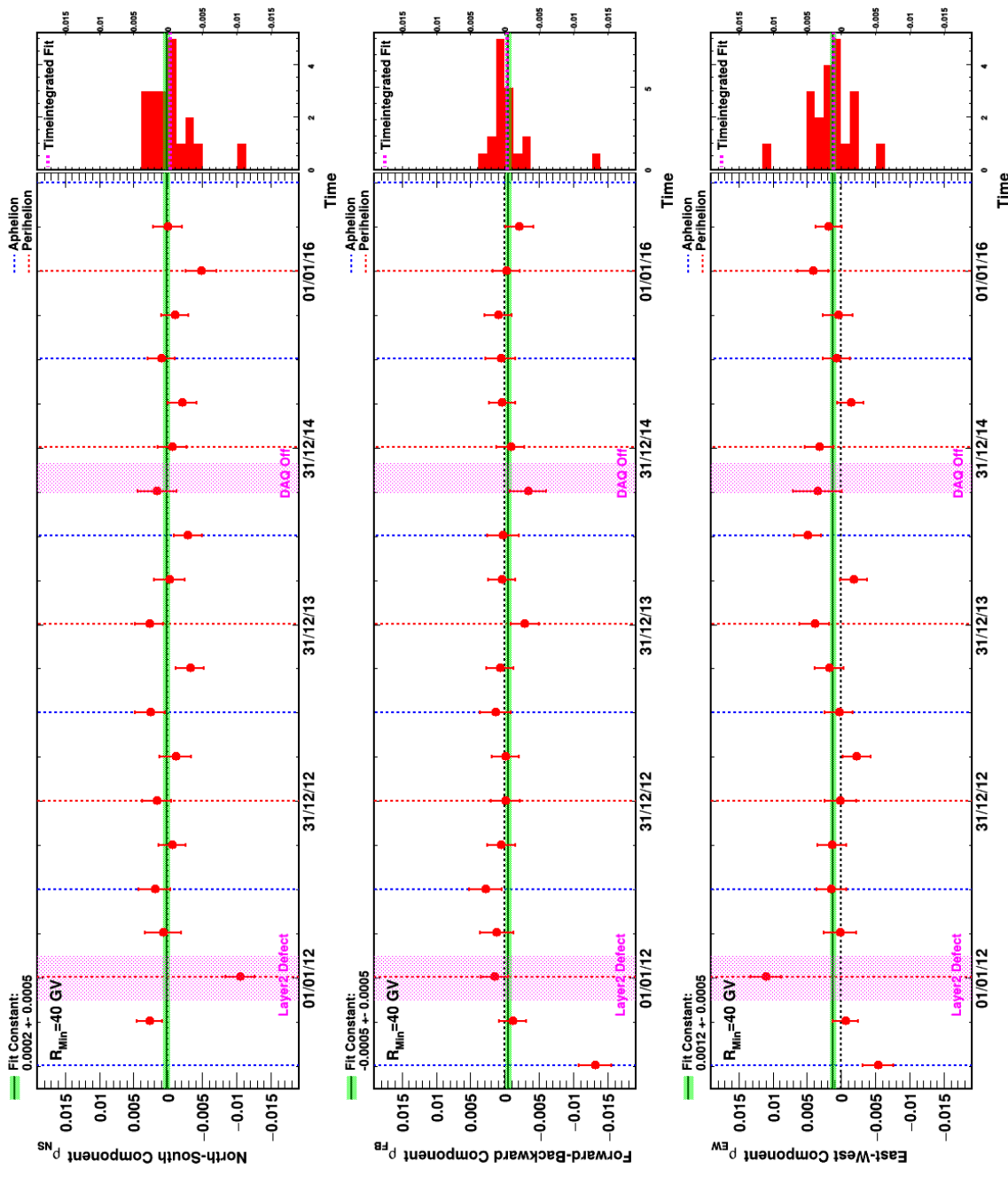
Figure B.34.: Seasonal fits of $R^{Rate}_{p/Isosky}$ proton absolute anisotropy at a minimum rigidity of 40 GV in **GAL**.
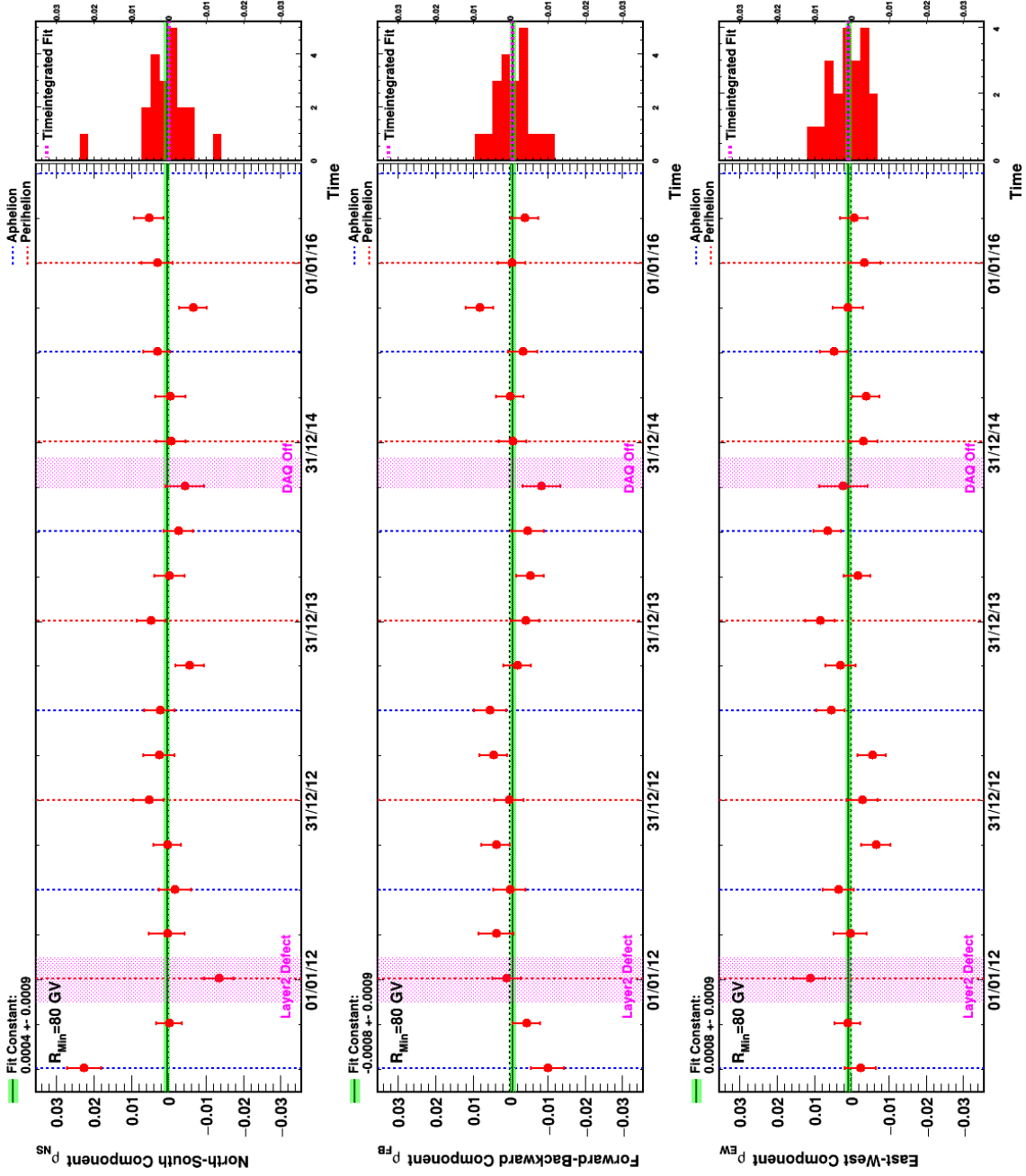
Figure B.35.: Seasonal fits of $R^{Rate}_{p/Isosky}$ proton absolute anisotropy at a minimum rigidity of 80 GV in **GAL**.

Figure B.36.: Seasonal fits of $R^{Rate}_{p/Isosky}$ proton absolute anisotropy at a minimum rigidity of 150 GV in **GAL**.

Figure B.37.: Seasonal fits of $R^{Rate}_{p/Isosky}$ proton absolute anisotropy at a minimum rigidity of 300 GV in **GAL**.

Figure B.38.: Seasonal fits of $R^{Rate}_{p/Isosky}$ proton absolute anisotropy at a minimum rigidity of 500 GV in **GAL**.

Figure B.39.: Seasonal fits of $R^{Rate}_{p/Isosky}$ proton absolute anisotropy at a minimum rigidity of 1000 GV in **GAL**.

B.8. Proton absolute anisotropy - GSE

R_{Min} (GV)	N_{Sig}	ρ_{NS}	$\sigma_{\rho NS}$	$\Delta_{\rho NS}$ (%)	ρ_{FB}	$\sigma_{\rho FB}$	$\Delta_{\rho FB}$ (%)	ρ_{EW}	$\sigma_{\rho EW}$	$\Delta_{\rho EW}$ (%)	δ	Syst. Limitation (%)	$\delta^{95\%}$ (%)
18	51211700	0.0273	0.0244	0.1695	0.0818	0.0240	0.0054	0.2161	0.0242	0.0046	0.2327	0.1697	0.2701
25	31428200	0.0157	0.0317	0.1642	0.0706	0.0303	0.0093	0.1792	0.0307	0.0046	0.1933	0.1645	0.2395
40	13374900	-0.0477	0.0487	0.1287	-0.0619	0.0465	0.0077	0.2150	0.0470	0.0049	0.2288	0.1290	0.2977
80	3843860	-0.0339	0.0907	0.1195	-0.3432	0.0866	0.0123	0.3122	0.0877	0.0072	0.4652	0.1204	0.5951
150	1231090	-0.0293	0.1603	0.1238	-0.8368	0.1530	0.0173	0.1929	0.1550	0.0110	0.8592	0.1255	1.0899
300	348584	-0.7145	0.3013	0.1227	-1.3119	0.2875	0.0247	0.7150	0.2912	0.0200	1.6561	0.1267	2.0908
500	133946	-0.5719	0.4858	0.1126	-1.9938	0.4636	0.0301	0.9518	0.4696	0.0217	2.2821	0.1186	2.9699
1000	29562	-1.1123	1.0346	0.1173	-2.1304	0.9869	0.0329	0.2420	0.9996	0.0265	2.4154	0.1247	3.6626

Table B.8.: Fit of $R_{p/Isosky}^{Rate}$ proton absolute anisotropy in **GSE**.
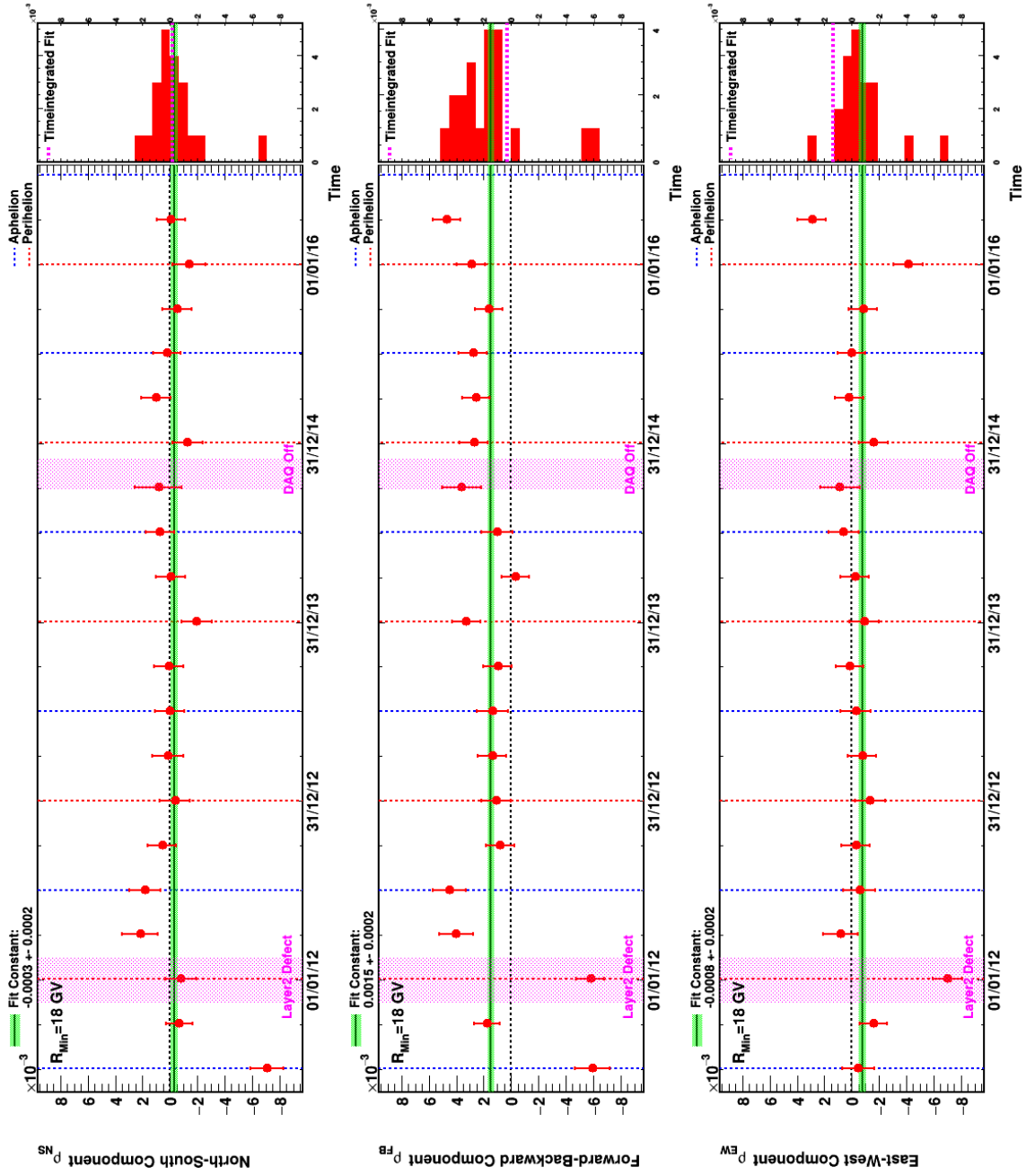
Figure B.40.: Seasonal fits of $R^{Rate}_{p/Isosky}$ proton absolute anisotropy at a minimum rigidity of 18 GV in **GSE**.
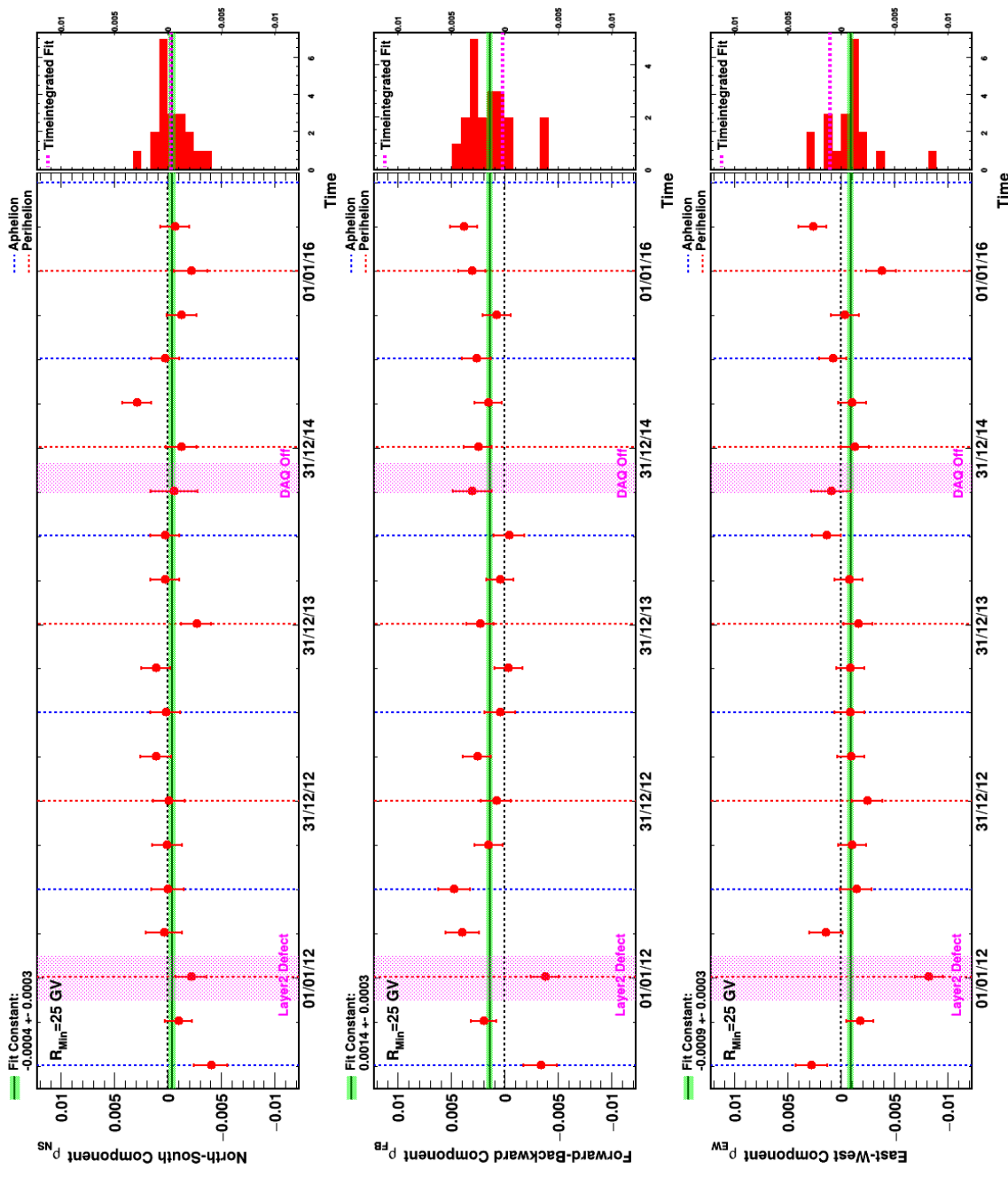
Figure B.41.: Seasonal fits of $R^{Rate}_{p/Isosky}$ proton absolute anisotropy at a minimum rigidity of 25 GV in **GSE**.
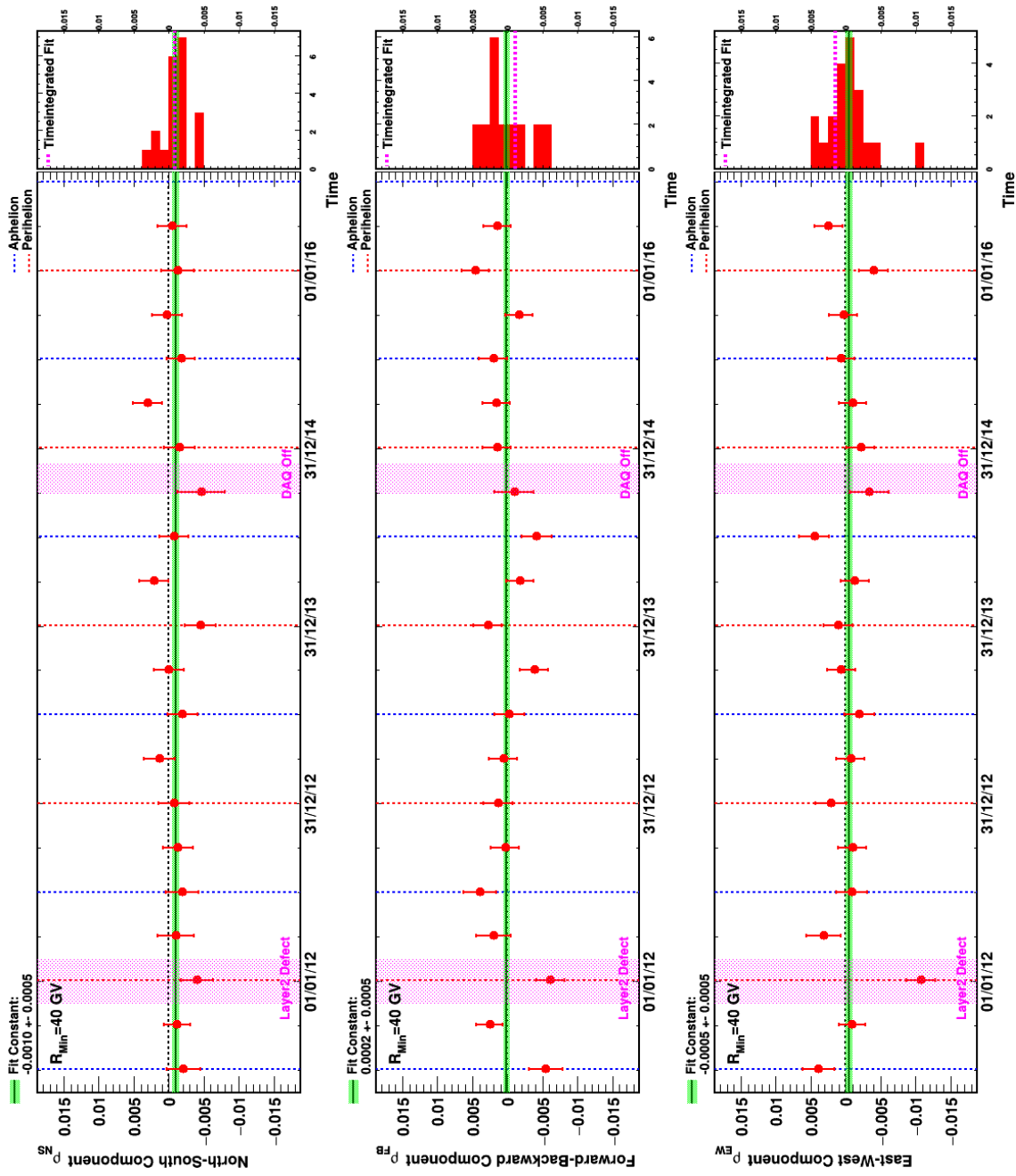
Figure B.42.: Seasonal fits of $R^{Rate}_{p/Isosky}$ proton absolute anisotropy at a minimum rigidity of 40 GV in **GSE**.
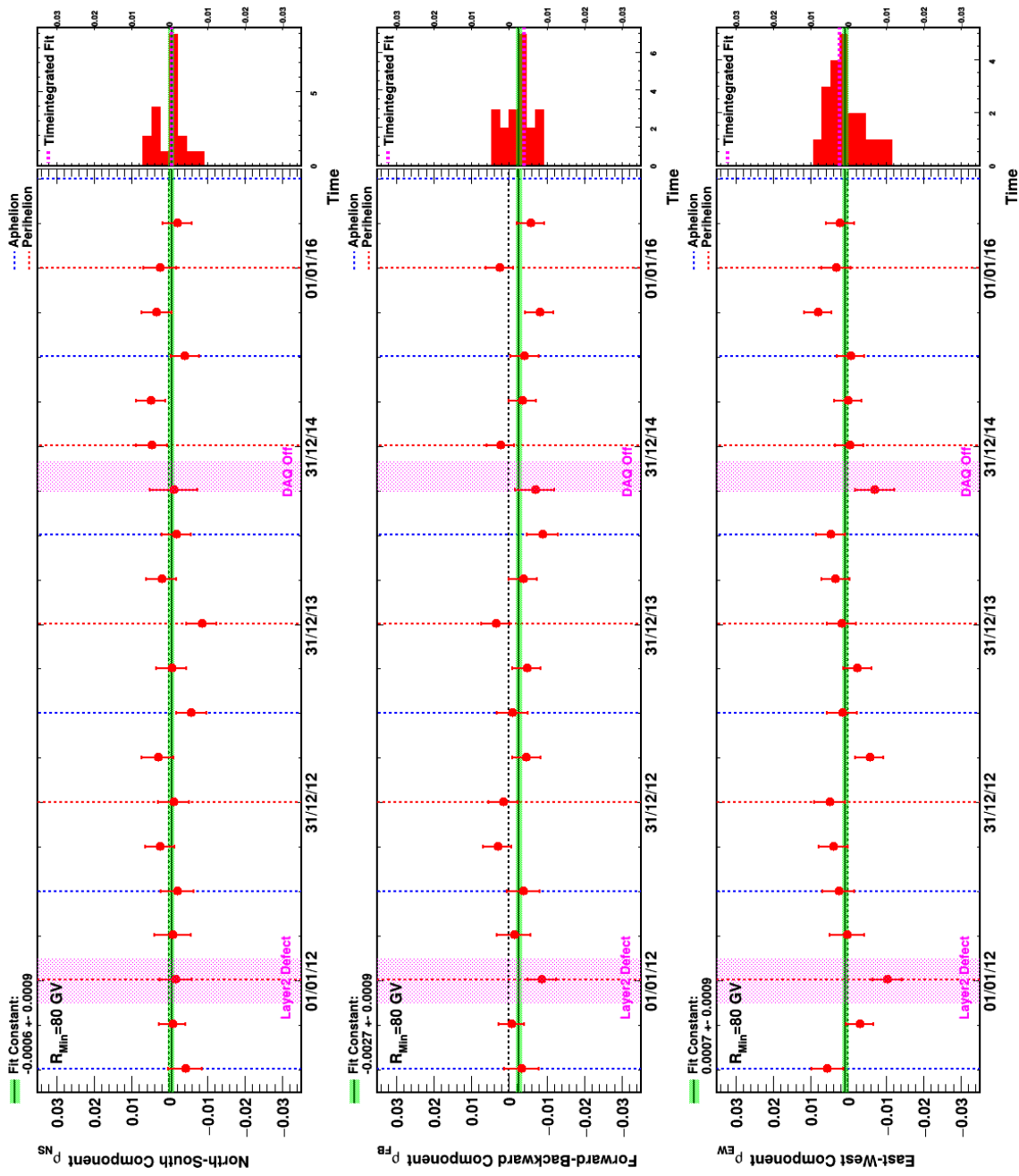
Figure B.43.: Seasonal fits of $R^{Rate}_{p/Isosky}$ proton absolute anisotropy at a minimum rigidity of 80 GV in **GSE**.
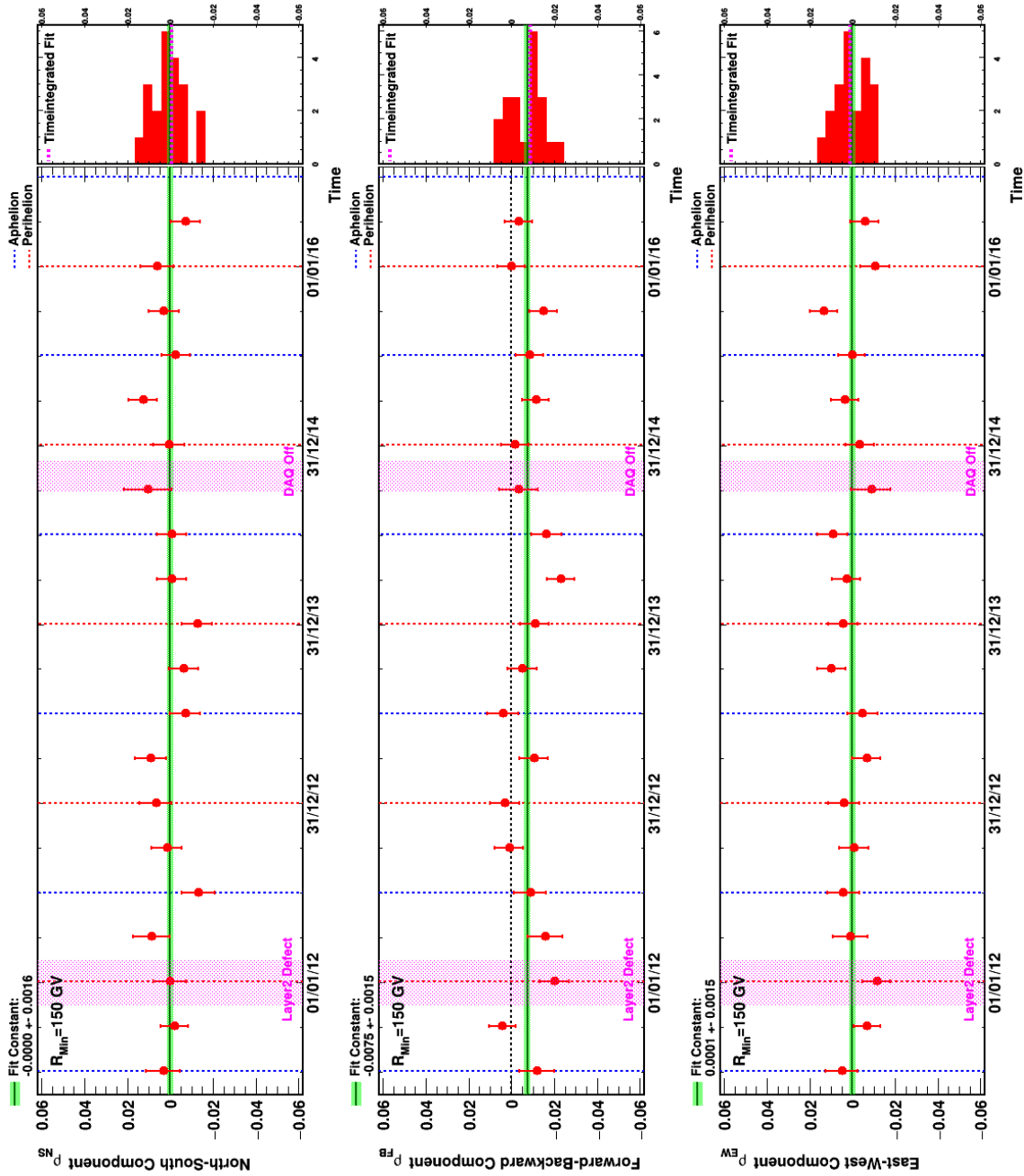
Figure B.44.: Seasonal fits of $R^{Rate}_{p/Isosky}$ proton absolute anisotropy at a minimum rigidity of 150 GV in **GSE**.

Figure B.45.: Seasonal fits of $R^{Rate}_{p/Isosky}$ proton absolute anisotropy at a minimum rigidity of 300 GV in **GSE**.

Figure B.46.: Seasonal fits of $R^{Rate}_{p/Isosky}$ proton absolute anisotropy at a minimum rigidity of 500 GV in **GSE**.
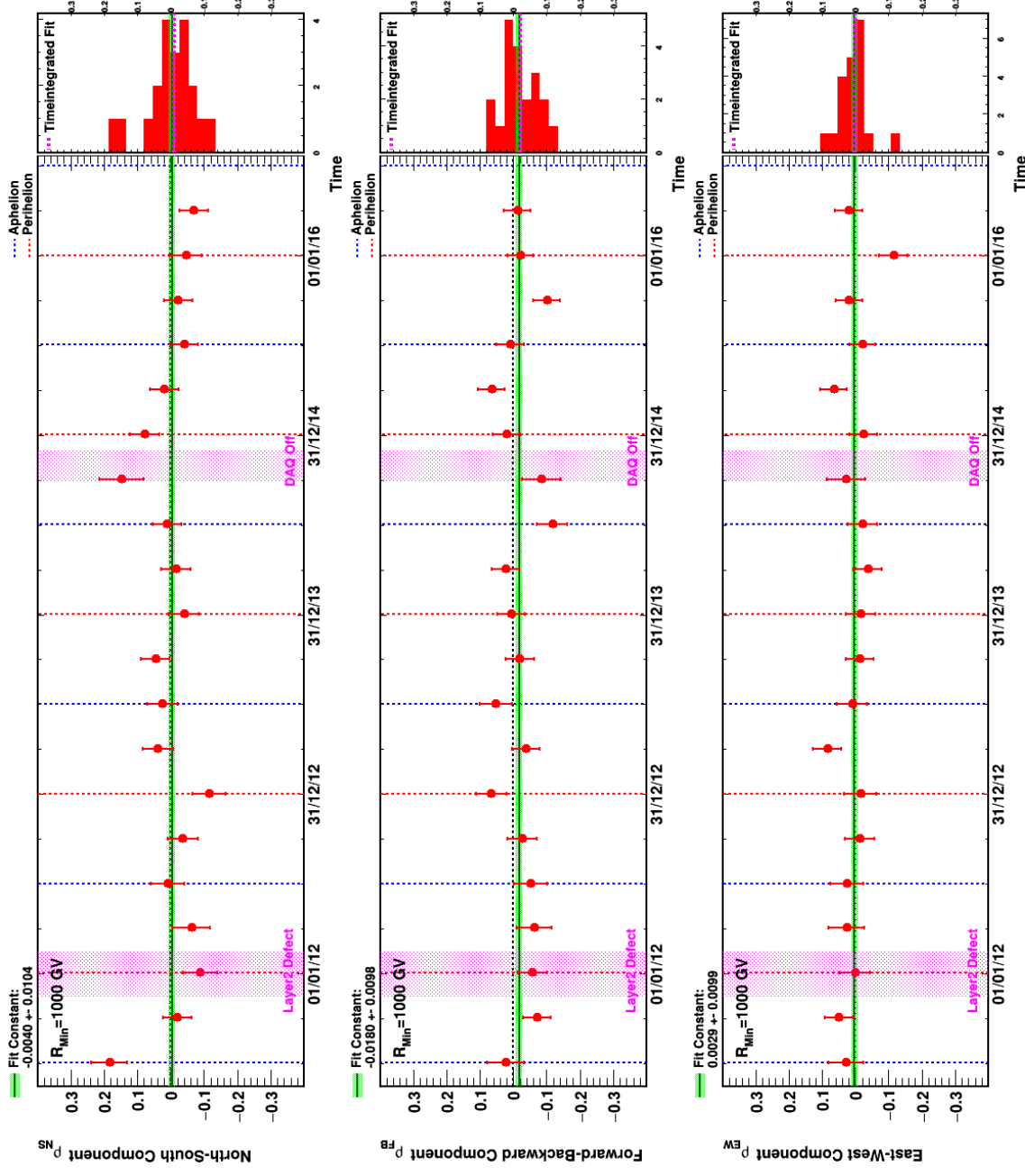
Figure B.47.: Seasonal fits of $R^{Rate}_{p/Isosky}$ proton absolute anisotropy at a minimum rigidity of 1000 GV in **GSE**.

B.9. Electron absolute anisotropy - GAL

E_{Min} (GeV)	N_{Sig}	ρ_{NS}	$\sigma_{\rho_{NS}}$	$\Delta_{\rho_{NS}}$ (%)	ρ_{FB}	$\sigma_{\rho_{FB}}$	$\Delta_{\rho_{FB}}$ (%)	ρ_{EW}	$\sigma_{\rho_{EW}}$	$\Delta_{\rho_{EW}}$ (%)	δ	Syst. Limitation (%)	$\delta^{95\%}$ (%)
16	913421	-0.132	0.184	0.007	-0.087	0.182	0.018	0.107	0.178	0.015	0.191	0.054	0.422
25	393084	-0.214	0.276	0.029	-0.069	0.274	0.027	0.193	0.277	0.012	0.296	0.042	0.645
40	129017	-0.282	0.481	0.054	-0.043	0.476	0.035	-0.231	0.482	0.060	0.367	0.060	1.032
65	39598	0.759	0.861	0.054	0.571	0.853	0.034	-1.141	0.864	0.073	1.485	0.076	2.498
100	13434	0.601	1.468	0.057	0.224	1.453	0.065	-0.157	1.473	0.064	0.661	0.061	2.969

Table B.9.: Fit of $R^{Rate}_{e^-/Isosky}$ electron absolute anisotropy in **GAL**.
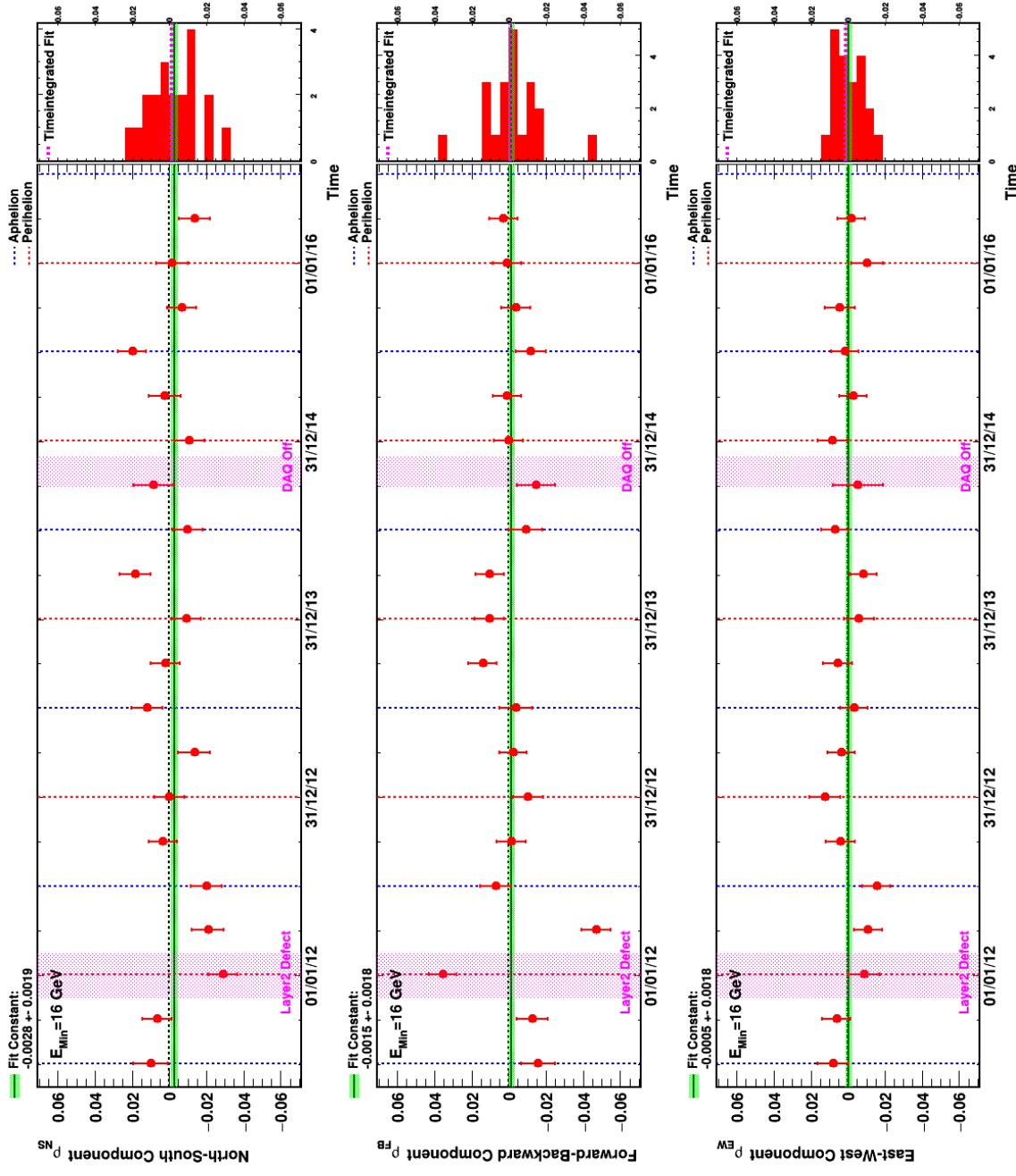
Figure B.48.: Seasonal fits of $R^{Rate}_{e^-/Isosky}$ electron absolute anisotropy at a minimum energy of 16 GeV in **GAL**.
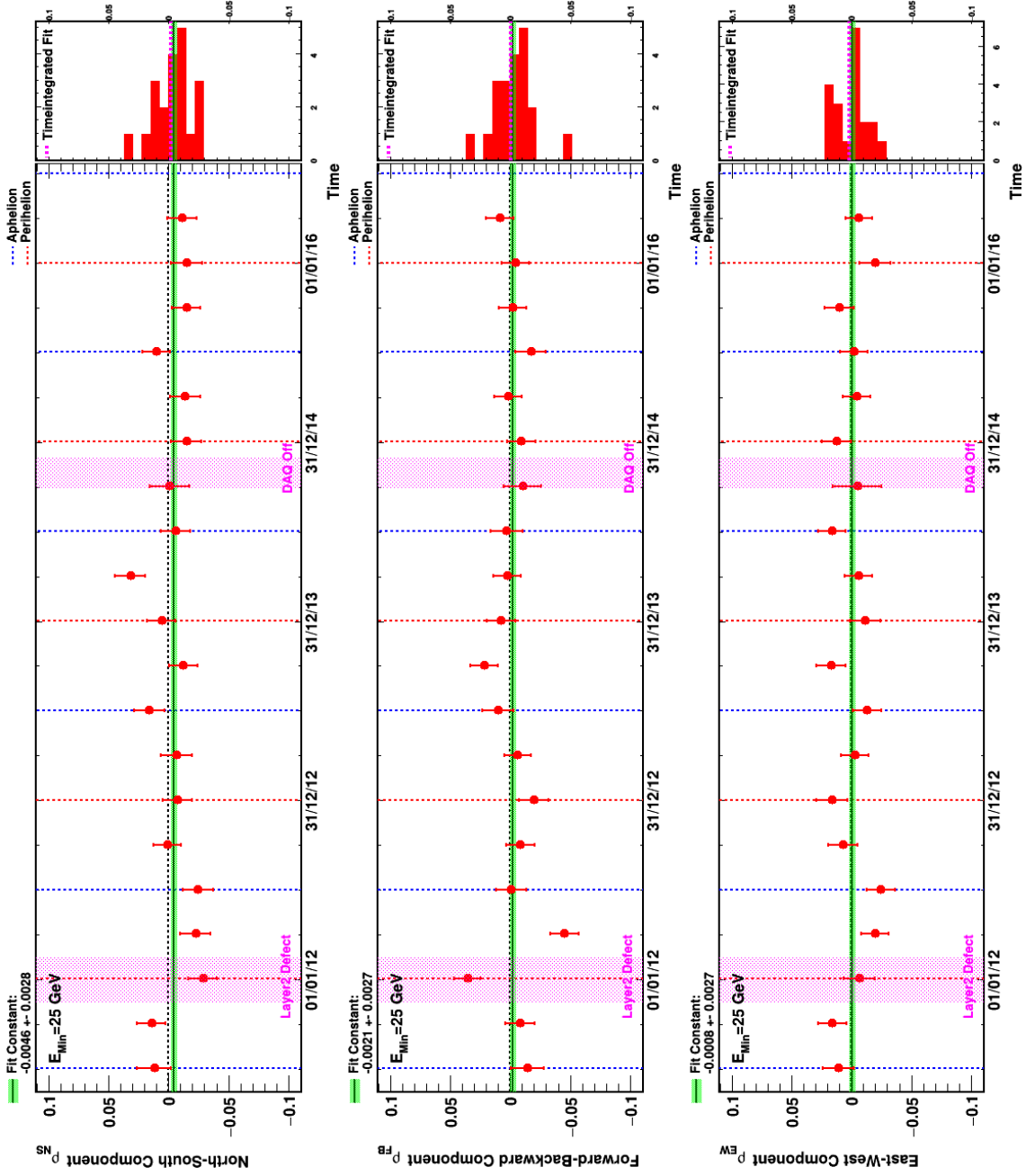
Figure B.49.: Seasonal fits of $R^{Rate}_{e^-/Isosky}$ electron absolute anisotropy at a minimum energy of 25 GeV in **GAL**.
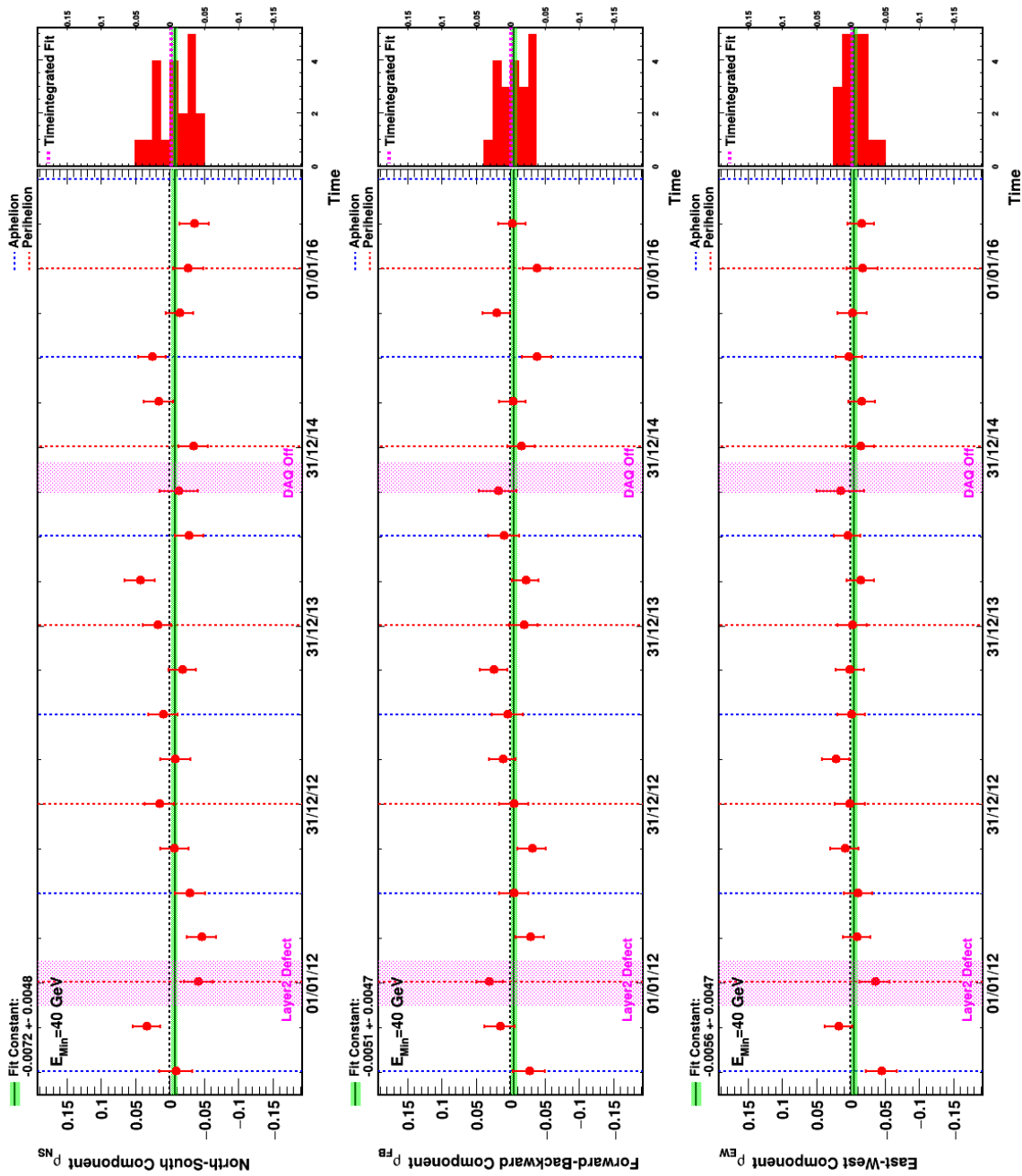
Figure B.50.: Seasonal fits of $R^{Rate}_{e^-/I_{sosky}}$ electron absolute anisotropy at a minimum energy of 40 GeV in **GAL**.
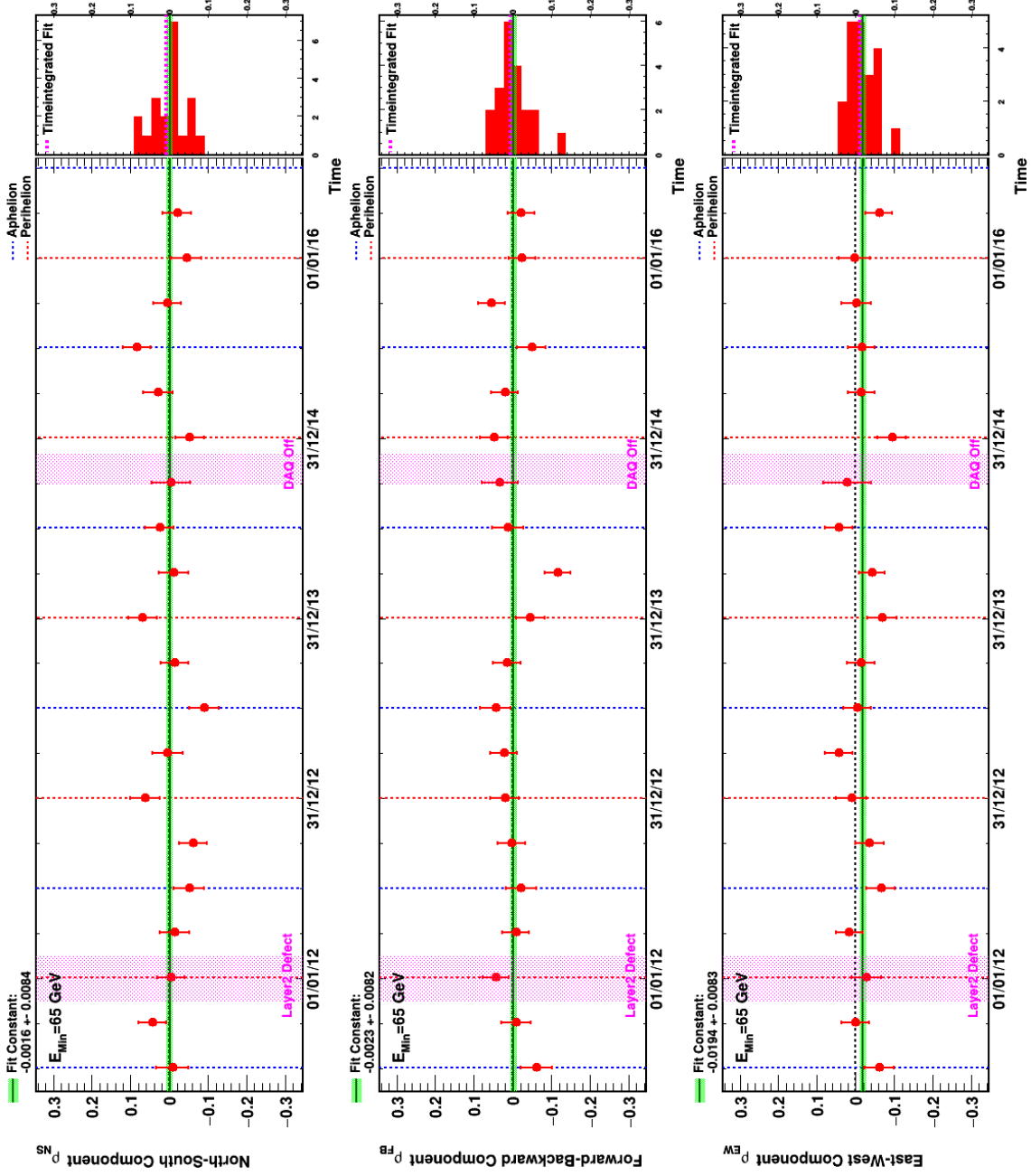
Figure B.51.: Seasonal fits of $R^{Rate}_{e^-/Isosky}$ electron absolute anisotropy at a minimum energy of 65 GeV in **GAL**.
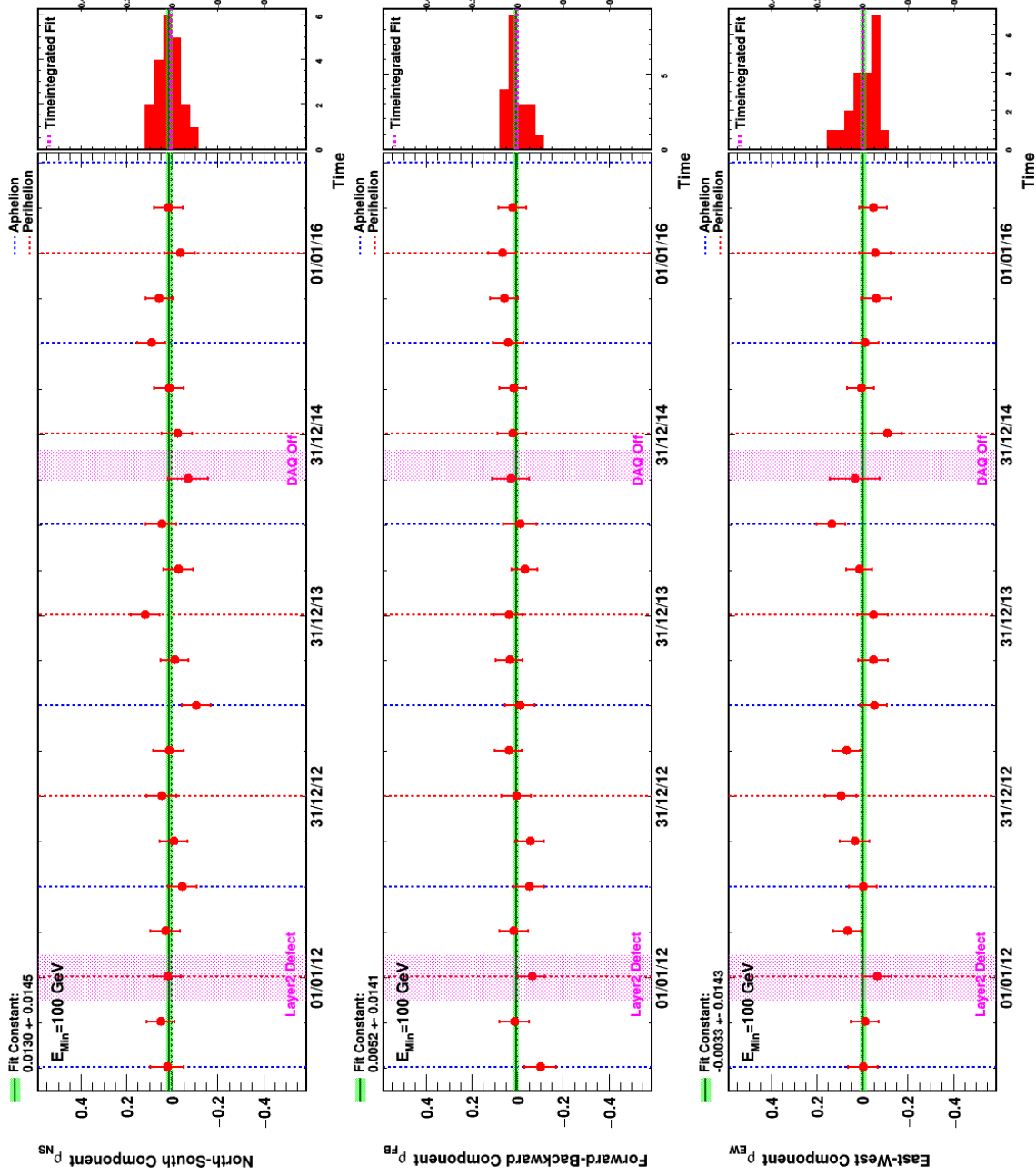
Figure B.52.: Seasonal fits of $R^{Rate}_{e^-/Isosky}$ electron absolute anisotropy at a minimum energy of 100 GeV in **GAL**.

B.10. Electron absolute anisotropy - GSE

E_{Min} (GeV)	N_{Sig}	ρ_{NS}	$\sigma_{\rho_{NS}}$	$\Delta_{\rho_{NS}}$ (%)	ρ_{FB}	$\sigma_{\rho_{FB}}$	$\Delta_{\rho_{FB}}$ (%)	ρ_{EW}	$\sigma_{\rho_{EW}}$	$\Delta_{\rho_{EW}}$ (%)	δ	Syst. Limitation (%)	$\delta^{95\%}$ (%)
16	913421	-0.016	0.176	0.249	-0.128	0.183	0.007	-0.859	0.184	0.025	0.868	0.070	1.131
25	393084	-0.011	0.282	0.011	-0.008	0.271	0.023	-0.993	0.274	0.031	0.993	0.032	1.374
40	129017	0.578	0.490	0.030	-0.075	0.470	0.033	-0.882	0.476	0.059	1.057	0.060	1.638
65	39598	1.195	0.877	0.052	-0.757	0.842	0.050	-0.448	0.852	0.055	1.484	0.058	2.495
100	13434	0.843	1.494	0.026	-1.571	1.434	0.060	-0.876	1.451	0.062	1.986	0.064	3.741

Table B.10.: Fit of $R^{Rate}_{e^-/Isosky}$ electron absolute anisotropy in **GSE**.
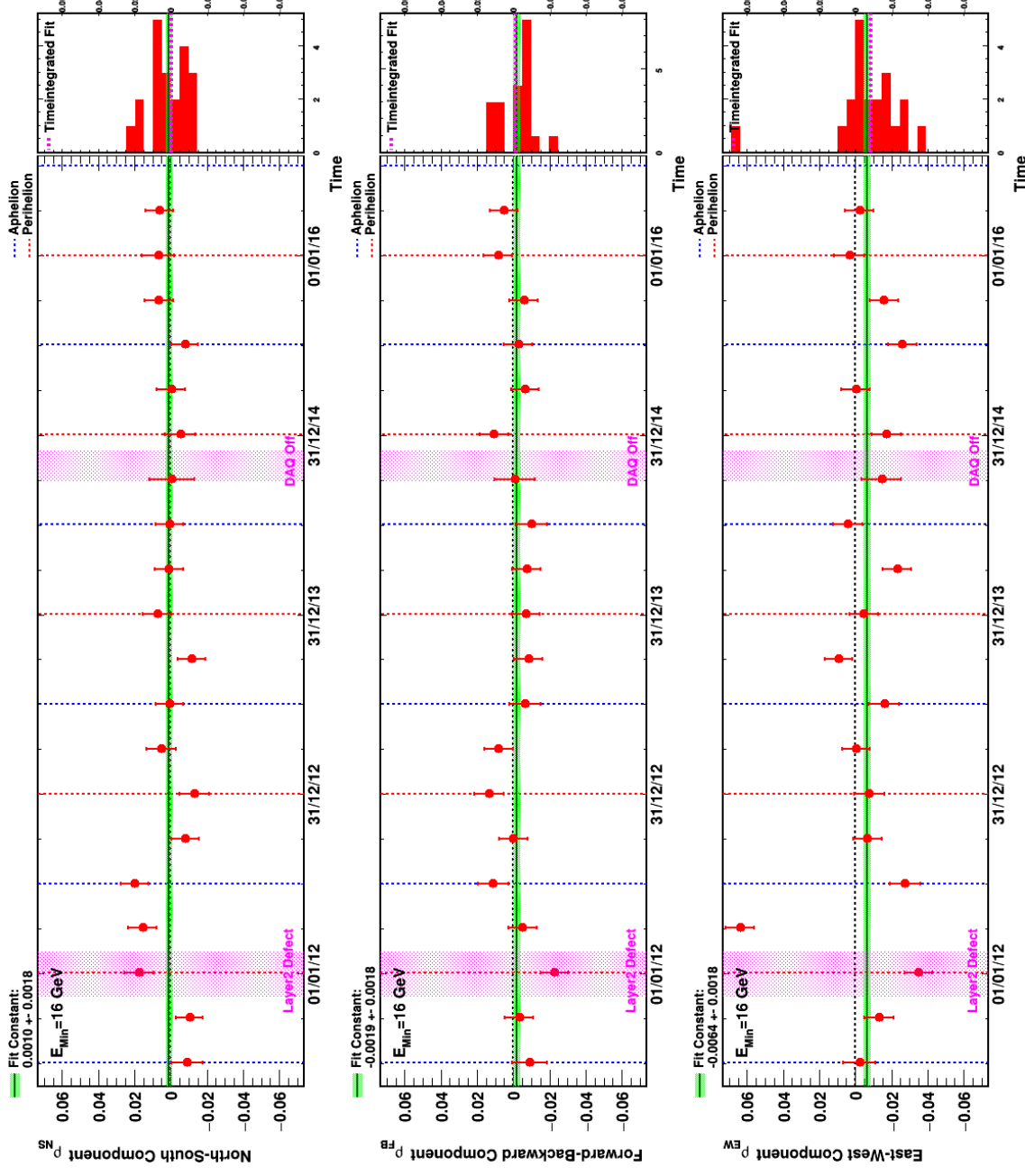
Figure B.53.: Seasonal fits of $R^{Rate}_{e^-/Isosky}$ electron absolute anisotropy at a minimum energy of 16 GeV in **GSE**.
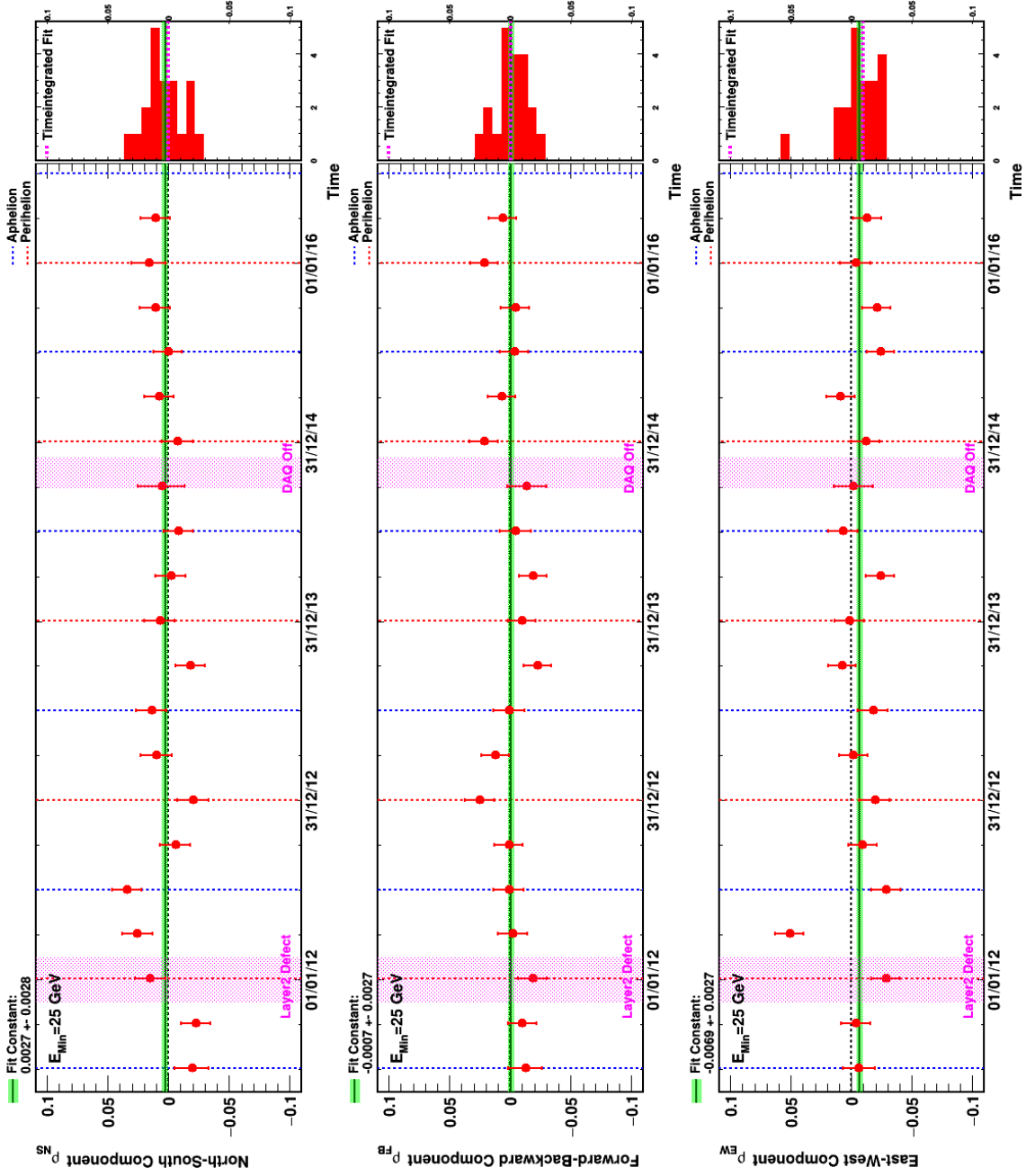
Figure B.54.: Seasonal fits of $R^{Rate}_{e^-/Isosky}$ electron absolute anisotropy at a minimum energy of 25 GeV in **GSE**.
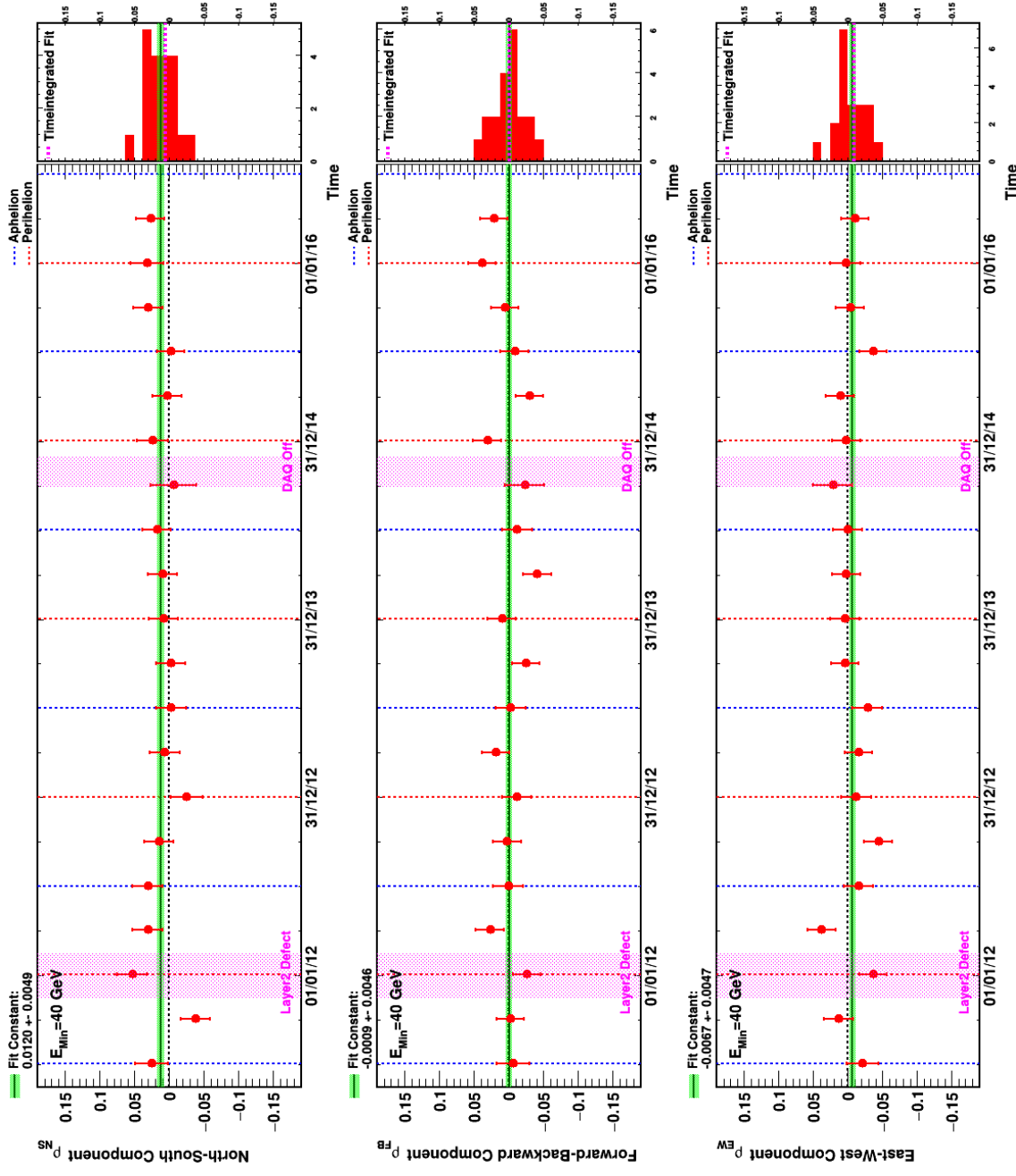
Figure B.55.: Seasonal fits of $R^{Rate}_{e^-/Isosky}$ electron absolute anisotropy at a minimum energy of 40 GeV in **GSE**.
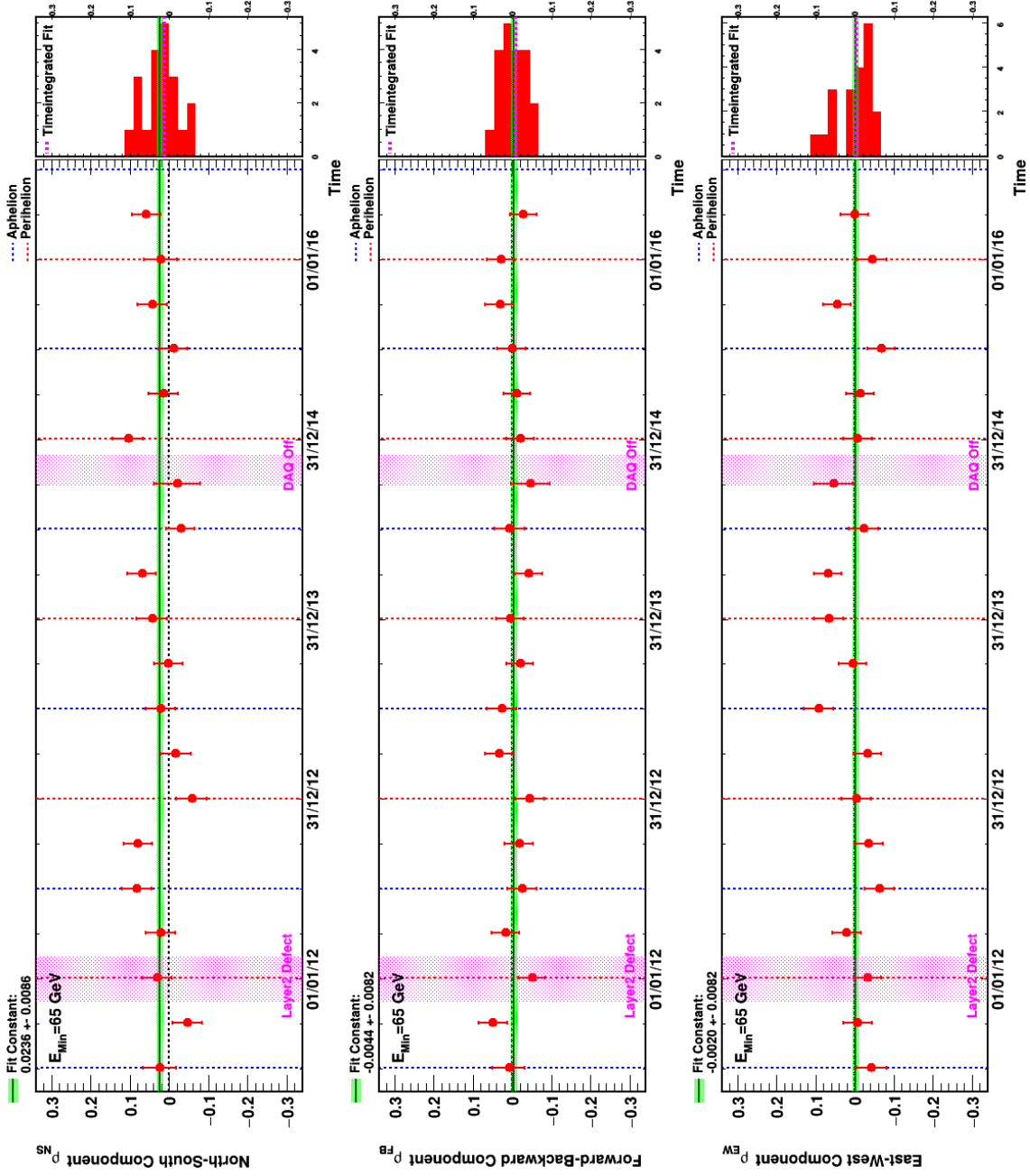
Figure B.56.: Seasonal fits of $R^{Rate}_{e^-/Isosky}$ electron absolute anisotropy at a minimum energy of 65 GeV in **GSE**.
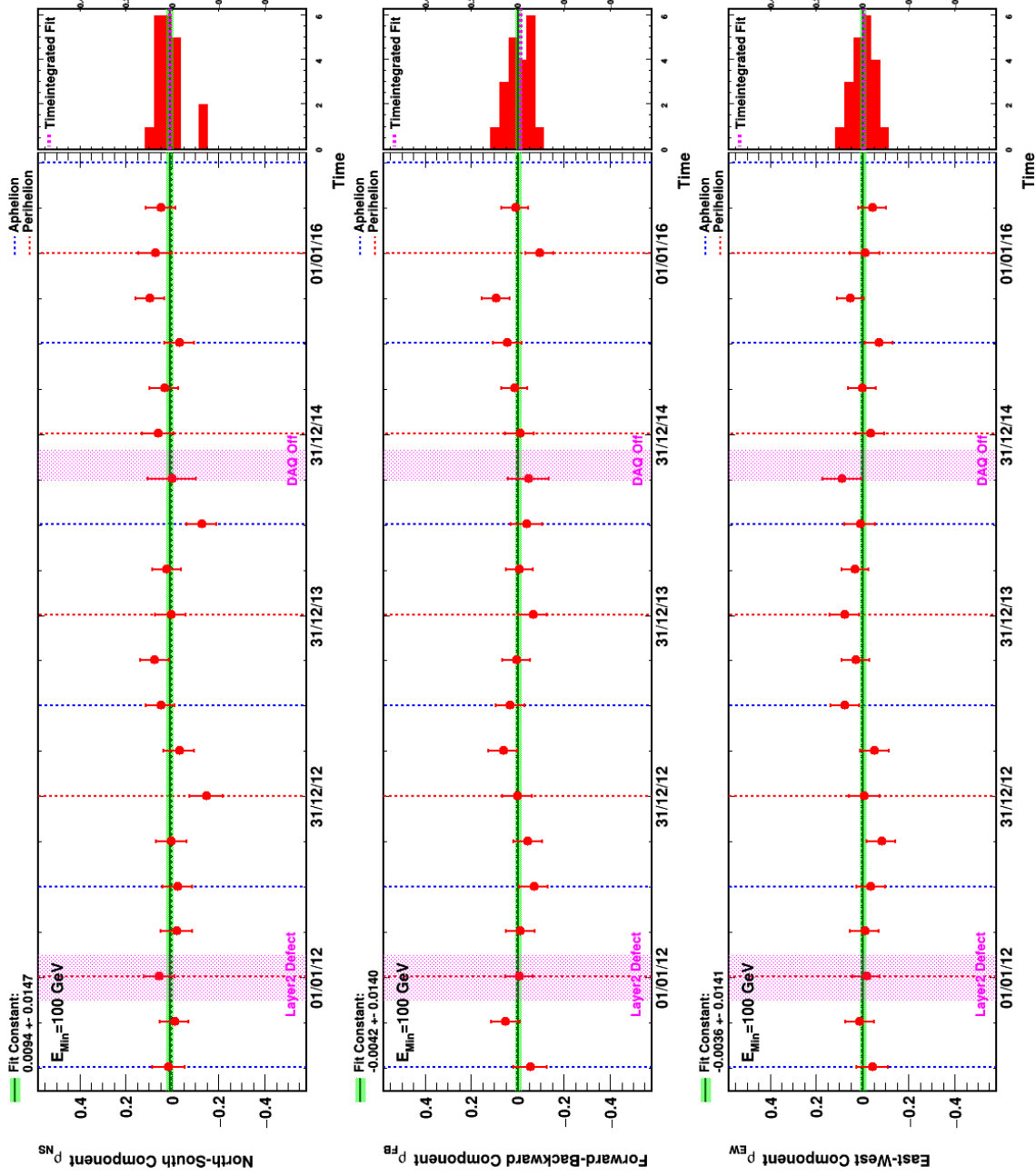
Figure B.57.: Seasonal fits of $R^{Rate}_{e^-/Isosky}$ electron absolute anisotropy at a minimum energy of 100 GeV in **GSE**.

B.11. Positron absolute anisotropy - GAL

E_{Min} (GeV)	N_{Sig}	ρ_{NS}	$\sigma_{\rho_{NS}}$	$\Delta_{\rho_{NS}}$ (%)	ρ_{FB}	$\sigma_{\rho_{FB}}$	$\Delta_{\rho_{FB}}$ (%)	ρ_{EW}	$\sigma_{\rho_{EW}}$	$\Delta_{\rho_{EW}}$ (%)	δ	Syst. Limitation (%)	$\delta^{95\%}$ (%)
16	69394	-0.623	0.655	0.034	-0.213	0.647	0.082	0.890	0.637	0.081	1.107	0.077	1.869
25	34422	-0.978	0.912	0.654	0.438	0.904	0.079	0.205	0.915	0.087	1.091	0.113	2.213
40	13937	-0.729	1.416	0.130	1.358	1.404	0.151	0.454	1.422	0.131	1.607	0.128	3.371
65	5401	-1.799	2.241	0.111	0.423	2.222	0.216	-0.319	2.243	0.150	1.875	0.151	4.899
100	2227	-1.103	3.498	0.152	0.163	3.475	0.153	-4.243	3.486	0.197	4.387	0.204	8.638

Table B.11.: Fit of $R_{e^+/Isosky}^{Rate}$ positron absolute anisotropy in **GAL**.
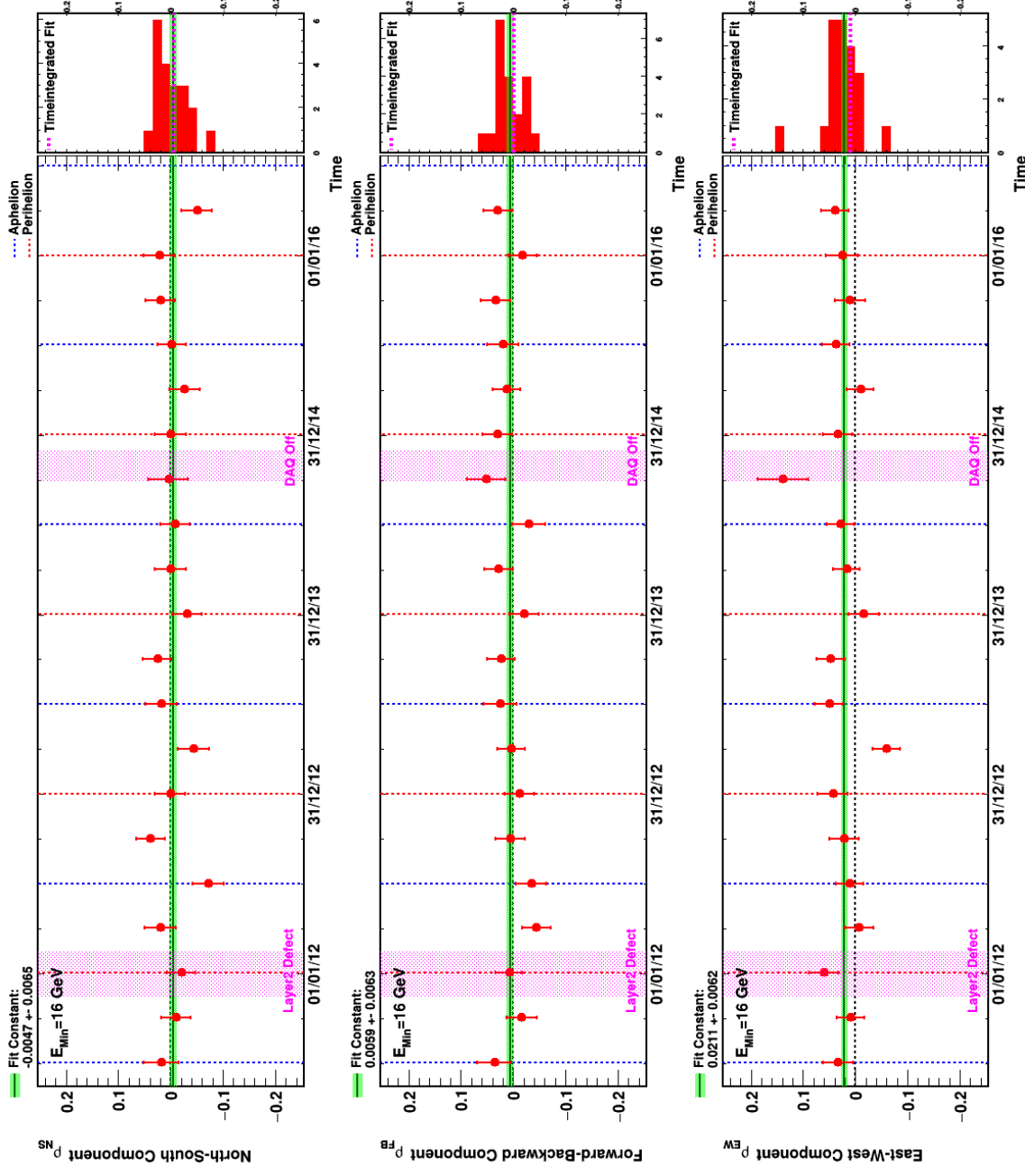
Figure B.58.: Seasonal fits of $R^{Rate}_{e^+/Isosky}$ positron absolute anisotropy at a minimum energy of 16 GeV in **GAL**.
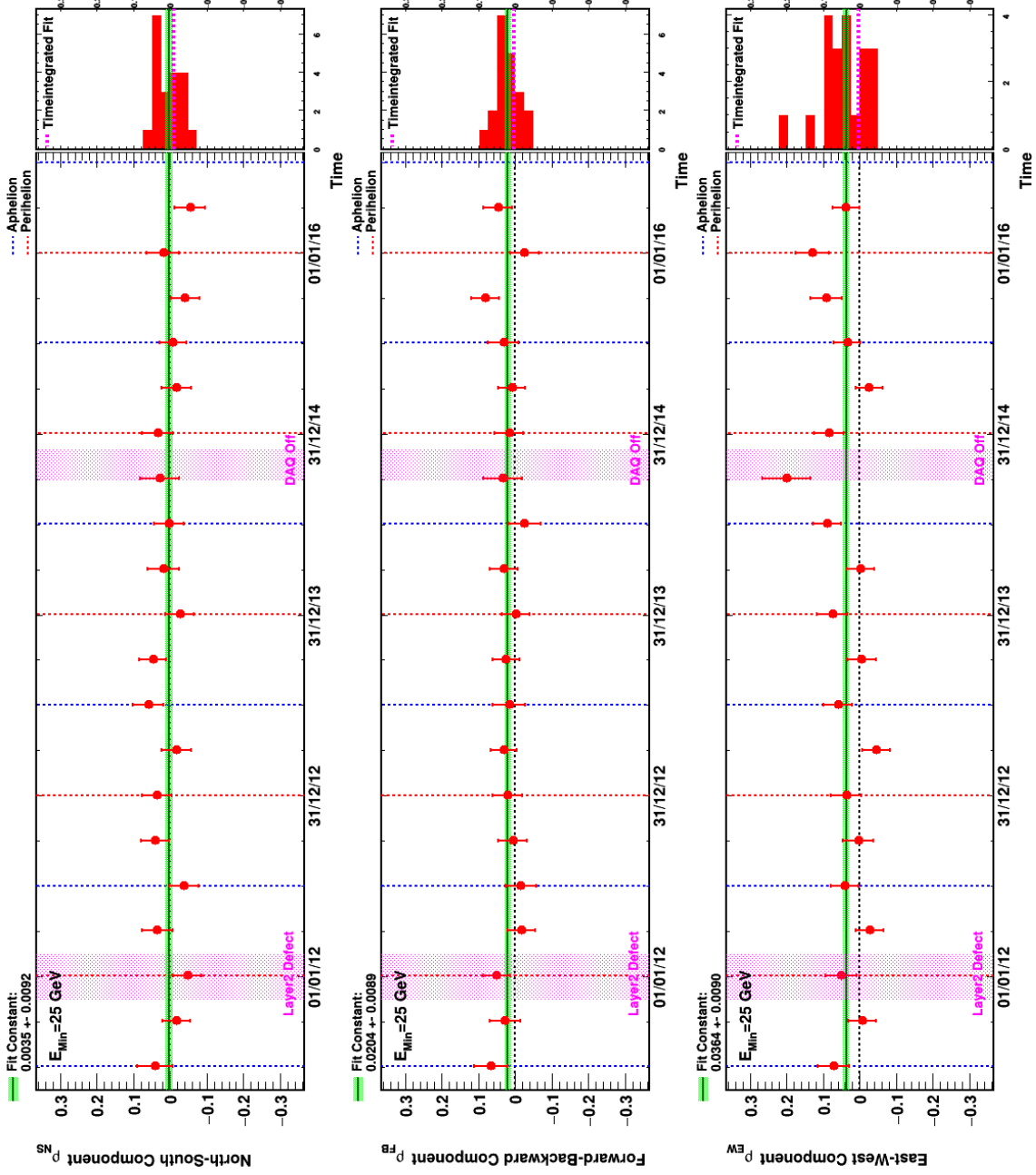
Figure B.59.: Seasonal fits of $R^{Rate}_{e^+/Isosky}$ positron absolute anisotropy at a minimum energy of 25 GeV in **GAL**.

Figure B.60.: Seasonal fits of $R^{Rate}_{e^-/Isosky}$ positron absolute anisotropy at a minimum energy of 40 GeV in **GAL**.

Figure B.61.: Seasonal fits of $R^{Rate}_{e^-/Isosky}$ positron absolute anisotropy at a minimum energy of 65 GeV in **GAL**.

Figure B.62.: Seasonal fits of $R^{Rate}_{e^-/Isosky}$ positron absolute anisotropy at a minimum energy of 100 GeV in **GAL**.

B.12. Positron absolute anisotropy - GSE

E_{Min} (GeV)	N_{Sig}	ρ_{NS}	$\sigma_{\rho NS}$	$\Delta_{\rho NS}$ (%)	ρ_{FB}	$\sigma_{\rho FB}$	$\Delta_{\rho FB}$ (%)	ρ_{EW}	$\sigma_{\rho EW}$	$\Delta_{\rho EW}$ (%)	δ	Syst. Limitation (%)	$\delta^{95\%}$ (%)
16	69394	-0.147	0.634	0.130	0.673	0.649	0.126	-0.534	0.654	0.022	0.872	0.117	1.649
25	34422	0.813	0.930	0.090	0.606	0.893	0.093	-0.951	0.903	0.090	1.390	0.092	2.466
40	13937	1.926	1.444	0.107	-0.860	1.383	0.048	-0.947	1.400	0.049	2.312	0.048	3.975
65	5401	4.700	2.281	0.172	-2.029	2.191	0.142	-2.389	2.221	0.114	5.649	0.111	8.452
100	2227	5.394	3.550	0.157	-1.422	3.417	0.059	-6.360	3.476	0.156	8.459	0.151	12.785

Table B.12.: Fit of $R_{e^+/Isosky}^{Rate}$ positron absolute anisotropy in **GSE**.
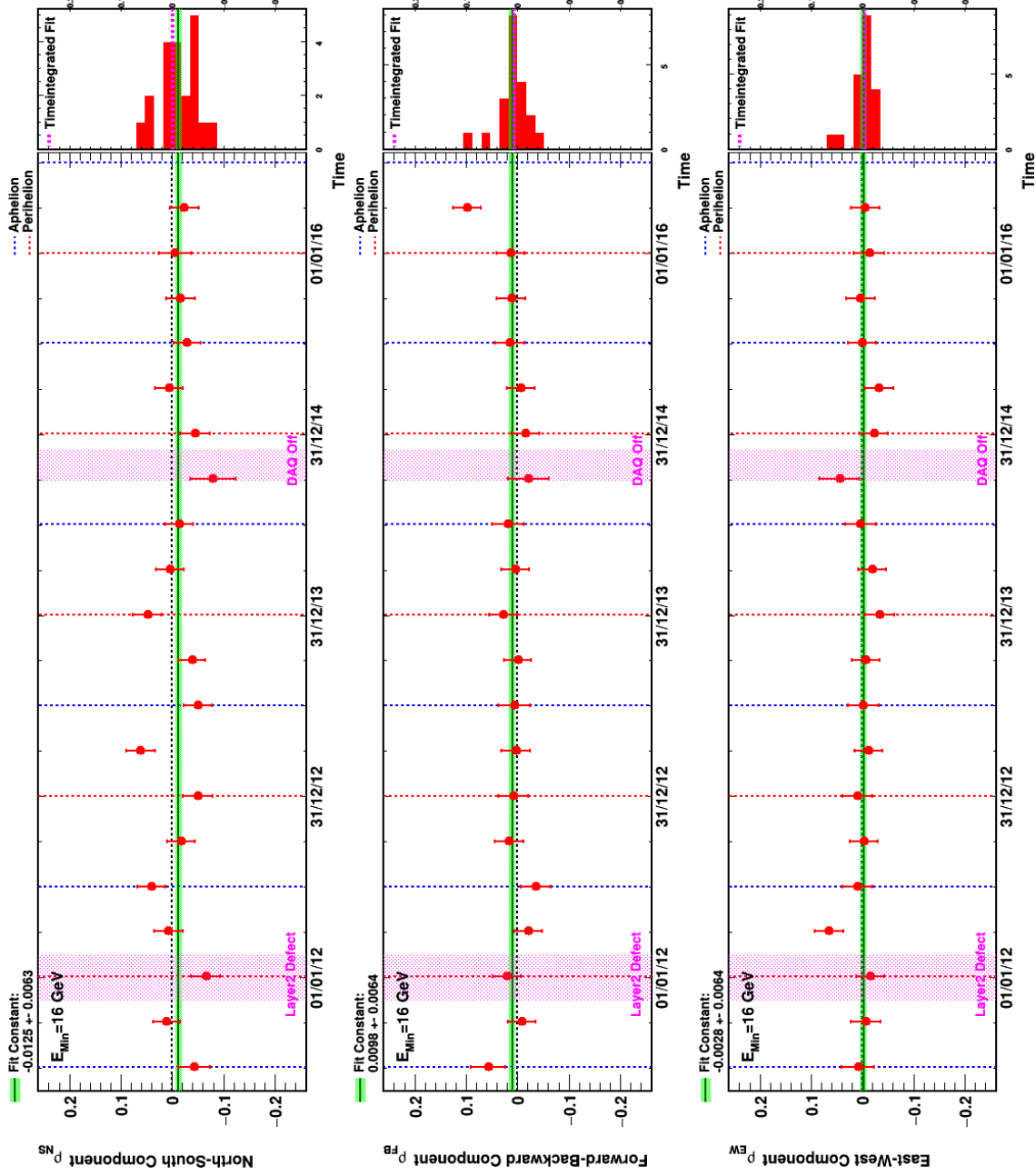
Figure B.63.: Seasonal fits of $R^{Rate}_{e^-/Isosky}$ positron absolute anisotropy at a minimum energy of 16 GeV in **GSE**.
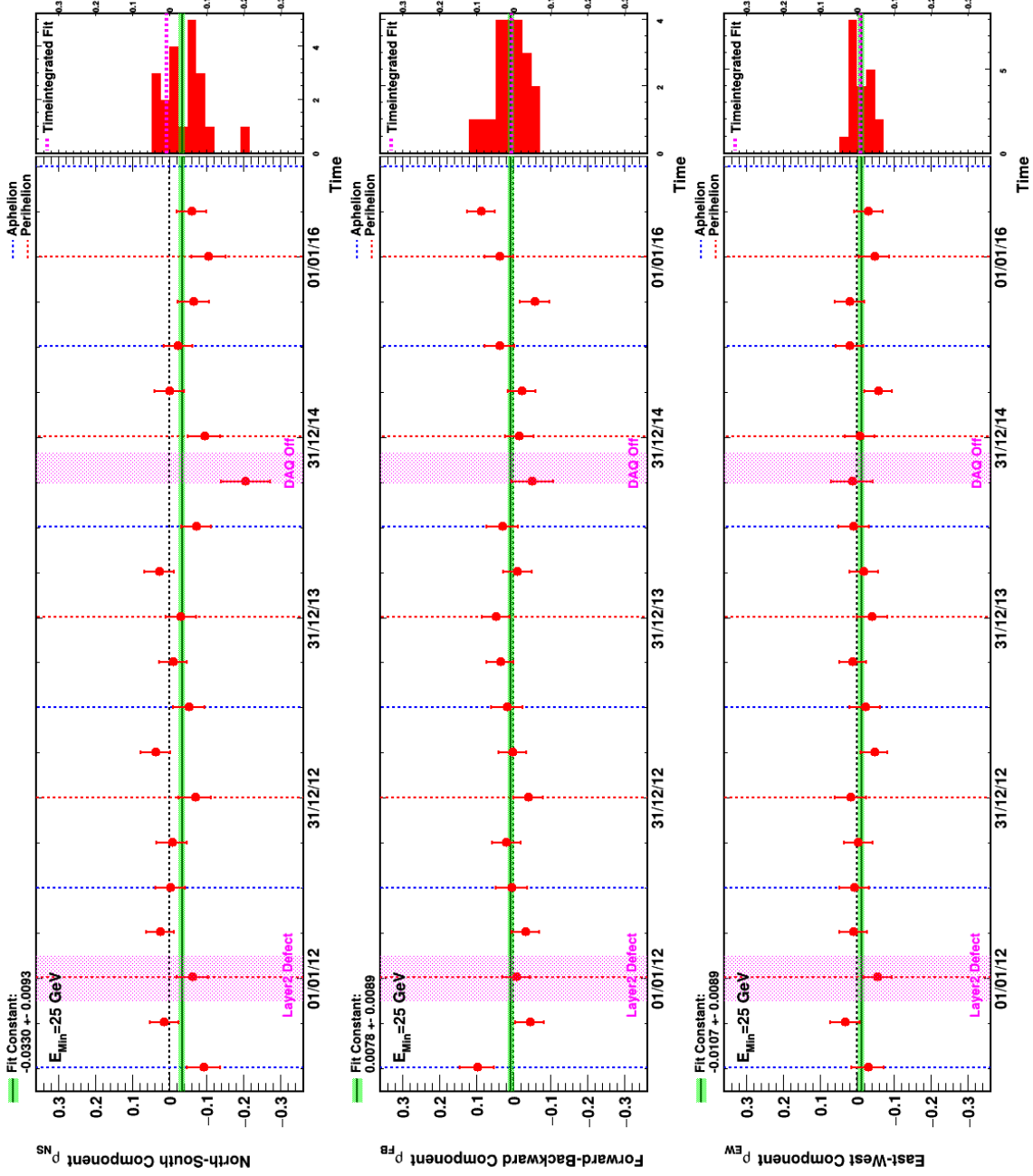
Figure B.64.: Seasonal fits of $R_{e^-/Isosky}^{Rate}$ positron absolute anisotropy at a minimum energy of 25 GeV in **GSE**.
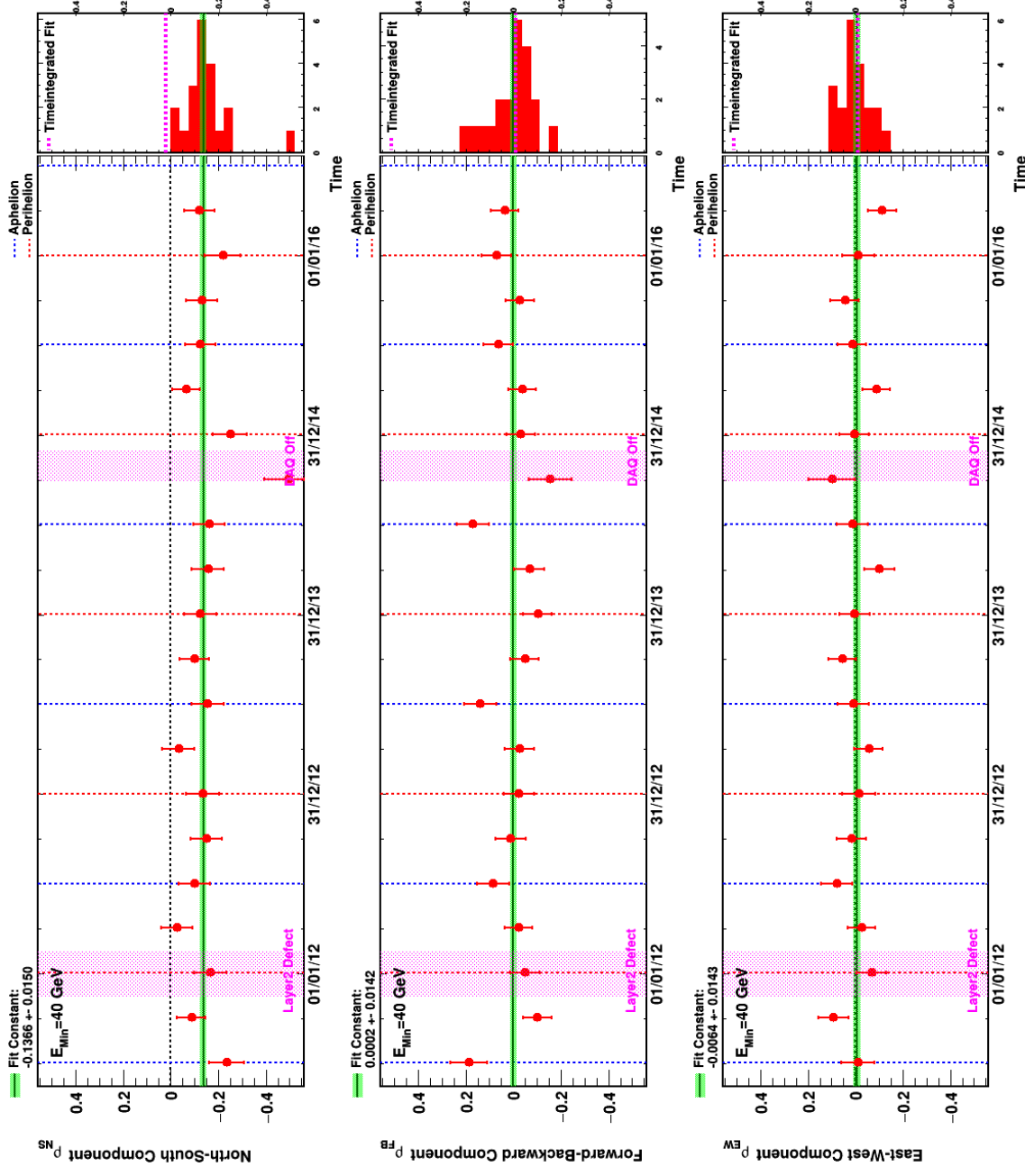
Figure B.65.: Seasonal fits of $R^{Rate}_{e^+/Isosky}$ positron absolute anisotropy at a minimum energy of 40 GeV in **GSE**.
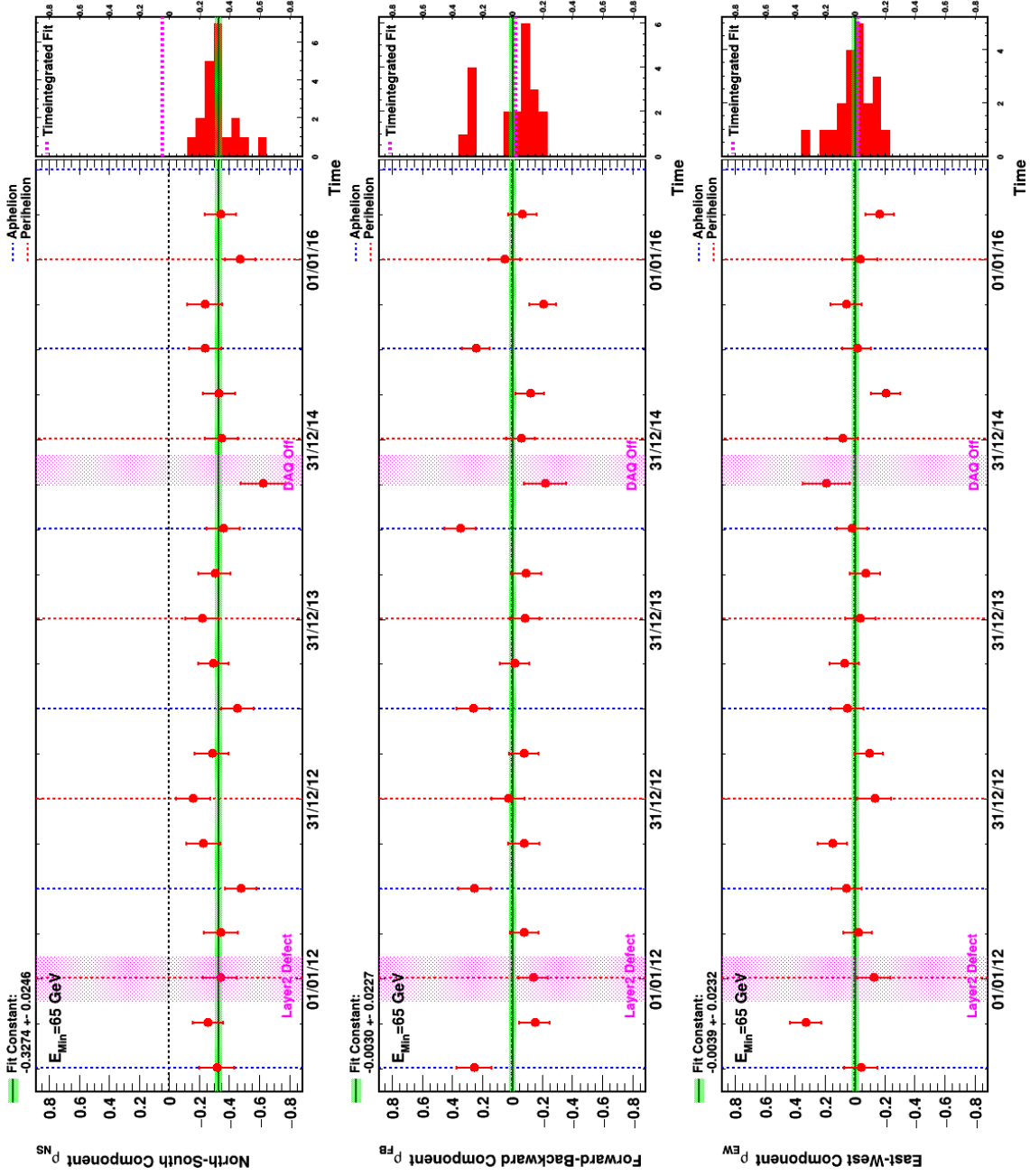
Figure B.66.: Seasonal fits of $R^{Rate}_{e^+/Isosky}$ positron absolute anisotropy at a minimum energy of 65 GeV in **GSE**.
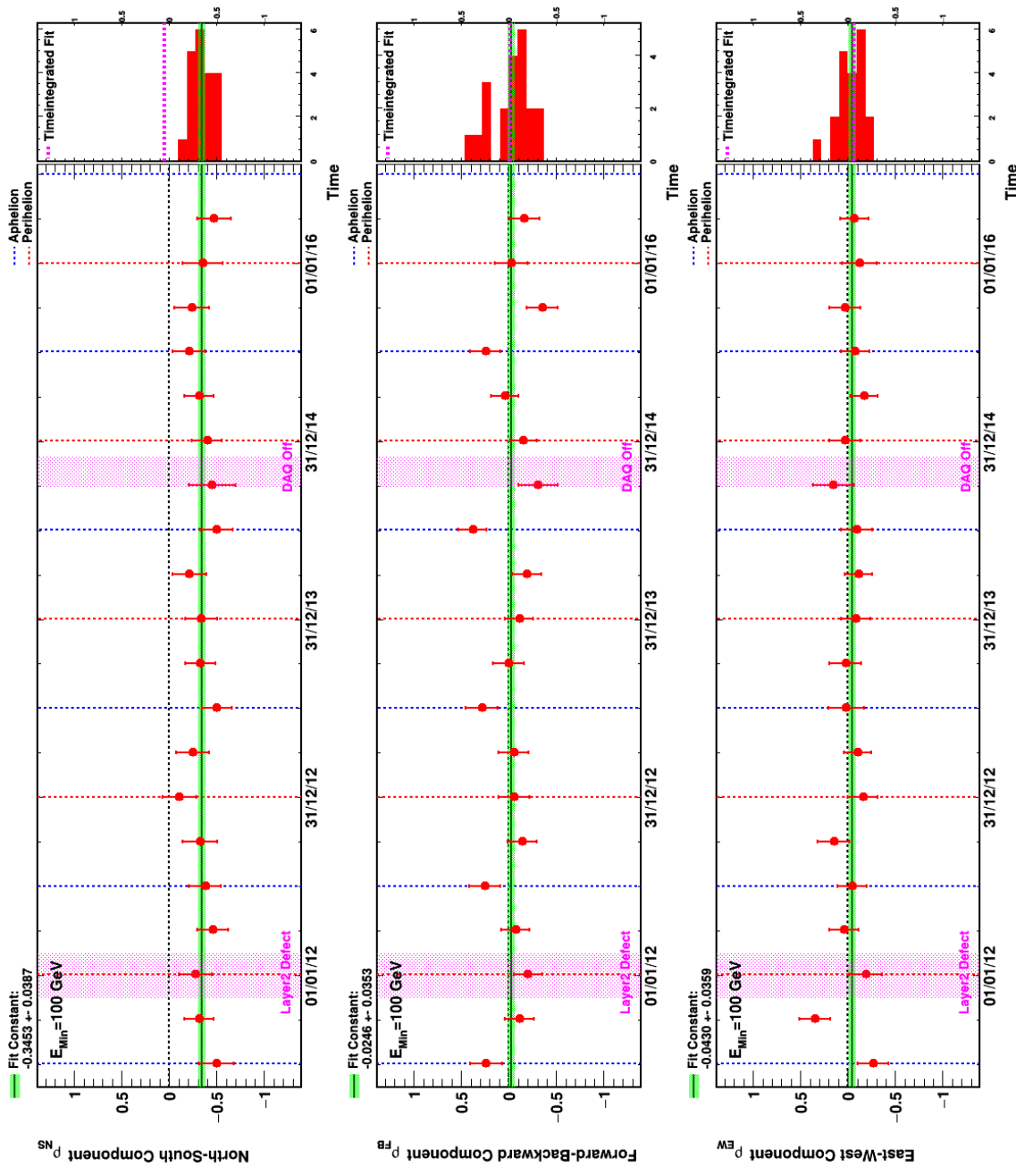
Figure B.67.: Seasonal fits of $R^{Rate}_{e^+/Isosky}$ positron absolute anisotropy at a minimum energy of 100 GeV in **GSE**.

C. AMS-02 collected data

Figure C.68 shows the cumulated number of collected CR events measured by AMS-02 with time from May 2011 to August 2017. The graph shows the number of events transferred to ground, and the number of events reconstructed in the POCC; both are overlayed. The grow in statistics in time is perfectly linear over the whole period. On 8th May 2017, AMS-02 measured 100 billion events [188]. In the analysis presented in this thesis, data up to 11th May 2016 was analyzed, including about 80 billion of collected events.
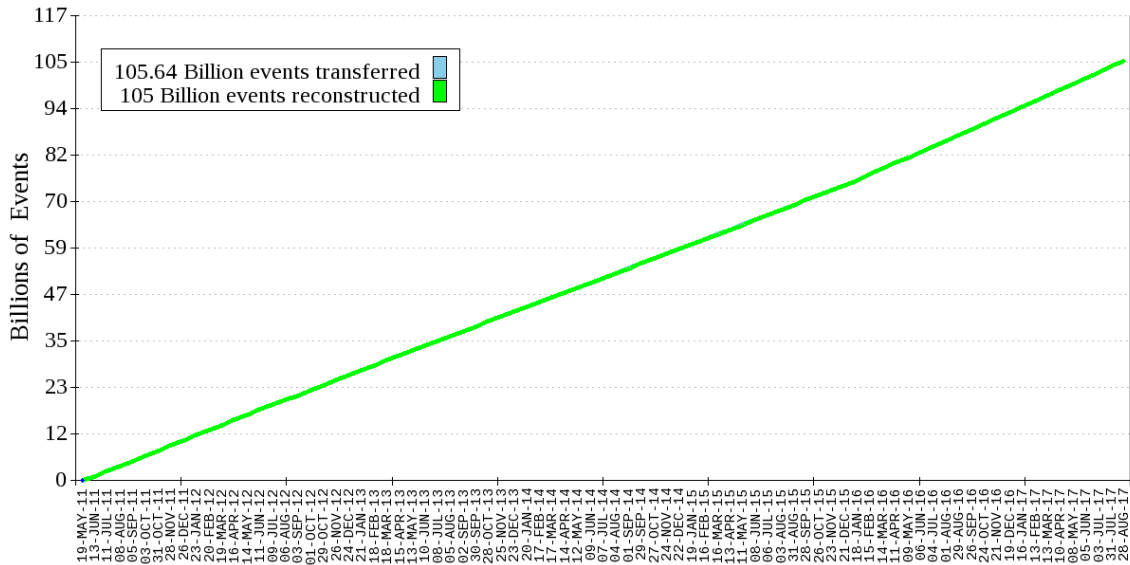
Figure C.68.: Cumulated number of collected events with time from May 2011 to August 2017 that were transferred to ground, and the number of events reconstructed [192]. Both graphs are overlayed and show a linear grow in statistics over the full measuring time.